Environmental
Studies
Research
Funds

193

Refinement and Validation of Numerical Risk Assessment Models for use in Atlantic Canada

Canada

2013

Refinement and Validation of Numerical Risk Assessment Models for use in Atlantic Canada

Final Report for Project 090585

Prepared for

Environmental Studies Research Funds

By

Haibo Niu, Kenneth Lee
Centre for Offshore Oil, Gas and Energy Research
Fisheries and Oceans Canada
Bedford Institute of Oceanography
Dartmouth, NS, B2Y 4A2

March 20, 2013

Abstract

To support the application of the DREAM model in Atlantic Canada, this study funded by ESRF conducted a series of model validation studies for discharges of both produced water and drilling wastes in the year 2010. For the produced water cross-validation study, the DREAM model was compared with the CORMIX model. Various conditions (densimetric Froude number from 0.5 to infinity, and velocity ratio from 0.5 to 40) that may occur in discharging produced waters were simulated using both the DREAM and CORMIX models and the predicted plume trajectory, radius and centerline dilution were compared. The comparison found that in most instances, the two models agreed better in cases of smaller densimetric Froude number and velocity ratio. This was especially true for plume trajectory and radius. The DREAM model was also compared with field data (concentrations of iron, ammonia, phenol and naphthalene) collected from the Venture platform located offshore of Nova Scotia and Terra Nova FPSO off Newfoundland. The results indicated that DREAM predicted both the dilution and trajectory very well. A case study was conducted to cross-validate the DREAM (ParTrack) and the bblt model. The scenarios studied were two bblt scenarios with different log-layer heights and two DREAM (ParTrack) scenarios with different discharge depths. Although DREAM (ParTrack) and bblt are formulated quite differently, the case study showed that the bblt-0.5 m case is comparable to that of the DREAM (ParTrack) results, especially for locations far from the discharge point. At locations close to the discharge, ParTrack predicted higher concentrations due to the deposition of particles.

Résumé

Pour appuyer l'application du modèle DREAM dans le Canada atlantique, cette étude financée par le Fonds pour l'étude de l'environnement (FEE) a réalisé une série d'études de validation du modèle touchant les rejets d'eau produite et de déchets de forage au cours de l'année 2010. Pour l'étude de contre-validation touchant l'eau produite, on a comparé le modèle DREAM au modèle CORMIX. Diverses conditions (nombre de Froude densimétrique allant de 0,5 à l'infini et vitesse de montée de la charge allant de 0,5 à 40) susceptibles de se produire dans les rejets d'eau produite ont été simulées au moyen des modèles DREAM et CORMIX et on a comparé la trajectoire prévue, le rayon prévu et la dilution au centre prévue du panache. La comparaison a révélé que dans la plupart des cas, les résultats des deux modèles sont plus proches dans les cas où le nombre de Froude densimétrique et le rapport de vitesse sont plus faibles, en particulier pour la trajectoire et le rayon du panache. Le modèle DREAM a également été comparé aux données de terrain (concentrations de fer, d'ammoniac, de phénol et de naphtalène) recueillies sur la plateforme Venture au large de la Nouvelle-Écosse et de l'unité flottante de production, stockage et déchargement en mer (FPSO) Terra Nova au large de Terre-Neuve. Les résultats indiquent que le DREAM a très bien prévu la dilution et la trajectoire. On a réalisé une étude de cas pour contre-valider le modèle DREAM (ParTrack) et le modèle de transport dans la couche limite de la zone benthique (*benthic boundary layer transport* – bblt). On a étudié deux scénarios de bblt avec différentes hauteurs de couche logarithmique et deux scénarios DREAM (ParTrack) avec différentes profondeurs de rejet. Même si les modèles DREAM (ParTrack) et bblt sont formulés de manière sensiblement différente, l'étude de cas a révélé que les résultats du cas bblt à 0,5 m sont comparables à ceux du DREAM (ParTrack), en particulier pour les endroits éloignés du point de rejet. Aux endroits près du point de rejet, ParTrack a prévu des concentrations plus élevées en raison du dépôt de particules.

Table of Contents

List of Figures

List of Tables

1. Introduction

The exploration and extraction of offshore oil and gas from beneath the ocean floor has led to the disposal of produced water in the marine environment. Produced water, also called ‘production’ water, is the aqueous fraction extracted along with oil and gas from geological formations. The produced water consists of formation water (water naturally present in the reservoir), flood water (seawater injected into the formation to maintain reservoir pressure), and condensed water (which is water that was in the vapour phase while in the reservoir but then condenses into a liquid state in the production separation system) (Clark and Veil, 2009).

A priority concern of regulators and the environmental community is that of production water discharges into the ocean that may cause contamination and ill effects on fish, fish habitat and benthic communities. There is some evidence from North Sea “biomarker” investigations that suggest offshore production water discharges may have impacts on the biota (invertebrates, fish and larvae) at an exposure dose of 0.125% (Sundt et al., 2012). Furthermore, greater awareness of its potential to induce environmental damage has been raised by the results of laboratory tests that suggested production water discharges could impact the reproductive success of commercial fish species such as cod.

Regional studies within Atlantic Canada are needed to assess the environmental risks associated with produced water discharges since the concentration and composition of contaminants within produced water can vary between geological formations and over the lifespan of the well.

In Canada, produced water discharges are currently regulated by a 30 day volume weighted average oil in water concentration which should not exceed 30 mg/L and a 24 hour average oil in water concentration which should not exceed 44 mg/L (measured at least twice a day). Regional studies are required to provide scientific data for the ongoing revision and update of Canada’s Offshore Waste Treatment Guidelines for the following reasons:

- the differences in composition and concentration of produced water discharges,
- potential synergistic effects between specific contaminant fractions, and
- the potential for inter-regional differences in sensitivity between common species.

The 2007 International Produced Water Conference (funded by Environmental Studies Research Funds) highlighted the level of international effort required to assess the toxicity and risk of produced water discharge into the ocean (Lee and Neff, 2011). The results of traditional regulatory toxicity tests (acute LC_{50}) do not appear to have the level of sensitivity to detect chronic effects associated with long-term exposure at low exposure levels. Environmental concern is now focused on cumulative effects as the rate of discharge and the number of offshore facilities increase. For environmental relevance, an integrated research program based on the development of environmental effects monitoring protocols for use in the field is recommended, as well as improvements in the application of risk prediction models.

Following the Norwegian authorities' requirements in 1997 of "zero harmful discharges to sea" by the end of 2005 (Smit et al., 2011), the companies operating on the Norwegian shelf initiated the development of a modeling tool used for guiding management decisions for reduction of potential harmful environmental effects associated with produced water discharges. This effort was embodied in the DREAM (Dose-related Risk and Effect Assessment Model) project, from which the Environmental Impact Factor for produced water (EIF_{PW}) was born. The EIF_{PW} was developed as a management tool to be applied by the oil industry. Its calculation is based on internationally accepted procedures for hazard and risk assessment using the PEC/PNEC ratio, also termed risk characterisation ratio (RCR). The PEC/PNEC approach compares the Predicted Environmental Concentration (PEC) of a pollutant with the predicted environmental tolerance level or the concentration below which the likelihood of adverse effects in the environment is considered to be acceptable (PNEC = Predicted No Effect Concentration). The EIF approach, implemented in DREAM, has proven to be very useful in decision-making for produced water treatment techniques and the use of offshore E&P chemicals; it represents the state of the art in marine water column risk assessment tools. The collection of reliable toxicity data for selection of reliable PNEC values was a major factor in the development of the DREAM/EIF model approach. Although the private sector is currently using the DREAM model in Atlantic Canada for risk assessment, the lack of region-specific toxicity data has limited the acceptance of predictive models such as DREAM.

To support the application of DREAM in Atlantic Canada, this study, funded by ESRF, had the following objectives:

1. simulate various conditions that may occur during the discharge of produced water using both the DREAM and CORMIX models, cross-validate the models to study the accuracy of DREAM;
2. compare data collected from offshore sampling missions conducted by COOGER with model predictions to validate the model's capability to simulate chemical/biological processes;
3. update the DREAM model with a regional-specific toxicity database which can be utilized in future risk assessments.

2. Produced Water Cross Validation Study

The performance of the EIF depends on the accuracy of DREAM's fate and transport model. The fate/transport model must be validated by comparing its prediction with experimental data. Validation improves user confidence in model predictions. However, full validation of a model with field data is often difficult due to the lack or unavailability of data. On the other hand, comparison of one model with similar models can also help to improve model confidence.

The DREAM model was compared with a widely used buoyant jet model, CORMIX (Doneker and Jirka, 1990). For buoyant jet models, the validation process generally involves the comparison with plume trajectory, downstream concentration, and plume width for various ambient conditions and discharge parameters.

2.1 Methodology

2.1.1 DREAM Model

DREAM (Dose-related Risk and Effects Assessment Model) is a software tool designed to support rational management of environmental risks associated with operational discharges of complex mixtures. The model includes calculations of exposure concentration, exposure time, uptake, depuration and effects for fish and zooplankton subjected to complex mixtures of chemicals. For each chemical in the mixture, the governing physical and chemical processes are taken into account individually, such as:

- vertical and horizontal dilution and transport,
- dissolution from droplet form,
- volatization from the dissolved or surface phase,
- particulate adsorption/desorption and settling,
- degradation, and
- sedimentation to the sea floor.

The model solves the generalized transport equation (Reed and Hetland, 2002)

$$\frac{\partial C_i}{\partial t} + \vec{V} \cdot \vec{\nabla} C_i = \vec{\nabla} \cdot D_k \vec{\nabla} C_i + \sum_{j=1}^{n} r_j C_i + \sum_{j=1}^{n} \sum_{i=1}^{n} r_{ij} C_i \qquad \textbf{(1)}$$

where C_i is the concentration of i^{th} chemical constituent in the release, $\vec{V}$ is the advective transport vector, $\vec{\nabla}$ is the gradient operator, D_k is the turbulent dispersion coefficient in x, y, z directions, and r_j are process rates including evaporation, dissolution, degradation, and deposition. The degradation term $\mathrm{r_{ij}}$ at the right hand side of the equation is to track degradation by-products as transfer of mass from one component to another.

The model solves the transport equation from the time- and space-variable distribution of individual pseudo-Lagrangian particles as it moves through space and time. Each mathematical particle represents a Gaussian puff of a contaminant and has the following attributes: special coordinates, mass of each chemical constituent represented by the particle, distance to and identity of the nearest neighbour particle, time since release, spatial standard deviation, and mean particle/droplet diameter and density. The concentration fields are computed from the superposition of these puffs.

The advection of the particles is simulated as the superposition of a mean local velocity (climatological, tidal, wind- and wave-driven components) plus a random turbulent component. The turbulent component, u_t, is calculated from

$$u_t = \sqrt{6D_k / \Delta t}\,. \tag{2}$$

The horizontal dispersion coefficient D_x is approximated from data on dye diffusion studies (Bowden, 1983) as

$$D_x = 0.0027t^{1.34}\,. \tag{3}$$

The D_x in equation (3) is in cm^2/s and t is in seconds. The vertical turbulent diffusion coefficient D_z is related to the wave conditions following Ichiye (1967), thus:

$$D_z = 0.028\frac{H^2}{T}\exp(-2Kh) \tag{4}$$

where H is the wave height, T is the wave period, K is the wave number, and h is the depth below sea surface.

In the near-field plume model of DREAM, the equations for the continuity of mass, momentum and scalar properties are defined for control volumes bounded by cross-sections normal to the trajectory of the plume. DREAM used the Lagrangian approach and the plume was represented by a series of non-interfering elements. Each jet element was treated as a section of a bent cone and the change in element properties was examined at discrete time steps, Δt. The entrainment of the ambient fluids into the jet element was determined at each time step. Based on the increase in element mass, the momentum, energy, and tracer mass conservation equations were solved in their integral form to give the velocity, density, and concentration at the next time step (Lee & Chu, 2003).

If the plume is assumed to be stationary (both currents and discharge rate are constant during the rise time), the plume can be described fully by tracking a single element through the water until the element eventually hits the surface (or seabed), or it is trapped by a density gradient. After plume termination, special advection rules are applied for the far-field particles depending on how the plume terminated. For surfacing plumes, a radial spreading velocity is superimposed on the common far-field advection rule after the plume phase has reached the surface (source flow). For plumes touching the sea bottom, a radial spreading velocity must be superimposed after the plume phase has reached the seabed (modified source flow including a bottom friction term). For trapped plumes, the common far-field rules apply.

2.1.2 CORMIX Model

CORMIX is a USEPA-supported mixing zone model and decision support system for environmental impact assessment of regulatory mixing zones resulting from continuous point source discharges. The system emphasizes the role of boundary interaction to predict steady-state mixing behaviour and plume geometry.

The current version of CORMIX includes three submodels—CORMIX1 for submerged single-port discharges, CORMIX2 for submerged multi-port discharges, and CORMIX3 for surface discharges. CORMIX also has a D-CORMIX submodel which extends the CORMIX expert system to water quality prediction from continuous dredge disposal sources.

CORMIX contains a rule-based flow classification scheme developed to classify a given discharge and environment interaction into one of several flow classes with distinct hydrodynamic features. The classification scheme places major emphasis on the near-field behaviour of the discharge and uses the length scale concept as a measure of the influence of each potential mixing process. Flow behaviour in the far field, after boundary interactions, is largely controlled by ambient conditions. Once a flow has been classified, integral, length scale, and passive diffusion simulation modeling methods are utilized to predict the flow process details (Doneker and Jirka, 2007).

The near field of CORMIX is an Eulerian formulation. For a discharge with an initial volume flux Q_0, momentum flux M_0, buoyancy flux B_0, and mass flux QC_0, the following bulk variables for total volume flux Q, momentum flux M, buoyancy flux B, and pollutant mass flux QC are obtained through cross-sectional integration (Jirka 2004):

$$Q = 2\pi \int_0^{Rj} Urdr = \pi b^2 (U_c + 2u_a \cos\phi \cos\theta) \tag{5}$$

$$M = 2\pi \int_0^{Rj} U^2 rdr = \pi \frac{b^2}{2} (U_c + 2u_a \cos\phi \cos\theta)^2 \tag{6}$$

$$B = 2\pi \int_0^{Rj} Ug' rdr = \pi \frac{b^2}{2} (U_c + 2u_a \cos\phi \cos\theta) g_c' \tag{7}$$

$$QC = 2\pi \int_0^{Rj} C \cdot Urdr = \pi b^2 (U_c \frac{\lambda^2}{1+\lambda^2} + \lambda^2 u_a \cos\phi \cos\theta) C_c \tag{8}$$

where r is radial distance in a local cylindrical coordinate system, Rj is an integration limit ($Rj \rightarrow \infty$), U is the jet velocity with subscript c denoting centerline values, b is the jet width, and λ describes a dispersion ratio for the scalar quantities.

For a jet element of length ds centered on the trajectory, the conservation principles for volume, momentum, and mass lead to the following Equations (Jirka, 2004):

volume change, $$\frac{dQ}{ds} = E; \tag{9}$$

x-momemtum change,

$$\frac{d}{ds}(M\cos\phi\cos\theta) = Eu_a + F_D\sqrt{1-\cos^2\phi\cos^2\theta}\,; \tag{10}$$

y-momemtum change,

$$\frac{d}{ds}(M\cos\phi\sin\theta) = -F_D\frac{\cos^2\phi\sin\phi\sin\theta}{\sqrt{1-\cos^2\phi\cos^2\theta}}\,; \tag{11}$$

z-momemtum change,

$$\frac{d}{ds}(M\sin\theta) = \pi\lambda^2 b^2 g'_c - F_D\frac{\sin\phi\cos\phi\cos\theta}{\sqrt{1-\cos^2\phi\cos^2\theta}}\,; \tag{12}$$

buoyancy change,

$$\frac{dB}{ds} = Q\frac{d\rho_a}{dz}g\sin\phi\ ; \tag{13}$$

pollutant mass flux change,

$$\frac{dQC}{ds} = 0\,; \tag{14}$$

jet trajectory,

$$\frac{dx}{ds} = \cos\phi\cos\theta,\ \frac{dy}{ds} = \cos\phi\sin\theta,\ \frac{dz}{ds} = \sin\phi\,; \tag{15}$$

where E is the entrainment rate and F_D is the ambient drag force acting on the jet element. The turbulence closure of the above formulations is obtained by specification of E and F_D.

In the intermediate field, the approach developed by Jones et al. (1983) is adopted. CORMIX also considers buoyant spreading and wind-induced entrainment. In the turbulent diffusion region, it assumes a top-hat profile and considers only the change of concentration along x- (downstream) and z-directions (vertical). By assuming that flow is affected by wind-induced entrainment, interfacial shear entrainment, and frontal entrainment, the following conservation equations were derived:

Continuity,

$$U_a\frac{\partial h}{\partial x} + \frac{\partial(v_{lat}h)}{\partial y} = w_{ew} + w_{ei} + w_{ef}\,; \tag{16}$$

Lateral Momentum,

$$v_{lat}\frac{\partial v_{lat}}{\partial y} = -g'\frac{\partial h}{\partial y} + \lambda_i\frac{v_{lat}^2}{h}\,; \tag{17}$$

Buoyancy,

$$U_a\frac{\partial(g'h)}{\partial x} + \frac{\partial(g'v_{lat}h)}{\partial y} = -k_{bl}g'\,; \tag{18}$$

where x is the downstream coordinate, y is the lateral coordinate, v_{lat} is the lateral velocity, h is the plume height, λ_i is the interfacial friction coefficient with values ranging from 0.002 to 0.005, w_{ew} is the wind-induced entrainment, w_{ei} is the interfacial shear entrainment, and w_{ef} is the frontal entrainment.

2.1.3 Selection of Cases

For studies of plume behaviour, the two most important dimensionless parameters are the densimetric Froude number, *Fr* (Eq. 19), and the exit-to-cross-flow velocity ratio, *K* (Eq. 20):

$$Fr = \frac{U_j}{\sqrt{g \frac{\Delta\rho}{\rho} D}} \qquad \textbf{(19)}$$

$$K = U_j / U_a \qquad \textbf{(20)}$$

where U_j is the exit velocity, D is pipe diameter, $\Delta\rho/\rho$ is the difference between the ambient density and that of the effluent, divided by the ambient density at the discharge point, g is the acceleration due to gravity, and U_a is the ambient velocity. The Froude number, *Fr*, indicates the relative importance of jet momentum versus buoyancy effects in determining plume behaviour. The exit-to-cross-flow velocity ratio, *K*, indicates the tendency of ambient current to deflect the plume.

Densimetric *Fr* numbers for produced water generally range from 0.1 to 10, whereas the *Fr* would be infinite for a neutrally buoyant plume. By assuming an ambient density of 1020 kg/m^3 and discharge density of 1060, Nedwed et al. (2004) have determined that the median *Fr* of 353 Gulf of Mexico produced waters is 0.32 and the maximum *Fr* is 7.2. The produced water from the study by Terrens and Tait (1994) has an *Fr* of 19.3. In this study, the range for *Fr* was 0.5 to infinity (Figure 1 and Table 1).

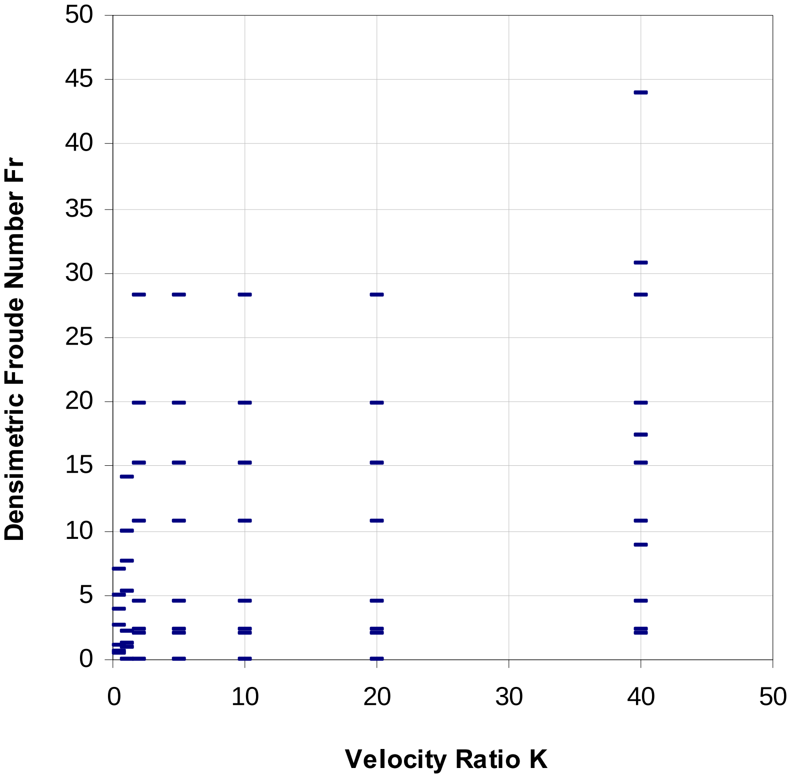

Figure 1: Range of *Fr* and *K* for the cross-validation cases. A case of *Fr*=infinite for *K*=40 was also conducted (not shown in the figure).

The exit-to-cross-flow velocity ratio can vary from 0 to infinity, theoretically. Nedwed et al. (2004) have stated the most likely range to be from 0.1 to 80. The range used in this study was from 0.5 to 40 based on available experimental data (Figure 1 and Table 1).

Table 1: Summary of Discharge Conditions of Cases for Cross-Validation Study

Group	No.	D (m)	U_j (m/s)	Q (m^3/d)	U_a (m/s)	ρ_i	ρ_a	K	Fr
A	1	0.05	1	169.64586	0.025	995.8739	998.4352	40	28.19071
	2	0.1	1	678.58344	0.025	995.8739	998.4352	40	19.93384
	3	0.17	1	1961.1061	0.025	995.8739	998.4352	40	15.28856
	4	0.35	1	8312.6471	0.025	995.8739	998.4352	40	10.65509
	5	0.5	1	16964.586	0.025	988.2826	998.4352	40	4.477666
	6	0.5	1	16964.586	0.025	988.2826	1024.981	40	2.386236
	7	0.5	1	16964.586	0.025	974.1203	1027.907	40	1.973877
B	8	0.05	1	169.64586	0.05	995.8739	998.4352	20	28.19071
	9	0.1	1	678.58344	0.05	995.8739	998.4352	20	19.93384
	10	0.17	1	1961.1061	0.05	995.8739	998.4352	20	15.28856
	11	0.35	1	8312.6471	0.05	995.8739	998.4352	20	10.65509
	12	0.5	1	16964.586	0.05	988.2826	998.4352	20	4.477666
	13	0.5	1	16964.586	0.05	988.2826	1024.981	20	2.386236
	14	0.5	1	16964.586	0.05	974.1203	1027.907	20	1.973877
C	15	0.05	1	169.64586	0.1	995.8739	998.4352	10	28.19071
	16	0.1	1	678.58344	0.1	995.8739	998.4352	10	19.93384
	17	0.17	1	1961.1061	0.1	995.8739	998.4352	10	15.28856
	18	0.35	1	8312.6471	0.1	995.8739	998.4352	10	10.65509
	19	0.5	1	16964.586	0.1	988.2826	998.4352	10	4.477666
	20	0.5	1	16964.586	0.1	988.2826	1024.981	10	2.386236
	21	0.5	1	16964.586	0.1	974.1203	1027.907	10	1.973877
D	22	0.05	1	169.64586	0.2	995.8739	998.4352	5	28.19071
	23	0.1	1	678.58344	0.2	995.8739	998.4352	5	19.93384
	24	0.17	1	1961.1061	0.2	995.8739	998.4352	5	15.28856
	25	0.35	1	8312.6471	0.2	995.8739	998.4352	5	10.65509
	26	0.5	1	16964.586	0.2	988.2826	998.4352	5	4.477666
	27	0.5	1	16964.586	0.2	988.2826	1024.981	5	2.386236
	28	0.5	1	16964.586	0.2	974.1203	1027.907	5	1.973877
E	29	0.05	1	169.64586	0.5	995.8739	998.4352	2	28.19071
	30	0.1	1	678.58344	0.5	995.8739	998.4352	2	19.93384
	31	0.17	1	1961.1061	0.5	995.8739	998.4352	2	15.28856
	32	0.35	1	8312.6471	0.5	995.8739	998.4352	2	10.65509
	33	0.5	1	16964.586	0.5	988.2826	998.4352	2	4.477666
	34	0.5	1	16964.586	0.5	988.2826	1024.981	2	2.386236
	35	0.5	1	16964.586	0.5	974.1203	1027.907	2	1.973877

Table 1 (continued): Summary of Discharge Conditions of Cases for Cross-Validation Study

	No.	D (m)	U_j (m/s)	Q (m^3/d)	U_a (m/s)	ρ_i	ρ_a	K	Fr
F	36	0.05	0.5	84.82293	0.5	995.8739	998.4352	1	14.09535
	37	0.1	0.5	339.29172	0.5	995.8739	998.4352	1	9.966921
	38	0.17	0.5	980.55307	0.5	995.8739	998.4352	1	7.644279
	39	0.35	0.5	4156.3236	0.5	995.8739	998.4352	1	5.327543
	40	0.5	0.5	8482.293	0.5	988.2826	998.4352	1	2.238833
	41	0.5	0.5	8482.293	0.5	988.2826	1024.981	1	1.193118
	42	0.5	0.5	8482.293	0.5	974.1203	1027.907	1	0.986939
G	43	0.05	0.25	42.411465	0.5	995.8739	998.4352	0.5	7.047677
	44	0.1	0.25	169.64586	0.5	995.8739	998.4352	0.5	4.98346
	45	0.17	0.25	490.27654	0.5	995.8739	998.4352	0.5	3.82214
	46	0.35	0.25	2078.1618	0.5	995.8739	998.4352	0.5	2.663772
	47	0.5	0.25	4241.1465	0.5	988.2826	998.4352	0.5	1.119417
	48	0.5	0.25	4241.1465	0.5	988.2826	1024.981	0.5	0.596559
	49	0.5	0.25	4241.1465	0.5	974.1203	1027.907	0.5	0.493469
H	1b	0.5	1	16964.586	0.025	998.33	998.4352	40	43.9783
	2b	0.5	1	16964.586	0.025	998.22	998.4352	40	30.752
	3b	0.5	1	16964.586	0.025	997.76	998.4352	40	17.36239
	4b	0.5	1	16964.586	0.025	995.8739	998.4352	40	8.914685
	K40N-1	0.5	1	16964.586	0.025	998.4352	998.4352	40	infinite
	K40N-2	0.05	1	169.64586	0.025	998.4352	998.4352	40	infinite

2.1.4 Comparison Methodology

Quantitative comparisons between the two model predictions were made by performing a simple difference calculation using equations (21) and (22), and regression analyses between predictions (Nedwed et al., 2004):

$$\text{absolute difference} = \text{absolute}(\text{model2} - \text{model1}) \, , \tag{21}$$

$$\text{relative difference} = \text{absolute}\left(\frac{\text{model2 - model1}}{\text{model1}}\right). \tag{22}$$

For plume trajectory and radius, both the absolute difference and the relative difference were calculated at the end of the near-field zone (Figure 2). However, the absolute difference is a more meaningful indicator than the relative difference for plume trajectory as the relative error can give misleading results for trajectory (Nedwed et al., 2004).

For the centerline dilution, regression was performed by pairing predictions from both models for locations along the plume trajectory. As the concentration covers a wide range, and linear regression (y=ax+b) may not be able to clearly show the differences, a power law fit ($y=a \cdot x^b$) was used instead, which is able to show the magnitude of differences more clearly.

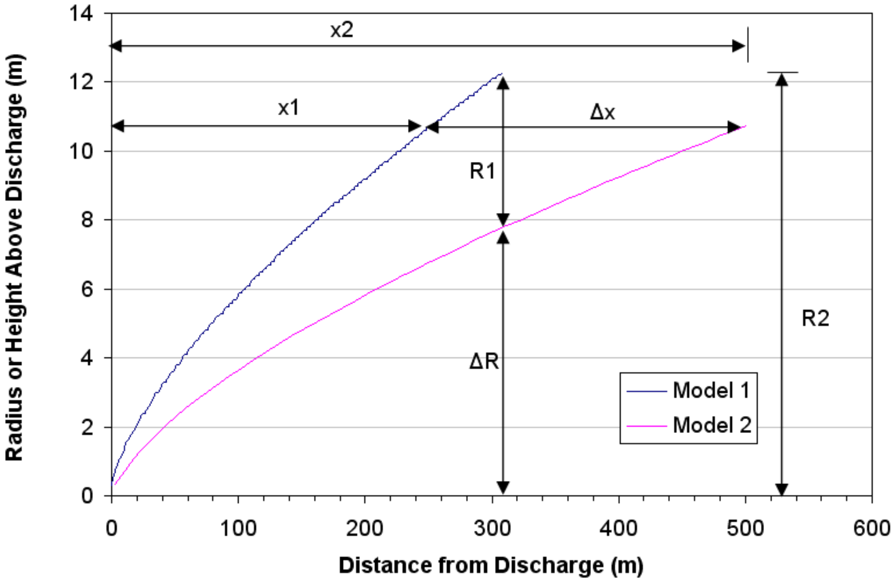

Figure 2: Difference Calculations for Trajectory and Plume Radius.

2.2 Results

2.2.1 Trajectory

The predicted plume centerline trajectories for the 49 cases (Groups A to G) are plotted in Figure 3 to Figure 9. A visual comparison shows that CORMIX predicted lower trajectory than DREAM for 4 of the 7 cases. For the 7 groups with different velocity ratio *K*, the results showed that better agreement was found with decreasing *Fr*. At higher densimetric Froude numbers (15.28-28.19), the two curves tended to diverge. The curves agreed more closely at *Fr* 1.97-10.65 for *K* of 10-40, but as *K* decreased, so did agreement (curves diverged) in spite of decreasing *Fr*.

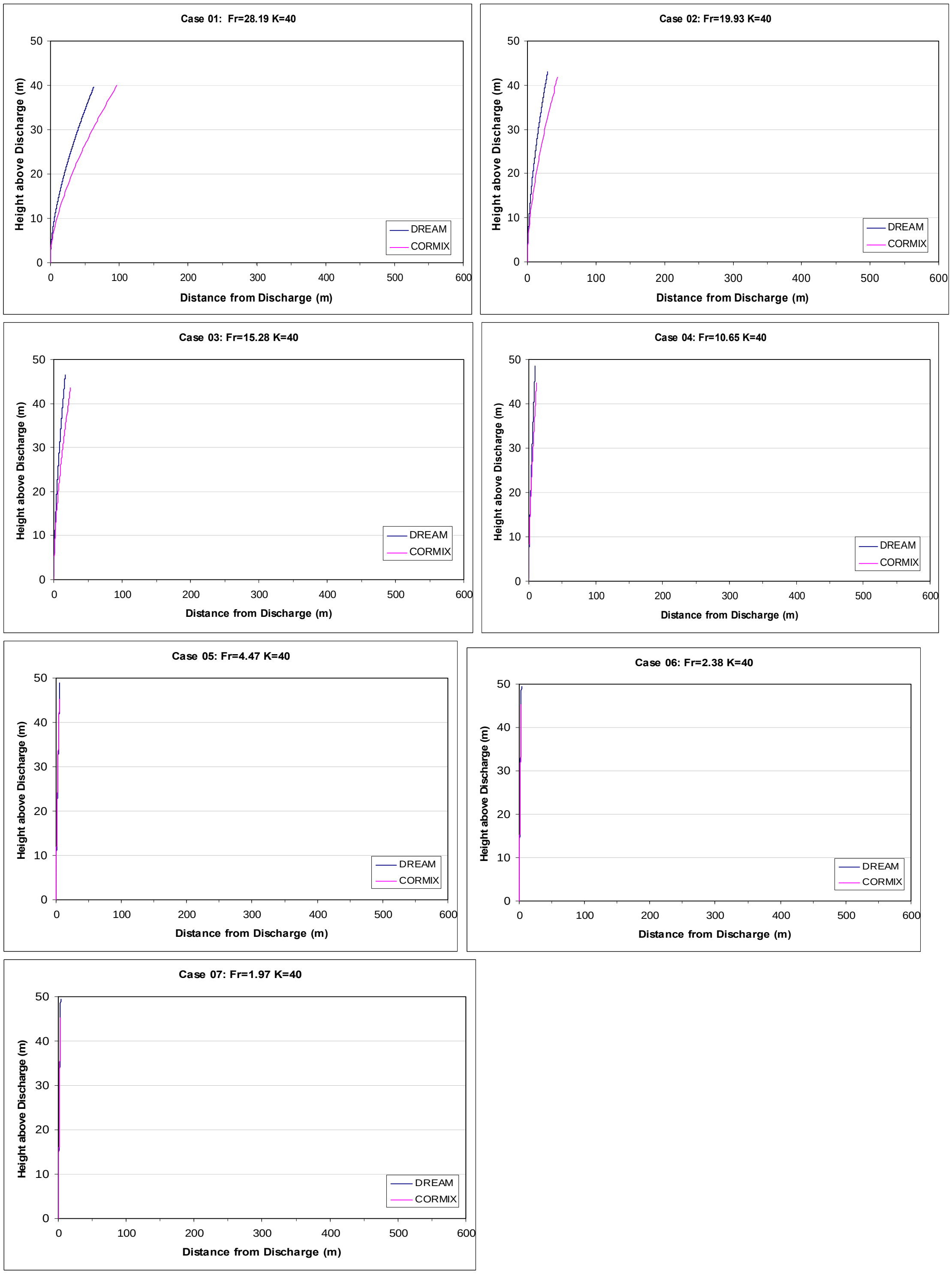

Figure 3: Comparison of Plume Trajectory: Effects of Densimetric Froude Number Fr (Group A: K=40).

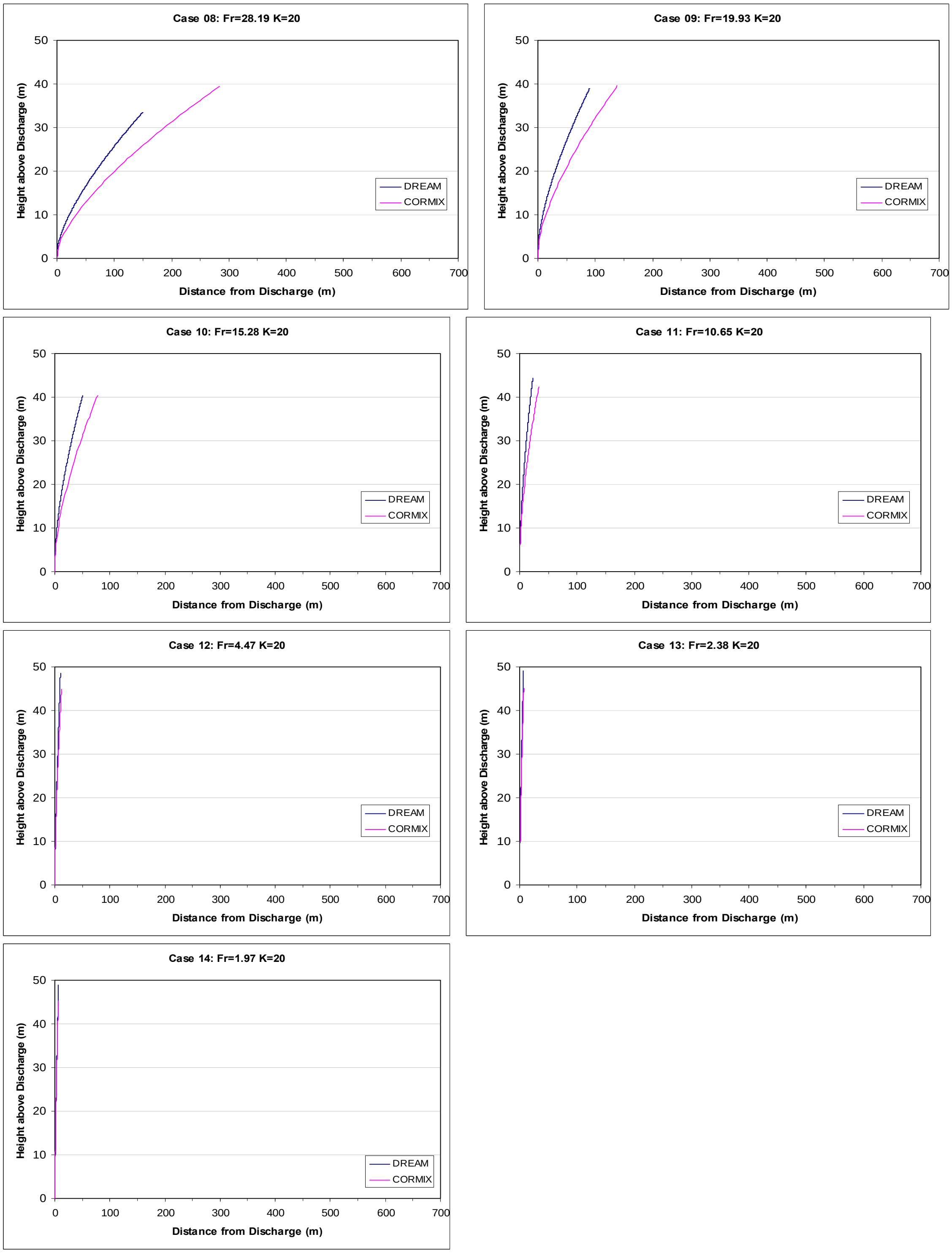

Figure 4: Comparison of Plume Trajectory: Effects of Densimetric Froude Number Fr (Group B: K=20).

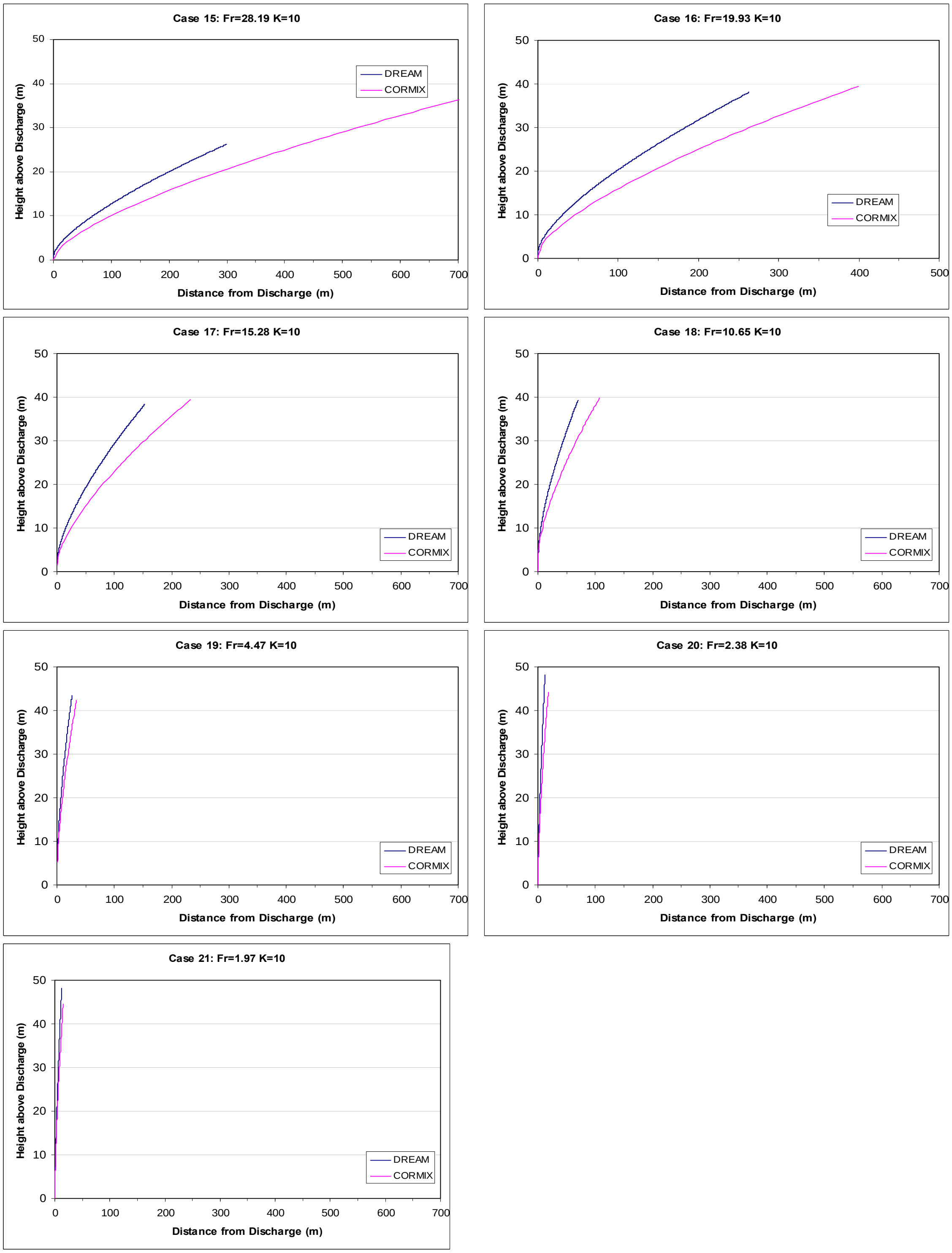

Figure 5: Comparison of Plume Trajectory: Effects of Densimetric Froude Number Fr (Group C: K=10).

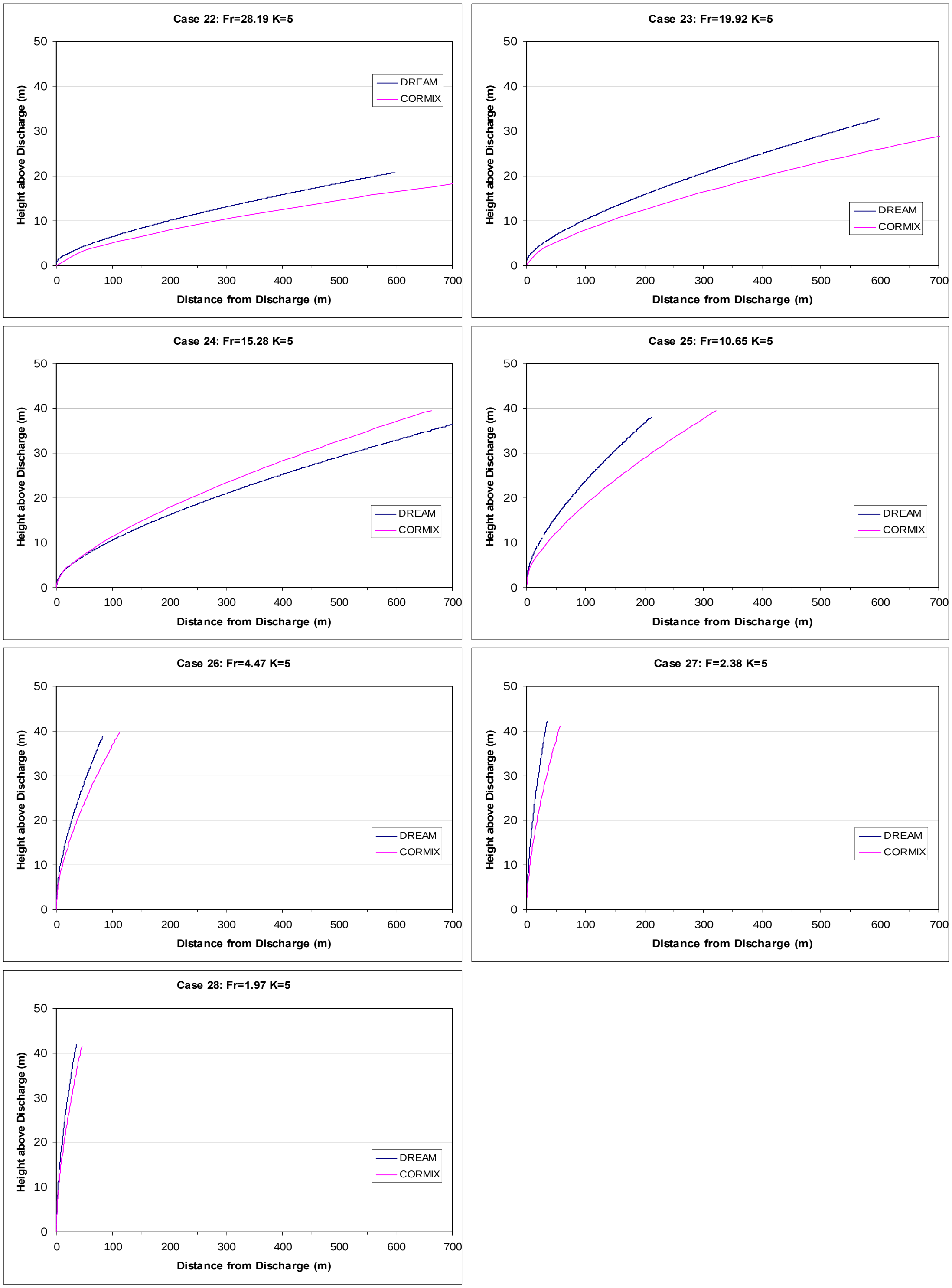

Figure 6: Comparison of Plume Trajectory: Effects of Densimetric Froude Number Fr (Group D: K=5).

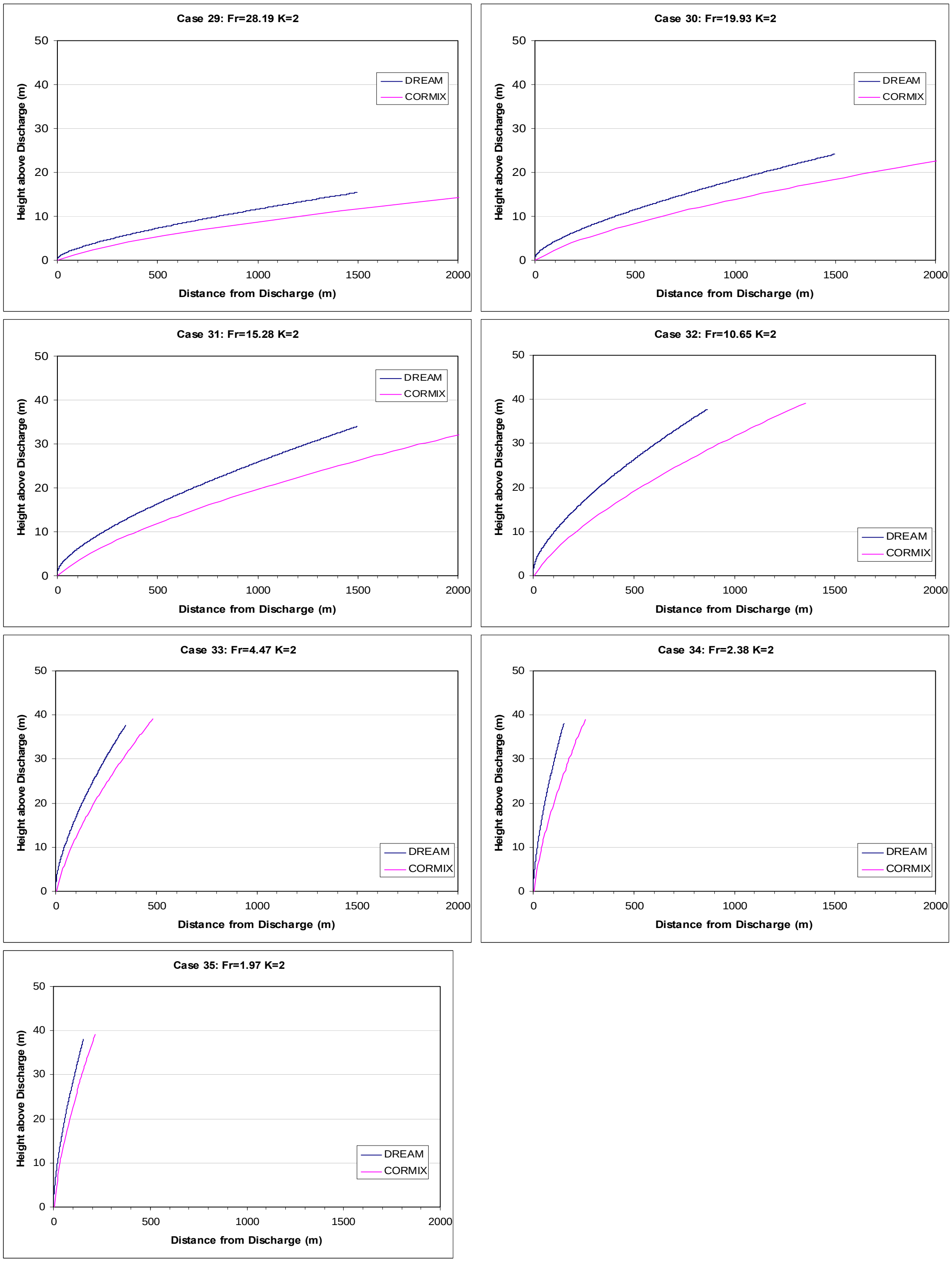

Figure 7: Comparison of Plume Trajectory: Effects of Densimetric Froude Number Fr (Group E: K=2).

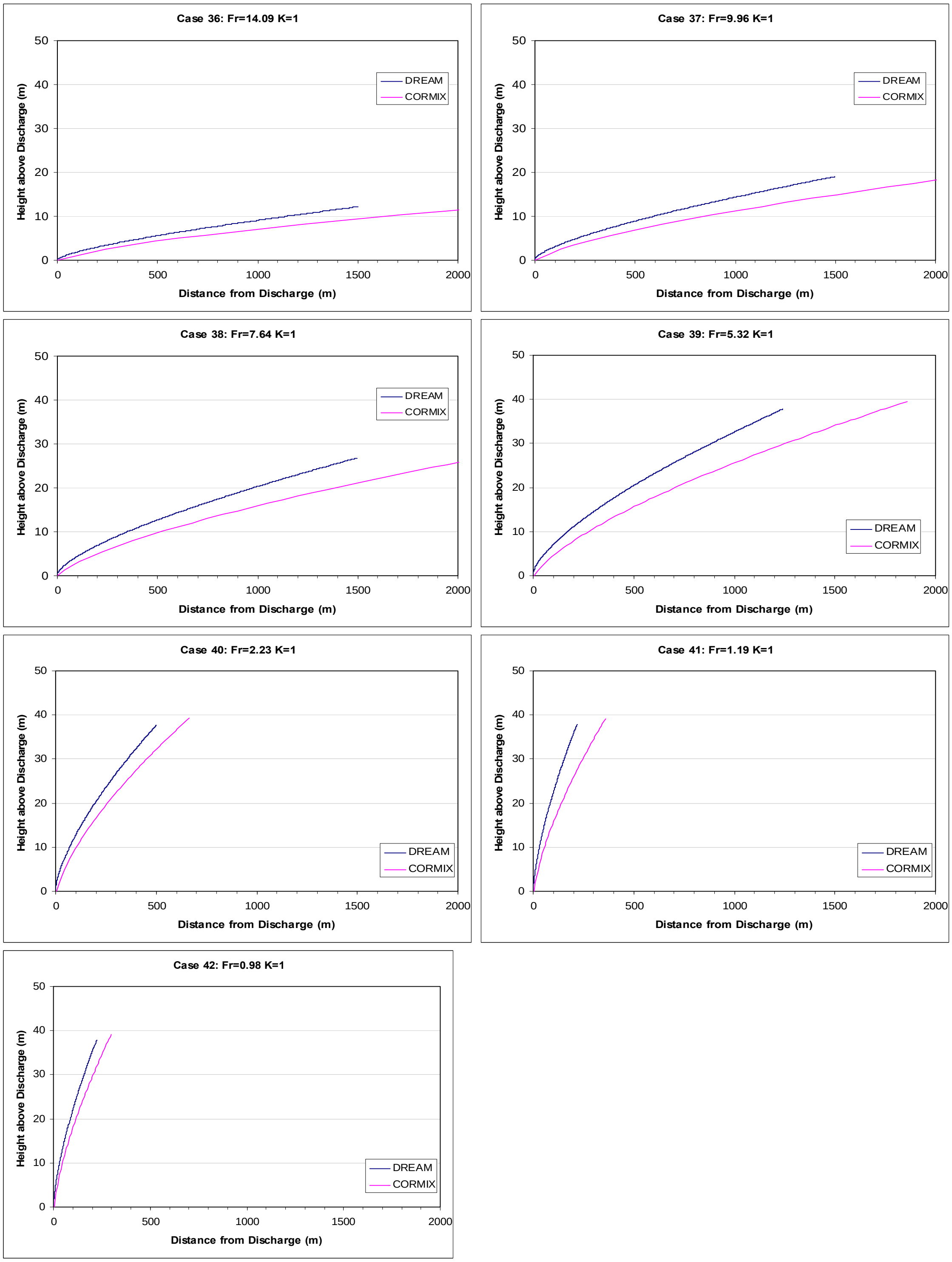

Figure 8: Comparison of Plume Trajectory: Effects of Densimetric Froude Number Fr (Group F: K=1).

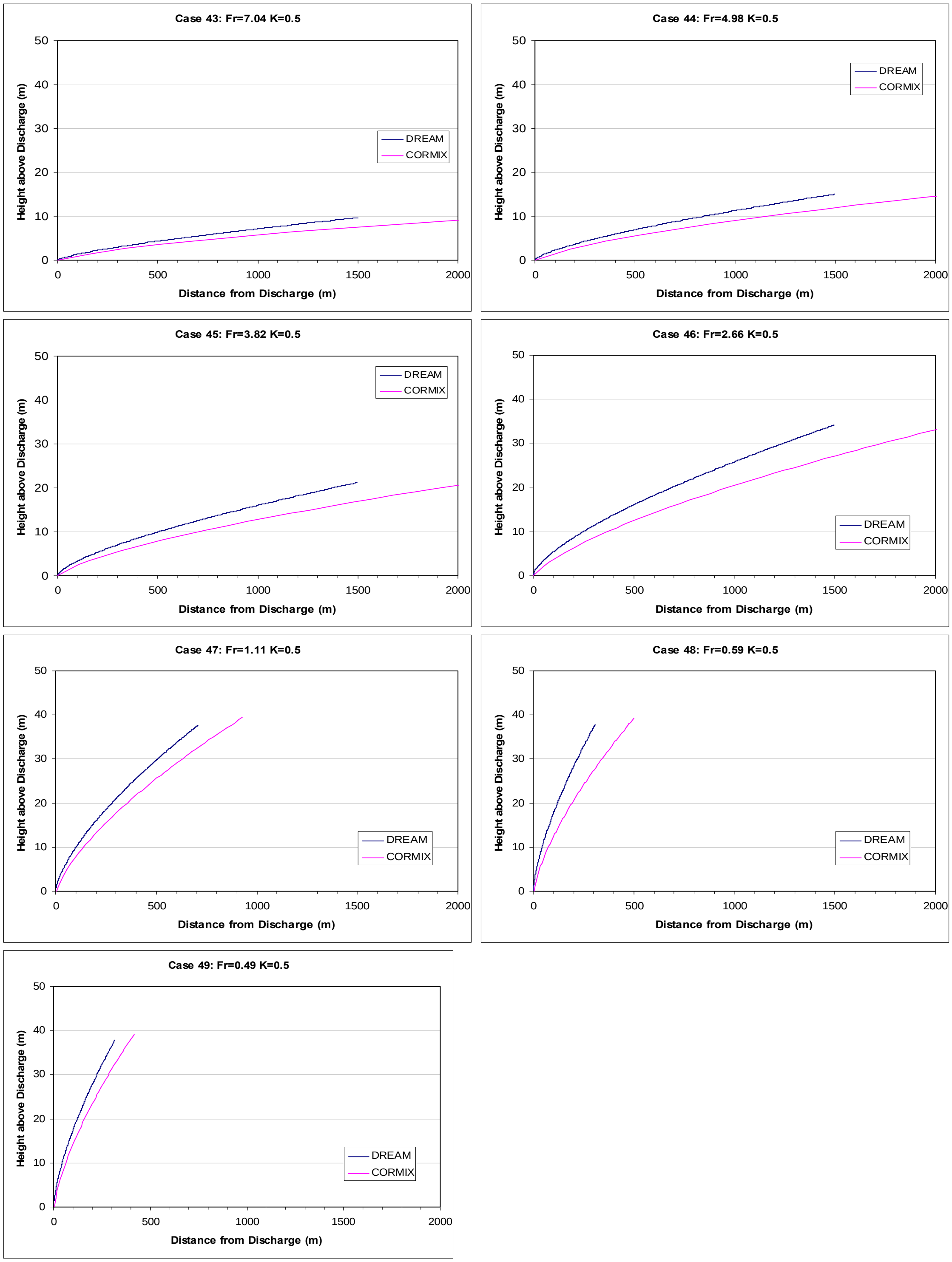

Figure 9: Comparison of Plume Trajectory: Effects of Densimetric Froude Number Fr (Group G: K=0.5).

Quantitative comparisons of the effects of *Fr* on the trajectories are plotted in Figure 10. The results on absolute differences (Figure 10, Top) confirmed the visual observation of increasing agreements with decreasing *Fr* and decreasing agreements with decreasing *K*. For a rise of less than 50 m above the discharge, the horizontal differences predicted by the two models ranged from 0 to 758 m. When *Fr* increased from 1.97 to 28.19, the absolute difference, Δx, increased from 0.12 to 32.27 (Δ(Δx)=32.15 m) for *K*=40, but the Δ(Δ*x*) became 708.3 m for *K*=2. The initial rate of increasing disagreement (Δ*x*/Δ*Fr*) seems to be more significant for smaller velocity ratio cases. The initial slope of the curves is steeper for the cases with a smaller velocity ratio, *K*. More detailed effects of velocity ratio (*K*) on the predictions will be discussed later. After a critical *Fr*, although the disagreements continue to increase, they do so at a much lower rate. The critical *Fr* is smaller for smaller *K*. This finding prompted further investigation of results at high *Fr*, for example *Fr*=infinite.

The changes of relative differences for the 49 cases were also calculated and plotted in Figure 10 (bottom). The overall trend for Groups A and B were an increase in relative difference as *Fr* increased, until a critical *Fr* was achieved. This was similar to the trend in absolute difference. For Groups C to G, their trends agree with that of Groups A and B if their second data points are not considered. The 2nd data point anomaly is uncertain, especially as *Fr*, *K*, *Q*, U_j, U_a were all or partially different. The only common feature for these was the discharge diameter of 0.1 m. This requires further study. The overall range of relative difference was 0% to 69.89% for *K* = 0.5 to 40 and *Fr* = 0.49 to 28.19.

As mentioned, the differences at high densimetric Froude numbers required further study. This is especially important as the Froude number is an important parameter that should be considered in the design of produced water outfall. The study by Cavola (1982) has concluded that both the densimetric Froude number and velocity ratio can affect the dilution ratio for a given discharge rate. It has been found that the Froude Number has the greatest effect on dilution, and both dilution and plume width increase with a decreasing Froude Number. The velocity ratio has a minor effect on dilution. Plume width decreases with increasing velocity ratio. Based on equation (19), a series of simulations for different designs with different Fr by varying port diameter (*D*) and discharge velocity (U_j) can be conducted to maximize the dilution and minimize environmental impacts.

For a velocity ratio of 40, two neutrally buoyant cases with *Fr* of infinite were simulated and the results are shown in Figure 11. Notice that both cases have the same *Fr* and *K* but are significantly different due to the change in discharge volume. Because the change of densimetric Froude number for the 7 groups were combined effects of density and discharge volume (velocity), the conclusions made earlier become questionable based on the results in Figure 11. The effects of *Fr* on the difference in predictions needs to be re-examined for cases with changing *Fr* but the same discharge volume *Q*.

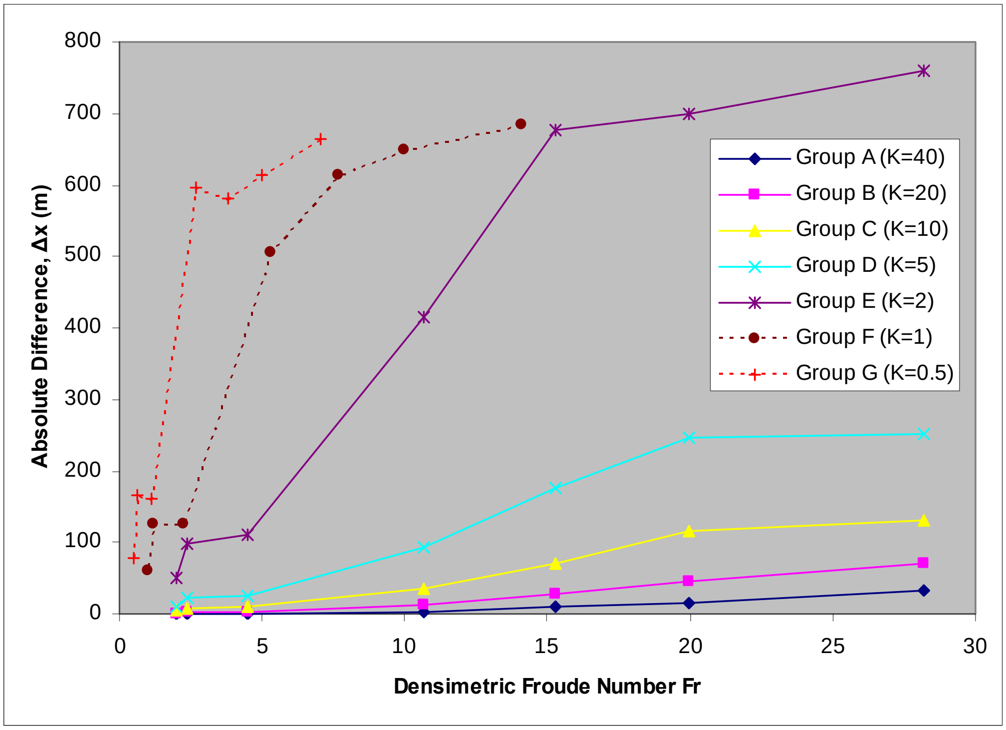

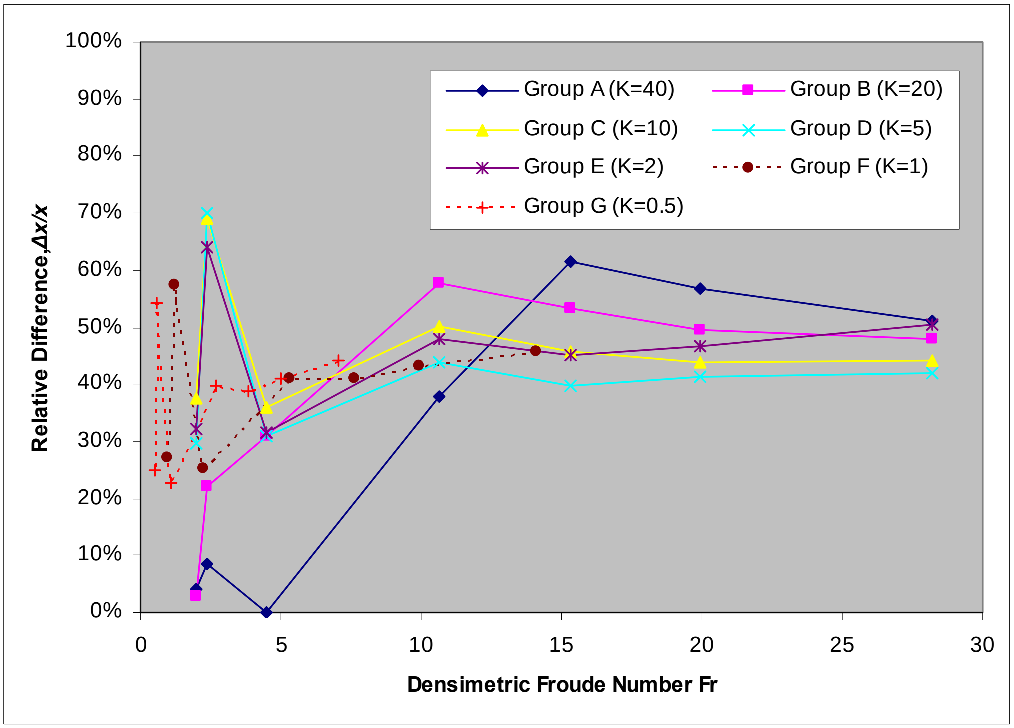

Figure 10: Difference of predicted downstream distance at the terminal layer, *x*, at mininum (H_{Dream}, H_{CORMIX}): variation with *Fr*; absolute difference (top) and relative difference (bottom).

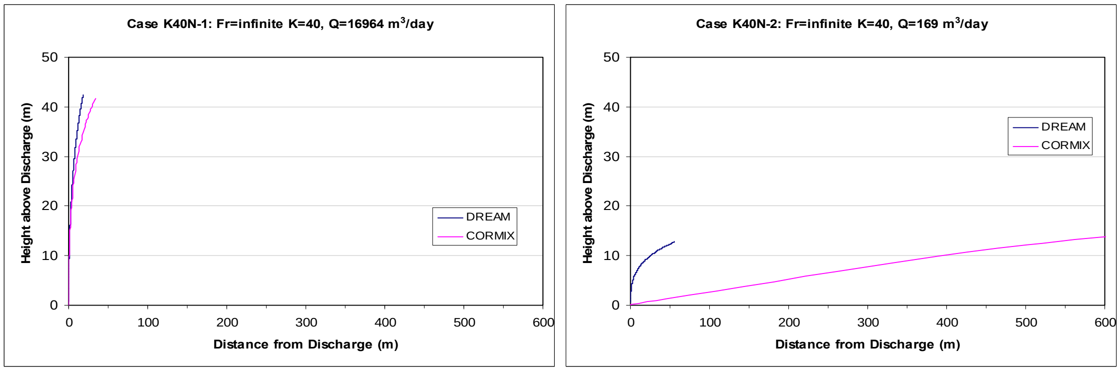

Figure 11: Comparison of Plume Trajectory: Effects of Discharge Volume (K=40)

The results for discharge with the same *K* and *Q* are presented in Figure 12 and Figure 13. Both the absolute and relative differences increase as *Fr* increases and reach a terminal point when *Fr* approaches infinity. The absolute difference increased from 2.85 at *Fr* = 1.97 to 23.57 as *Fr* approaches infinity. The relative difference increased from 3.98% (*Fr* = 1.97) to 93.79% (*Fr* = infinite). The difference reached 48.36% (*Fr* = 17.36) and increased approximately another 50% when *Fr* increased from 17.36 to infinity. This means the initial rate of increase was high and then fell once the critical *Fr* (= ~17.36) was reached. For the case with the same discharge volume, the trend observed is the same as that described earlier (Figure 3 to Figure 9), and therefore the conclusions made earlier still hold true.

To study the effects of velocity ratio (*K*), Figure 14 to Figure 17 were plotted. For all seven *Fr*, it can be seen from the plots that with the increase in velocity ratio (from 2 to 40), the agreement (absolute difference) between predictions increases. However, there is no consistent trend for relative difference. The general trend for the three lines with smaller *Fr* (1.97, 2.38, and 4.47) is the same as the overall trend for absolute difference. The relative difference for the relationship with *Fr* = 10.65 seems to fluctuate around a constant value of ~50%. For the three cases with larger *Fr*, the relative difference seems to increase slightly as *K* increases and this is a reversal of the trend for absolute difference.

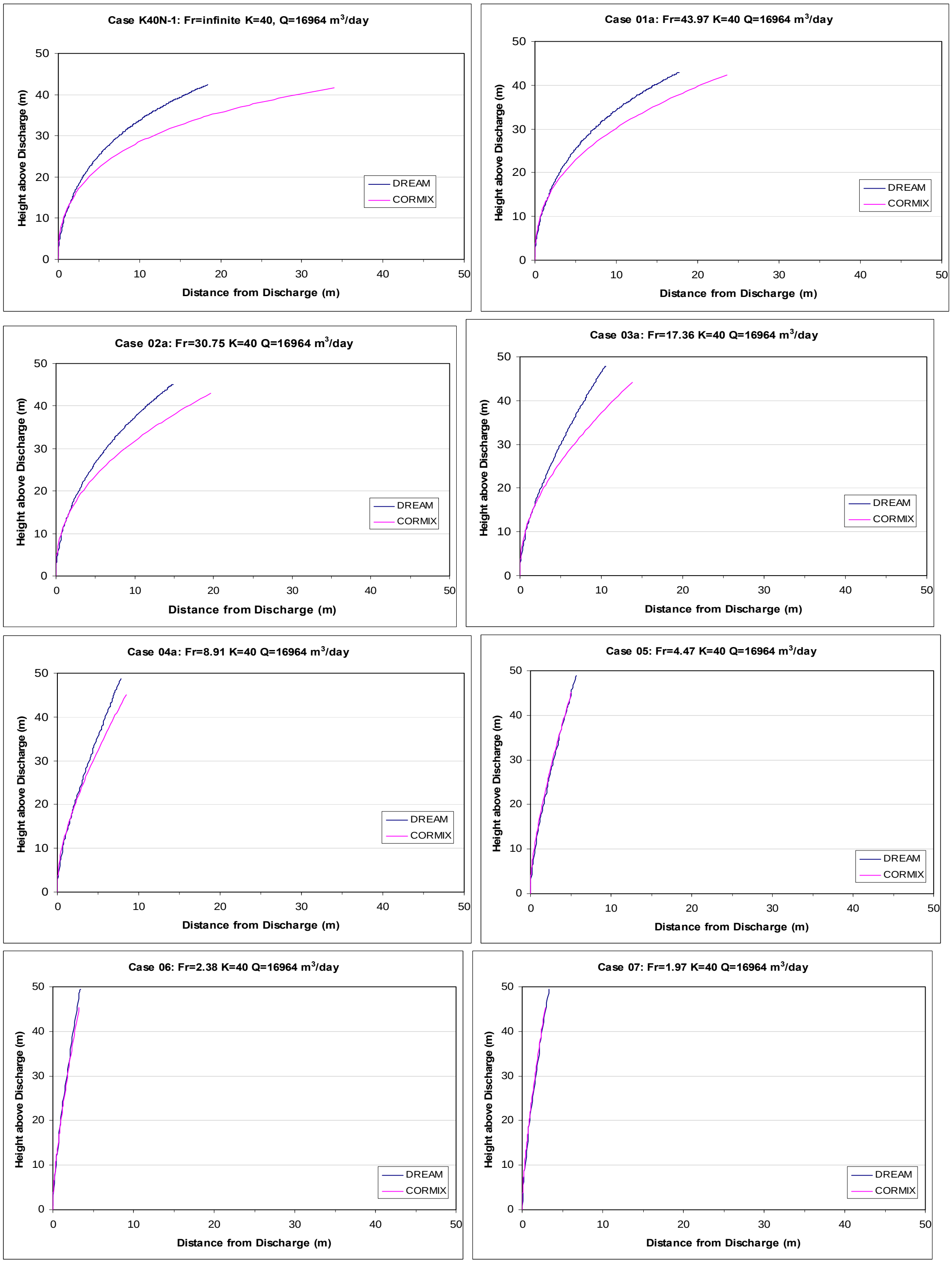

Figure 12: Comparison of Plume Trajectory: Effects of Discharge Froude Number for Same Velocity Ratio and Discharge Volume (K=40).

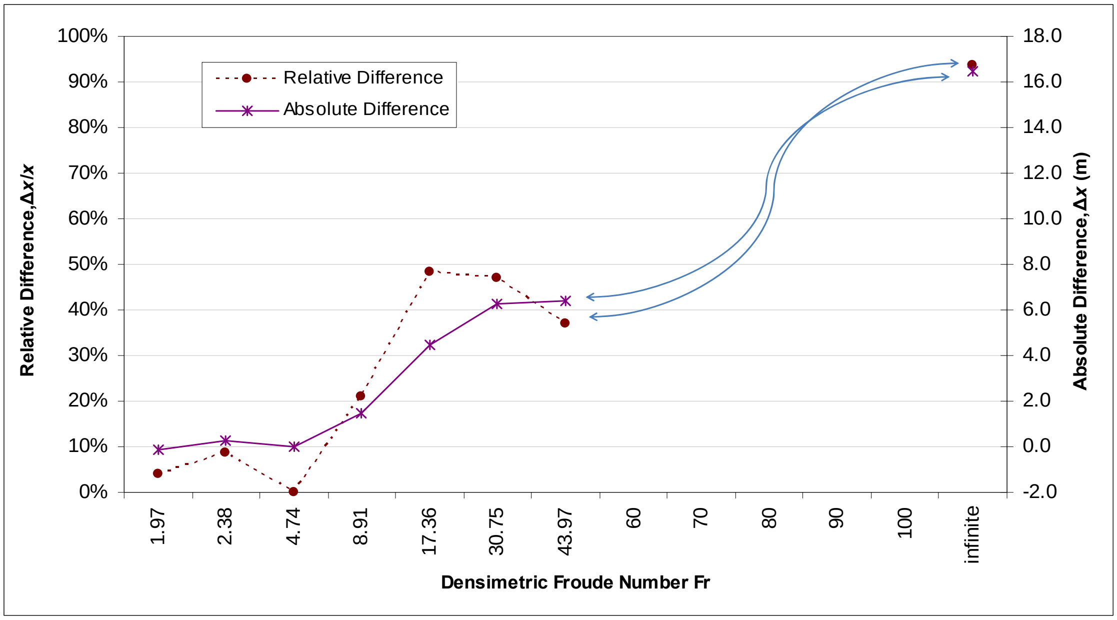

Figure 13: Difference of predicted downstream distance at the terminal layer, *x* at mininum (H_{Dream}, H_{CORMIX}) for same *K* and *Q*. The two lines with arrowhead are plotted to show the trends between Fr=43.97 and Fr≈Infinity.

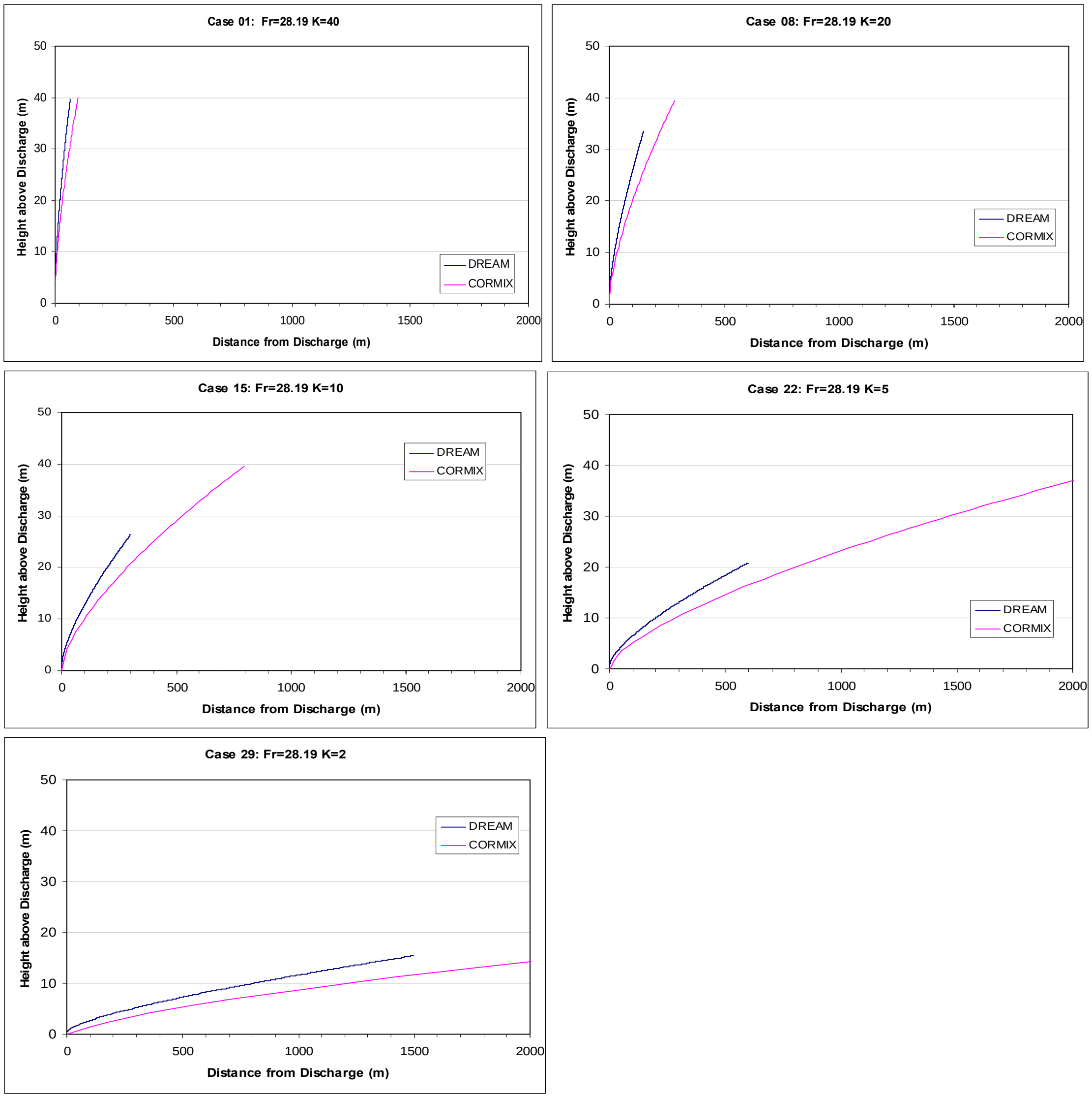

Figure 14: Comparison of Plume Trajectory: Effects of Velocity Ratio K for Same Densimetric Froude Number and Discharge Volume (Fr=28.19).

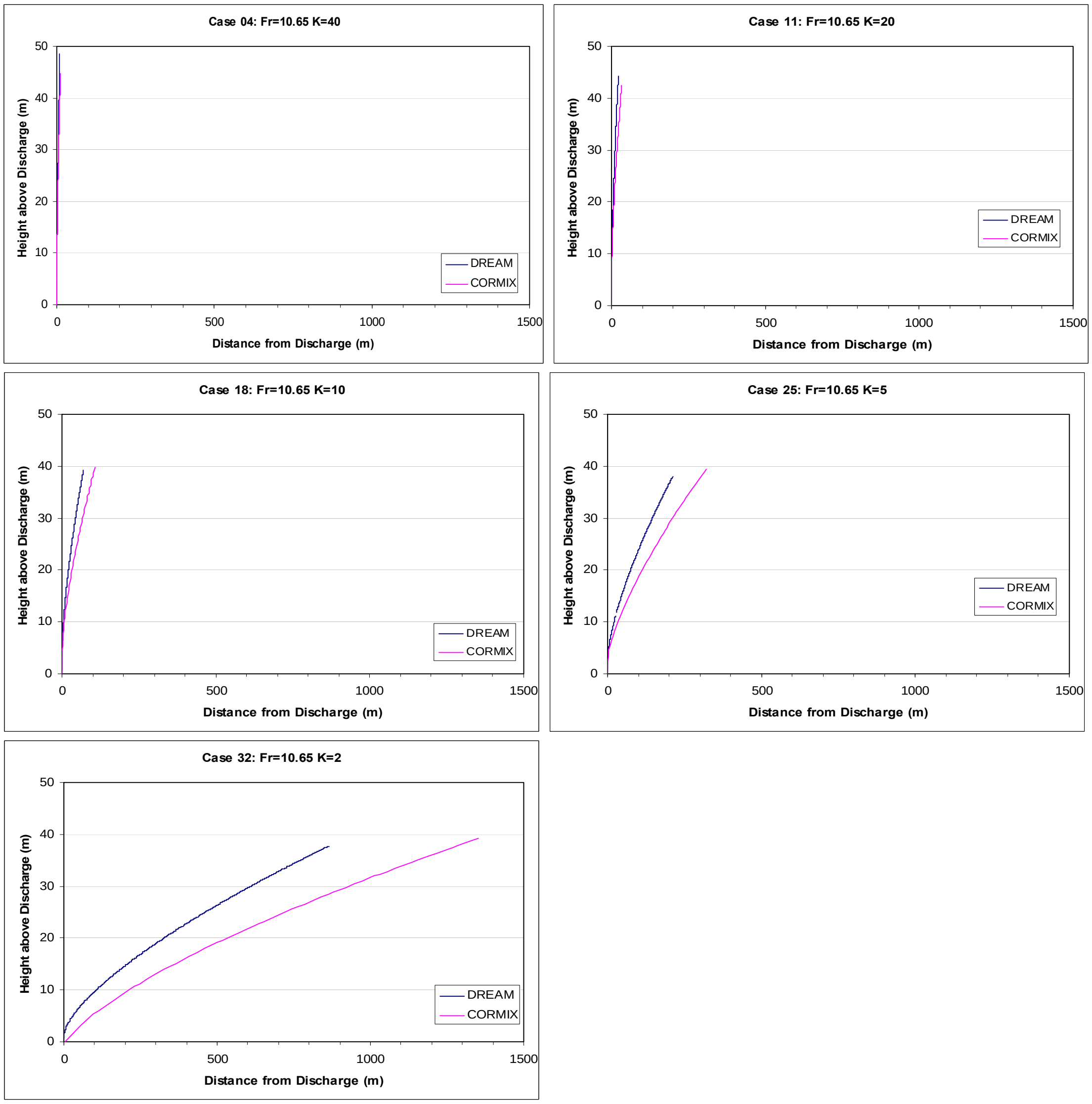

Figure 15: Comparison of Plume Trajectory: Effects of Velocity Ratio K for Same Densimetric Froude Number and Discharge Volume (Fr=10.65).

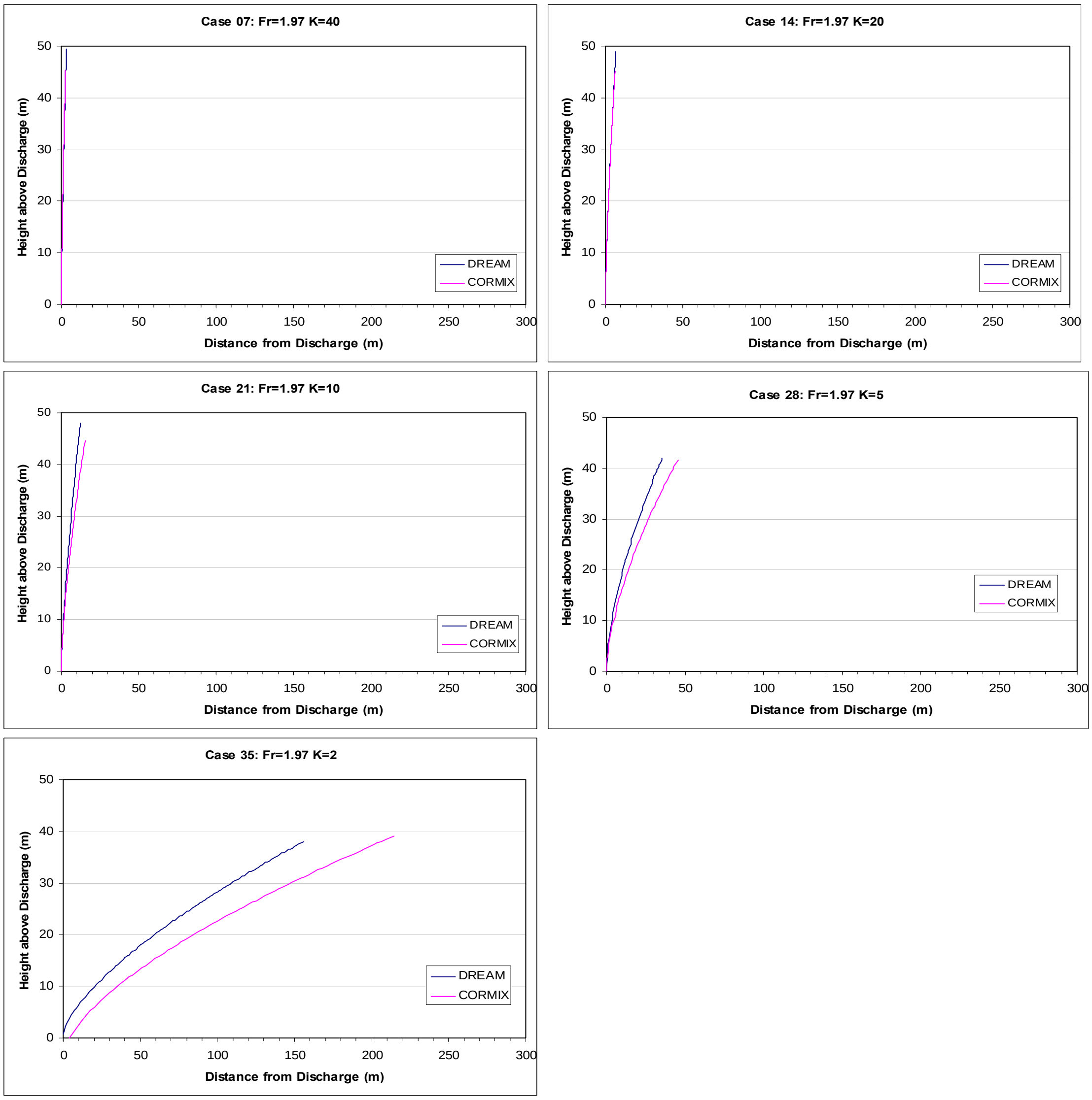

Figure 16: Comparison of Plume Trajectory: Effects of Velocity Ratio K for Same Densimetric Froude Number and Discharge Volume (Fr=1.97).

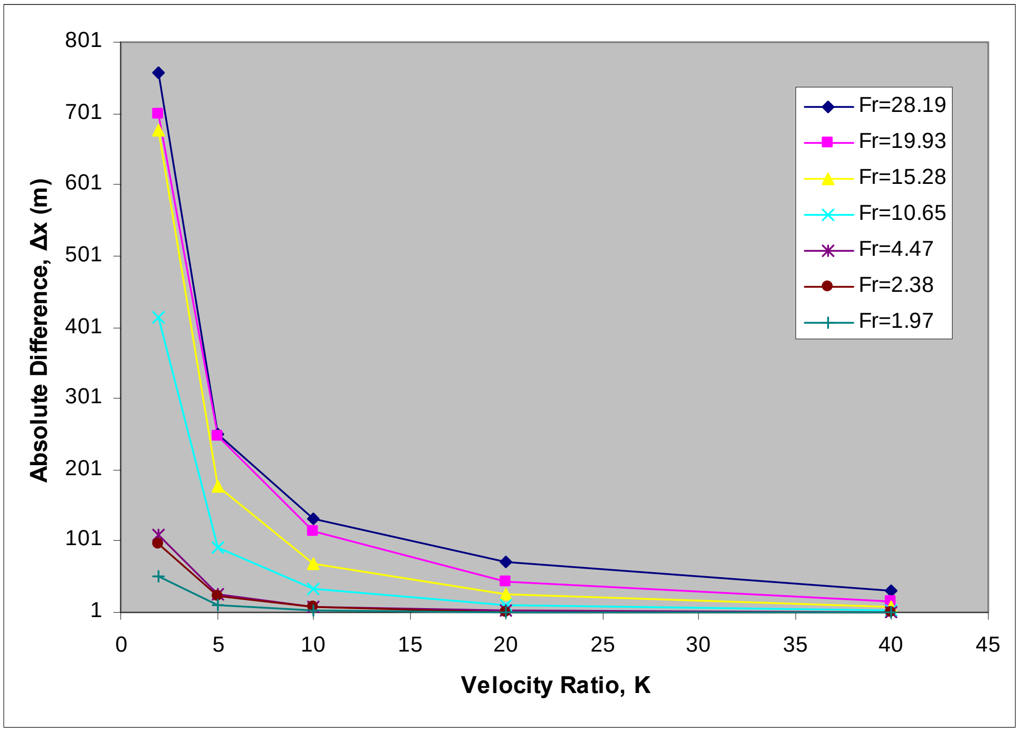

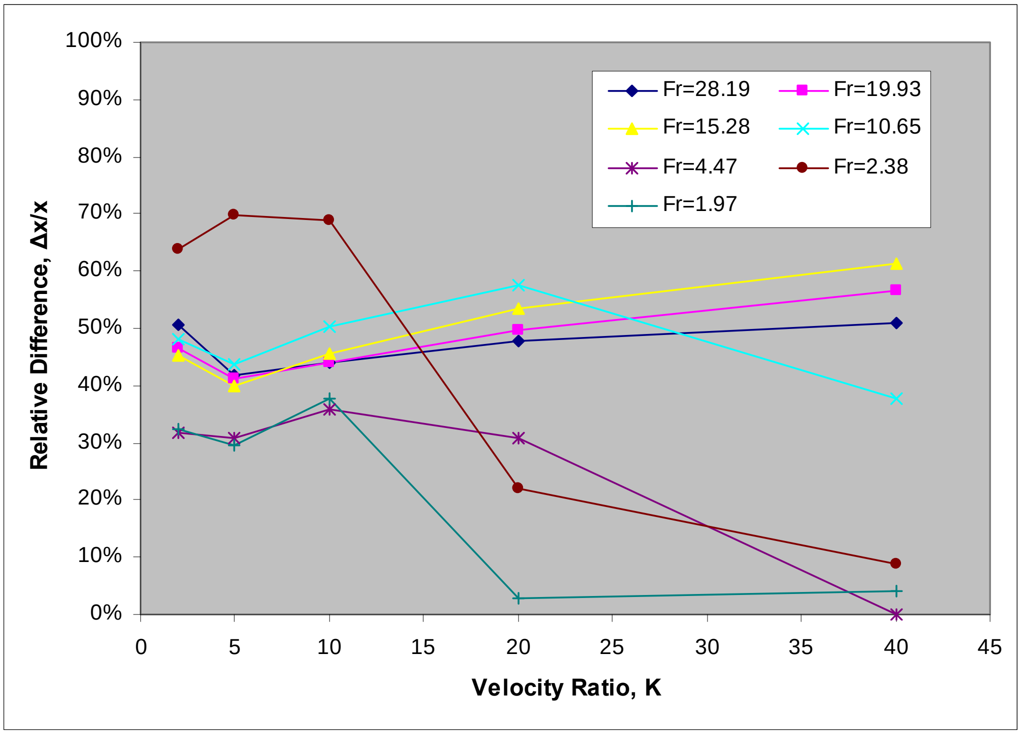

Figure 17: Difference of predicted downstream distance at the terminal layer, *x* at mininum (H_{Dream}, H_{CORMIX}): Variation with K. Absolute difference (Top) and relative difference (bottom).

2.2.2 Plume Radius

The predicted plume radius for 49 cases (Group A to G) is plotted in Figure 18 to Figure 24. In the same manner as the plume trajectory, a visual comparison showed that CORMIX always predicted a smaller radius than DREAM for almost all cases. For the 7 groups with different velocity ratio *K*, the results showed that the two curves tended to diverge at higher *Fr*, and the two curves converged when the densimetric Froude number decreased from 28.19 to 1.97 (Group A to E), 14.09 to 0.98 (Group F) and 7.04 to 0.49 (Group G).

Quantitative comparisons of the effects of *Fr* on the trajectories are plotted in Figure 25. The results from the quantitative comparison contradict the visual observation of improved agreement with decreased densimetric Froude number. The tendency to converge is only caused by the decreasing of Δx with decreasing *Fr* (as discussed in section 2.2.1 for trajectory). The vertical difference (ΔR) did not follow the same trend. The plot of absolute difference (Figure 25, top) shows that the overall trend for Group A to C is smaller absolute differences at smaller *Fr*. For Group D to G, the trend is larger absolute differences at smaller *Fr*. Except for some data points of Group A to C, there is a constant relative difference (~30% to 40%) for all data points (Figure 25, bottom).

As with the comparison of plume trajectory, the effect of discharge volume was not definitive in Figure 18 to Figure 25. To study the effects of *Fr* more specifically, results for eight cases with same discharge volume and velocity ratio but different densimetric Froude number were compared in Figure 26 and Figure 27. The results show an overall trend of increasing difference with increasing *Fr*. The absolute difference increased from 1.04 to 3.36 m and relative difference has increased from 18.42% to 62.11% for *Fr* from 1.97 to infinity.

Unlike the results for trajectory and similar to the effects of *Fr* on radius, the variation of difference with *K* was not consistent for the seven groups with different *Fr* (Figure 28). The overall trends for the relationship with smaller *Fr* (1.97, 2.38 and 4.47) are a sharp initial decrease of absolute difference with *K* followed by almost constant values. For the cases with *Fr* = 10.65, the trend was a constant decrease of absolute difference with *K*. For *Fr* = 15.28 and 19.93, the trend was a small initial increase in absolute difference and then a slow decrease in the difference. The trend for *Fr* = 28.19 was a continual increasing of absolute difference with *K*. While there was no unique trend for absolute difference, the overall trend for relative difference was to remain almost constant (~ 20% to 40%) for all data points.

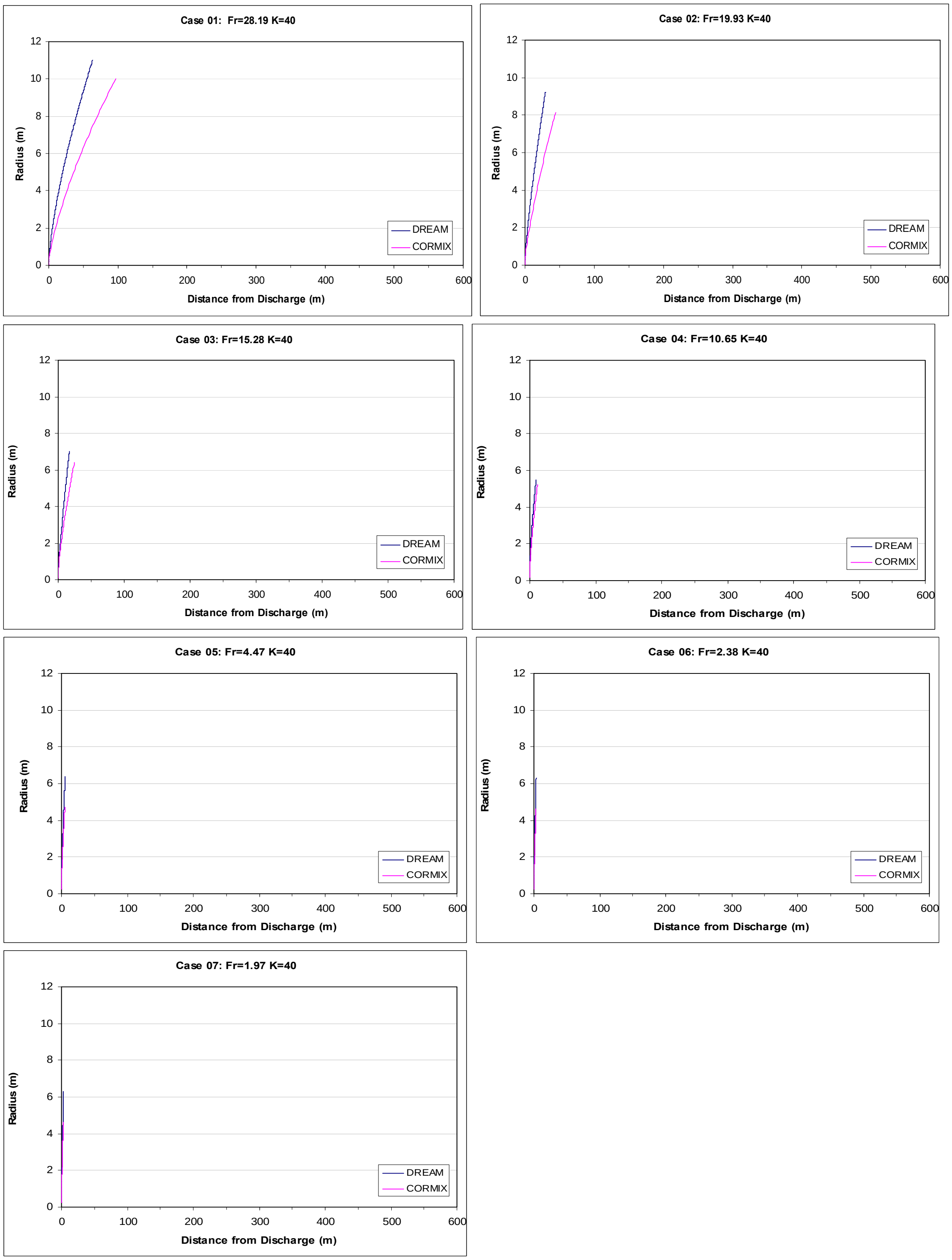

Figure 18: Comparison of Plume Radius: Effects of Densimetric Froude Number *Fr* (Group A: *K*=40)

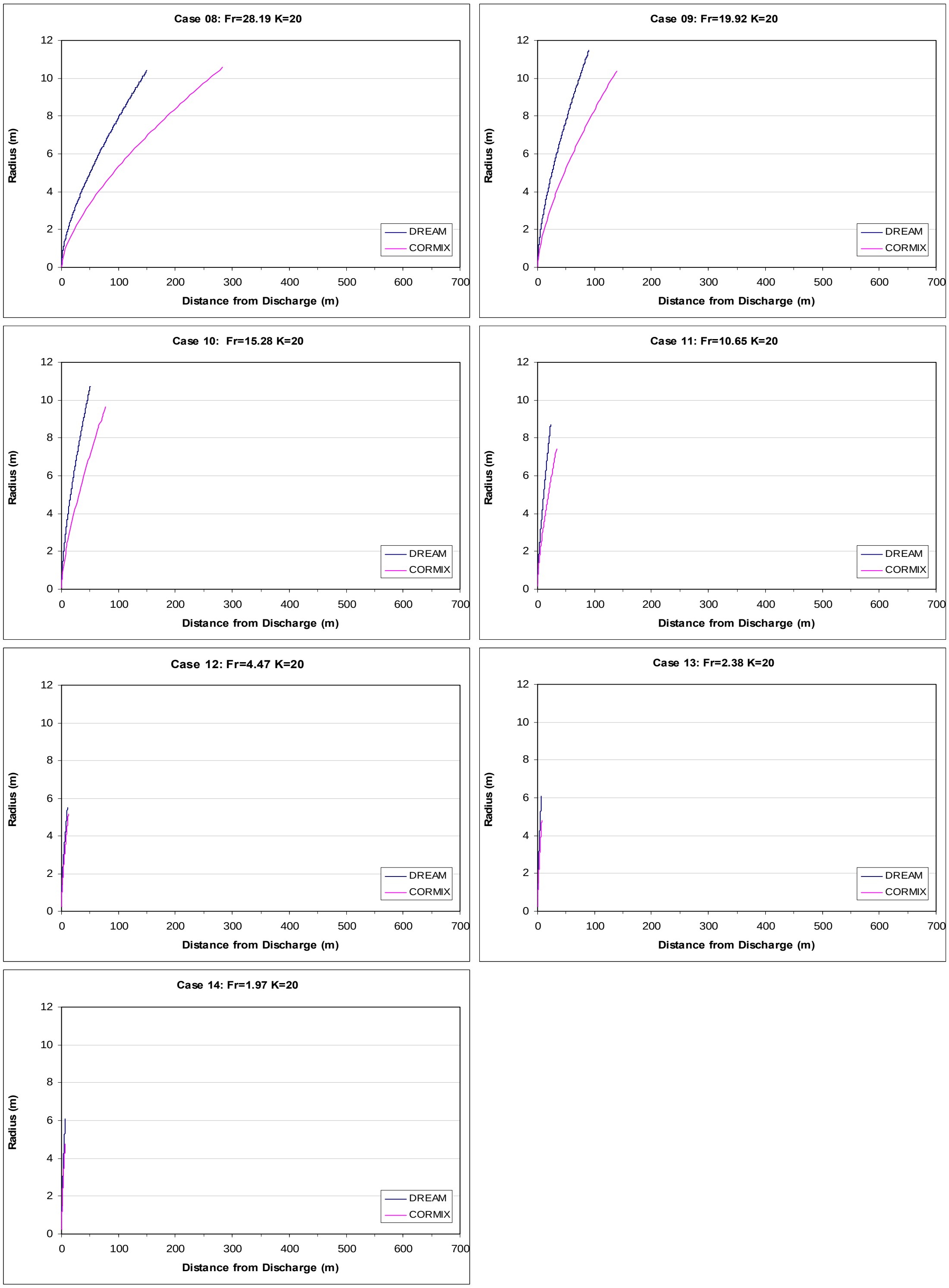
Case 08: Fr=28.19 K=20

Case 09: Fr=19.92 K=20

Case 10: Fr=15.28 K=20

Case 11: Fr=10.65 K=20

Case 12: Fr=4.47 K=20

Case 13: Fr=2.38 K=20

Case 14: Fr=1.97 K=20

Figure 19: Comparison of Plume Radius: Effects of Densimetric Froude Number *Fr* (Group B: *K*=20)

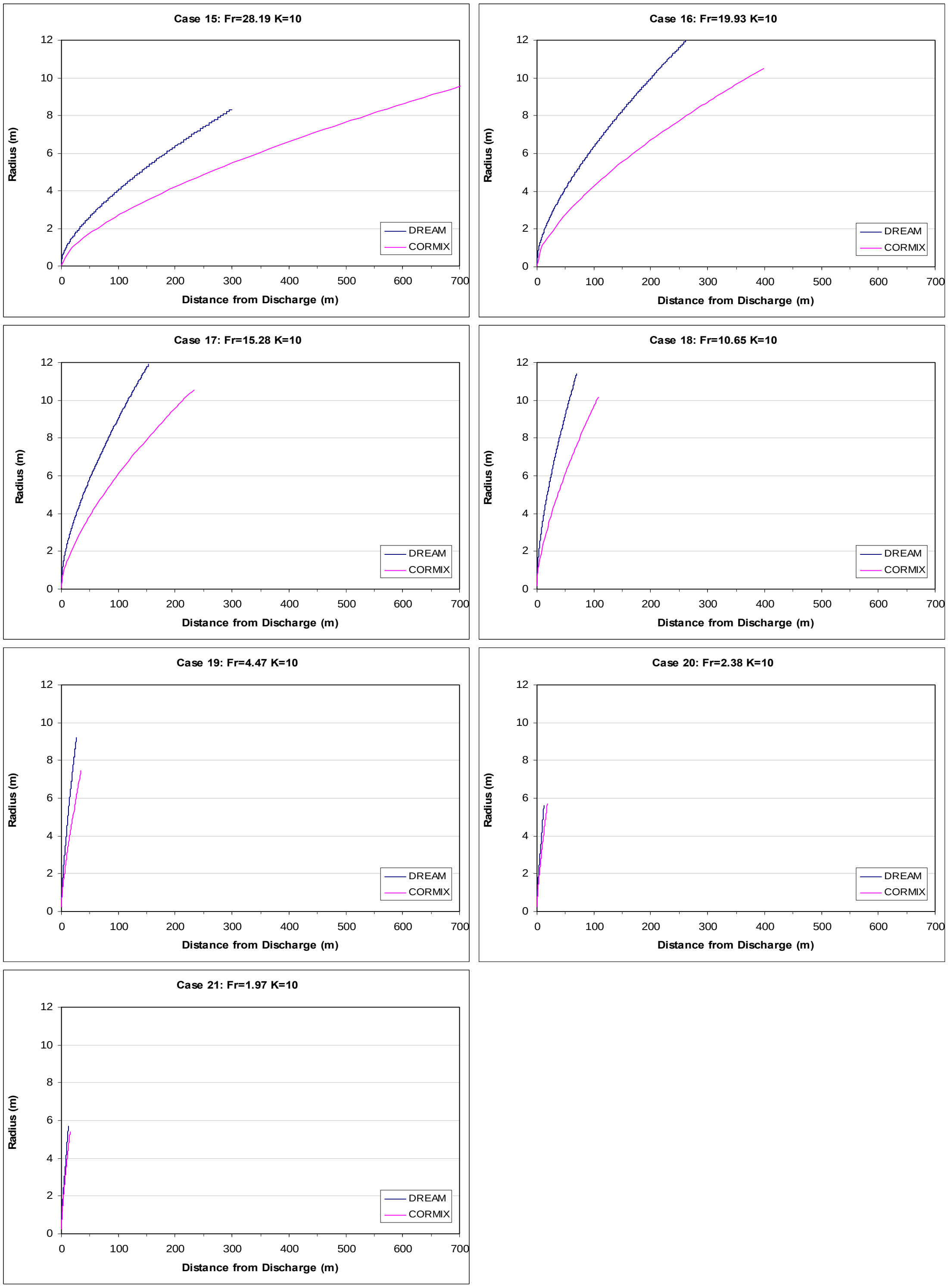
Case 15: Fr=28.19 K=10

Case 16: Fr=19.93 K=10

Case 17: Fr=15.28 K=10

Case 18: Fr=10.65 K=10

Case 19: Fr=4.47 K=10

Case 20: Fr=2.38 K=10

Case 21: Fr=1.97 K=10

Figure 20: Comparison of Plume Radius: Effects of Densimetric Froude Number *Fr* (Group C: *K*=10)

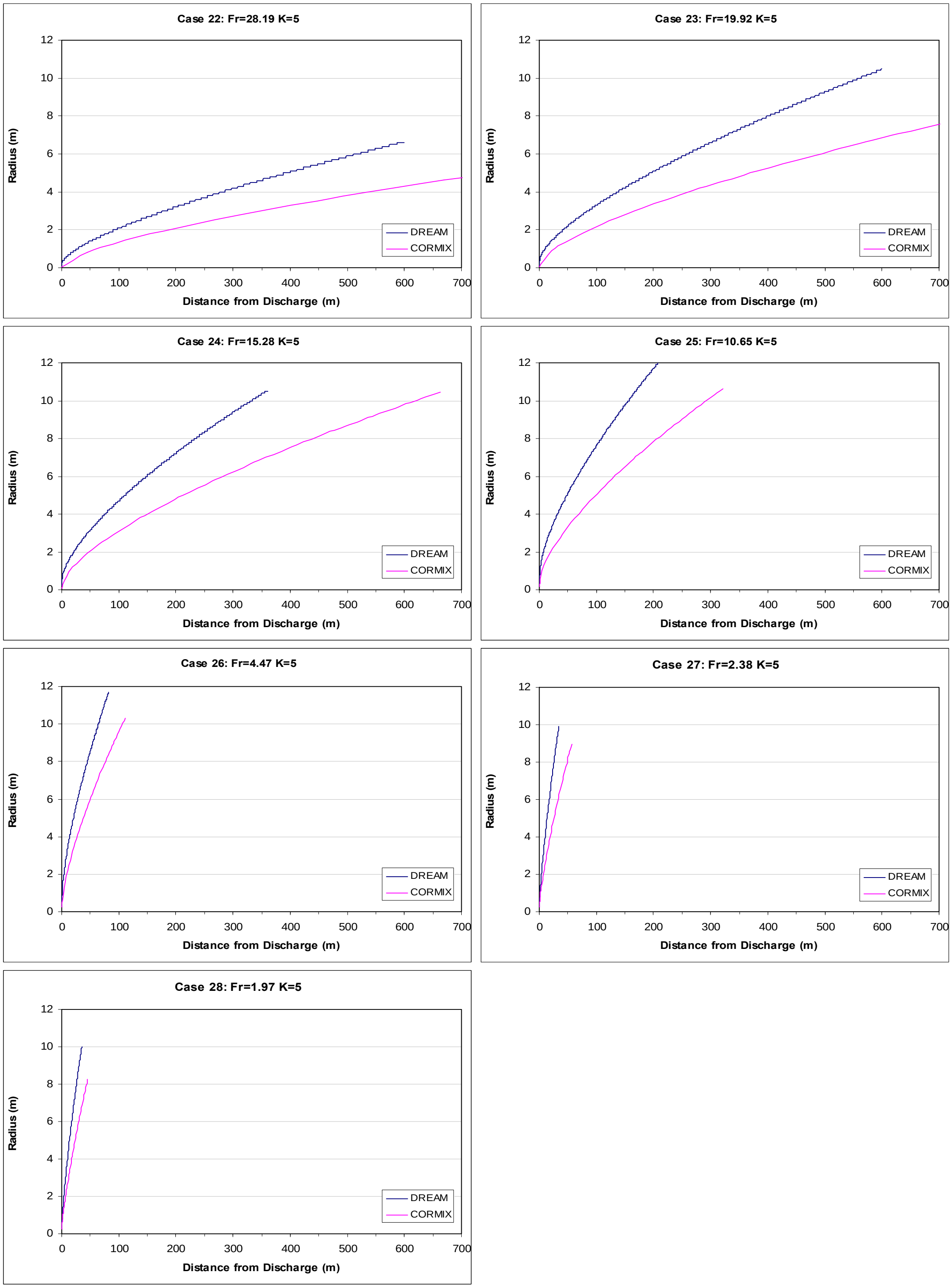

Figure 21: Comparison of Plume Radius: Effects of Densimetric Froude Number *Fr* (Group D: *K*=5)

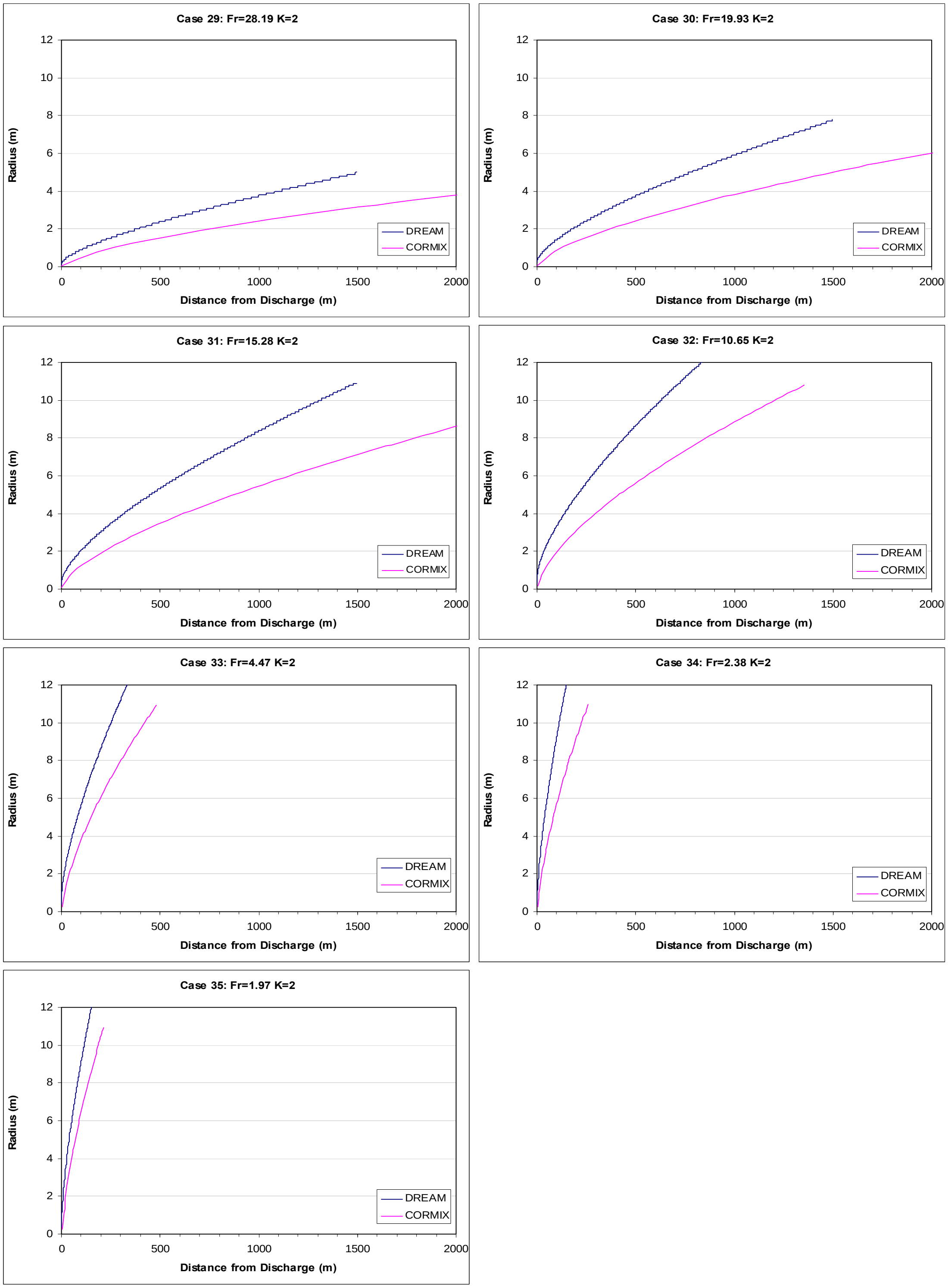

Figure 22: Comparison of Plume Radius: Effects of Densimetric Froude Number *Fr* (Group E: *K*=2)

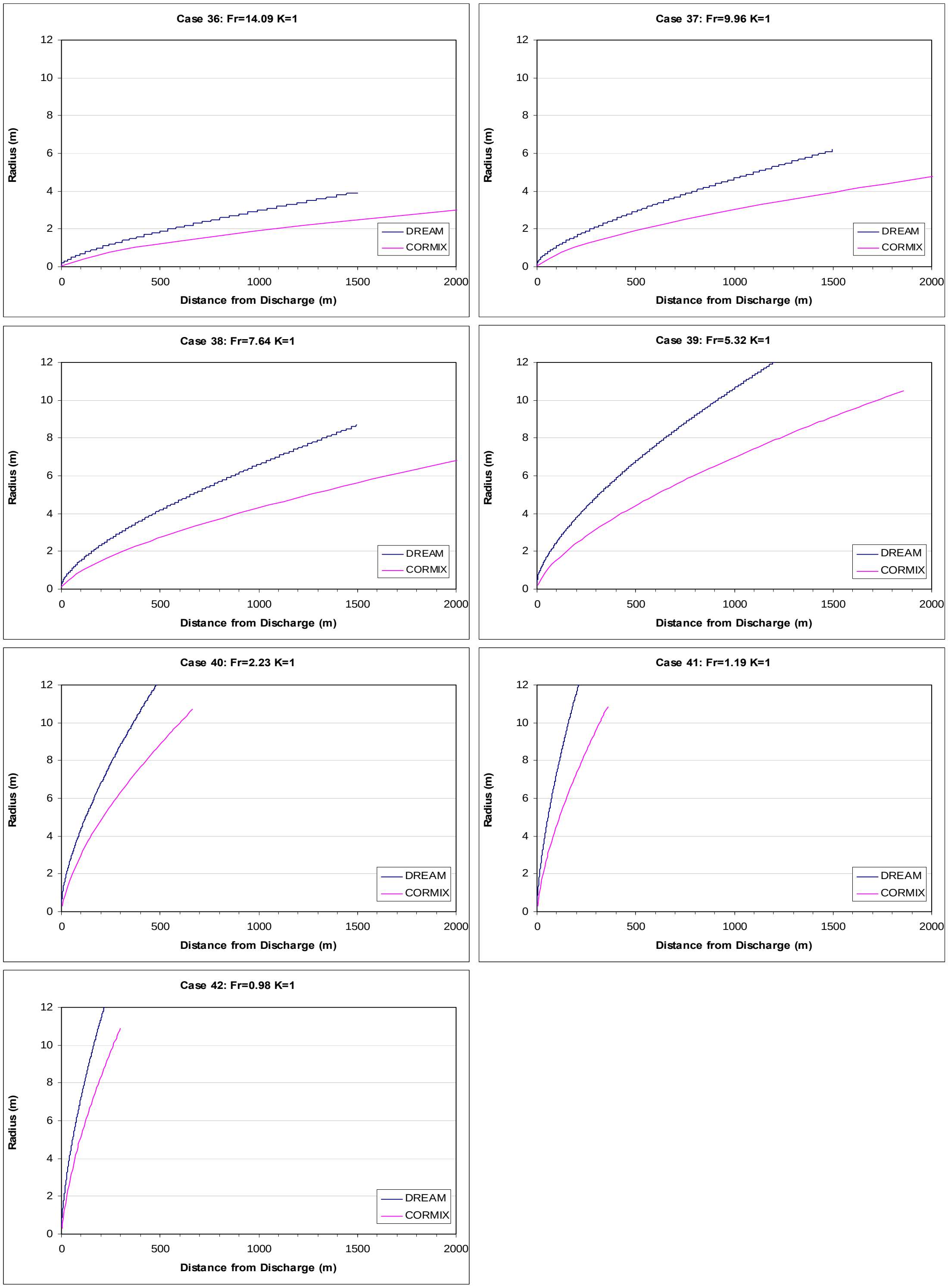

Figure 23: Comparison of Plume Radius: Effects of Densimetric Froude Number *Fr* (Group F: *K*=1)

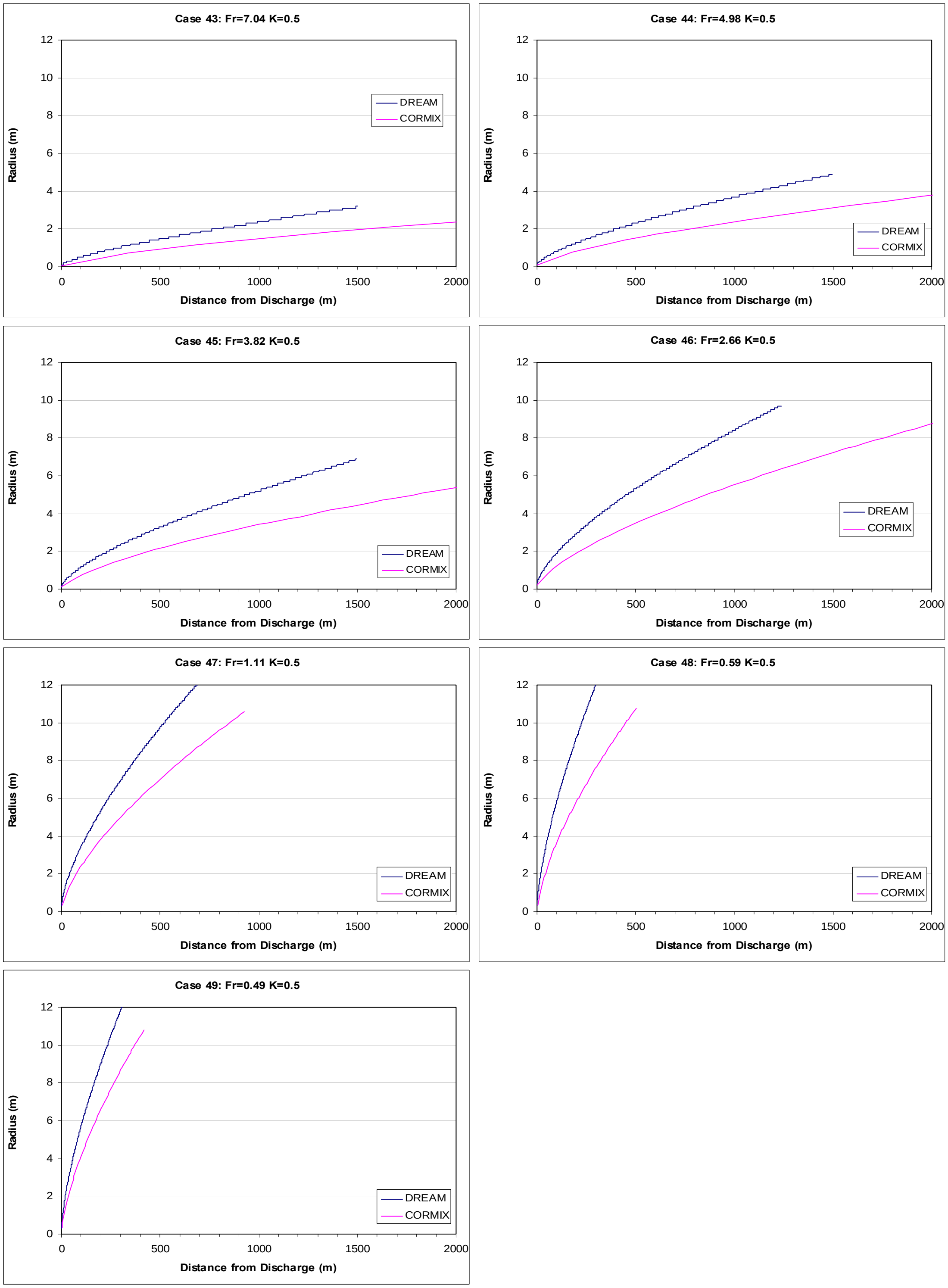

Figure 24: Comparison of Plume Radius: Effects of Densimetric Froude Number *Fr* (Group G: *K*=0.5)

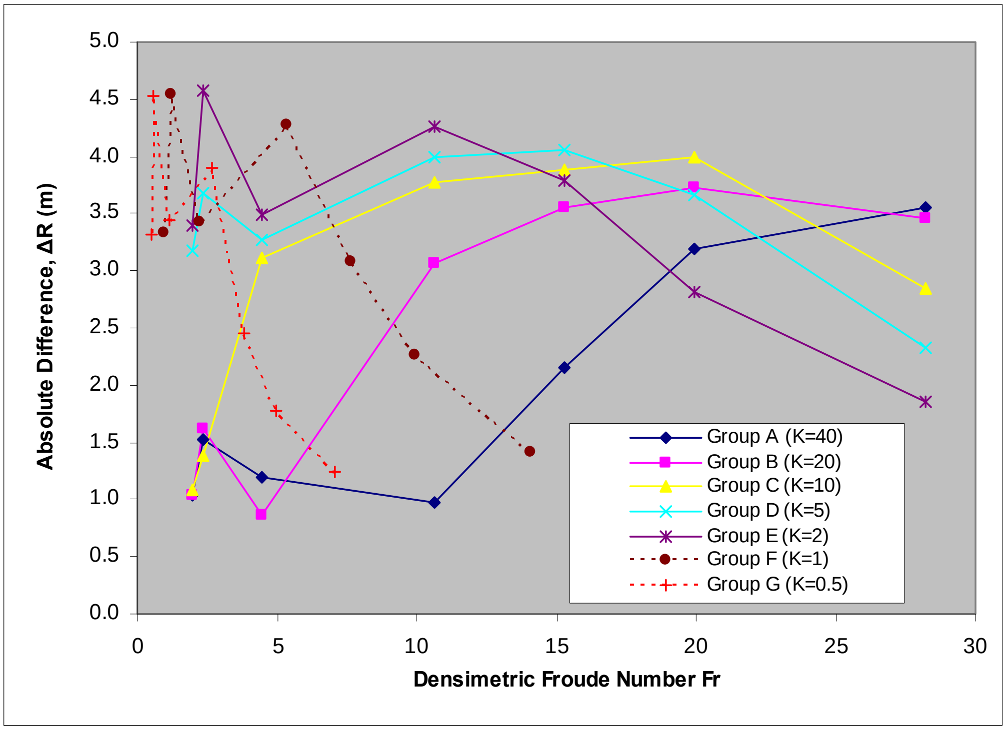

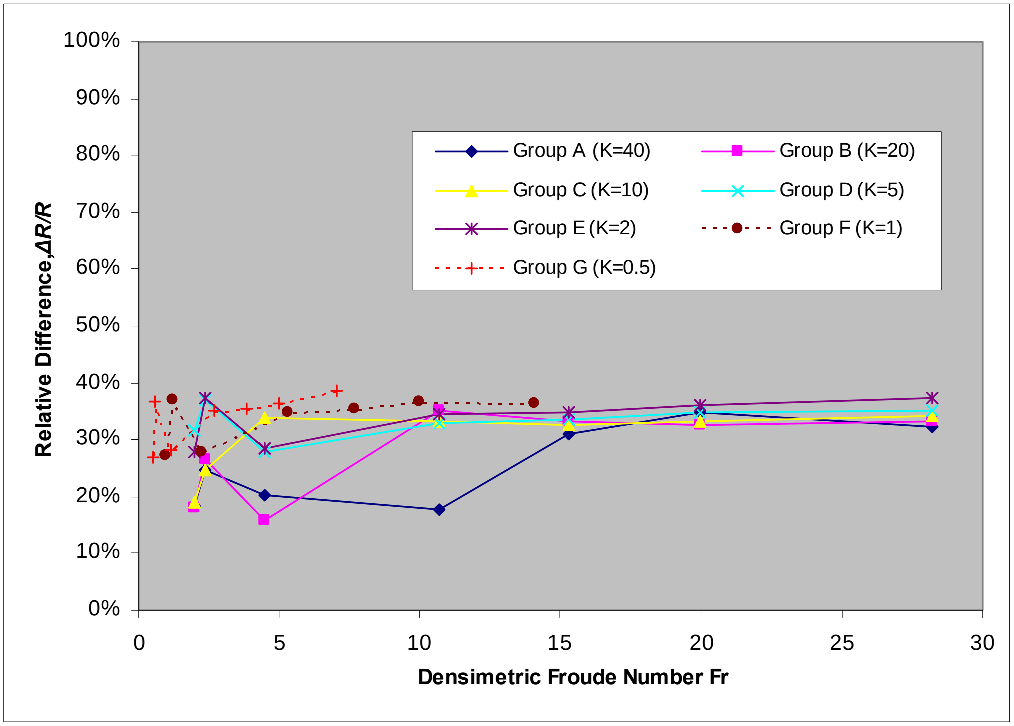

Figure 25: Difference of Predicted Plume Radius at the End of Near-Field, R at Minimum (x_{Dream}, x_{CORMIX}): Variation with Fr. Absolute Difference (Top) and Relative Difference (Bottom).

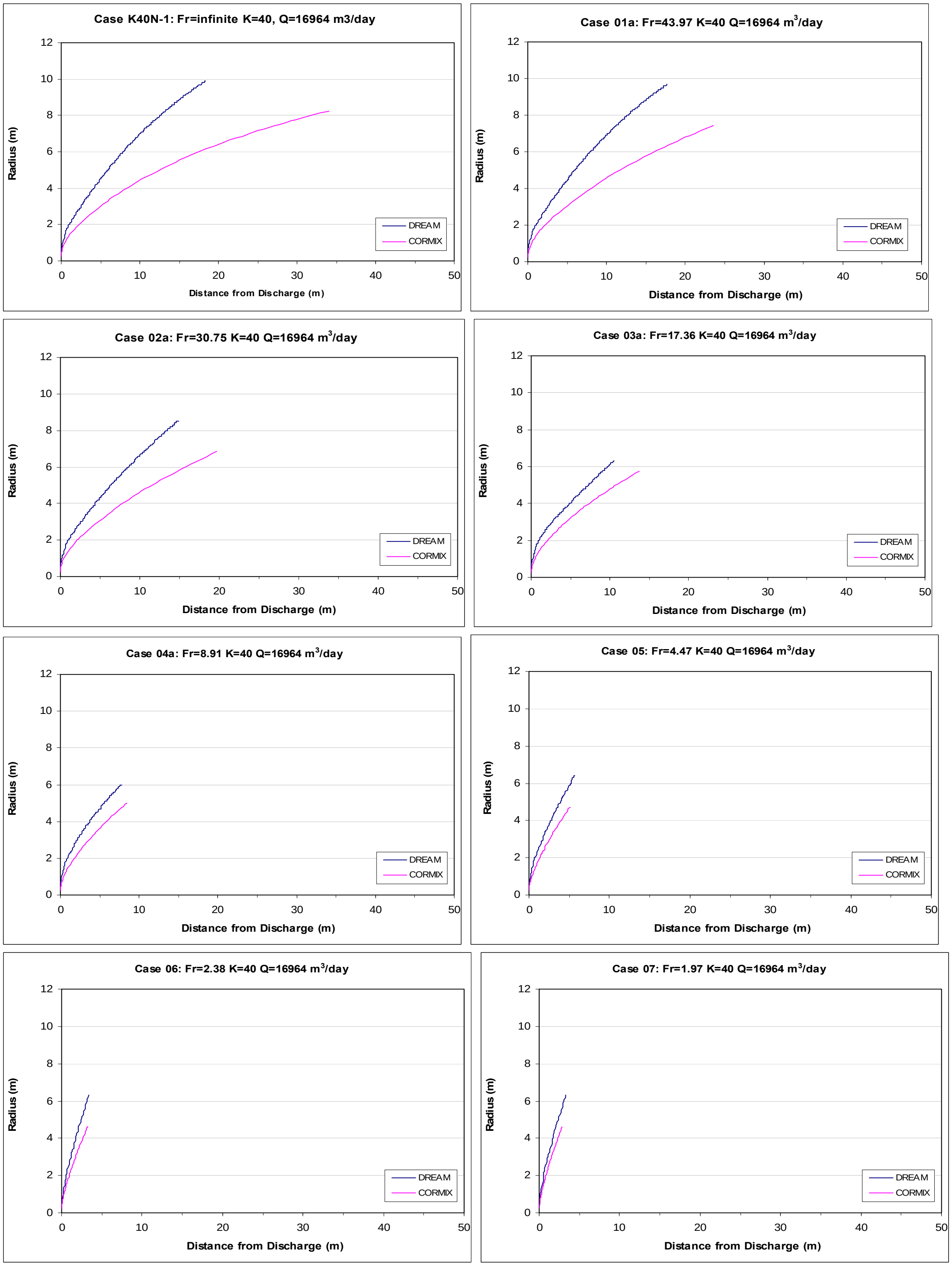

Figure 26: Comparison of Plume Radius: Effects of Discharge Froude Number for Same Velocity Ratio and Discharge Volume (K=40).

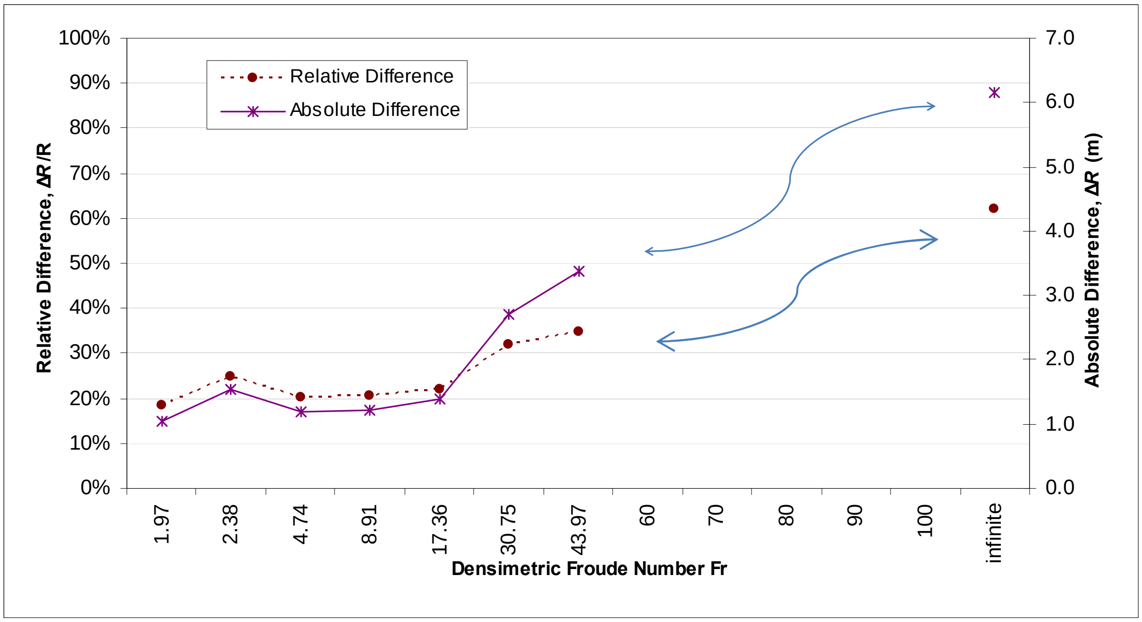

Figure 27: Difference of Predicted Plume Radius at the End of Near-Field, R at Minimum (x_{Dream}, x_{CORMIX}) for the Same K and Q.

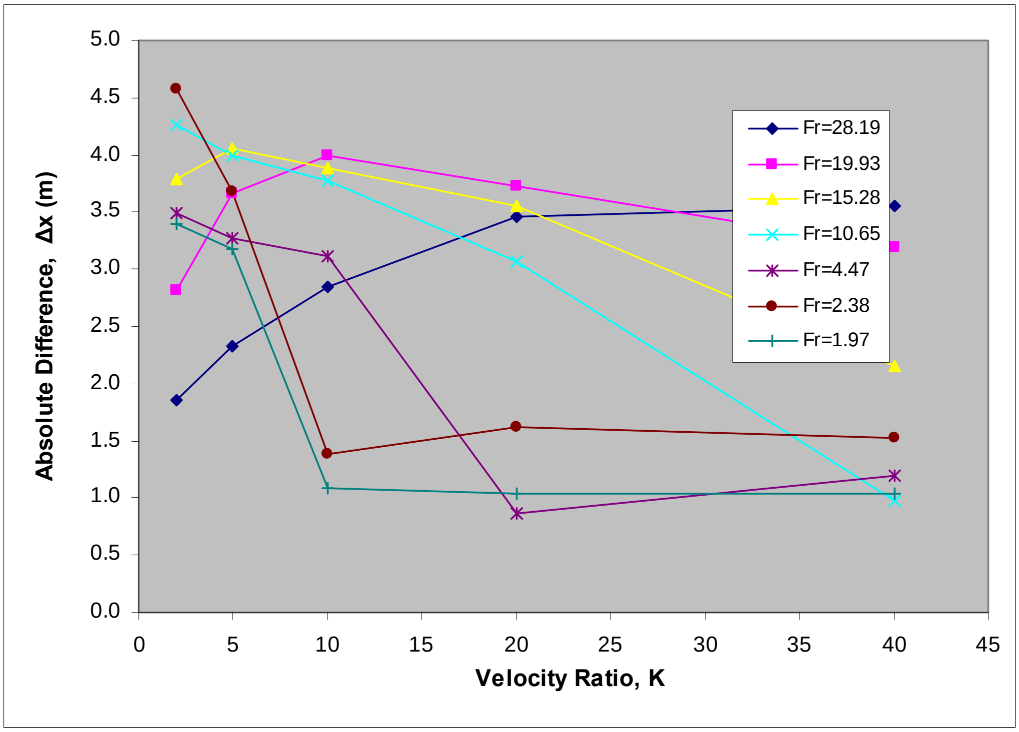

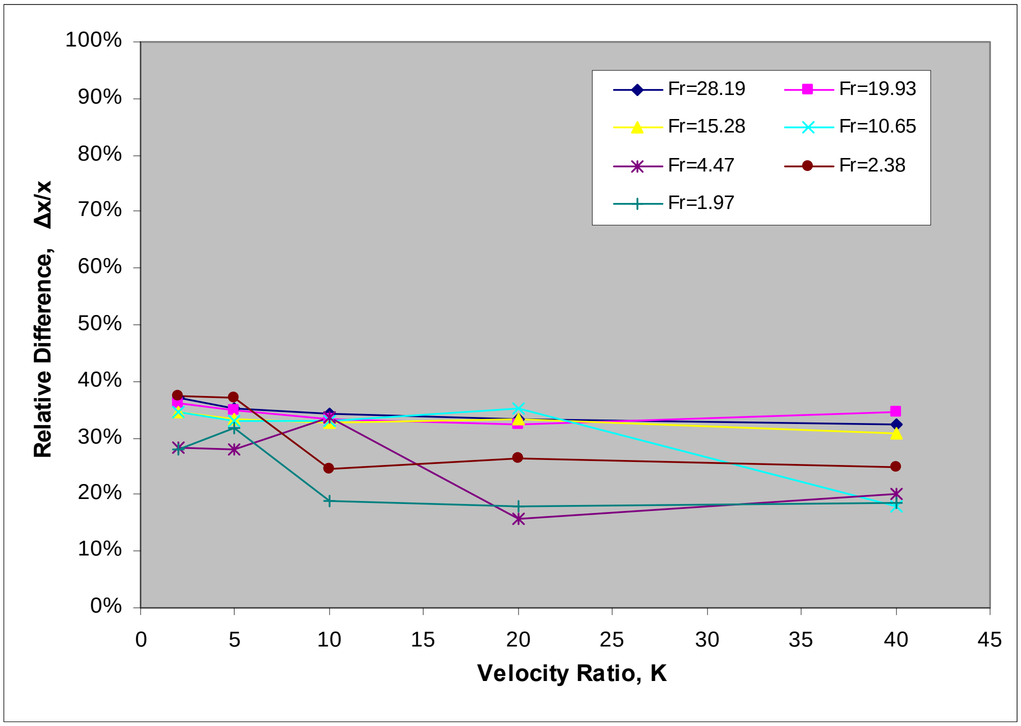

Figure 28: Difference of Predicted Plume Radius at the End of Near-Field, R at Minimum (x_{Dream}, x_{CORMIX}): Variation with *K*. Absolute Difference (Top) and Relative Difference (Bottom).

2.2.3 Concentration

The predicted plume centerline concentration (% of initial concentration) for 49 cases (Groups A to G) is plotted in Figure 29 to Figure 35. For Group A (K = 40), a visual comparison shows that CORMIX usually predicted higher far-field concentration than DREAM. For Groups B to G, while only the first two or three cases with higher densimetric Froude number showed this trend, the cases with smaller *Fr* showed better agreement between the two models. Apart from Group A, this indicated decreased velocity ratio led to better agreements, that is, the two models only possess good agreement in the far field for smaller velocity ratios.

For the seven groups compared in Figure 29 to Figure 35, the discharge volumes are not the same. The previous comparison of plume trajectory and radius indicated that the discharge volume may also affect plume behaviour. To study the effect of discharge volume, Figure 36 was plotted for comparison of eight different *Fr* (from 1.97 to infinity) with *K* = 40. The results showed a systematic difference at far field and that the discharge volume and *Fr* have little influence on these differences.

The effects of velocity ratio are shown in Figure 37 to Figure 39. For all three groups with different *Fr*, the overall trend is that better agreement is found for smaller *K* (except the case with *Fr* = 28). Further comparisons were conducted using paired regression analysis (

Figure **40**). For the case of *K* = 10, the regression line approaches the reference line (DREAM=CORMIX) as *Fr* decreases, which indicates better agreements.

For the comparison of *Fr* and *K* above, it can be concluded that better agreement of the two models was only found for cases with smaller *Fr* and smaller *K*. The range in which good agreement is found was plotted in Figure 41. It can be seen that for any given *K* except 40, as *Fr* increases, the disagreement increases and the critical *Fr* is *K*-dependent. The general trend is the larger the velocity ratio, the larger the critical Fr for the ranges studied.

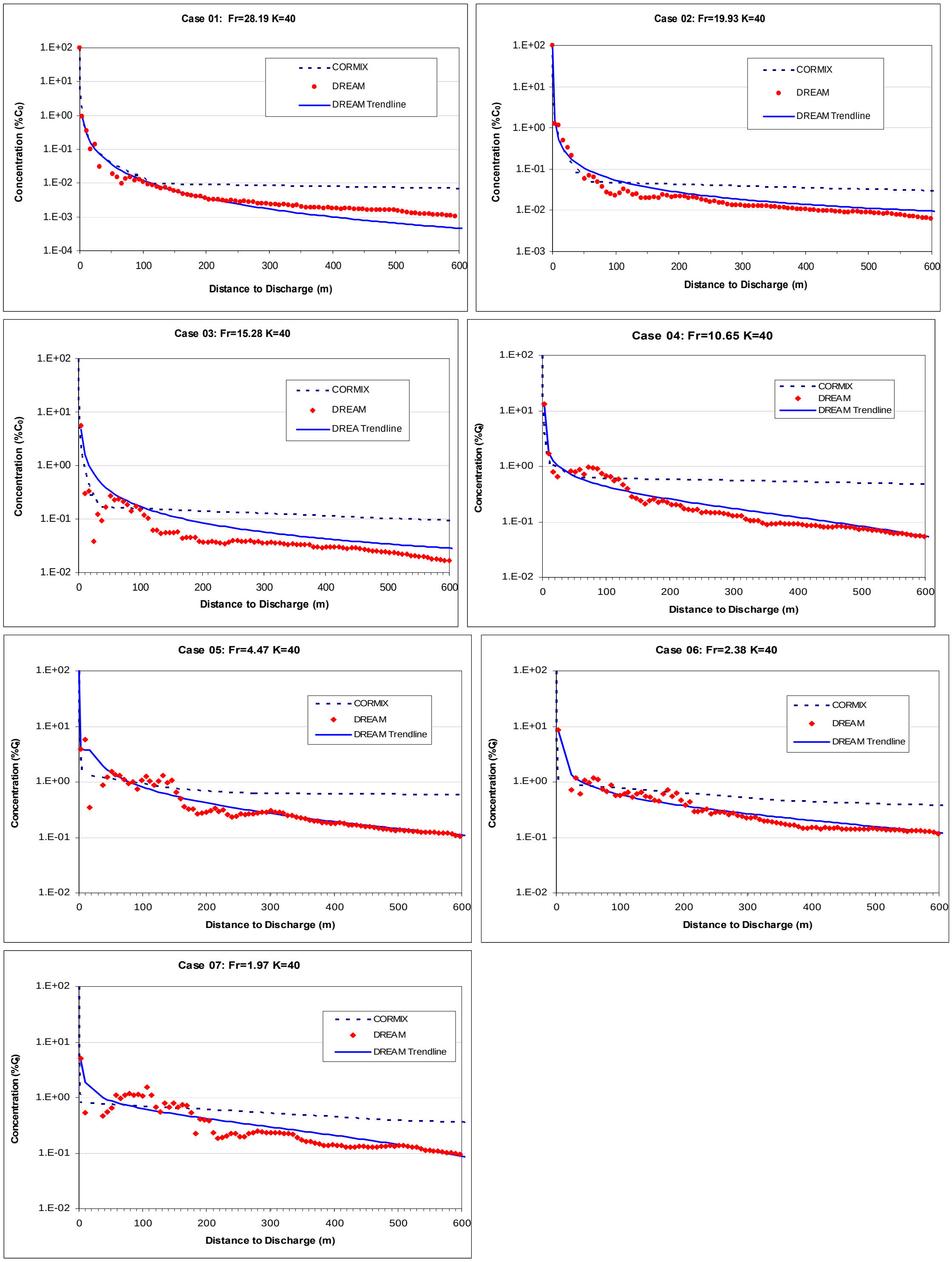

Figure 29: Comparison of Centerline Dilution: Effects of Densimetric Froude Number (Group A: K=40)

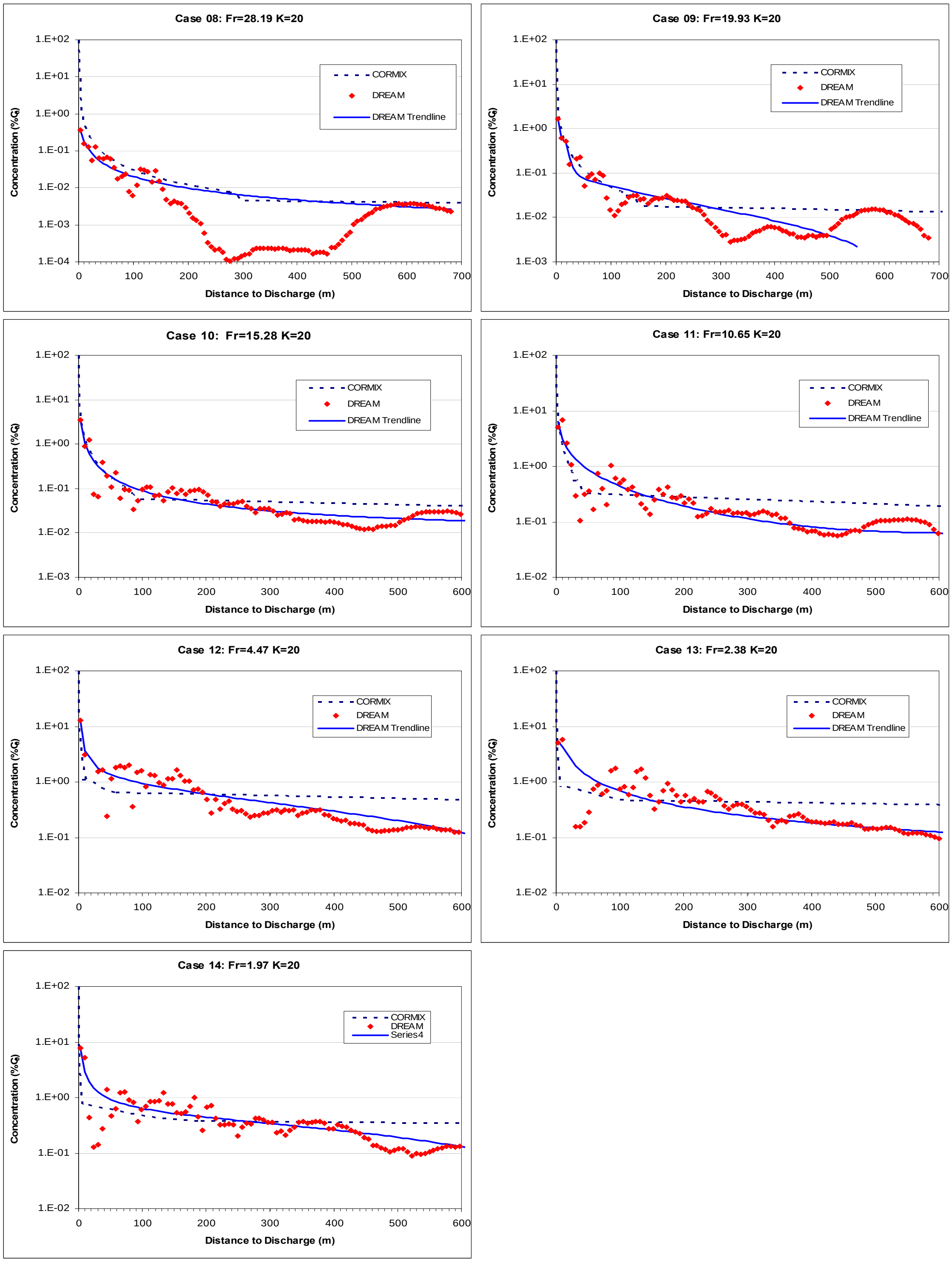

Figure 30: Comparison of Centerline Dilution: Effects of Densimetric Froude Number (Group B: K=20)

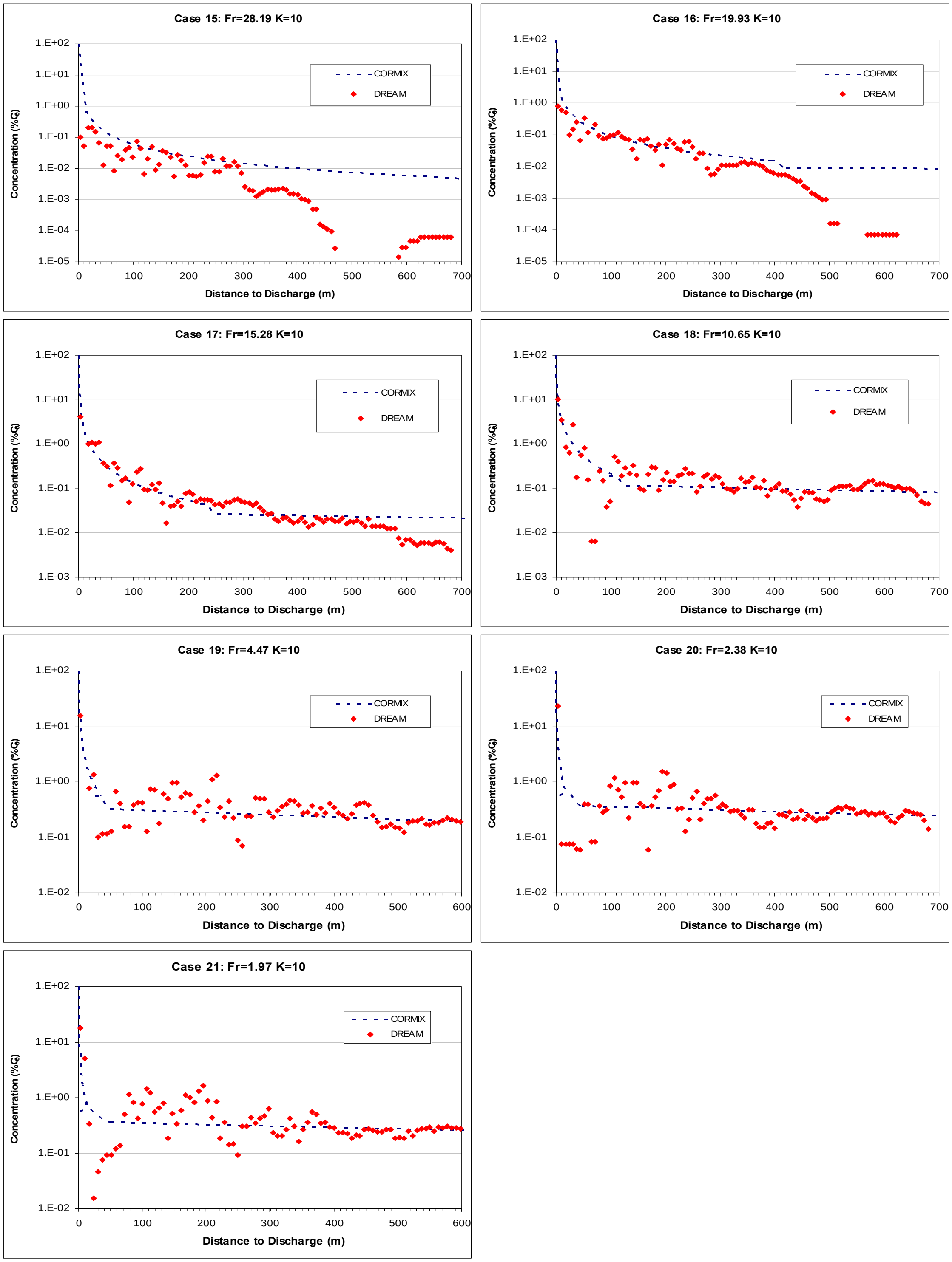

Figure 31: Comparison of Centerline Dilution: Effects of Densimetric Froude Number (Group C: K=10)

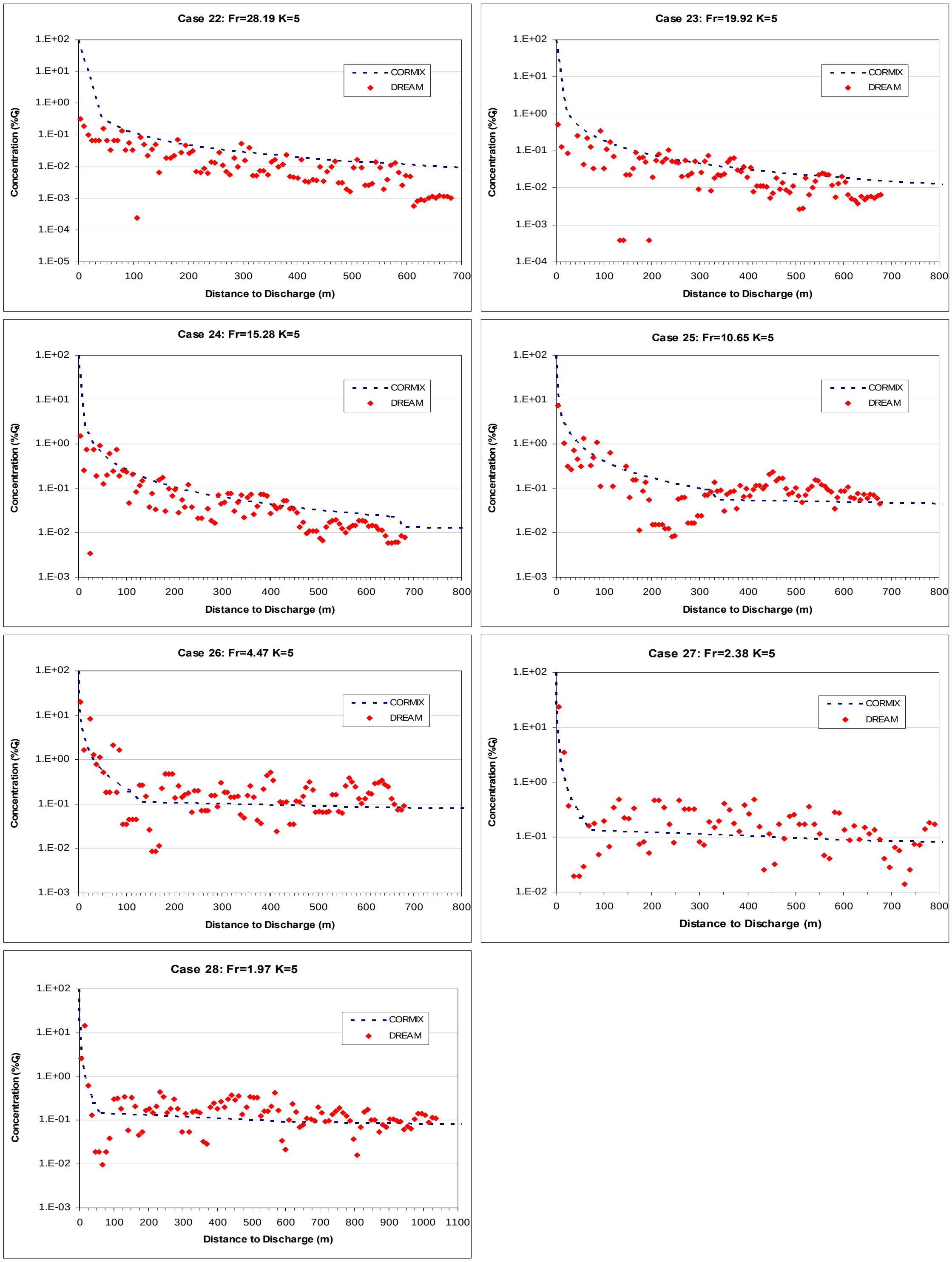

Figure 32: Comparison of Centerline Dilution: Effects of Densimetric Froude Number (Group D: K=5)

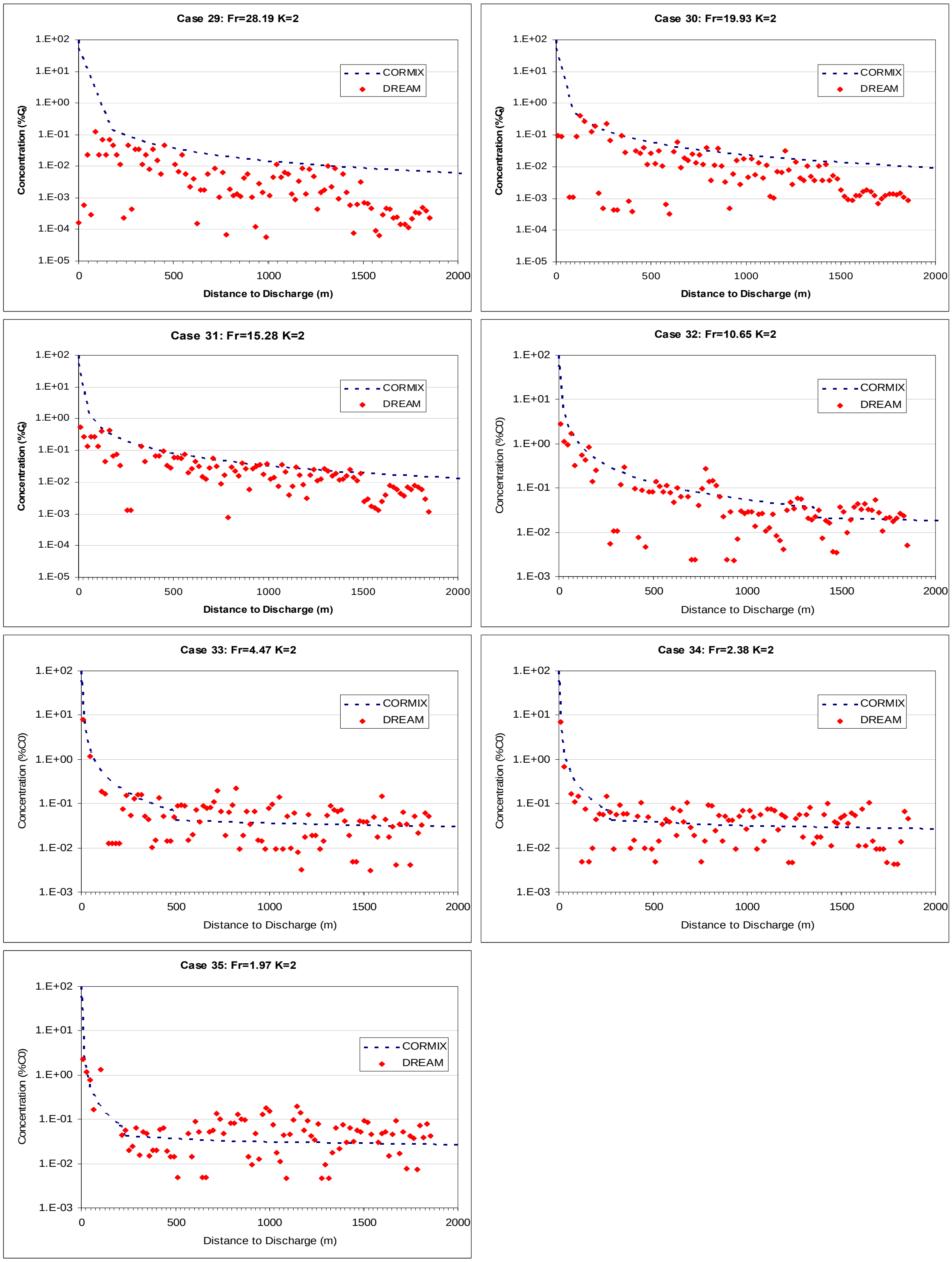

Figure 33: Comparison of Centerline Dilution: Effects of Densimetric Froude Number (Group E: K=2)

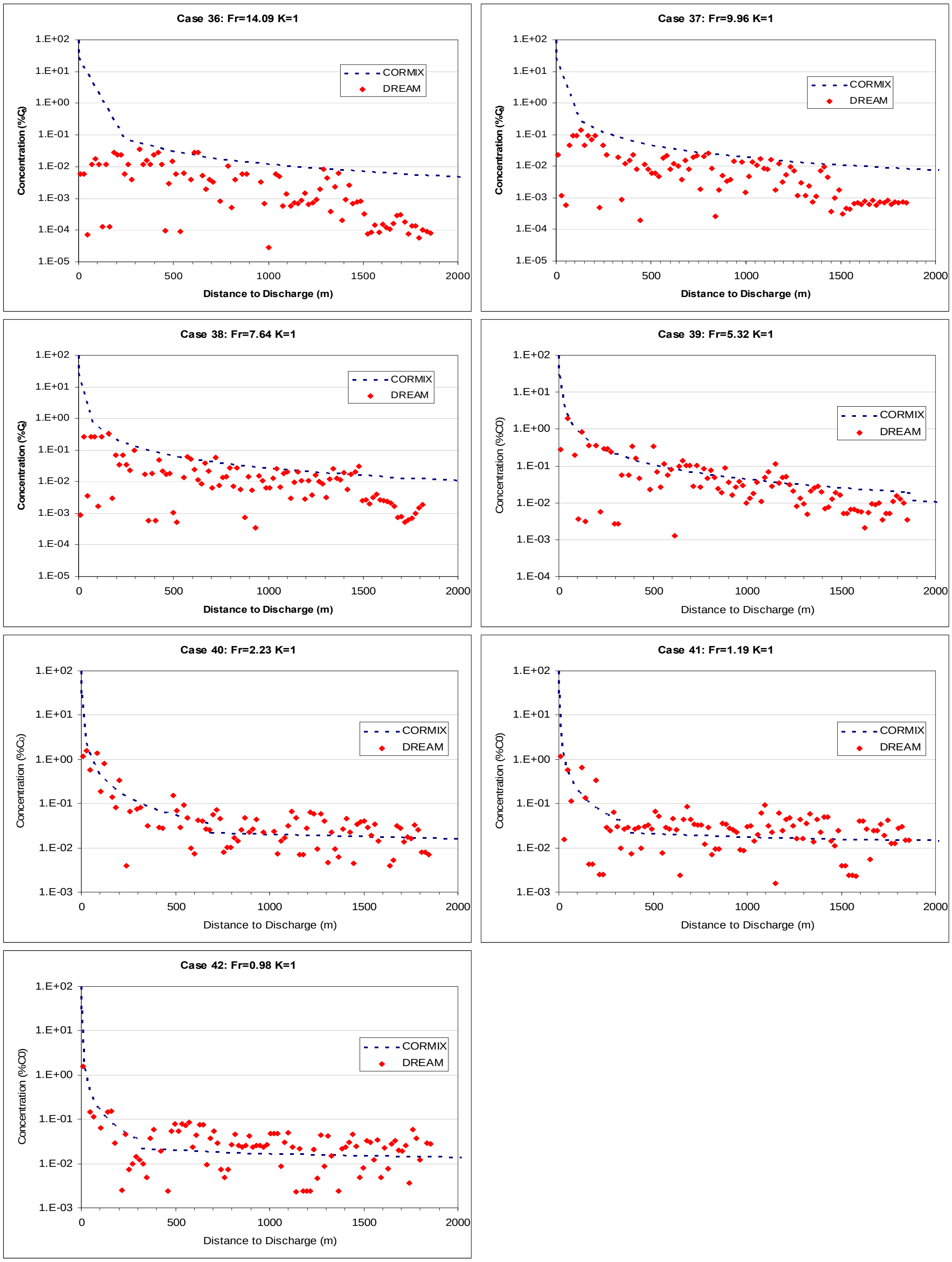

Figure 34: Comparison of Centerline Dilution: Effects of Densimetric Froude Number (Group F: K=1)

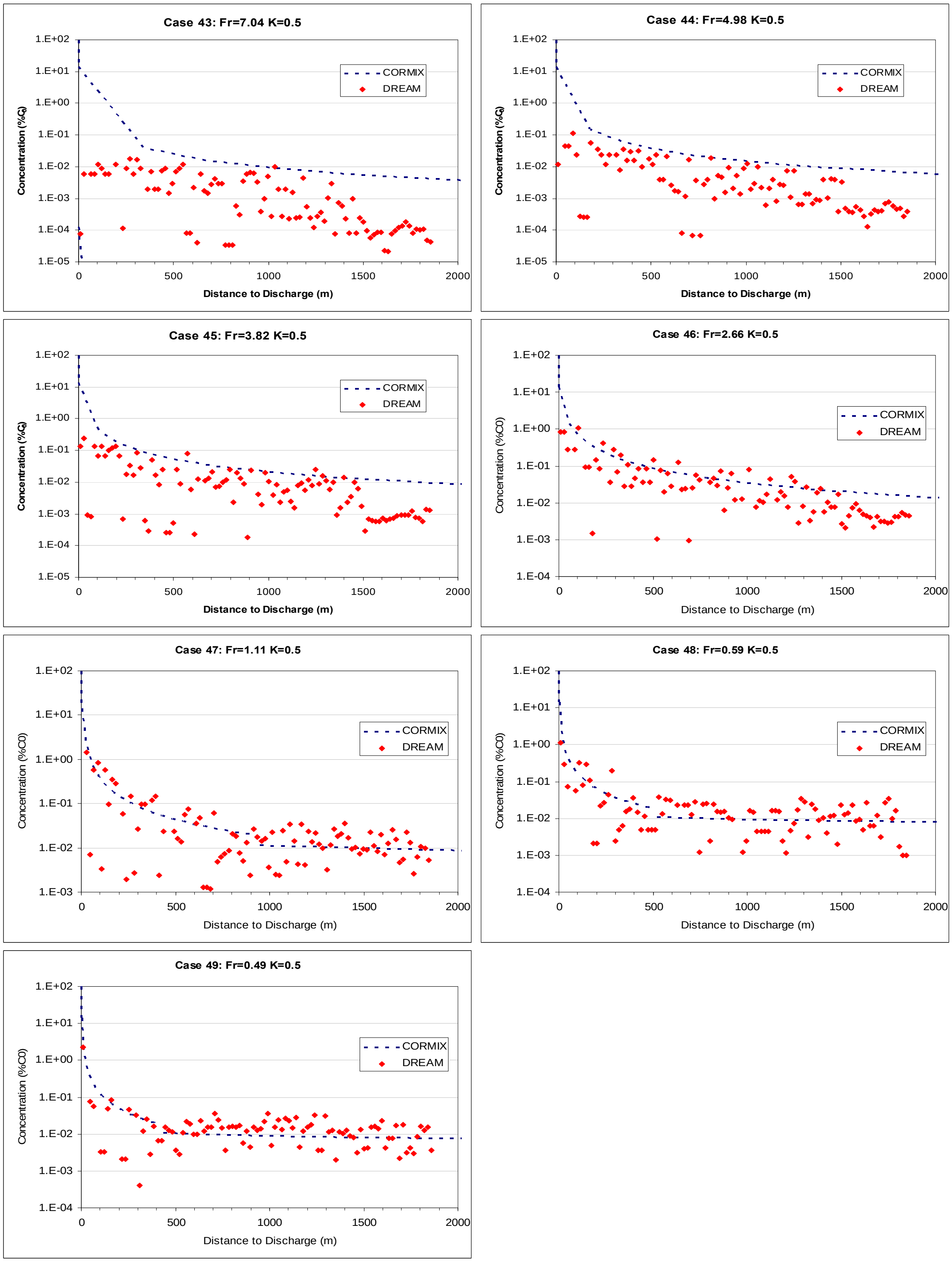

Figure 35: Comparison of Centerline Dilution: Effects of Densimetric Froude Number (Group G: K=0.5)

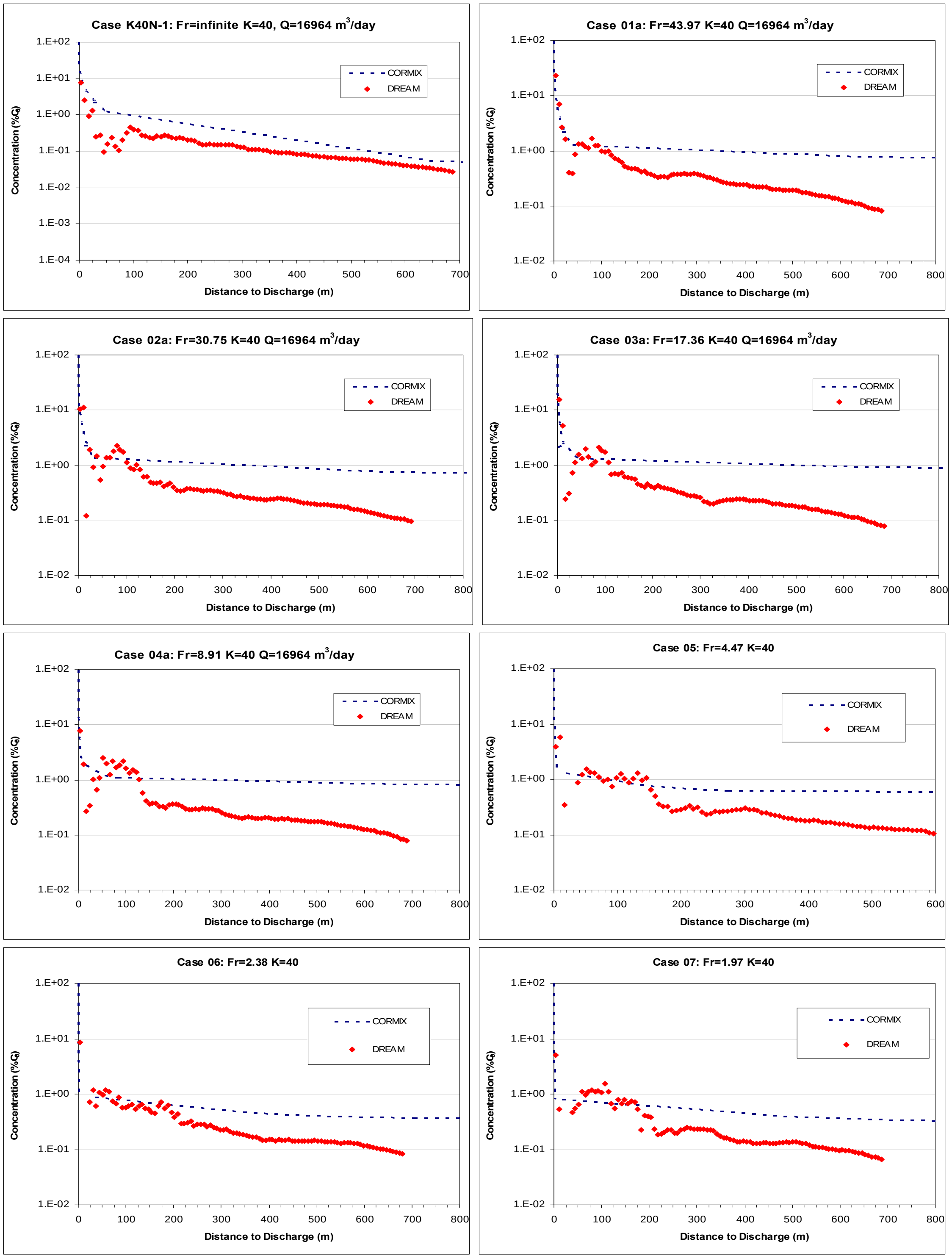

Figure 36: Comparison of Centerline Dilution: Effects of Densimetric Froude Number for Same Velocity Ratio (K=40) and Discharge Volume.

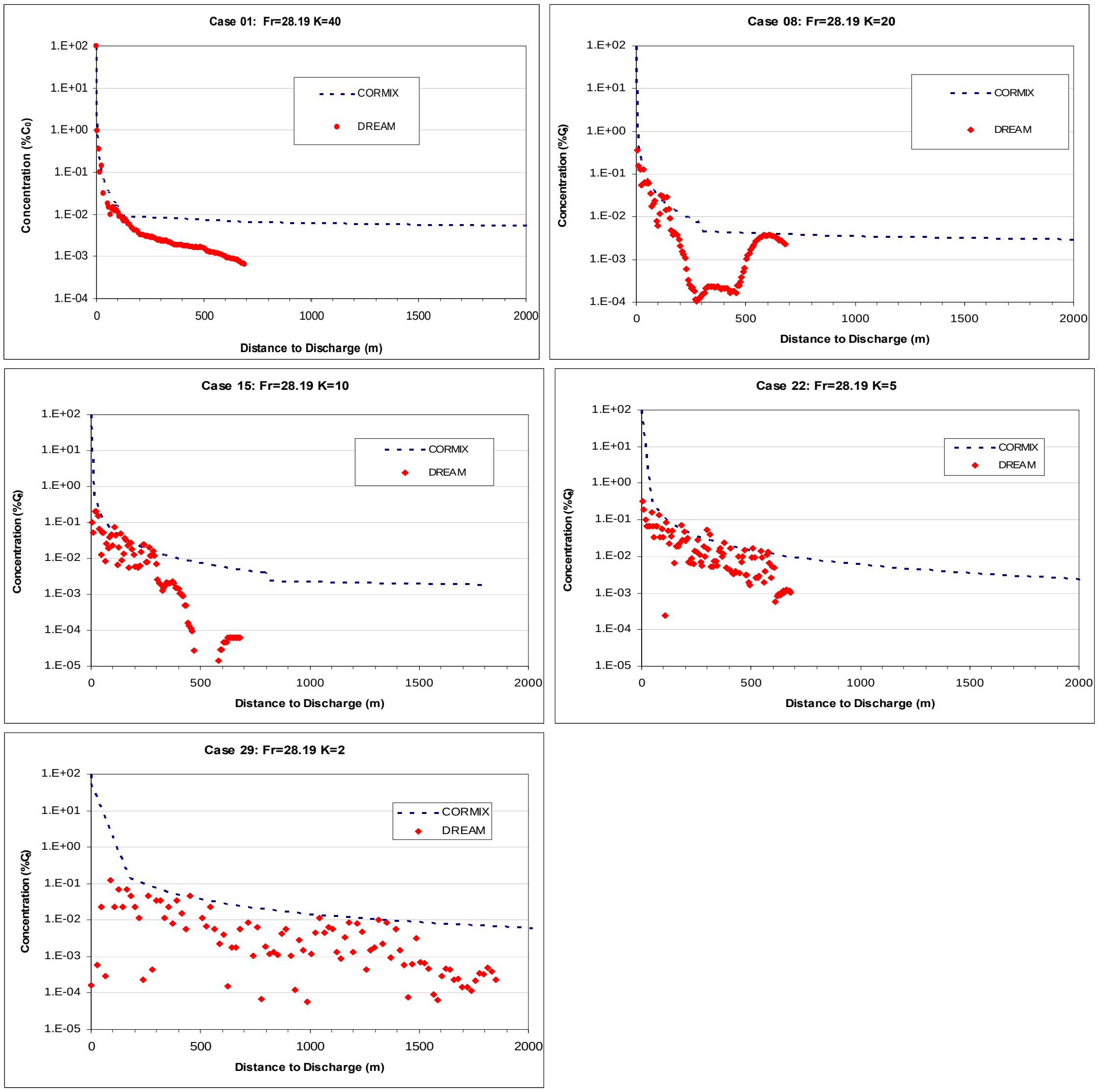

Figure 37: Comparison of Centerline Dilution: Effects of Velocity Ratio K for Same Densimetric Froude Number (Fr=28.19).

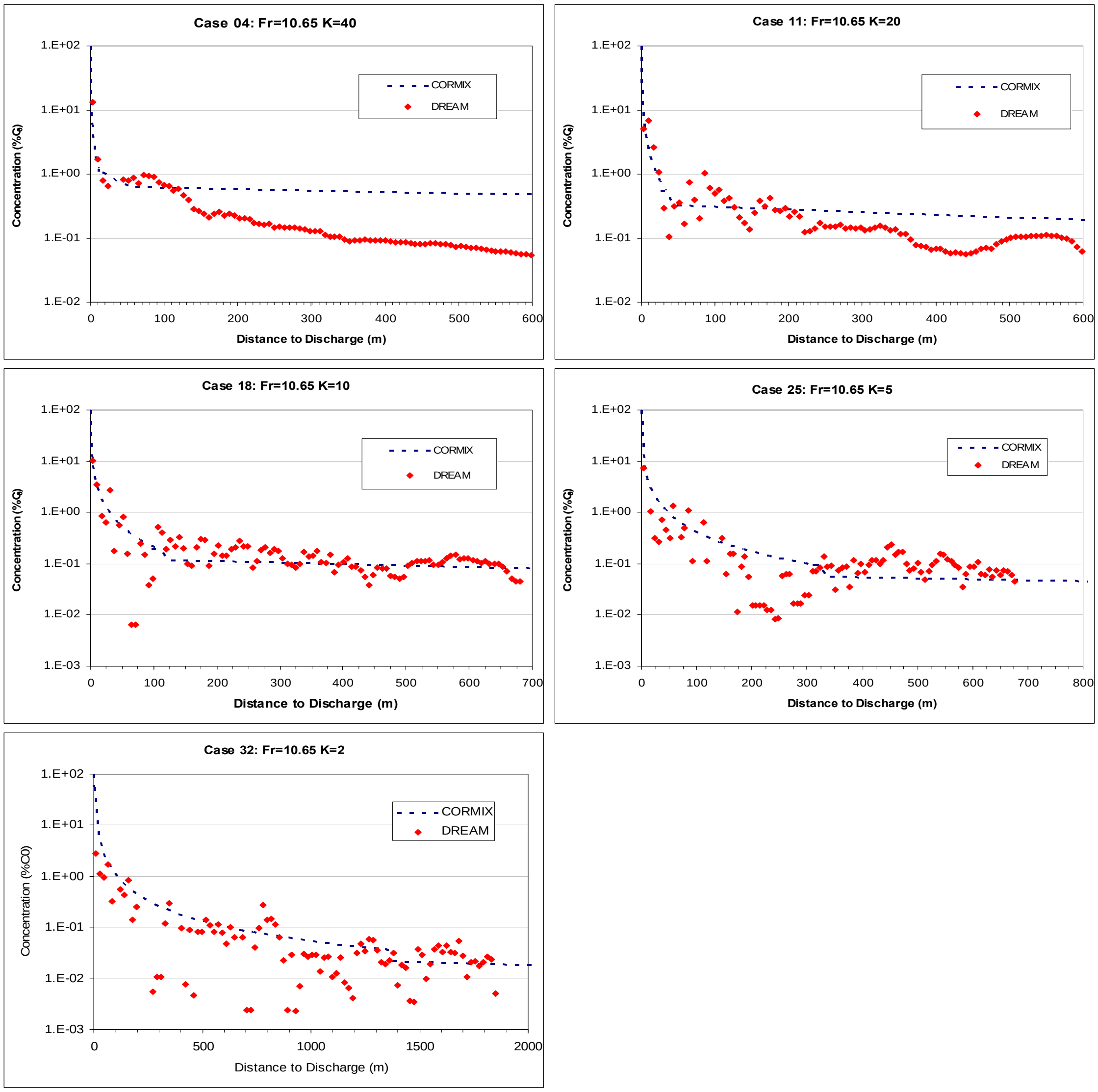

Figure 38: Comparison of Centerline Dilution: Effects of Velocity Ratio K for Same Densimetric Froude Number (Fr=10.65).

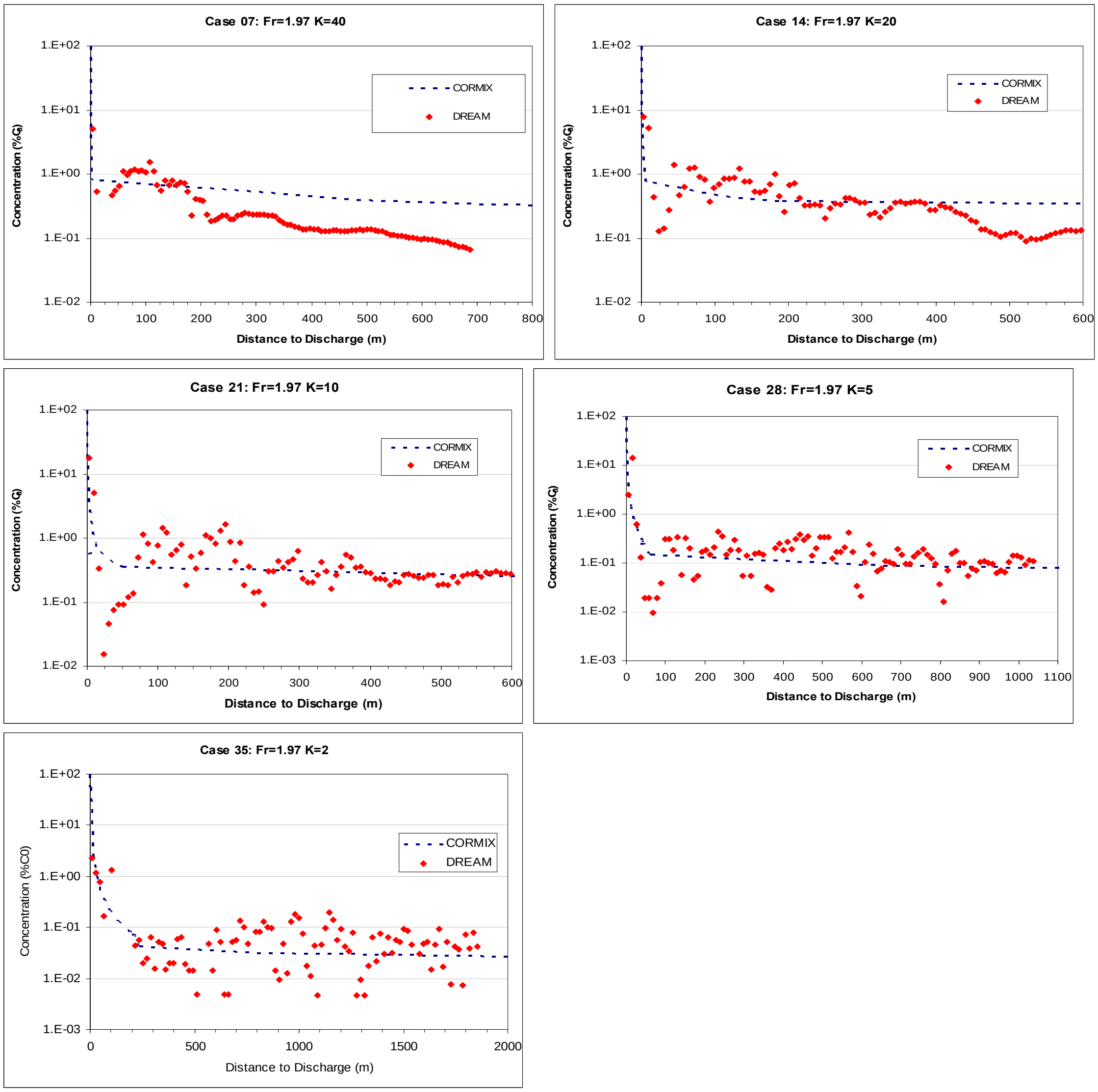

Figure 39: Comparison of Centerline Dilution: Effects of Velocity Ratio K for Same Densimetric Froude Number (Fr=1.97).

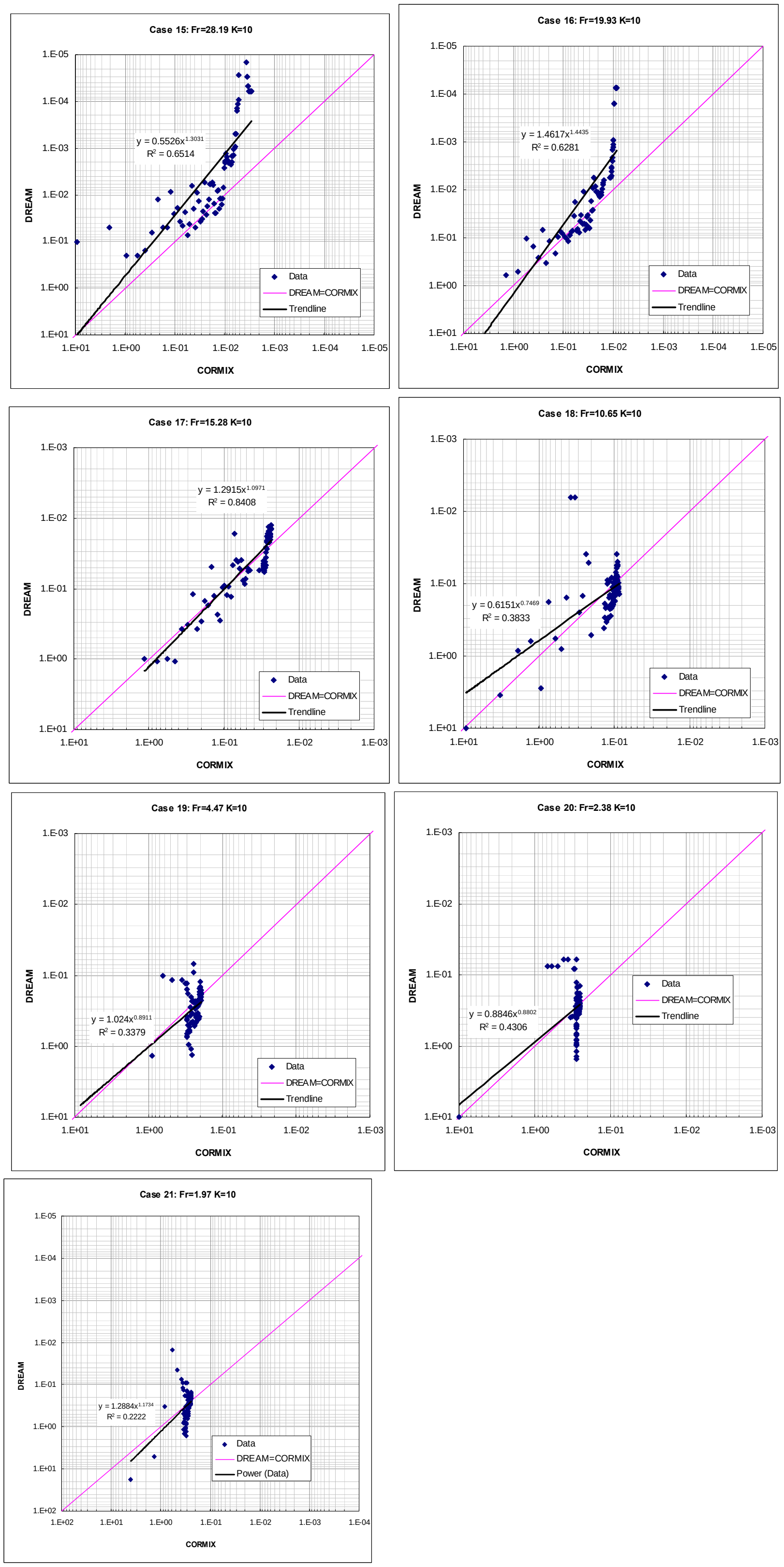

Figure 40: Comparison of Centerline Dilution: Effects of Densimetric Froude Number (Group C: K=10)

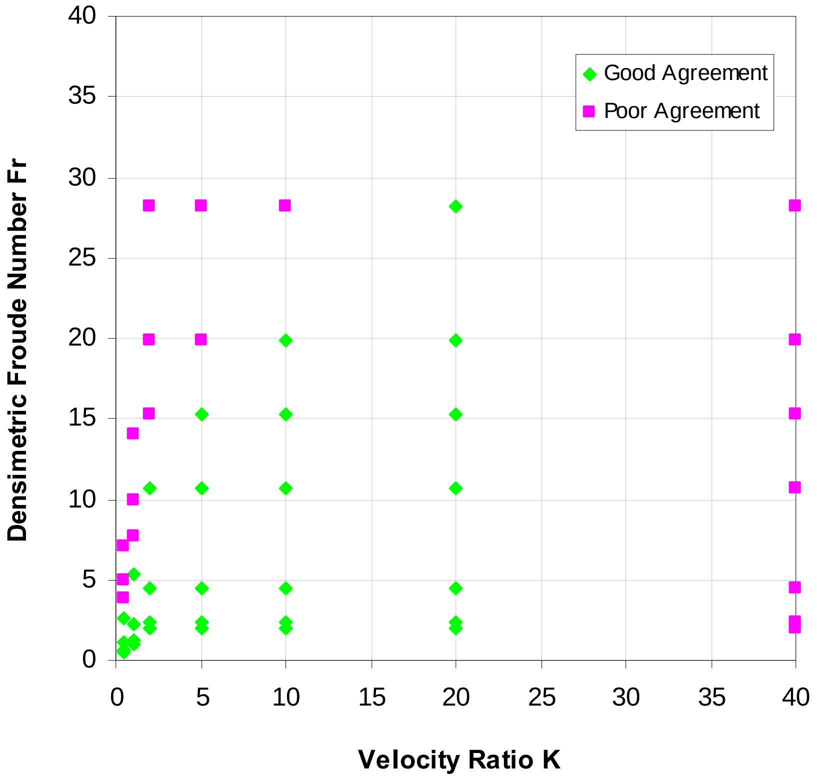

Figure 41: Ranges for Good Agreement for Centerline Concentration

2.4 Summary

From the comparison of plume trajectory, radius, and centerline dilution predicted by DREAM and CORMIX models, it was found that although there was some agreement achieved, the disagreements may have been the result of several factors.

Disagreements generally occurred in the far-field region. One of the causes of the disagreement was that the far-field concentration predicted by CORMIX was uniform (Figure 42c) but DREAM produced a Gaussian profile (Figure 42b and d). However, this system difference should lead to higher concentrations for DREAM than CORMIX, but this did not occur for most of the cases studied. Another likely reason may be the contribution from the additional mixing mechanism and subsequent buoyant spreading process in CORMIX. These processes are not modeled in DREAM.

To further understand the causes of differences, and to improve confidence in using the model, validation of models with field measurements is important.

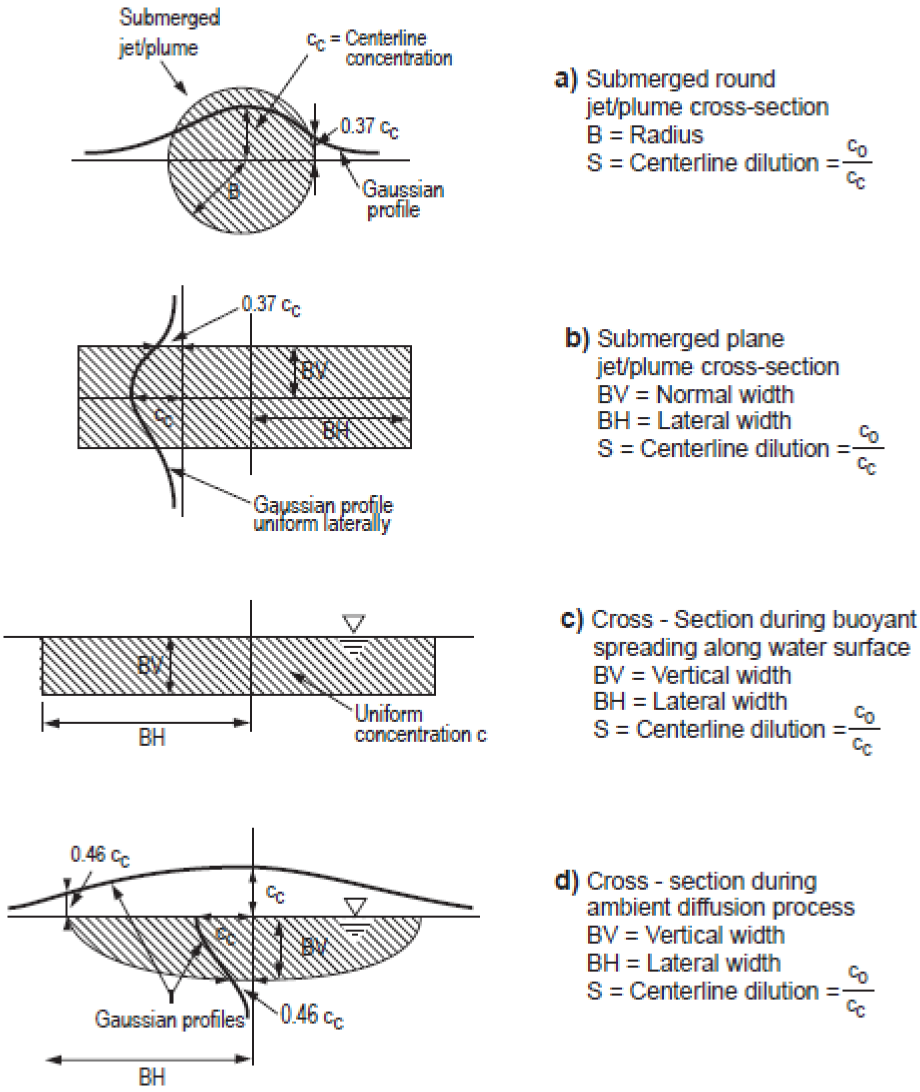

a) Submerged round jet/plume cross-section
B = Radius
S = Centerline dilution = $\frac{c_0}{c_c}$

b) Submerged plane jet/plume cross-section
BV = Normal width
BH = Lateral width
S = Centerline dilution = $\frac{c_0}{c_c}$

c) Cross - Section during buoyant spreading along water surface
BV = Vertical width
BH = Lateral width
S = Centerline dilution = $\frac{c_0}{c_c}$

d) Cross - section during ambient diffusion process
BV = Vertical width
BH = Lateral width
S = Centerline dilution = $\frac{c_0}{c_c}$

Figure 42: Cross-sectional Distributions of CORMIX Predicted Jet/Plume Sections (Doneker and Jirka, 2007).

3. Validation against Field Measurements of Produced Water Data (Venture Field)

To improve the confidence in using DREAM mode, it has been planned to use data collected around Venture, Hibernia and Terra Nova to compare with model predictions.

3.1 The Venture field

The Sable Offshore Energy Project (SOEP) is located offshore Nova Scotia, near Sable Island, 10 to 40 km north of the edge of the Scotian Shelf in water depths ranging between 20 and 80 m. SOEP, comprised of five gas fields (Venture, South Venture, Thebaud, North Triumph, and Alma), currently produces between 250 and 300 million cubic feet (7.1 to 8.5 million m^3) of natural gas and 8,200 barrels (1,300 m^3) of natural gas liquids daily. Significant amounts of produced water, which is water in the aqueous fraction extracted along with condensate and gas from geological formations, are generated along with the recovery of natural gas. Historically, the largest volume of produced water has been associated with the Venture platform (Figure 43). As the largest waste stream from the offshore oil and gas industry frequently discharged at sea, there is concern that the ocean discharge of produced water and its associated manufactured and naturally occurring chemicals may pose adverse impacts to the marine ecosystem (Din and Abu, 1992; Krause et al, 1992; Stagg and McIntosh 1996; Holdway 2002; Querbach et al., 2005; Homoutene et al, 2010; Perz-Casanova et al., 2010). Despite predicted and measured high rates of dilution for the produced water plume following discharge (Neff, 1987), a level of concern still remains as recent studies suggest that some components such as metals, high molecular weight aromatic hydrocarbons and saturated hydrocarbons may accumulate in the sediments and the surface micro-layer as a result of natural physico-chemical processes (Neff, 2002; Durell et al., 2004; Lee et al., 2005; Azetsu-Scott et al., 2007).

To understand the potential effects of discharged produced water from SOEP facilities, the Centre for Offshore Oil, Gas and Energy Research (COOGER), Department of Fisheries and Oceans Canada (DFO), conducted a field program in 2009/10 under a Joint Partnership Agreement (JIP) with AMEC Earth & Environmental, a Division of AMEC Americas Limited, and ExxonMobil Canada East – Halifax. The study focused on produced water discharged from the Venture and Thebaud offshore production facilities (Figure 44). The main purpose of the research was to gain insight into the character and composition of produced water from the production fields, and to assess the potential impact that discharged water might have on the marine environment. As well, empirical data could be used to further validate the Dose-related Risk and Effect Assessment Model (DREAM) that industry operators, scientists and regulators currently apply to predict the movement, concentration and environmental risk posed by produced water discharge at sea.

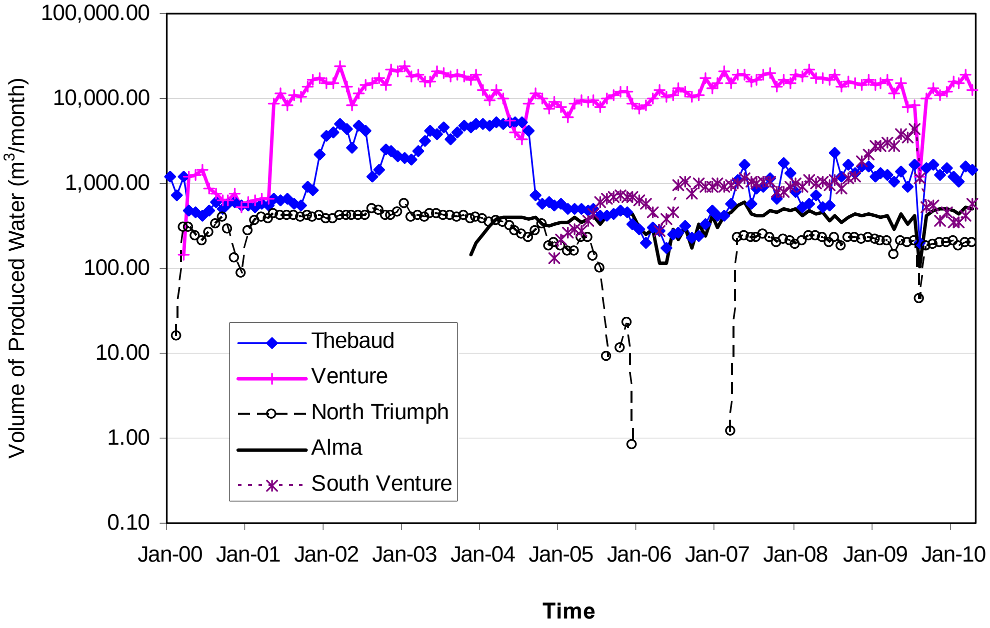

Figure 43: Historical data of produced water volume from five SOEP production facilities on the Scotian Shelf.

The research program was conducted at sea onboard the offshore supply vessel *MV Ocean Tern* in July 2009, and in the laboratories of the Bedford Institute of Oceanography (BIO), between July 2009 and February 2010. Over a period of eight days in the field, samples of seawater were collected at known depths from numerous pre-determined locations around the Venture platform. For certain standard protocols such as pH, conductivity, temperature and salinity, the analyses were conducted at sea. Samples from each station were preserved for later analysis on-shore in the COOGER laboratory facility at BIO. Samples of treated but non-discharged produced water were collected from Venture and Thebaud to characterize their composition, in order to compare the known constituents and concentrations against the various seawater samples collected in the field. Data collected from field samples were ultimately used to determine the relative accuracy of predictions made by the computer model.

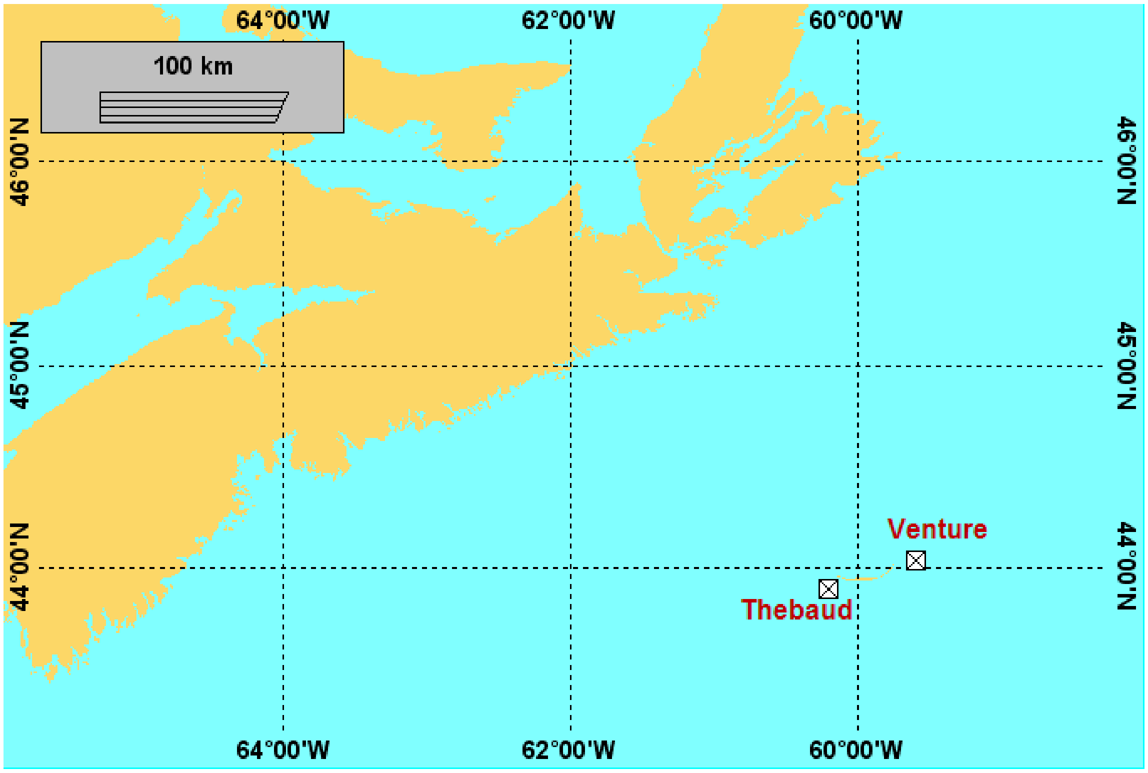

Figure 44: Location of Venture Platform.

3.2 Discharge Parameters

The following parameters for the production water discharged from the Venture platform were required for the fate/transport modeling:

- **Volume/amount.** The mean discharge rate during the study period was 112 m^3/day with a maximum value of 133 m^3/day and a minimum value of 94 m^3/day (Figure 45).
- **Density, salinity and temperature.** The salinity of produced water discharged from the Venture platform during the study period was about 202.4 ppt, which is much higher than the ambient seawater. The temperature of the produced water was 56 °C.
- **Depth of discharge point, pipeline diameter and angle.** The produced water was discharged from a submerged pipe (diameter = 324 mm) at approximately 11 m below the surface (Lowest Astronomic Tide). The pipe is oriented vertically downward.
- **Geographical coordinates of discharge point.** Coordinates of the discharge are 44°1.9913’ N, 59°34.9040’ W.
- **Chemical composition.** The detailed chemical composition of produced water from Venture is reported in Section 3.

3.3 Characteristics of Ambient Water

Site-specific hydrographical data is required to run the model. Temperature and salinity profiles measured at the 28 sampling stations are presented in **Figure 46**. The variation of salinity for the 28 stations is relatively small, being ~0.3 ppt at the surface and ~0.15 ppt near bottom, with the exception of the profile at SE25 (53 m southeast of the platform) which exhibited an abnormal trend at 5 m depth. While a salinity thermocline is observed for some stations, others have profiles close to linear stratification. A similar trend is shown for the temperature profile. While the temperature difference between surface and bottom for the majority of the stations is no more than 1.5°C, the two sites farthest from the platform (far-field 18 km reference and near-field SE5000) have a $\Delta T = 2.5 - 4.5°C$.

To determine temperature and salinity profiles that are representative of the Venture site, profiles from near-field stations were excluded, as they potentially might be affected by the discharge. Analysis of the remaining data showed that the reference site had a profile for each of these parameters that was similar to the average profile of the remaining stations; it was thus selected for use in the model with simplification by smoothing the curves (shown in green in Figure 46).

To model the transport of produced water, time series current data were required. As there was no current mooring at the Venture platform, data from an ocean circulation model (NEMO, 2010) were used. The data are available at 3, 9, 16, and 23 m depths and two-hour intervals. Sample data at 16 m have been plotted in Figure 47.

3.4 Model Setup

A domain of approximately 6 km × 6 km (Figure 48) was selected as the area to be modeled. The domain was divided into 500 × 500 cells and the size of each cell was about 12 m × 12 m. The model used a time step of one minute and an output interval of ten minutes.

Although a large number of different organic chemicals were found in the produced water, it was unrealistic to simulate all of them individually using the model, because simulation time increases considerably with an increase in chemical components. In this study, the organic chemicals were grouped according to the recommendation of SINTEF (2009). The chemical components included in the simulation are shown in Figure 49.

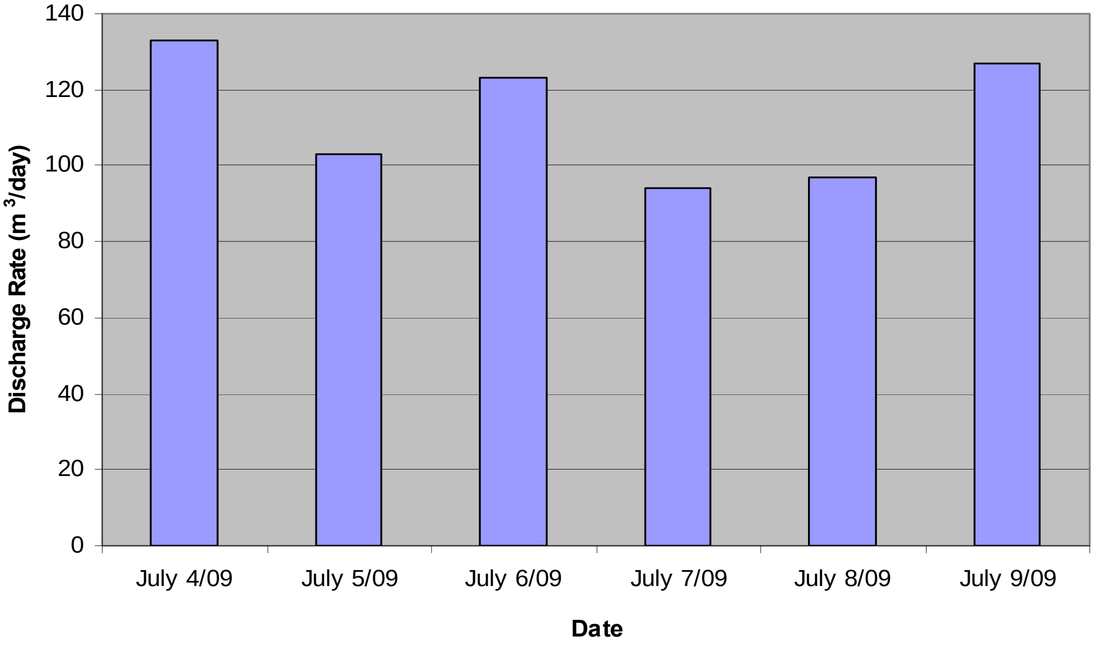

Figure 45: Daily discharge rate of produced water from Venture platform.

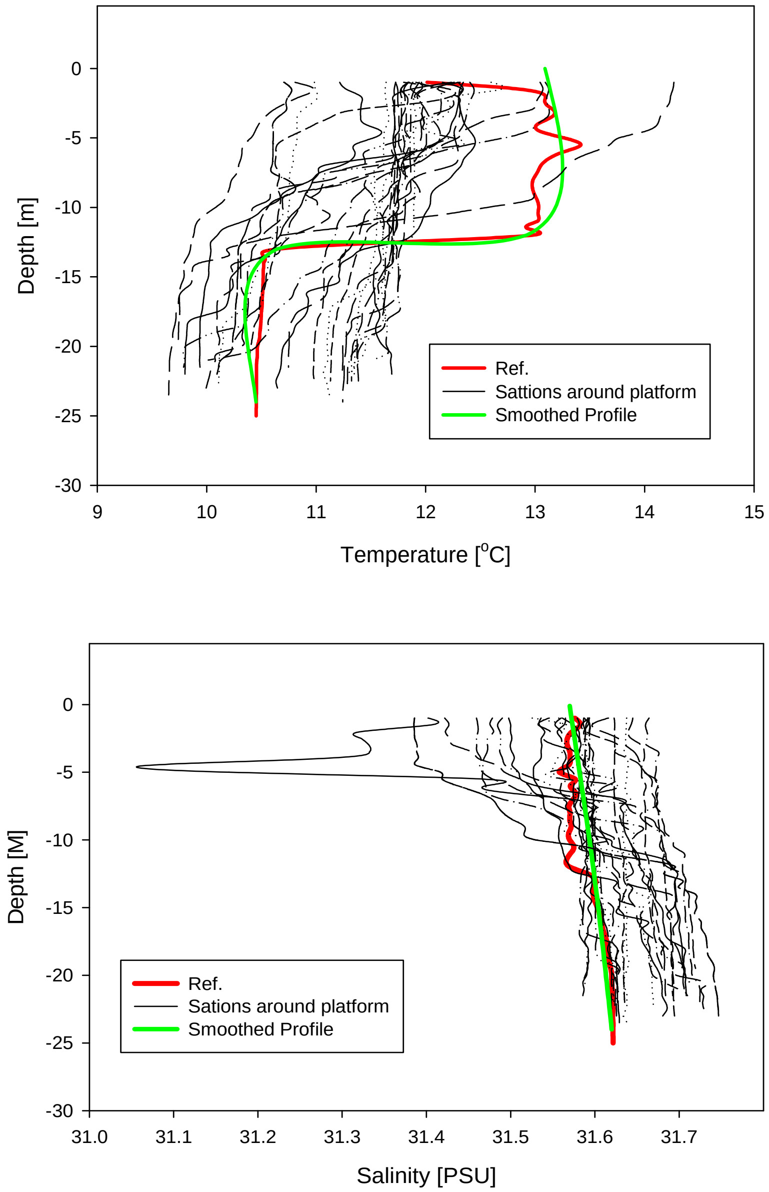

Figure 46: Combined CTD profiles for all stations. The green line is the smoothed profile derived from the reference (Ref.) that was used in the model.

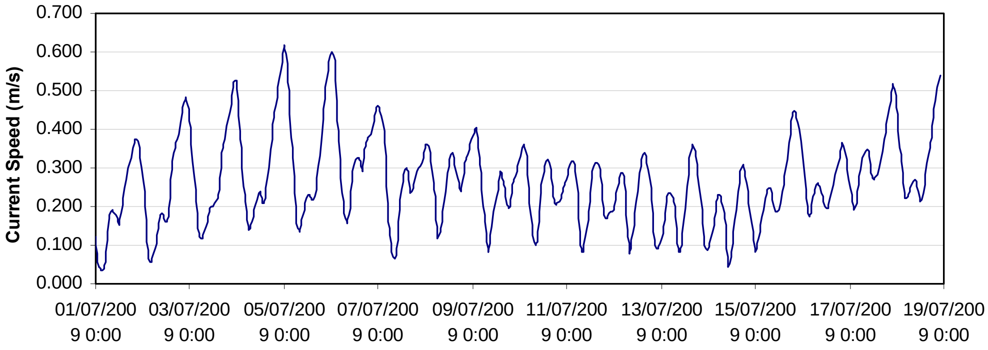

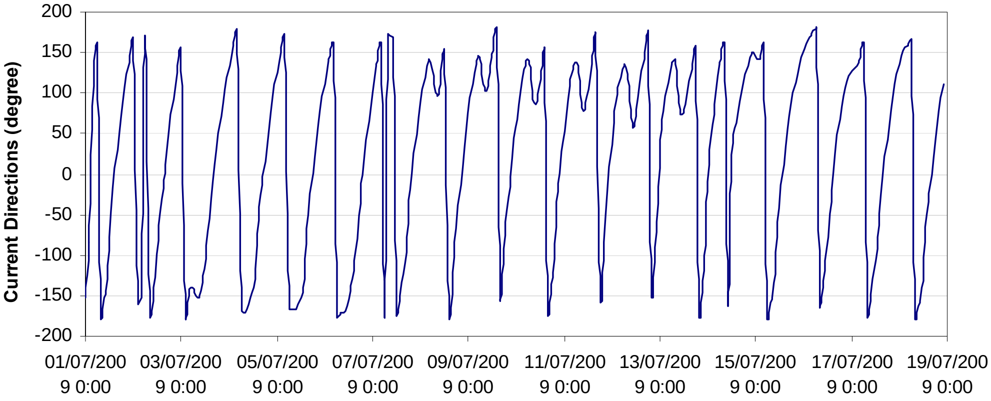

Figure 47: Currents at 16 m depth.

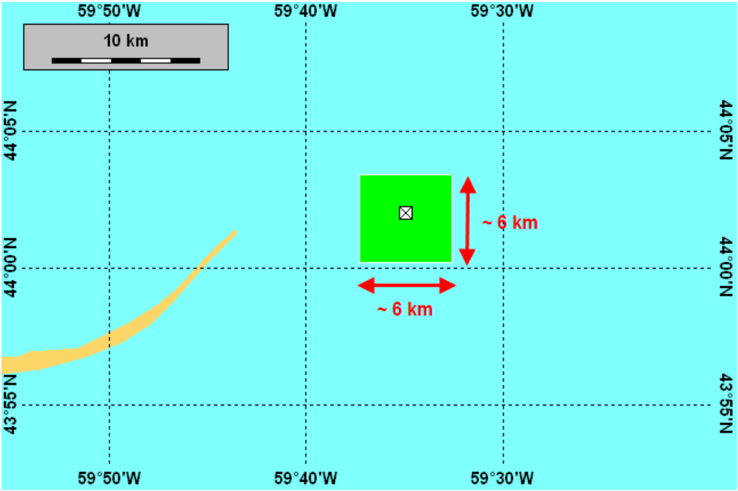

Figure 48: Model domain around the Venture platform.

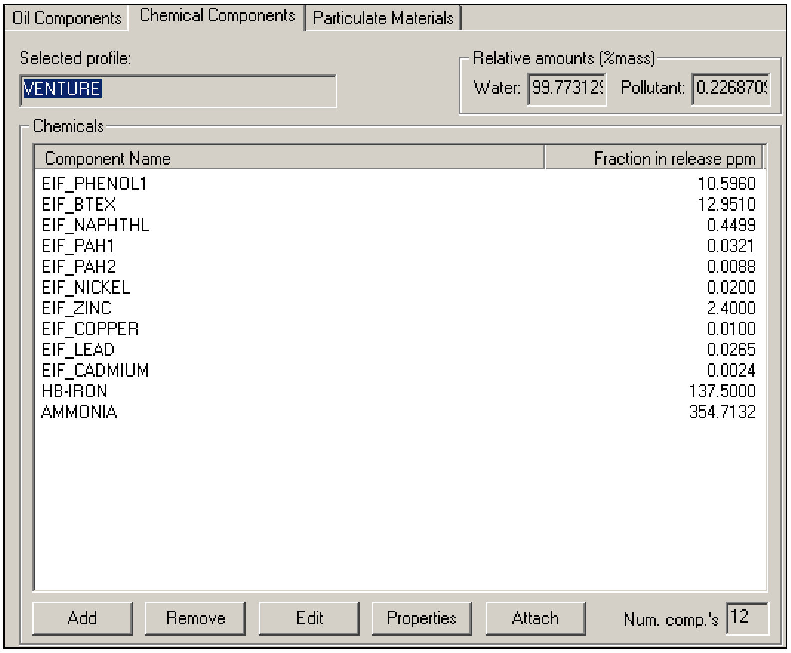

Selected profile: VENTURE

Relative amounts (%mass)
Water: 99.77312
Pollutant: 0.226870

Chemicals

Component Name	Fraction in release ppm
EIF_PHENOL1	10.5960
EIF_BTEX	12.9510
EIF_NAPHTHL	0.4499
EIF_PAH1	0.0321
EIF_PAH2	0.0088
EIF_NICKEL	0.0200
EIF_ZINC	2.4000
EIF_COPPER	0.0100
EIF_LEAD	0.0265
EIF_CADMIUM	0.0024
HB-IRON	137.5000
AMMONIA	354.7132

Num. comp.'s 12

Figure 49: Modeled chemical components.

3.5 Modeling Results

The predicted produced water plume profiles at 0.5, 1, 2.5, and 5 days are shown in Figure 50 (the complete chemical mixture) and Figure 51 (an individual chemical class, PAHs in this case). The horizontal profiles show that a narrow plume (width = ~100 m at ~500 m from the platform) constantly changes location with the tidal currents. The vertical profiles indicate that the plume sinks to and spreads out on the bottom after discharge. The maximum concentration of the complete chemical mixture is approximately 28-35 ppb, and the maximum concentration of PAHs is approximately 0.003 ppb.

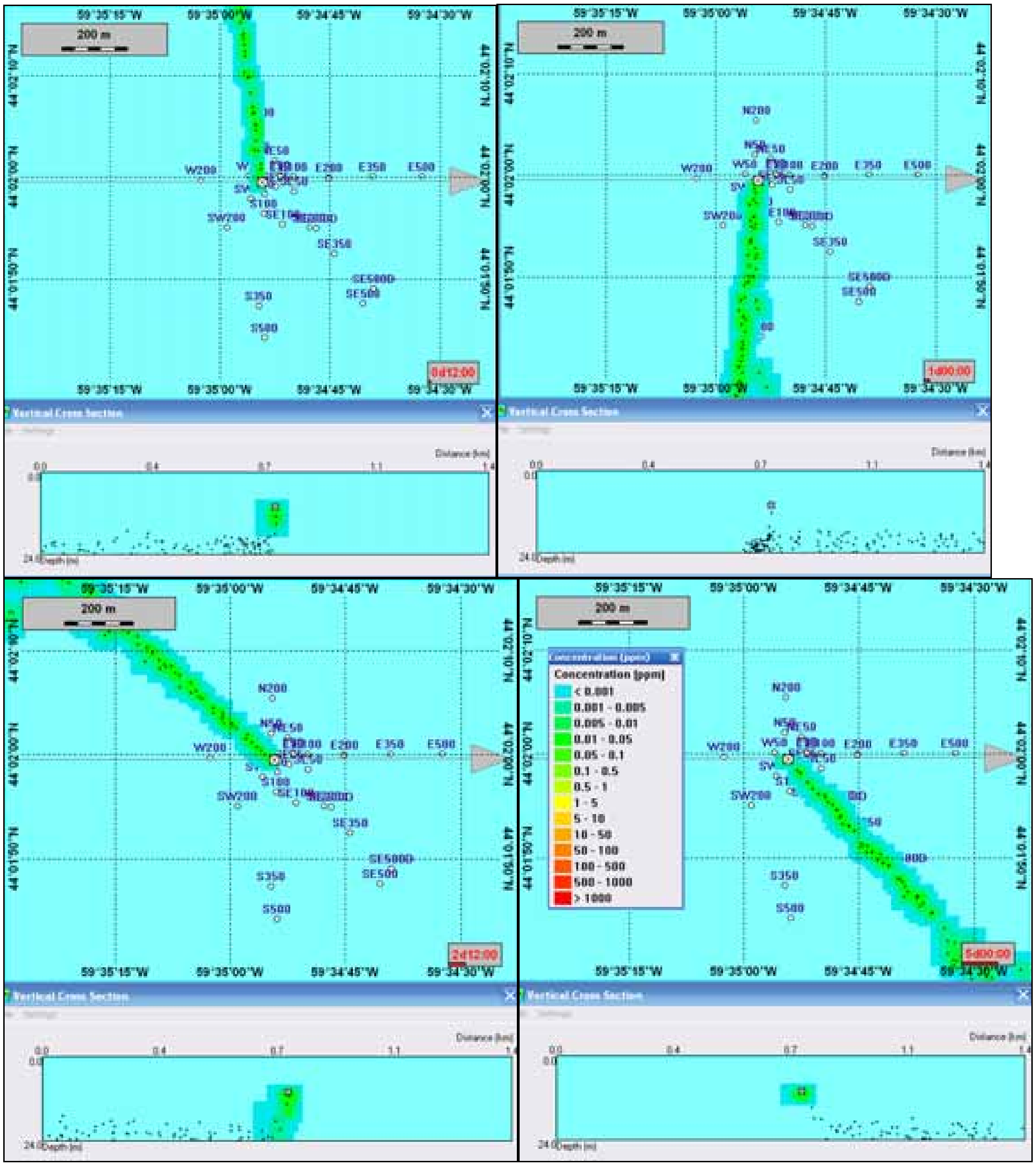

Figure 50: Horizontal (top section) and vertical (bottom section) dispersion of complete chemical mixture at 0.5 (top left panel), 1 (top right), 2.5 (bottom left), and 5 (bottom right) days.

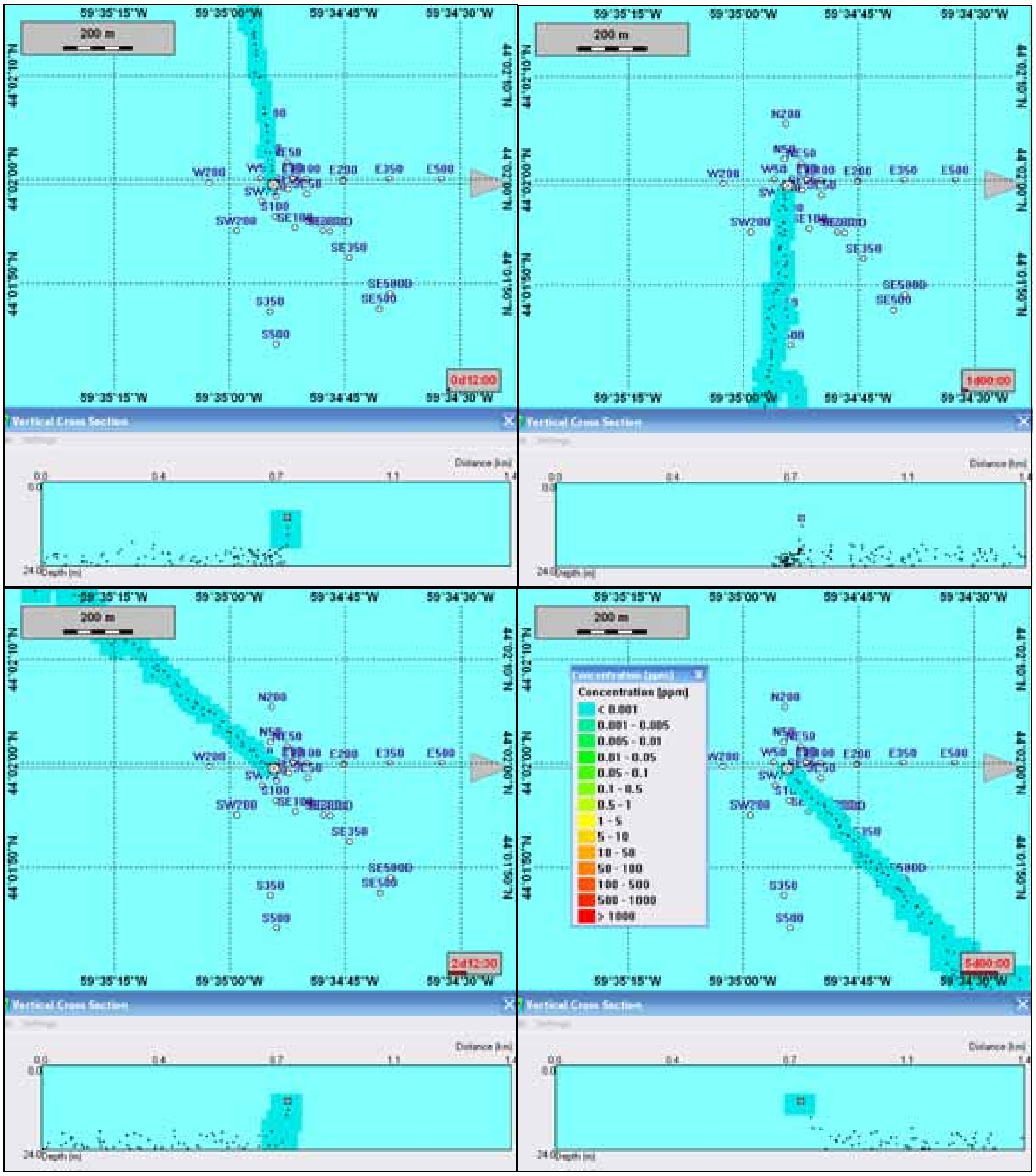

Figure 51: Horizontal (top section) and vertical (bottom section) dispersion pattern of all PAHs at 0.5, 1, 2.5, and 5 days.

To show the change of concentration with distance to the platform, concentrations of individual chemicals from the plume at 1 day 5 hours were plotted (Figure 52 and Figure 53). The reason for choosing 1 day 5 hours was because the produced water discharge rate was at the maximum level (133 m^3/day) and the current speed was close to the minimum value at that time. As a result, the dilution rate and concentrations for this period represented a worst case scenario.

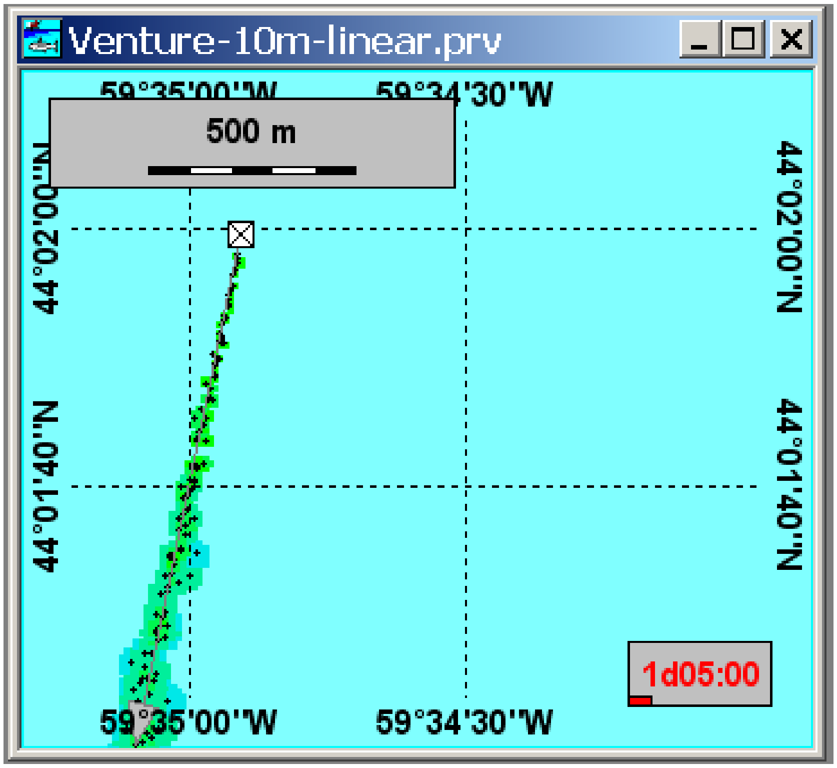

Figure 52: Location of the plume centre line.

Figure 53 shows that the concentration of all of the simulated chemicals decreased with increasing distance from the platform to less than 10 ppb within about 500 m, with the exception of Fe and ammonia. By comparing the chemical concentrations with their initial concentrations in produced water, it can be determined that the dilution factor was initially very high (>1500-fold). Subsequently, it decreased to a very low ~10-fold factor with increasing distance from the platform out to 1.2 km. A similar pattern was found for the barite. The maximum deposition of barite on the seabed was less than 1.3 g/m^2 and it decreased to less than 0.2 g/m^2 at 1.2 km.

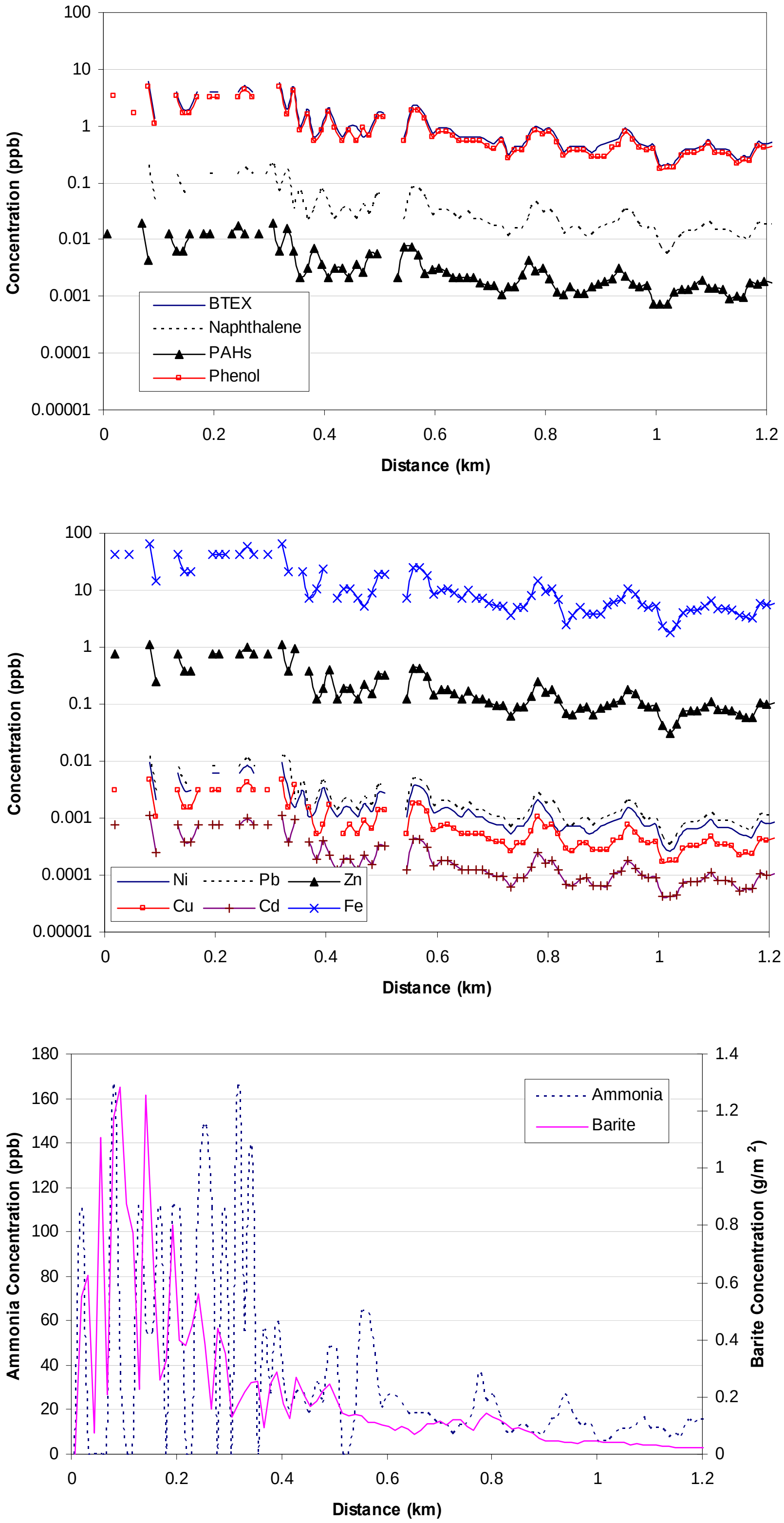

Figure 53: Concentration of various pollutants along the plume centre line (time = 1 day 5 hours).

3.6 Model Validation

3.6.1 Comparison with Measurements

The time series concentrations at 27 stations (excluding the far-field reference site) around Venture were extracted. Most of the stations had profiles similar to that presented in Figure 54 for station SE25. Because selection of sampling locations was based on mean current directions which do not necessarily match the dynamics of the real-time currents, and because the discharge volume and size of the plume are small, most of the samples were taken outside the plume. Although these stations cannot be used to validate the dilution ratios, the comparison of modeling and measurements using data for these stations proved the following.

- The model predicted that for 26 stations (except NE50), chemical concentrations would be at near background. This agreed with the observed near background values for these stations.
- Examination of the time series data for any given station (Figure 54) showed that the model predicted that the plume was constantly moving, and this explains why the seawater monitoring samples mostly showed near background concentrations for all 26 stations as they were always located outside the plume at the time of sampling.
- Both the model and field measurements indicated that there was no detectable background accumulation of chemicals outside the plume.

Figure 55 shows the plume profile for the NE50 station. Notice that the plume was at the NE50 station at the time of sampling and therefore the comparison of data for this station provides information on how well the model can predict the dilution ratio. A comparison of modeled and measured concentrations for iron, ammonia, phenol and naphthalene at the bottom- and mid-depths were plotted (Figure 56 and Figure 57). Based on these results the following is clear:

- The model predicted the dilution very well. The ratios of measured to predicted concentrations for the near bottom sample were 1.55, 1.12, 1.12, and 1.25 for iron, ammonia, phenol and naphthalene, respectively. The mean value was 1.26.
- For the mid-depth sample, the ratios of measured to predicted concentrations were 0.88, 0.77, and 1.56 for iron, ammonia and phenol. The mean value was 1.07. The model predicted a naphthalene concentration of 17 ppt which was below the detection limit and agreed with the non-detectable level of naphthalene for this sample.
- The model predicted the plume location well.

3.6.2 Advantages and Limitations

The advantages of the sampling design used in this study were that it provided an overall picture of the level of chemicals associated with produced water around the platform, and demonstrated that there was no elevated level of produced water constituents outside the plume. Although the study provided quantitative validation of site-specific predictions, it demonstrated that further research is required to more accurately determine how well the model can predict how concentrations change with increasing distance from the platform. This can be achieved by design sampling locations based on forecasted real-time currents.

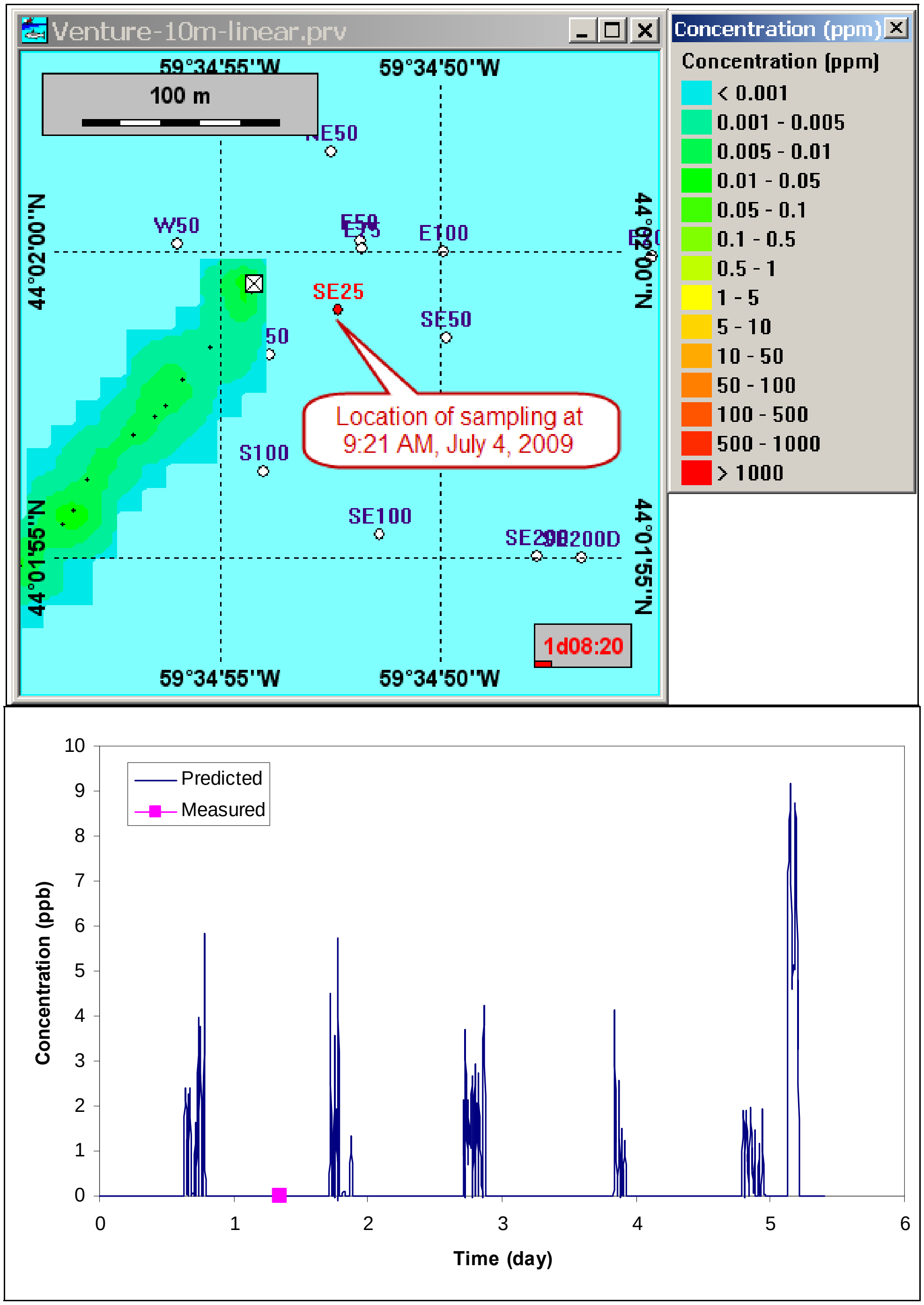

Location of sampling at 9:21 AM, July 4, 2009

Figure 54: Field vs. modeled data for Fe concentration at SE25.

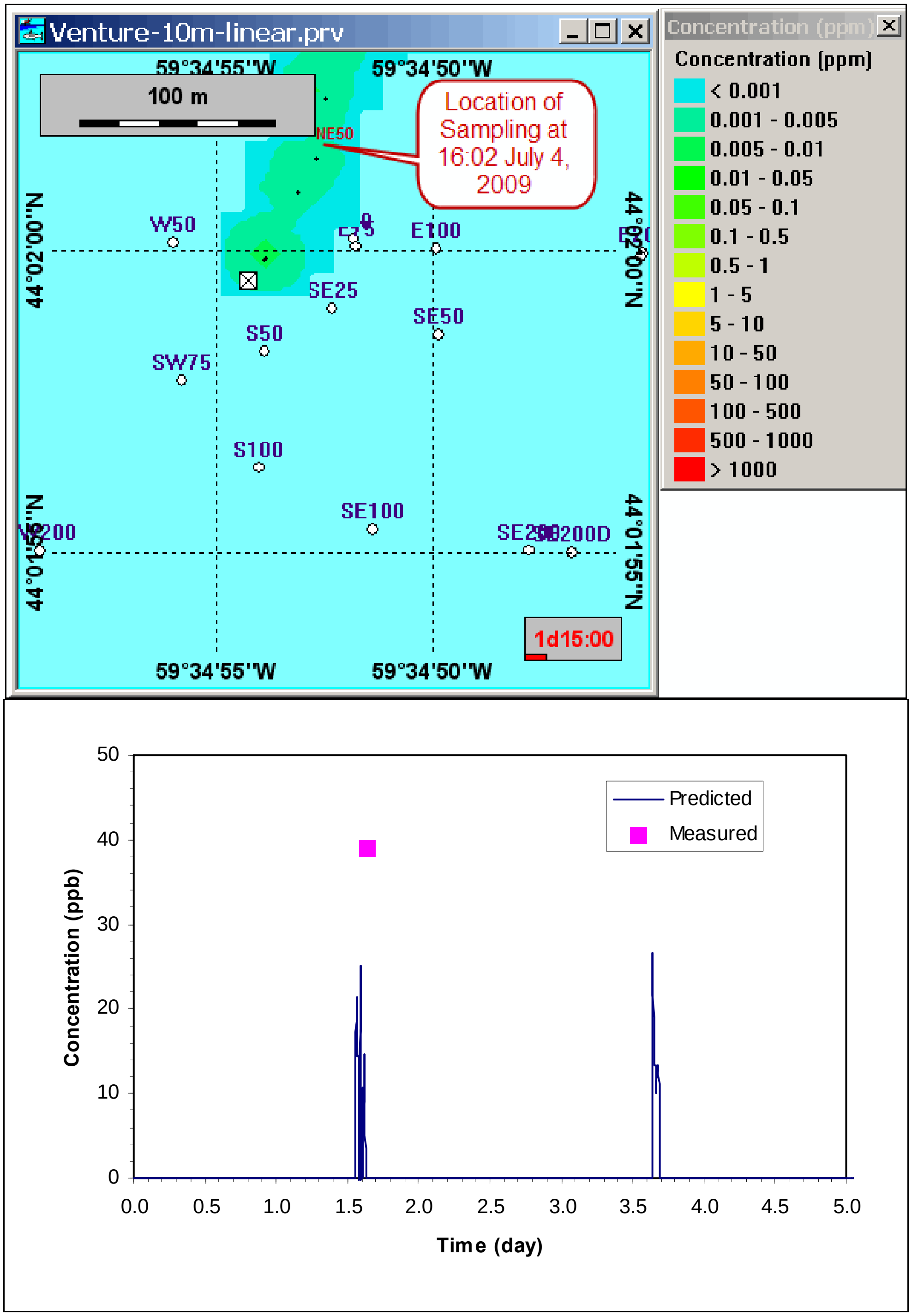

Location of Sampling at 16:02 July 4, 2009

Figure 55: Field vs. modeled data for Fe concentration at NE50.

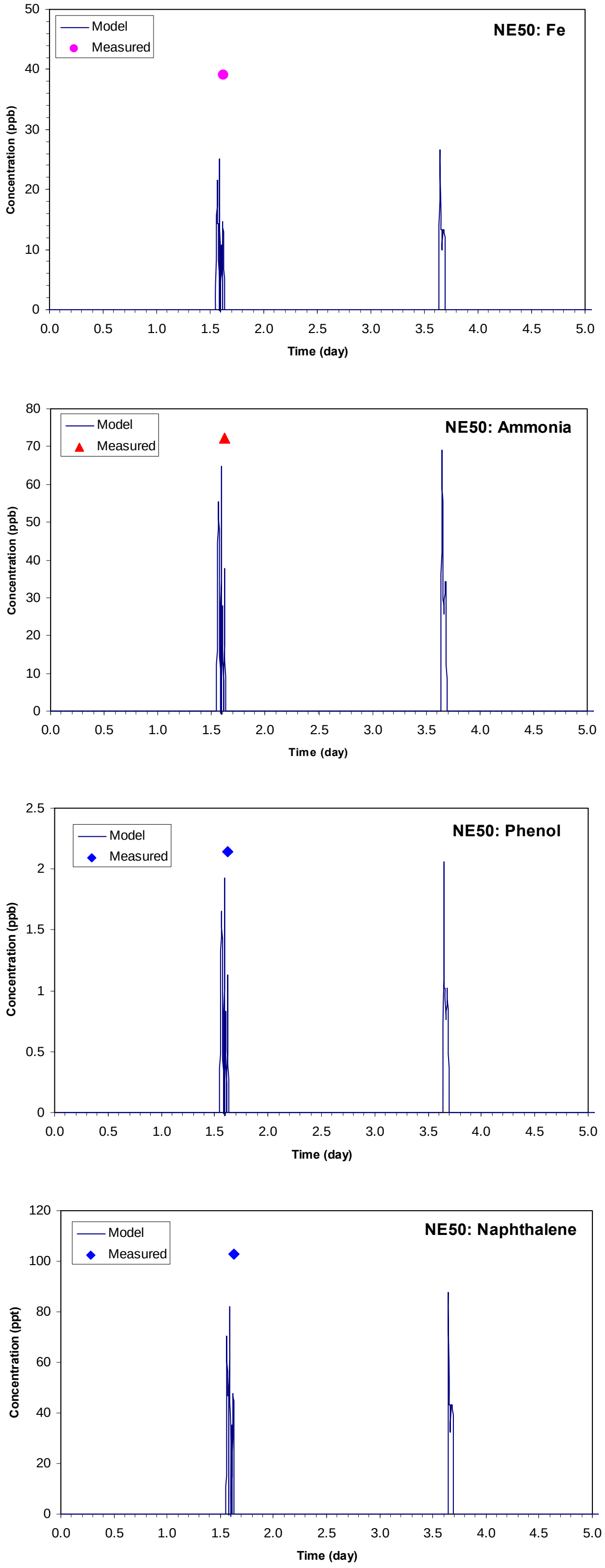

Figure 56: Comparison of field vs. modeled data for NE50 near bottom depth.

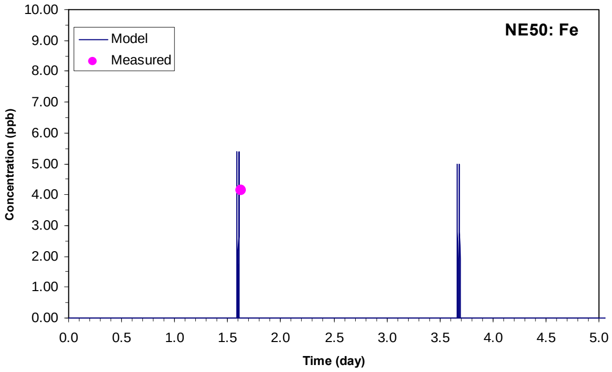

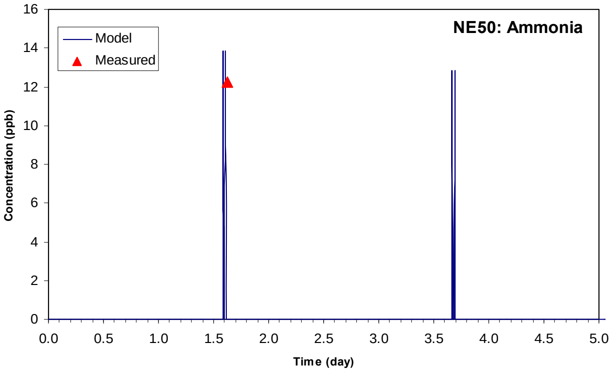

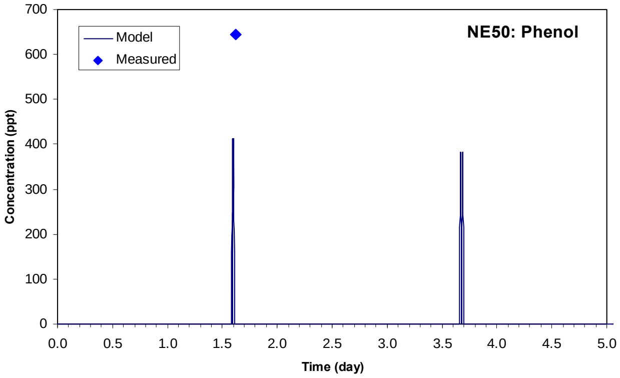

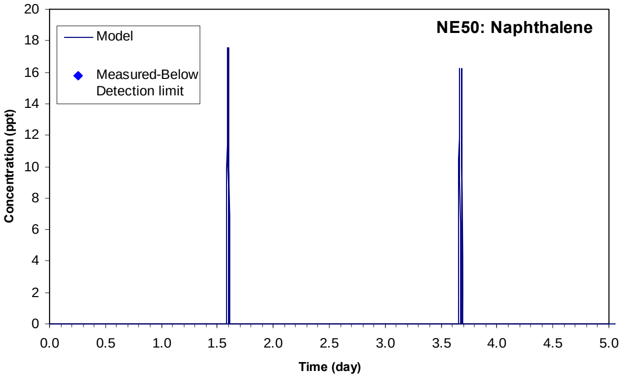

Figure 57: Comparison of field vs. modeled data for NE50 mid-depth.

4. Validation against Field Measurements of Produced Water Concentrations (Terra Nova Field)

4.1 *The Terra Nova Oil Field*

The Terra Nova oil field is located on the Grand Banks, approximately 350 km east-southeast of St. John's and 35 km southeast of the Hibernia oil field (Figure 58). Suncor Energy acts as operator for the development on behalf of the owners (Suncor Energy, Mobil Oil Canada Properties, Husky Energy Inc., StatoilHydro ASA, Murphy Oil Company Ltd., Mosbacher Operating Limited and Chevron Canada Resources).

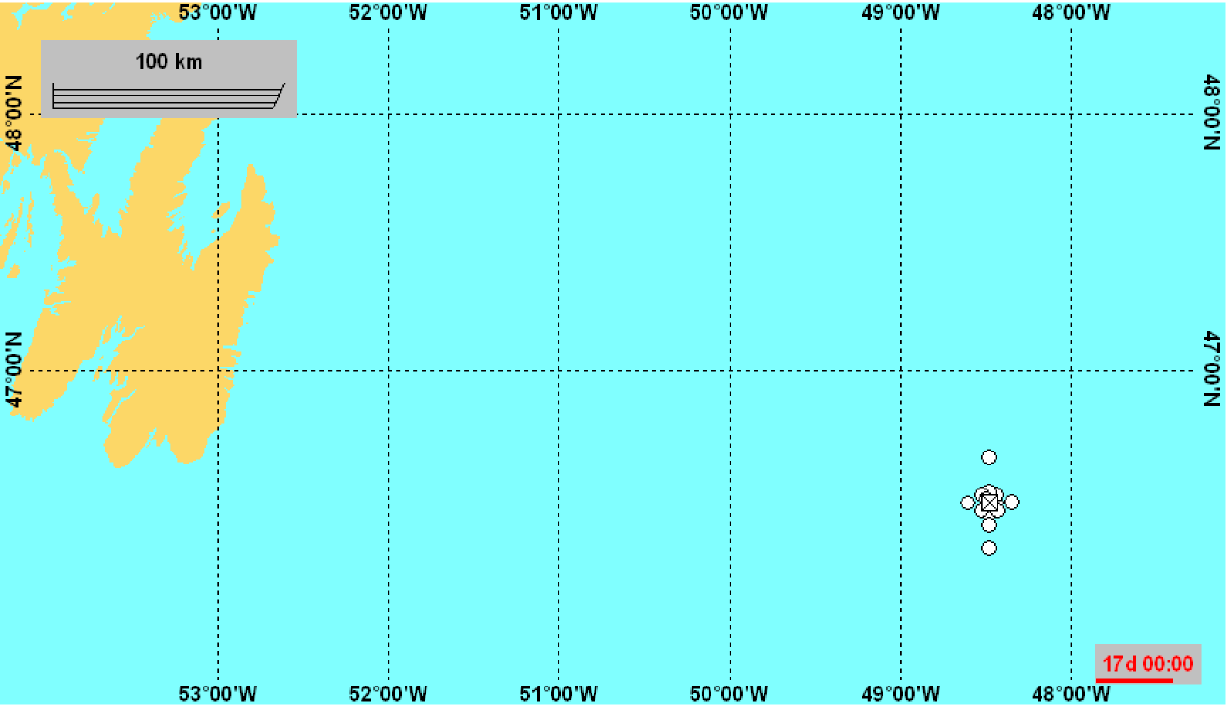

Figure 58: Location of Terra Nova Oil Field. The square is the Terra Nova FPSO and circles are sampling stations.

4.2 *Discharge Parameters*

The Terra Nova FPSO has a length of 292 m, a beam of 45.5 m, and a maximum draught of 20 m (Figure 2). Produced water is discharged downward through a caisson located approximately mid-ship toward the port side and approximately 67 m aft of the Turret Area which remains at a fixed location, and about which the FPSO can pivot (Figure 59). The depth of discharge can vary from 13-20 m, depending on the vessel draught.

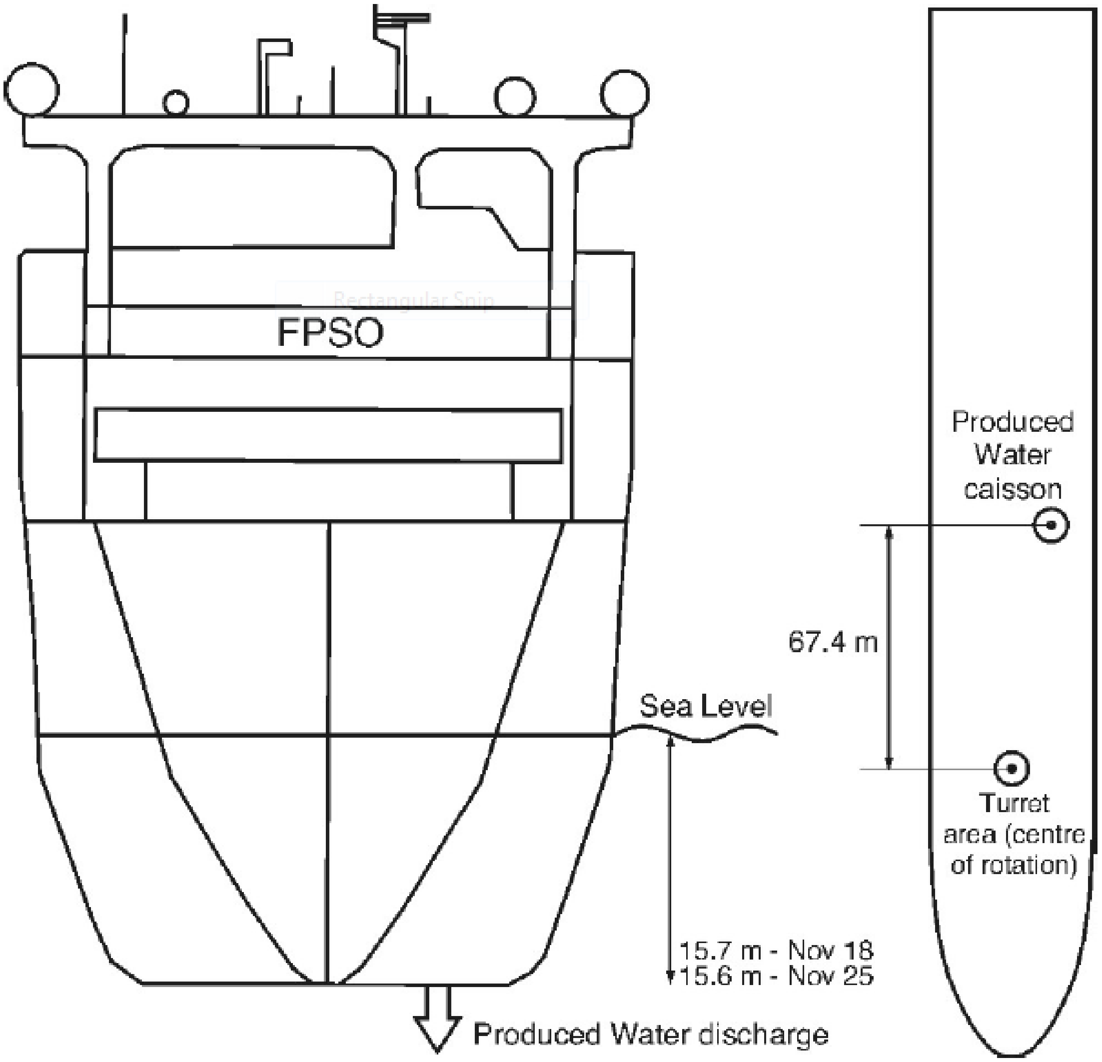

Figure 59: Schematic of FPSO showing location and depth of produced water discharge (Lorax, 2006)

The following parameters for the production water discharged from the Terra Nova FPSO were required for the fate/transport modeling.

- **Volume/amount.** The discharge rate during the study period (August 2007) ranging from 8,330 m^3/day to 10,079 m^3/day (Table 2).
- **Density, salinity and temperature.** The produced water is discharged from the FPSO at a temperature of 60° C and with a salinity from 65 to 70 ppt. Using the standard UNESCO equation of state for seawater, this yields a corresponding density of at least 1,030 kg/m^3. In addition, Petro-Canada has reported corrected densities exceeding 1,050 kg/m^3.
- **Geographical coordinates of discharge point.** Coordinates of the discharge are 46°28.53’ N, 48°28.86’ W.
- **Chemical composition.** The detailed chemical composition of produced water from Terra Nova is reported in Section 4.

Table 2: Produced water discharge rate.

Date	Volume Discharged (m^3/day)
15-Aug-07	8,330
16-Aug-07	10,079
17-Aug-07	9,801
18-Aug-07	9,746
19-Aug-07	9,896
20-Aug-07	9,545
21-Aug-07	9,346

4.3 Characteristics of Ambient Water

Site-specific hydrographical data is required to run the model. Temperature and salinity profiles were measured at more than 31 stations. An example plot of temperature and salinity profiles at three sampling stations are presented in Figure 60. The sampling stations are: (1) R50k (46°42.166'N, 49°25.556'W), (2) TN20k (46°39.254'N, 48°28.876'W), and (3) TS10k (46°23.043, 48°28.915). While the variations of salinity and temperature between 20 m to 60 m are relatively small, there is a noticeable difference at the surface layer (0 – 30 m) and the maximum variation is 0.46 ppt at 14 m and 2°C at 26 m.

To determine temperature and salinity profiles that are representative of the Terra Nova site, profiles from near-field stations (within 5 km) were excluded, as they potentially might be affected by the discharge. Analysis of the remaining data (10, 20, and 50 km) showed that the reference site had a profile for each of these parameters that was similar to the 10 km stations, and an average profile of the Reference and S10k was used.

To model the transport of produced water, time series current data were required. There is a current mooring near the Terra Nova platform, and the data are available at 10, 47, and 84 m depths and two-hour intervals. Sample data at 16 m have been plotted in Figure 61. The figure shows that the tidal influence is strong and the directions of currents continue to change periodically. With the influences of wind, the surface current is much stronger than that of the mid-depth and bottom. The maximum current at surface was 48.53 cm/s with a mean value of 18.58 cm/s. The maximum current at mid-depth was 25.22 cm/s with a mean value of 9.9 cm/s. The magnitudes of near bottom current are very close to the mid-depth with a maximum value of 22.50 cm/s and a mean value of 8.7 cm/s. The details of the currents are summarized in Table 3.

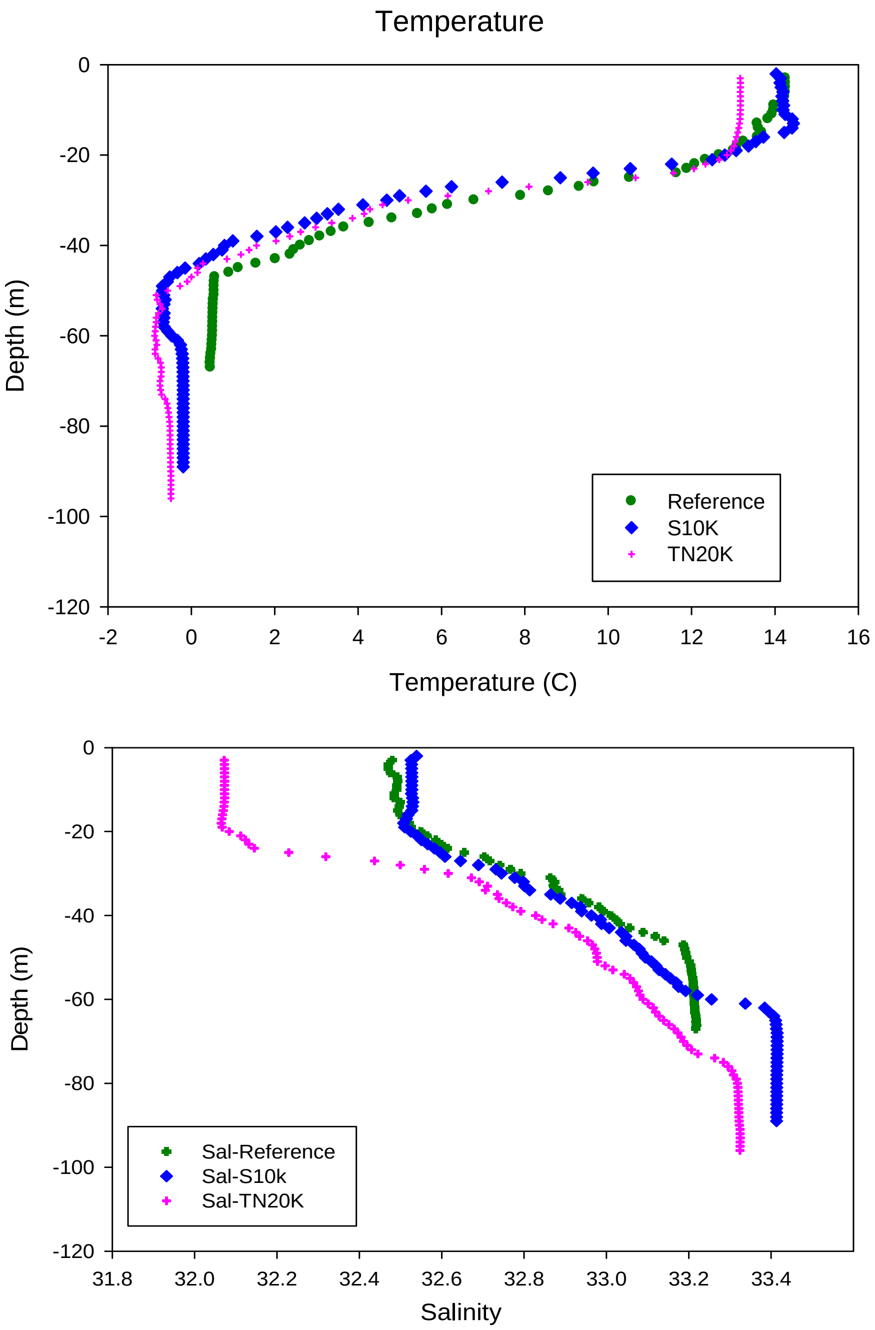

Figure 60: **CTD profiles at three stations.**

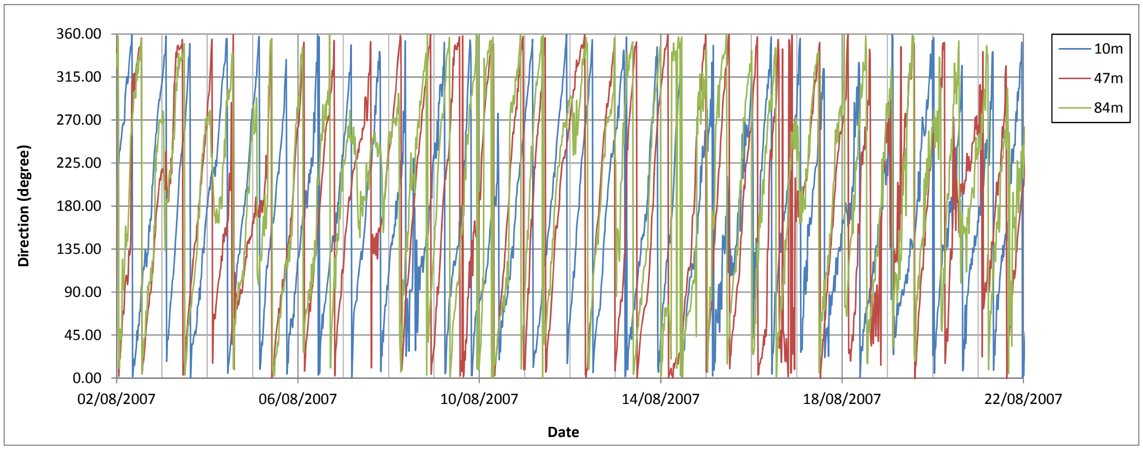

Figure 61: Currents at Terra Nova during the study period.

Table 3: Summary statistics of the currents at Terra Nova in August 2007.

Parameters	10 m	47 m	84 m
Mean	18.59	9.90	8.70
Standard Error	0.21	0.11	0.09
Median	17.78	8.95	8.22
Mode	11.44	3.72	6.82
Standard Deviation	9.98	5.24	4.17
Sample Variance	99.62	27.44	17.35
Range	48.24	24.12	21.00
Minimum	0.29	1.10	1.50
Maximum	48.53	25.22	22.50

4.4 Model Setup

A domain of approximately 100 km × 100 km (Figure 62) was selected as the area to be modeled. The boundary of the domain is from 45°57'N, 49°08'W to 46°56'N, 47°49'W. The domain was divided into 500 × 500 cells and the size of each cell was about 200 m × 200 m. The model used a time step of 20 minutes and an output interval of 30 minutes.

Although a large number of different organic chemicals were found in the produced water, it was unrealistic to simulate all of them individually using the model, because simulation time increases considerably with an increase in chemical components. In this study, the organic chemicals were grouped according to the recommendation of SINTEF (2009). The chemical components included in the simulation are shown in Figure 63. It should be noted that the unit for ammonia and silicate is μmol/L, although the model shows it as ppm due to the model's restriction on manual inputting of units. In other words, a model output of concentration of 1 ppm ammonia (or silicates) equals 1 μmol/L ammonia (or silicates).

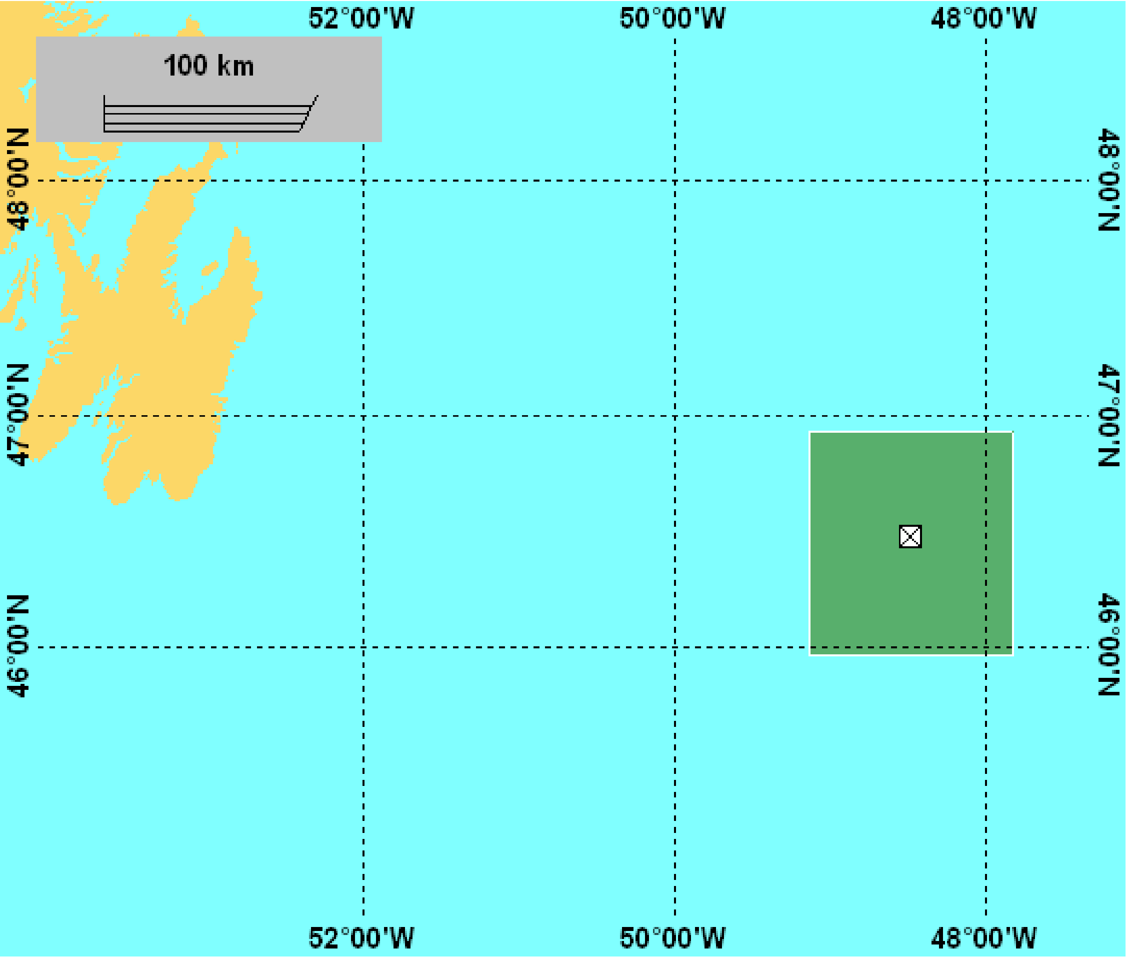

Figure 62: Model domain around the Terra Nova platform.

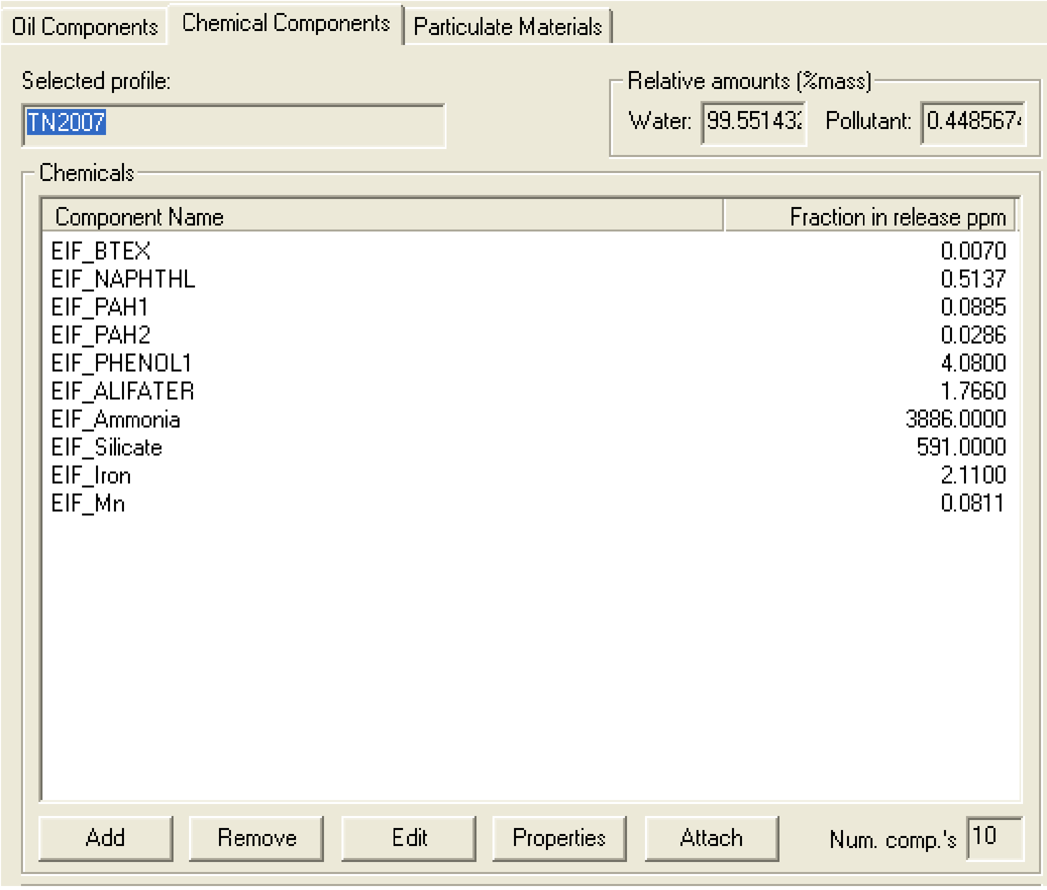

Selected profile: TN2007

Relative amounts (%mass)
Water: 99.55143
Pollutant: 0.448567

Chemicals

Component Name	Fraction in release ppm
EIF_BTEX	0.0070
EIF_NAPHTHL	0.5137
EIF_PAH1	0.0885
EIF_PAH2	0.0286
EIF_PHENOL1	4.0800
EIF_ALIFATER	1.7660
EIF_Ammonia	3886.0000
EIF_Silicate	591.0000
EIF_Iron	2.1100
EIF_Mn	0.0811

Num. comp.'s 10

Figure 63: Modeled chemical components.

4.5 Measured Data

4.5.1 Raw Produced Water

The concentration of Phenols, BTEX, Alkanes, and PAHs are listed in Table 4 to Table 6. The average total phenol in raw produced water is 4.08 ppm (4080 ng/mL) and the BTEX is 0.007 ppm (7044 ng/L). The total alkane is 1.76 ppm and total PAHs is 0.168 ppm. Metals and nutrients in produced water were also analyzed and the results are presented in Table 7 and Table 8.

Table: 4 Phenol in raw produced water.

	Raw I	Raw II	Raw III	Raw IV	
	Merged	Merged	Merged	Merged	Average
Sample ID	314278	314315	314312	314277	GBS
Units	ng·ml-1	ng·ml-1	ng·ml-1	ng·ml-1	ng·ml-1
d6-phenol	na	na	na	na	
phenol	1781.54	1432.87	1516.15	1340.29	1517.71
o-cresol	900.99	729.22	845.33	750.81	806.59
m & p-cresol	970.57	829.19	948.40	826.91	893.77
2,6-dimethylphenol	46.50	39.05	49.85	40.08	43.87
2-ethylphenol	75.77	72.29	80.38	70.47	74.73
2,4 and 2,5-dimethylphenol	203.46	147.27	246.34	216.03	203.28
3 and 4-ethylphenol	250.07	244.12	270.58	250.23	253.75
2,3-dimethylphenol	35.47	33.90	38.99	33.42	35.45
2-isoproplyphenol	48.92	47.30	53.01	45.76	48.75
2-proplyphenol	16.11	15.49	17.28	15.29	16.04
3 and 4-isopropylphenol	121.57	115.06	137.02	121.79	123.86
2-sec-butylphenol	11.02	10.93	12.08	10.54	11.14
3 and 4-tert butylphenol	35.18	33.90	39.24	33.82	35.54
4-sec-butylphenol	1.24	13.00	13.64	12.45	10.08
4-isopropyl-3-methylphenol	5.63	5.80	6.20	5.80	
4-nonylphenol	n.d.	n.d.	n.d.	n.d.	
∑ Phenols (ng·ml-1)	**4504**	**3769**	**4274**	**3774**	**4080**

Table 5: BTEX in raw produced water.

Station Sample ID	Terra Nova Raw I - ng·L-1	Terra Nova Raw II - ng·L-1	Terra Nova Raw III - ng·L-1	Terra Nova Raw IV - ng·L-1	Terra Nova Average ng·L-1
∑ BTEΞ (νγ•Λ−1	**5827**	**7528**	**7979**	**6841**	**7044**
	Merged	**Merged**	**Merged**	**Merged**	
Compound	**ng·L-1**	**ng·L-1**	**ng·L-1**	**ng·L-1**	
Benzene	**3312**	**4027**	**4220**	**3713**	**3818**
Toluene	**1867**	**2507**	**2690**	**2300**	**2341**
Ethyl Benzene	**123**	**193**	**206**	**166**	**172**
p-Xylene	**227**	**353**	**378**	**277**	**309**
m-Xylene	**47**	**67**	**73**	**58**	**61**
o-Xylene	**251**	**381**	**412**	**328**	**343**

Table 6: Alkanes and PAHs in raw produced water.

	Merged	Merged	Merged	Merged	Avaerage
Totals	Terra Nova Raw I	Terra Nova Raw II	Terra Nova Raw III	Terra Nova Raw IV	
Sample ID	314278	314315	314312	314277	
Surrogates	% Recovery	% Recovery	% Recovery	% Recovery	
∑ Alkanes (ng·L-1)	1744558	2670456	1300187	1349403	1766151
∑ Methyalted PAHs (ng·L-1)	287337	422807	281227	254585	311489
∑ PAHs (ng·L-1)	153056	201269	176175	144018	168630

Table 7: Trace metal concentrations in raw produced water.

Parameter	2007	2008	Parameter	2007	2008
Aluminum	14.5	25	Molybdenum	< 1	0.14
Antimony	0.6	< 2	Nickel	17	< 20
Arsenic	< 10	< 50	Phosphorus	--	< 50
Barium	308	355	Potassium	250000	240000
Beryllium	0.345	0.43	Rubidium	--	430
Bismuth	--	< 0.5	Selenium	< 10	< 50
Boron	34650	46000	Silicon	--	24200
Cadmium	0.05	0.02	Silver	< 0.2	< 0.2
Calcium	984000	1100000	Sodium	15850000	16400000
Chromium	< 1	< 10	Strontium	59350	56200
Cobalt	< 0.5	< 10	Sulfur	667500	730000
Copper	< 5	< 10	Tellurium	< 0.5	< 2
Iron	2110	2250	Thallium	< 5	< 2
Lanthanum	< 0.2	< 1	Thorium	--	< 0.2
Lead	0.19	< 0.05	Tin	--	< 0.5
Lithium	1960	3500	Titanium	--	< 1
Magnesium	386500	417000	Uranium	< 0.1	< 0.005
Manganese	81.5	69.4	Vanadium	0.35	< 5
Mercury	--	--	Zinc	3	< 5

Table 8: Nutrient concentrations in raw produced water.

Sample ID	SILICATE μm/L	PHOSPHATE μm/L	NO_3/NO_2 NITRATE μm/L	AMMONIA μm/L	NO_2 NITRITE μm/L
314302	591	0.528	0.09	3866	0.16
314302	487	0.485	0.08	3023	0.15
	539	1	0.08	3444	0.15

4.5.2 Seawater Samples

Seawater samples were taken at 31 stations at various (1 to 5) depths depending on the location. At distances greater than 500 m from the FPSO, sampling was taken by deploying Rosette bottles from the CCGS Hudson. At distances close to the FPSO, samples were collected by launching Niskin bottles from FRC. Sampling locations are plotted in Figure 64.

Although many parameters (Phenol, BTEX, PAHs, Hg, Cu, Cd, Ni, Pb, Zn, Fe, Mn, Ammonia, Silicate, Nitrate, Nitrite etc.) for seawater samples were analyzed, only data for Ammonia, Silicate, Fe, and Mn were selected for the purpose of model validation. This is due to the fact that almost all samples showed below detection level hydrocarbons, and the data is insufficient for model validation. Although there are traceable amounts of some metals and nutrients (Nitrate and Nitrite), their initial concentrations in produced water were too low to be selected as tracer.
The concentrations for Fe, Mn, Ammonia, and Silicates are plotted in Figure 65 and Figure 66.

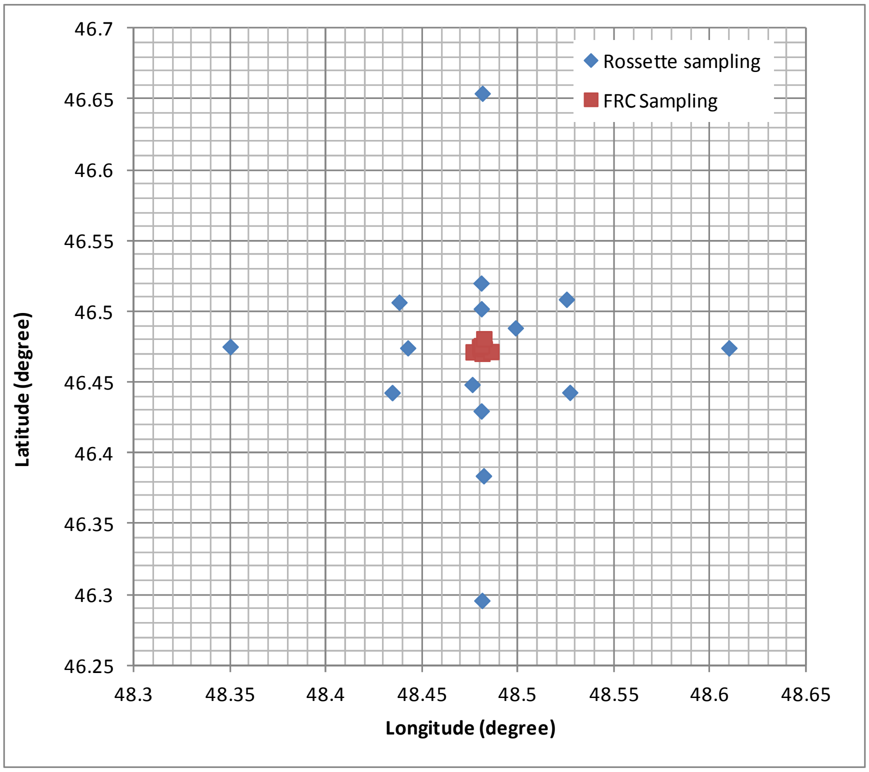

Figure 64: Location of sampling (Terra Nova 2007).

It can be seen from Figure 65 that the concentrations of Fe at most stations including those within 500 m from the platform are less than 0.5 µg/L. There are three stations that have concentrations higher than 1.0 µg/L, especially the TE10k (~10 km) and TS(2)0 (immediate vicinity of the FPSO) have concentrations greater than 3.5 µg/L which are much higher than the rest of the stations. The overall trend is that Fe concentrations are slightly higher at bottom level (80 m).

For Mn, the trend of higher concentrations at the bottom layer is more apparent than Fe. While most of the stations have mid-depth (45 m) and surface (10 m) concentrations between 0.1 and 0.15 µg/L, there are two stations that have relatively high concentrations. The Mn at TNW5k(45 m) is 0.35µg/L and at TS(2)0 (10 m) is 0.37 35µg/L. The occurrence of higher than average concentrations of both Fe and Mn indicates that produced water might be traceable at the immediate vicinity of the FPSO. For TE10k and TNW5k, due to the mismatch of Fe and Mn, it is unclear if the higher concentration can be related to produced water.

From the plots of ammonia and silicate in Figure 66, it can be seen that both ammonia and silicate concentrations are higher at 80 m. This is in agreement with that of Mn and Fe. However, the concentrations of ammonia and silicate at TE10k and TNW5k are not significantly different from the rest of the stations. For TS(2)0, unfortunately the sample was lost during transportation and there is no further data to confirm the assumption that produced water might be traceable at the immediate vicinity of the FPSO.

For all 4 parameters, there is no strong evidence that samples collected within 500 m have concentrations higher that those collected outside 500 m.

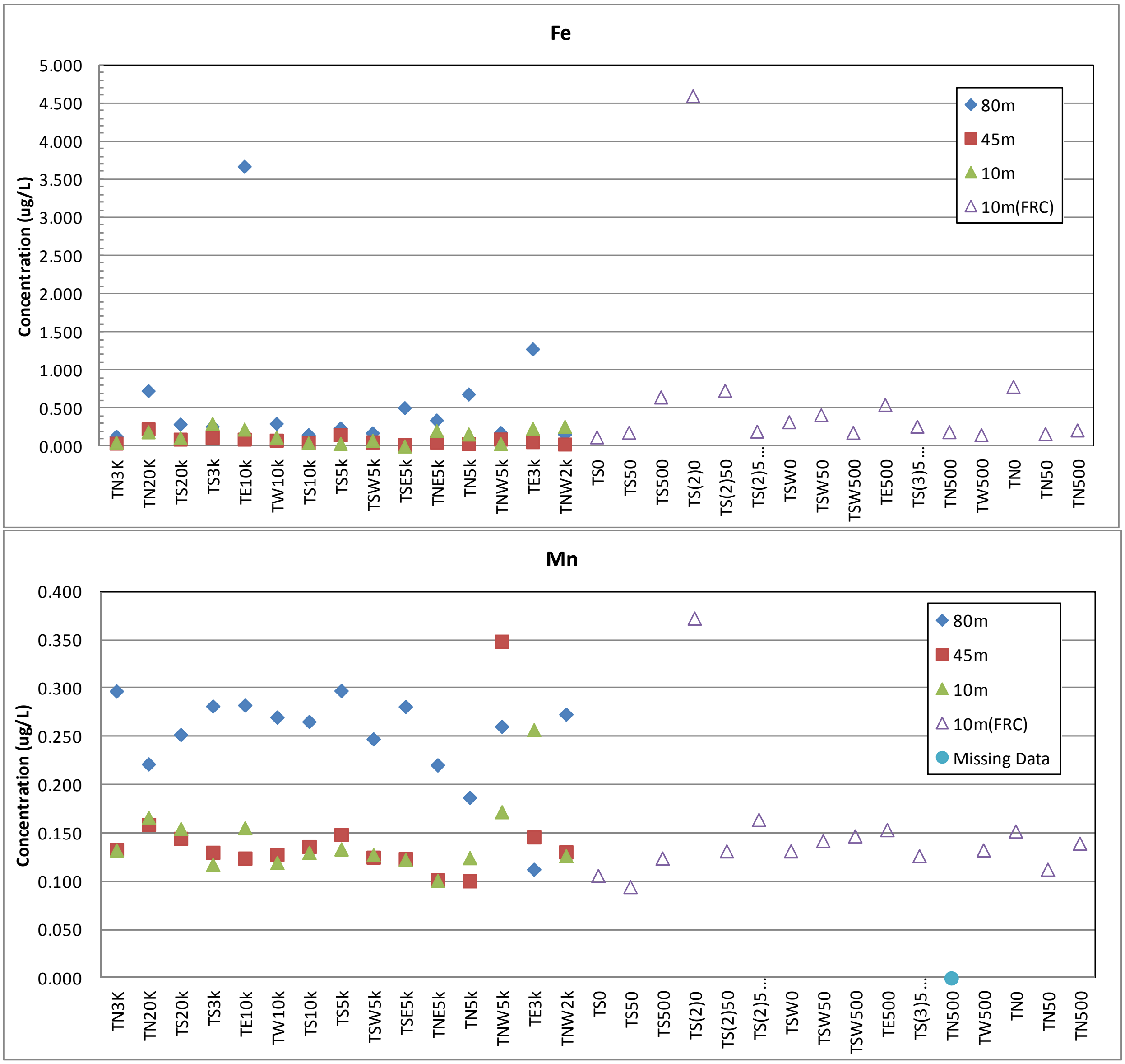

Figure 65: Average Fe & Mn Concentrations.

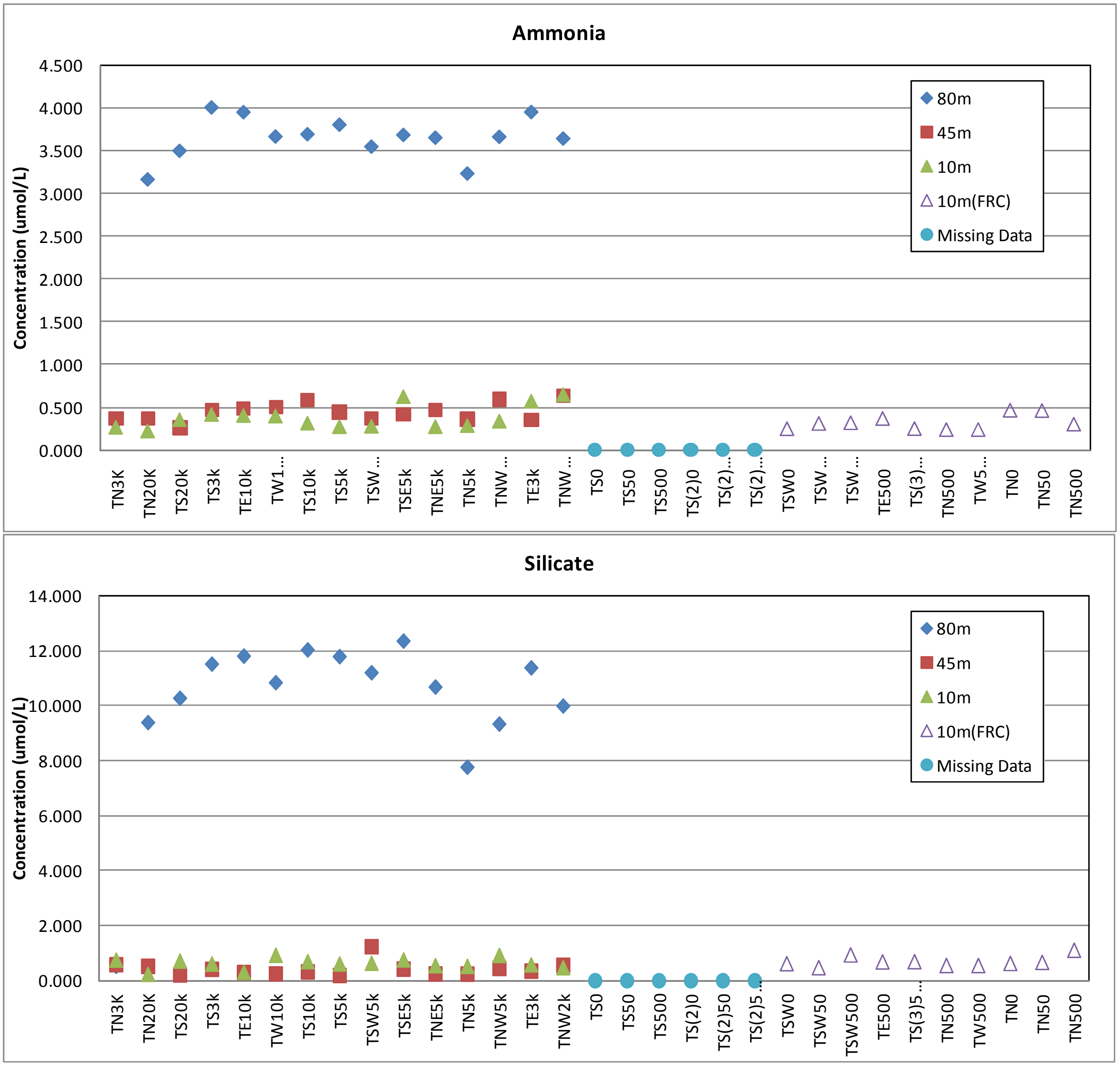

Figure 66: Average Ammonia & Silicate Concentrations.

4.6 Modeling Results and Comparison with Measurements

The predicted produced water plume profiles at August 15, 17, 19, and 22, 2007 are shown in Figure 67. The plot indicates although the plume keeps changing directions, the mean direction is south-eastward. The vertical profiles indicate that although produced water may impact the entire water column, the plume does sink to the bottom and concentrations are higher near bottom.

Although many produced water associated chemicals are modeled, the data in Table 9 indicates that the results of Fe and ammonia should be the focus. Silicate data may also be considered but it might be very limited due to the high background concentration near bottom which only gives a ratio of C_0/C_a of 63-folder.

Modeled concentrations of ammonia at 16 stations at distance from 3 km to 20 km are plotted in Figure 69 to Figure 83. From the data for TN20k (Figure 69) it can be seen that there is almost no change of concentration at this station and therefore using measurements from this station as background is acceptable from the modeling point of view.

At TN3k (Figure 70), the change of concentration is noticeable, at which the maximum concentration becomes about 2 times the background value. While one measurement at 10 m, 45 m, and 80 m agree with the model very well, the other measurement is about 2 times the prediction. Considering the high variation/uncertainty in measurements, the model is considered to have good prediction at this station.

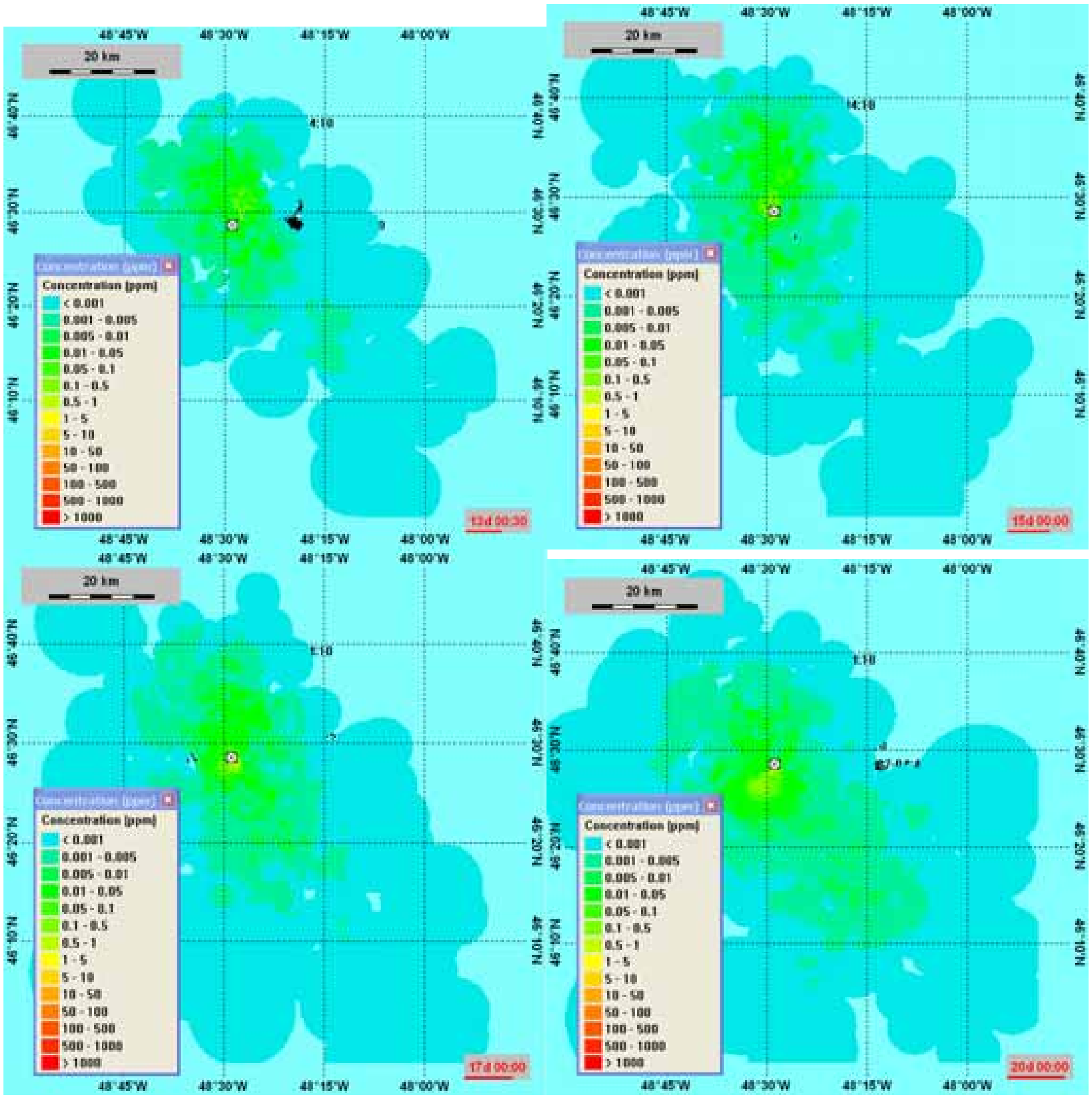

Figure 67: Concentration of produced water associated chemicals at August 15, 17, 19, and 22, 2007.

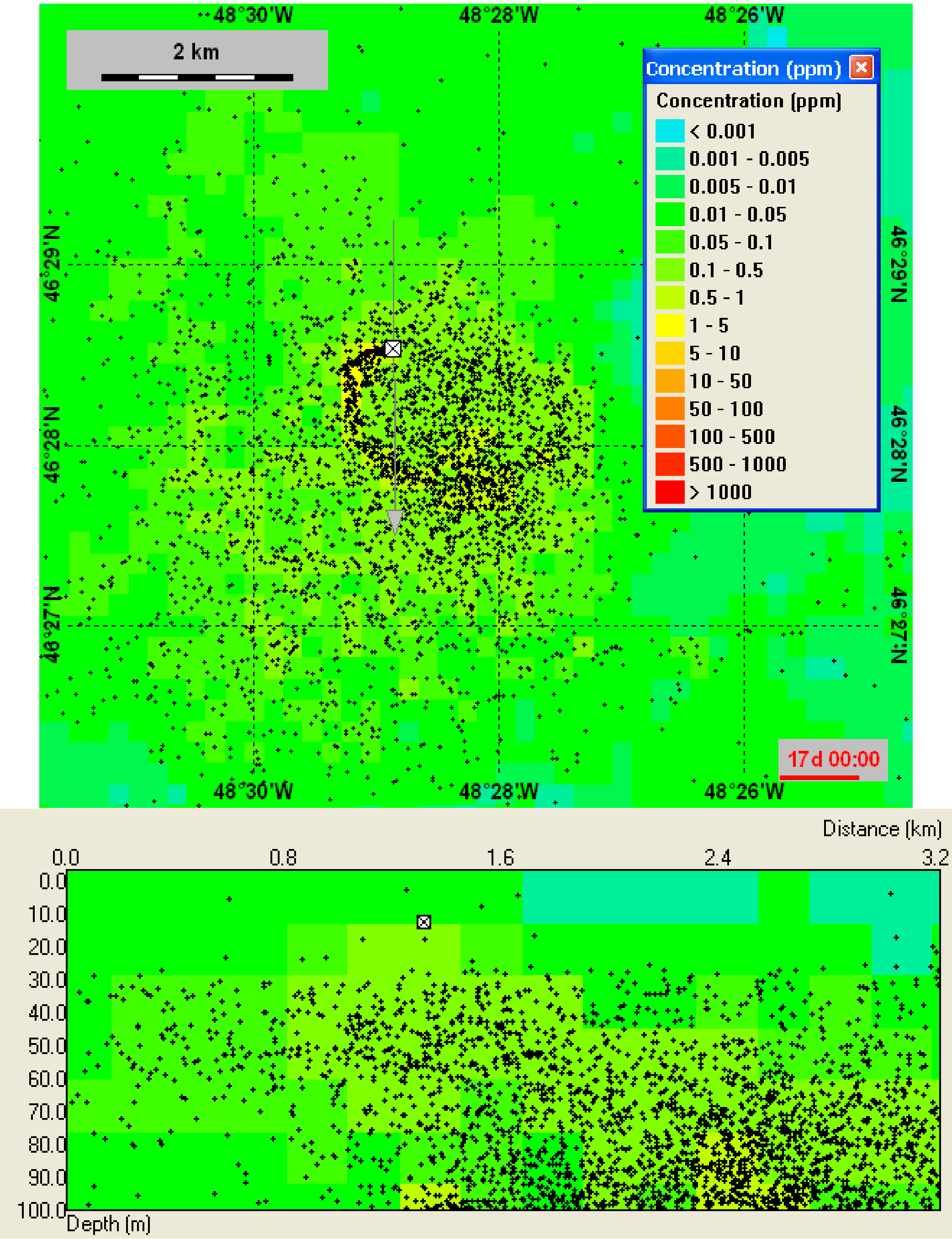

Figure 68: Horizontal and vertical profiles of produced water plume.

At Ts20k (Figure 71), the predicted concentration change (<0.002) is much smaller than the measurement uncertainty. The predicted maximum change is only 1.1% to 7.4% of the measurement uncertainty (ΔM=M2-M1). This indicated that the effects of produced water are almost non-detectable at this site. As the predicted line (10 m) lies between the two measurements and the 45 m line is very close to the measurements, it can be concluded that prediction and measurements still agree as no significant increasing of concentration has been predicted.

Table 9: Concentration of potential tracers and the ratio of initial concentration C_0 to ambient concentration C_a at TN20k (Reference station).

Parameter	Raw	80m	10m
Ammonia	3886	3.166 1227	0.216 17991
Silicate	591	9.39 63	0.234 2526
Phosphate	0.528	0.979 0.54	0.16 3.30
Nitrate	0.09	8.68 0.01	1.58 0.06
Nitrite	0.16	0.21 0.76	0.06 2.67
Fe	2110	0.732 2883	0.193 10933
Mn	81.5	9.39 9	0.234 348
Ni	17	0.339 50	0.261 65

Although the agreement between predicted and measured for 10 m and 45 m is found, the measured value is much higher than predicted for the 80 m case. To understand this observation, two hypotheses can be assumed: 1) the model underestimates the concentration at 80 m, or 2) the higher level in measurement is a phenomenon due to uncertainty that the model could not resolve. Based on the measured data in Figure 66, there is a consistent trend of higher bottom concentration from TNW2k (~2km away from FPSO) to TN20 (~20km from FPSO) except TN3k. If the high level at the bottom is caused by produced water inputs, there should be a decreasing trend from 2 km to 20 km, however this cannot be observed in the figure. On the other hand, the limitation of the DREAM model is that only single values rather than profiles can be used as background. In the setup, the model used a single background value of 0.216 µmol/L from 45m at TN20k. Even with the maximum predicted concentration change of 0.004 µmol/L, the predicted concentration of 0.22 µmol/L is only 6% of the measured bottom concentration. If the model can use the bottom background concentration of 3.166 µmol/L at TN20, the prediction can be much closer to the 3.5 µmol/L at this station (TS20).

The results for other stations (> 2km from the FPSO) are similar to that of TS20 but with different predicted maximum concentration changes. The results all support the assumption described above that the higher level in measurement (80 m) is naturally occurring rather than an effect of produced water.

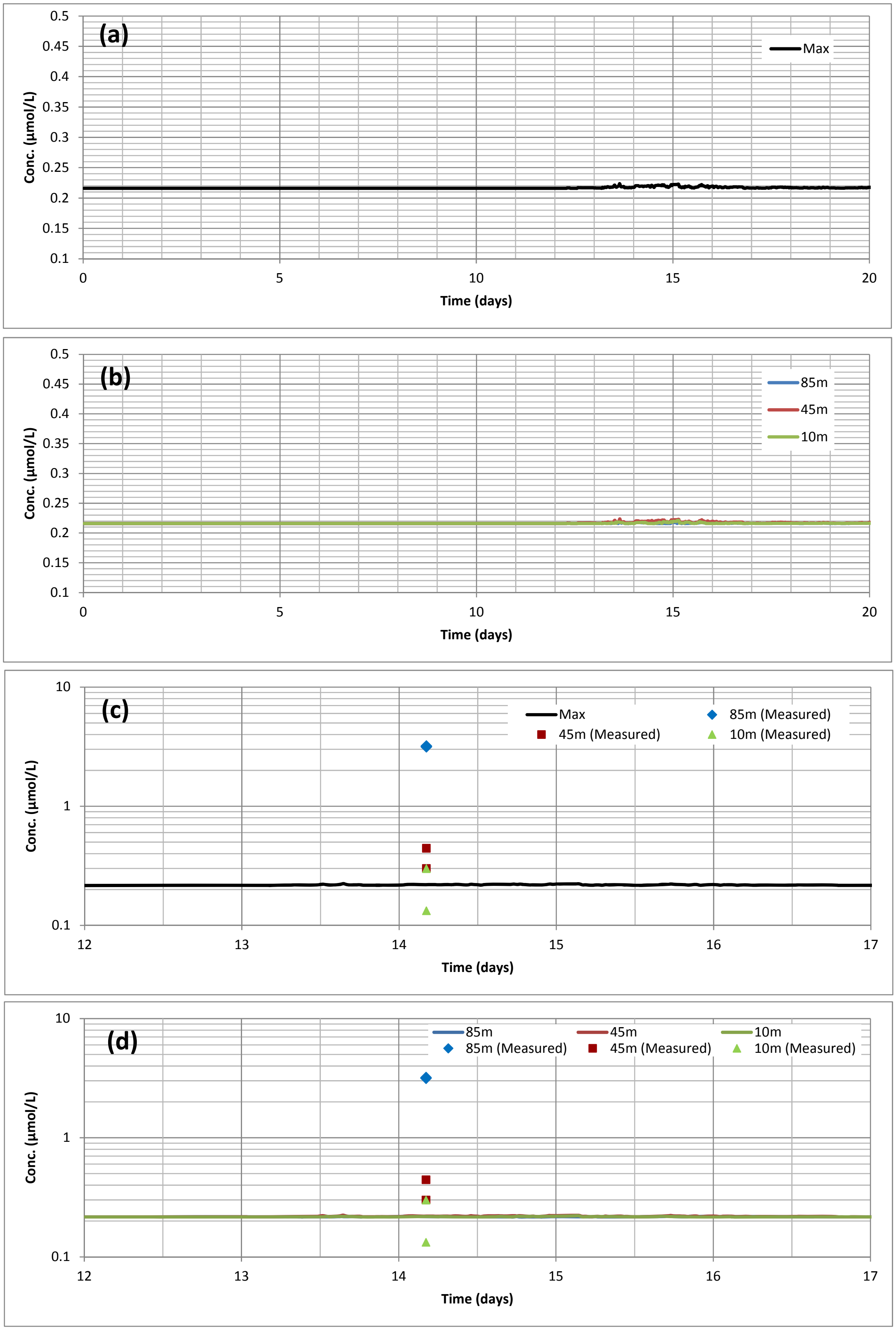

Figure 69: Concentration of Ammonia at TN20k (Reference Station).

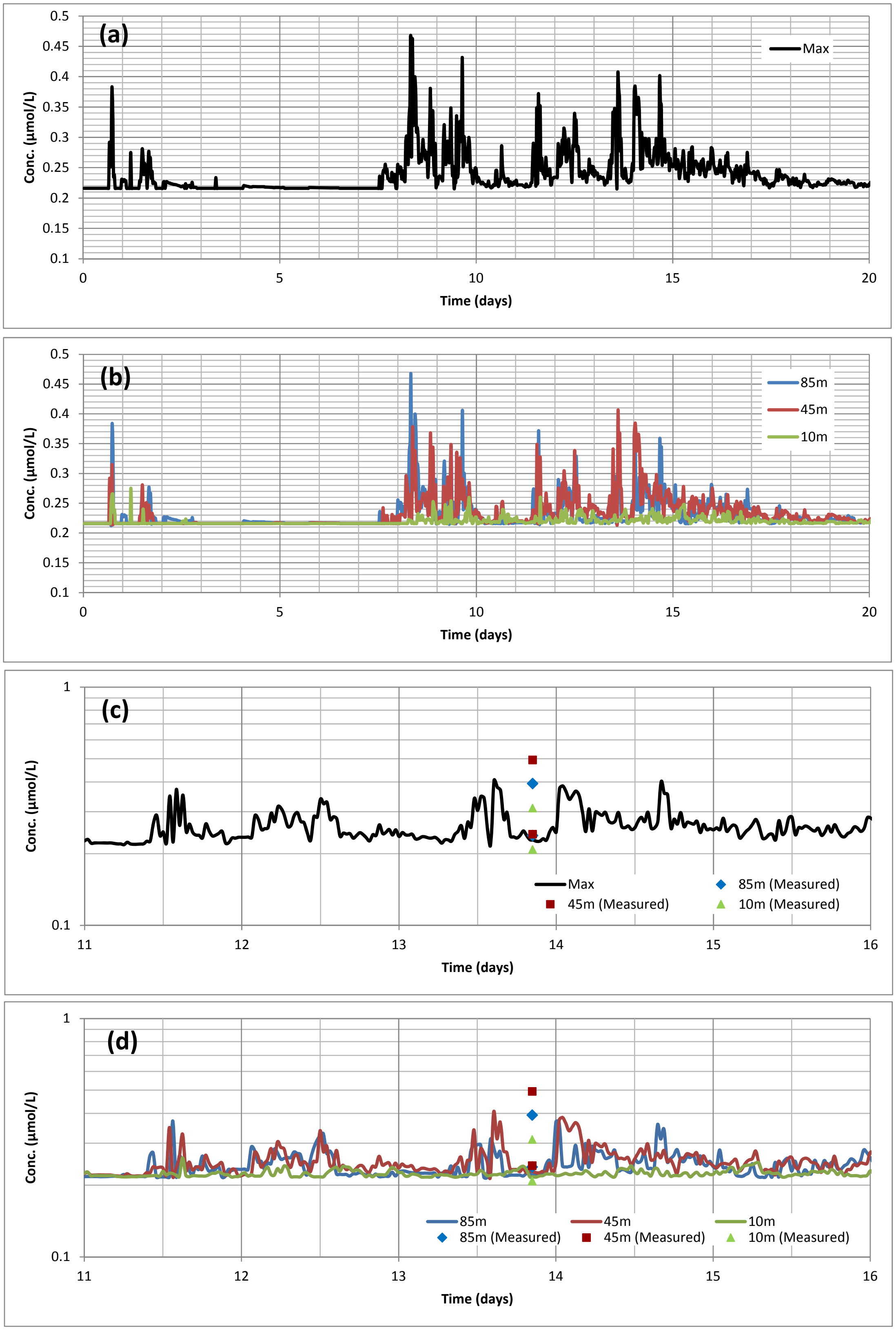

Figure 70: Concentration of Ammonia at TN3k.

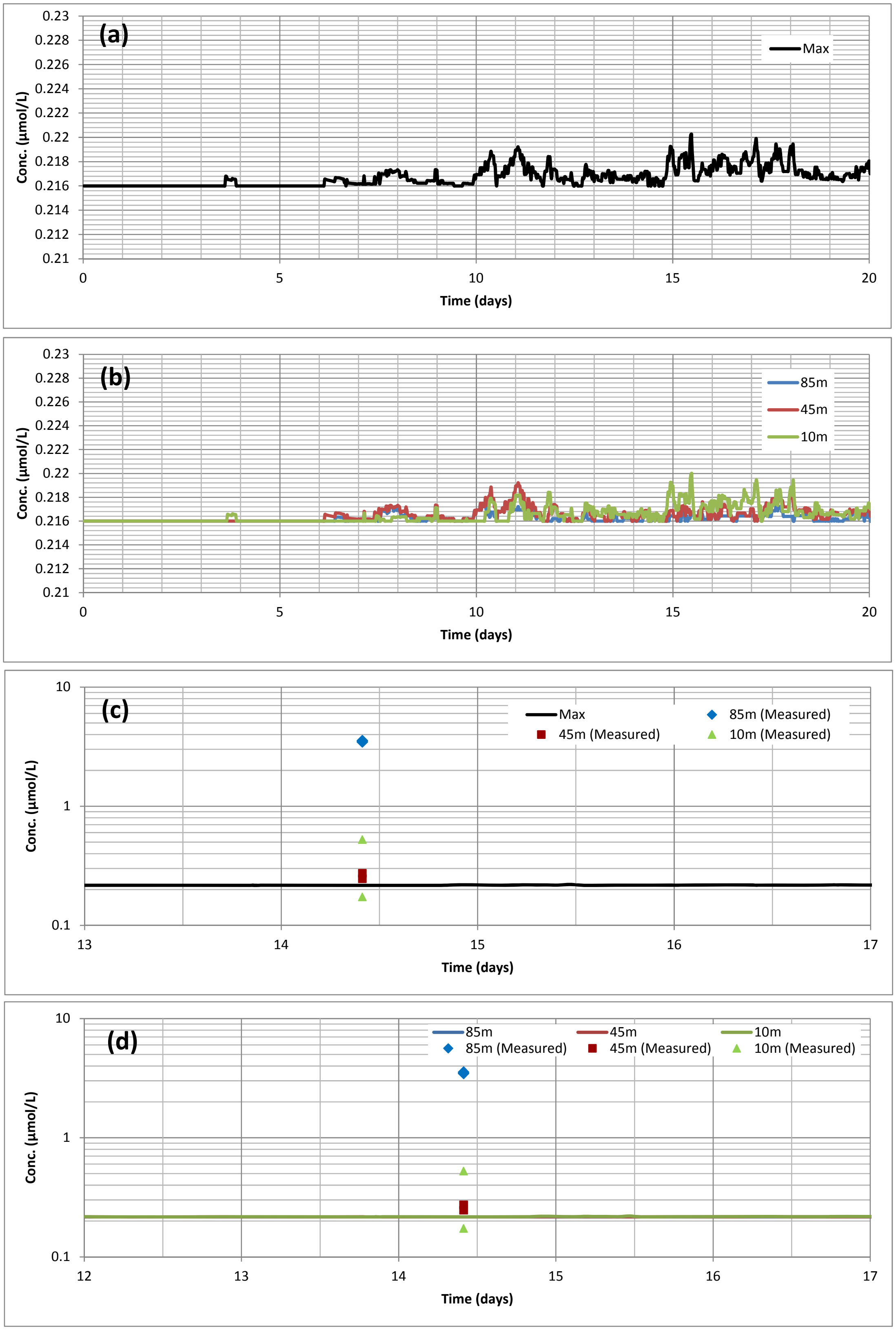

Figure 71: Concentration of Ammonia at TS20k.

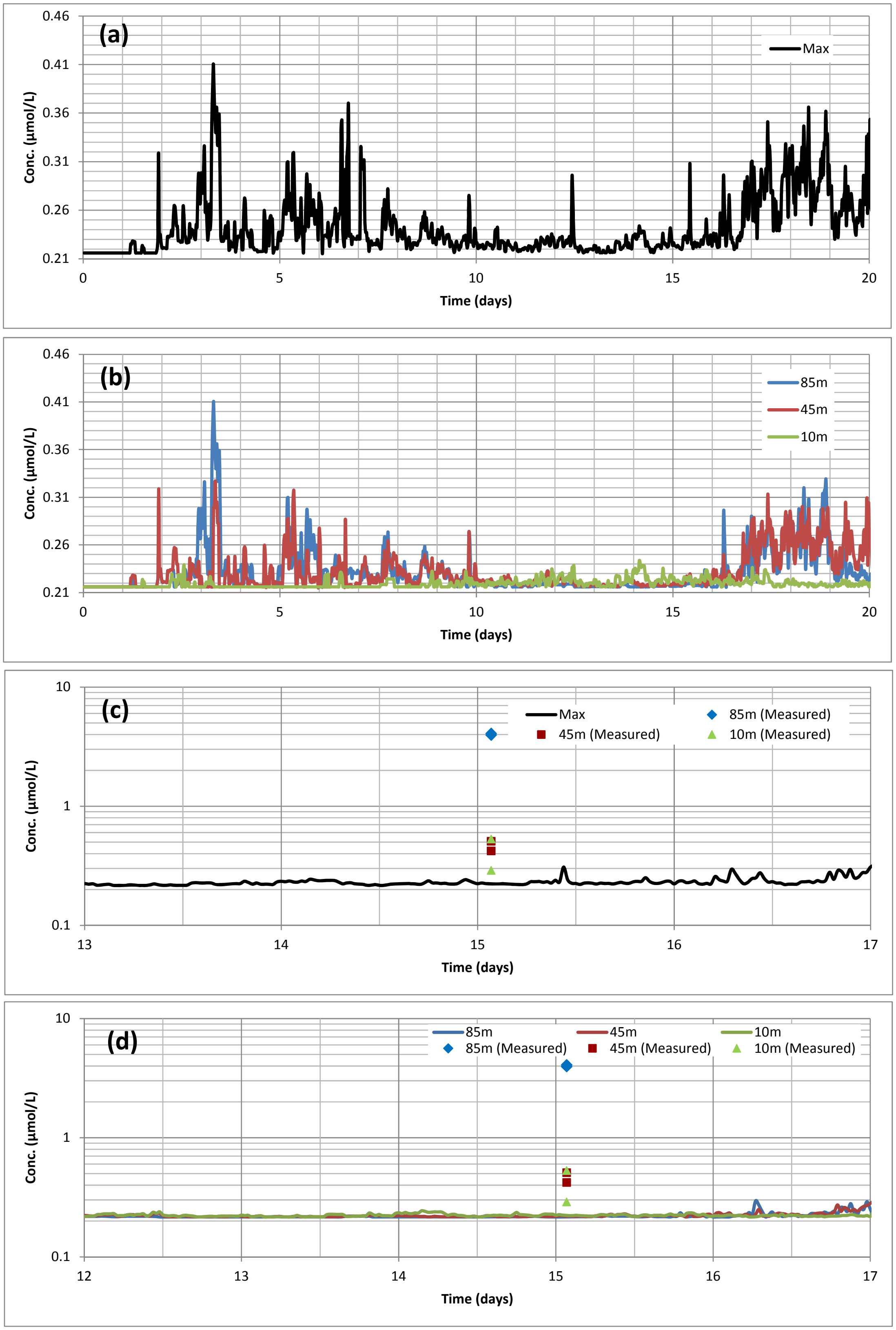

Figure 72: Concentration of Ammonia at TS3k.

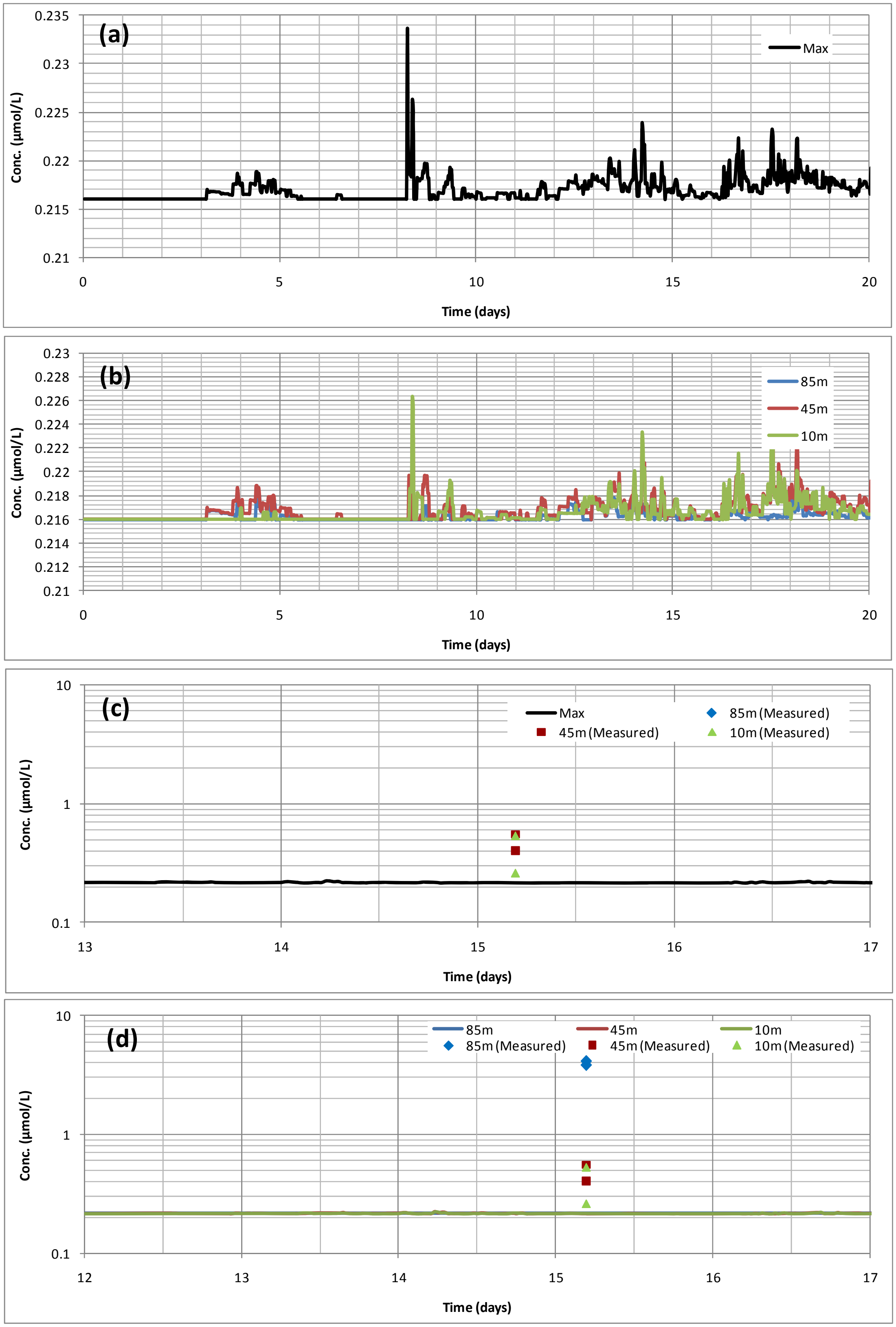

Figure 73: Concentration of Ammonia at TE10k.

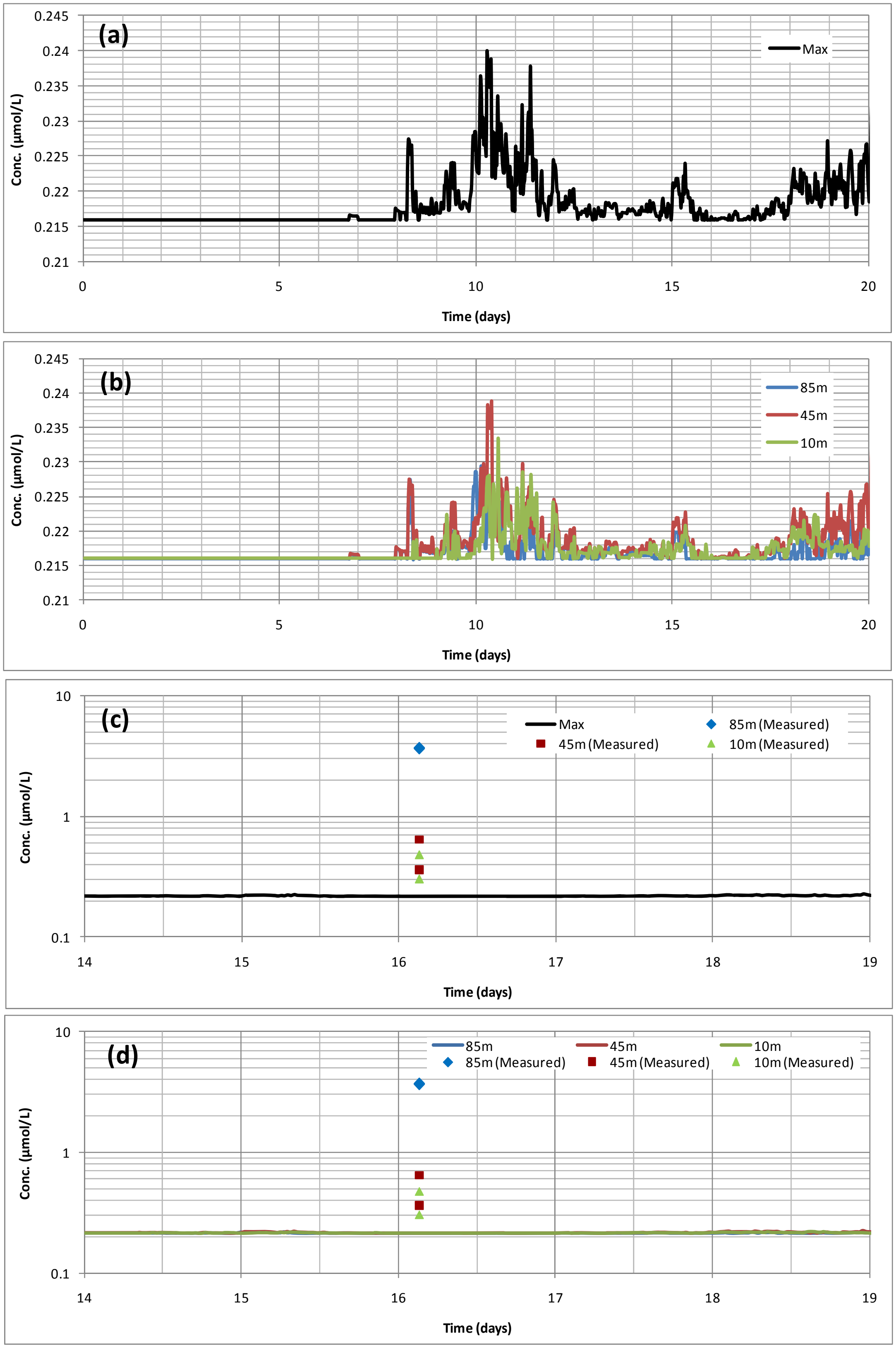

Figure 74: Concentration of Ammonia at TW10k.

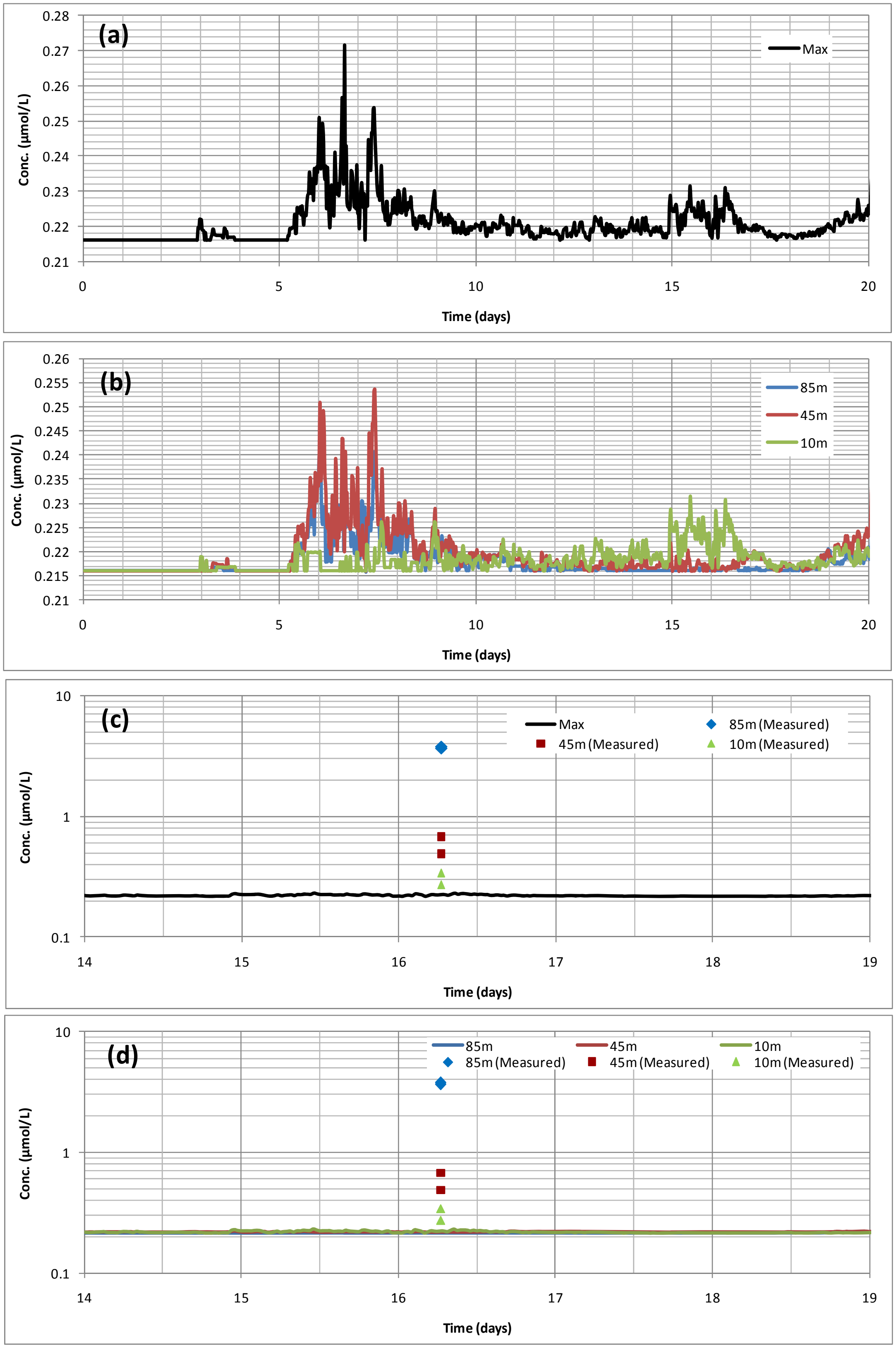

Figure 75: Concentration of Ammonia at TS10k.

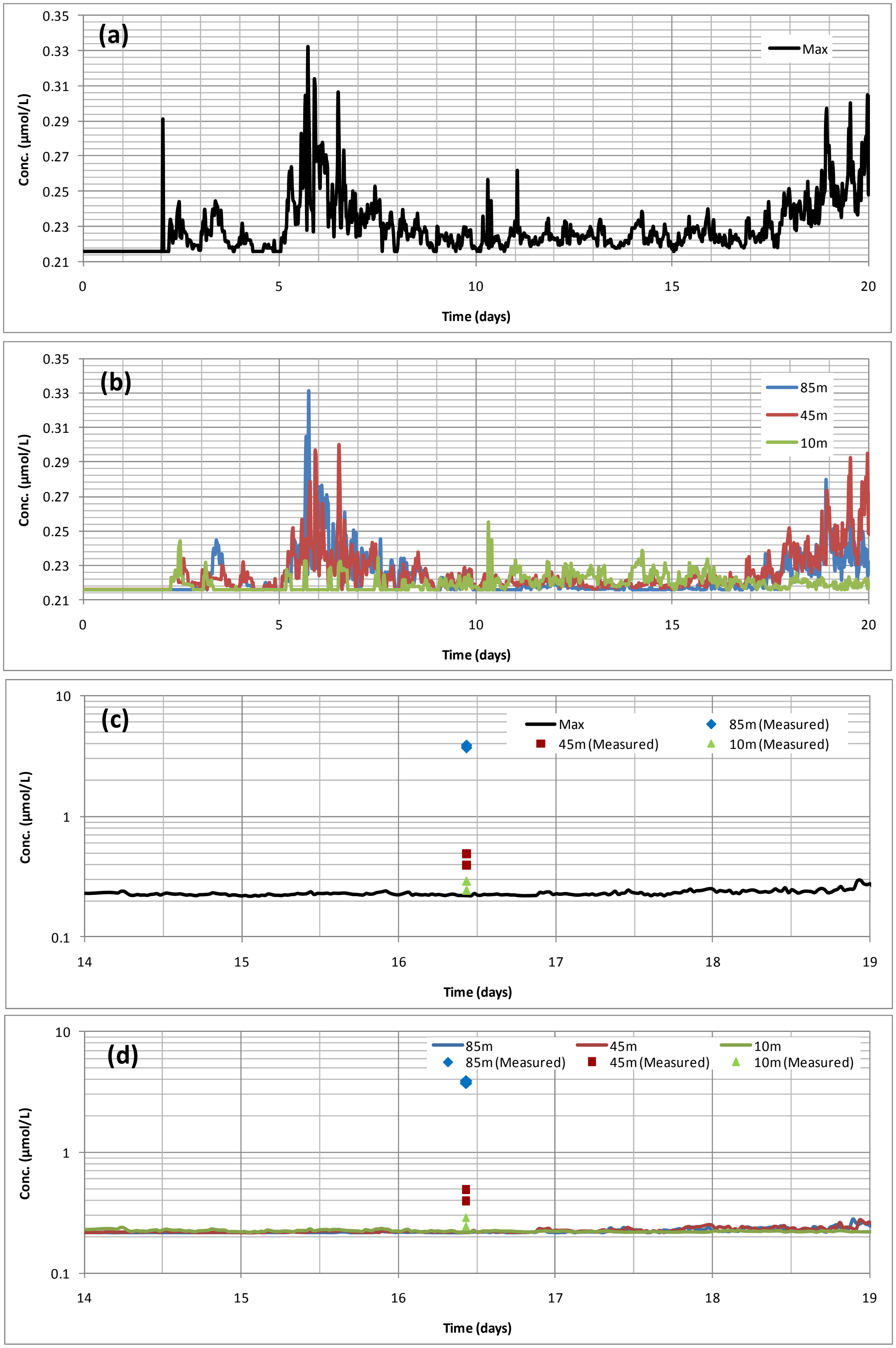

Figure 76: Concentration of Ammonia at TS5k.

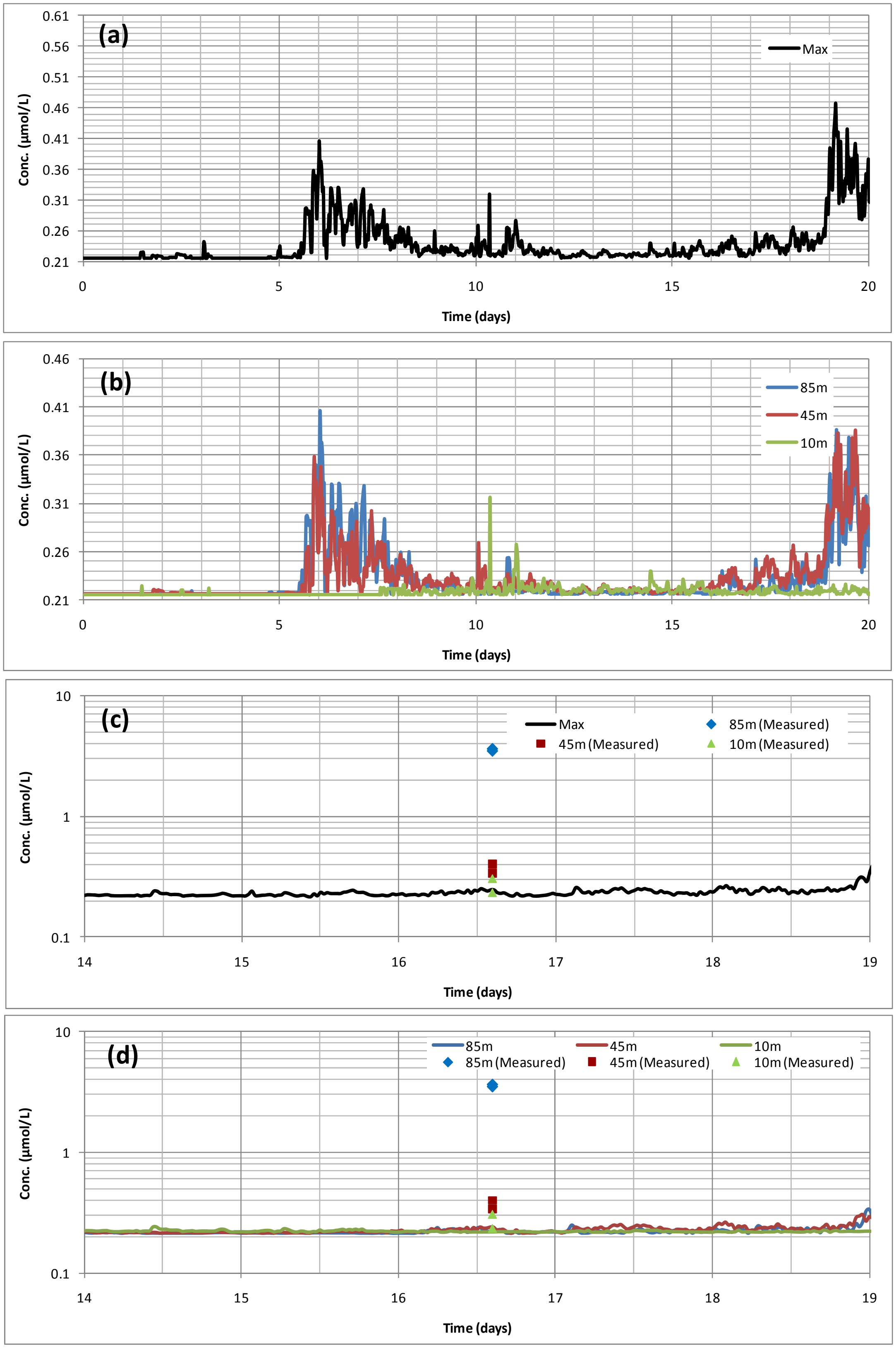

Figure 77: Concentration of Ammonia at TSW5k.

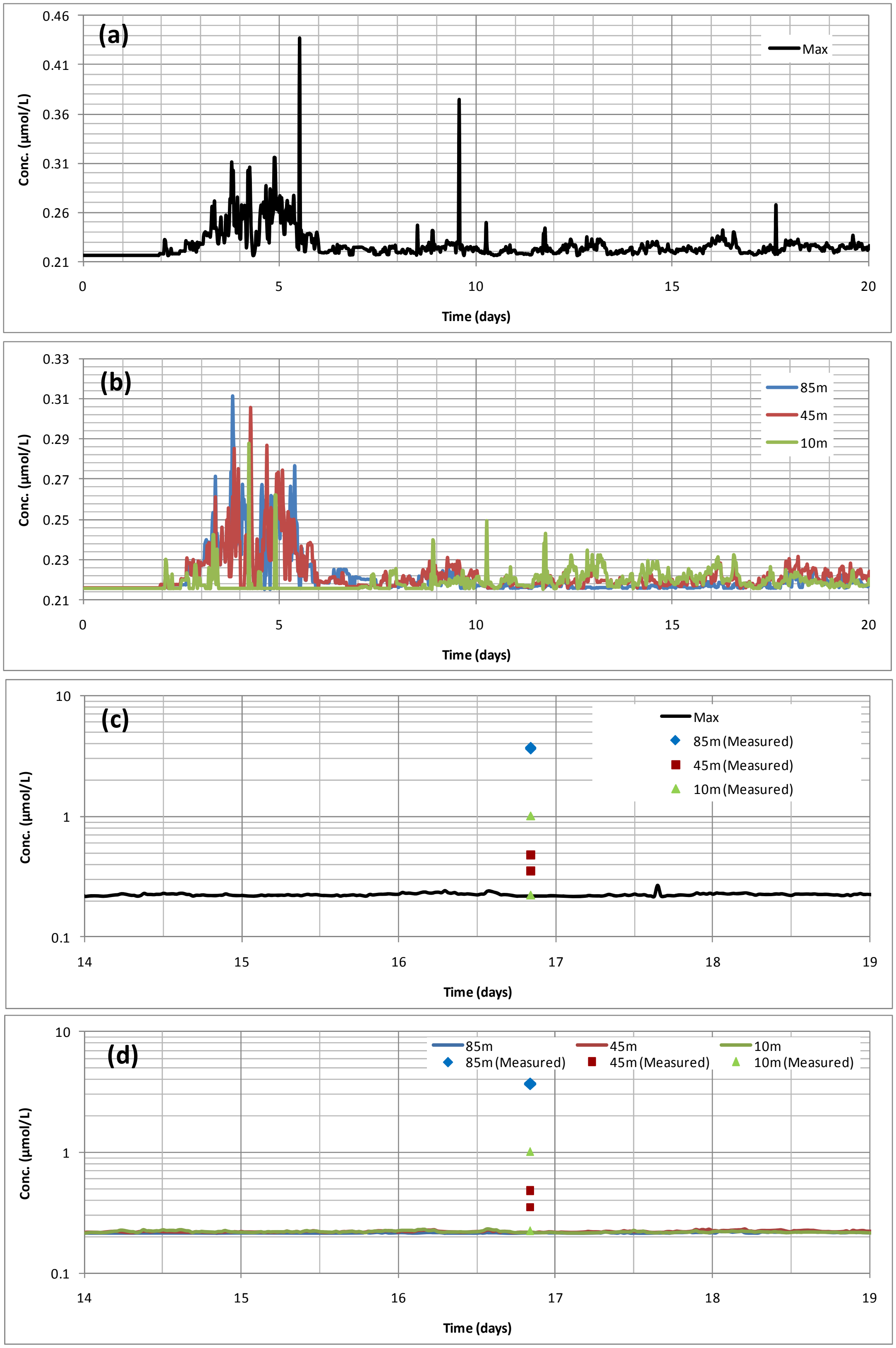

Figure 78: Concentration of Ammonia at TSE5k.

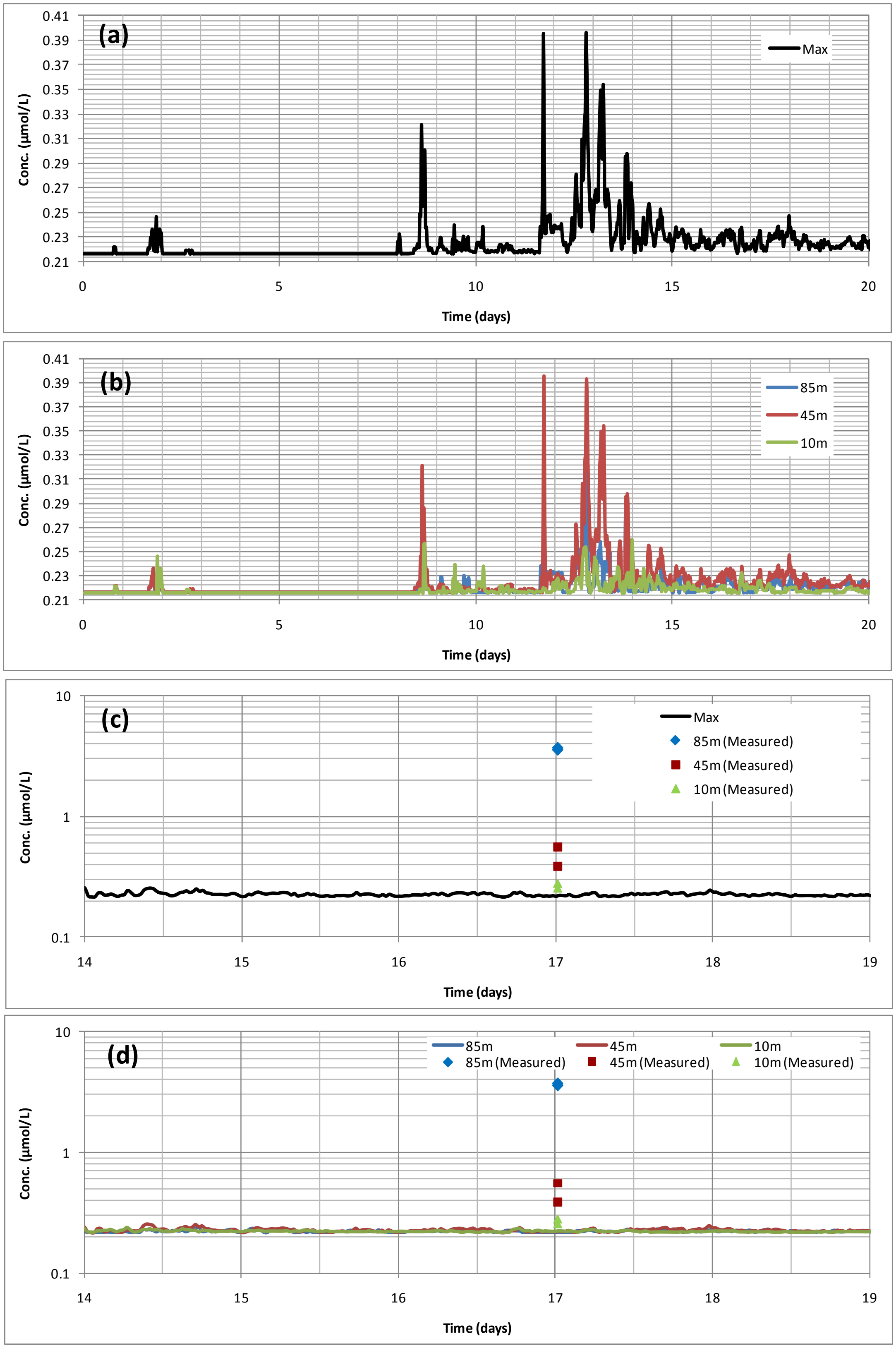

Figure 79: Concentration of Ammonia at TNE5k.

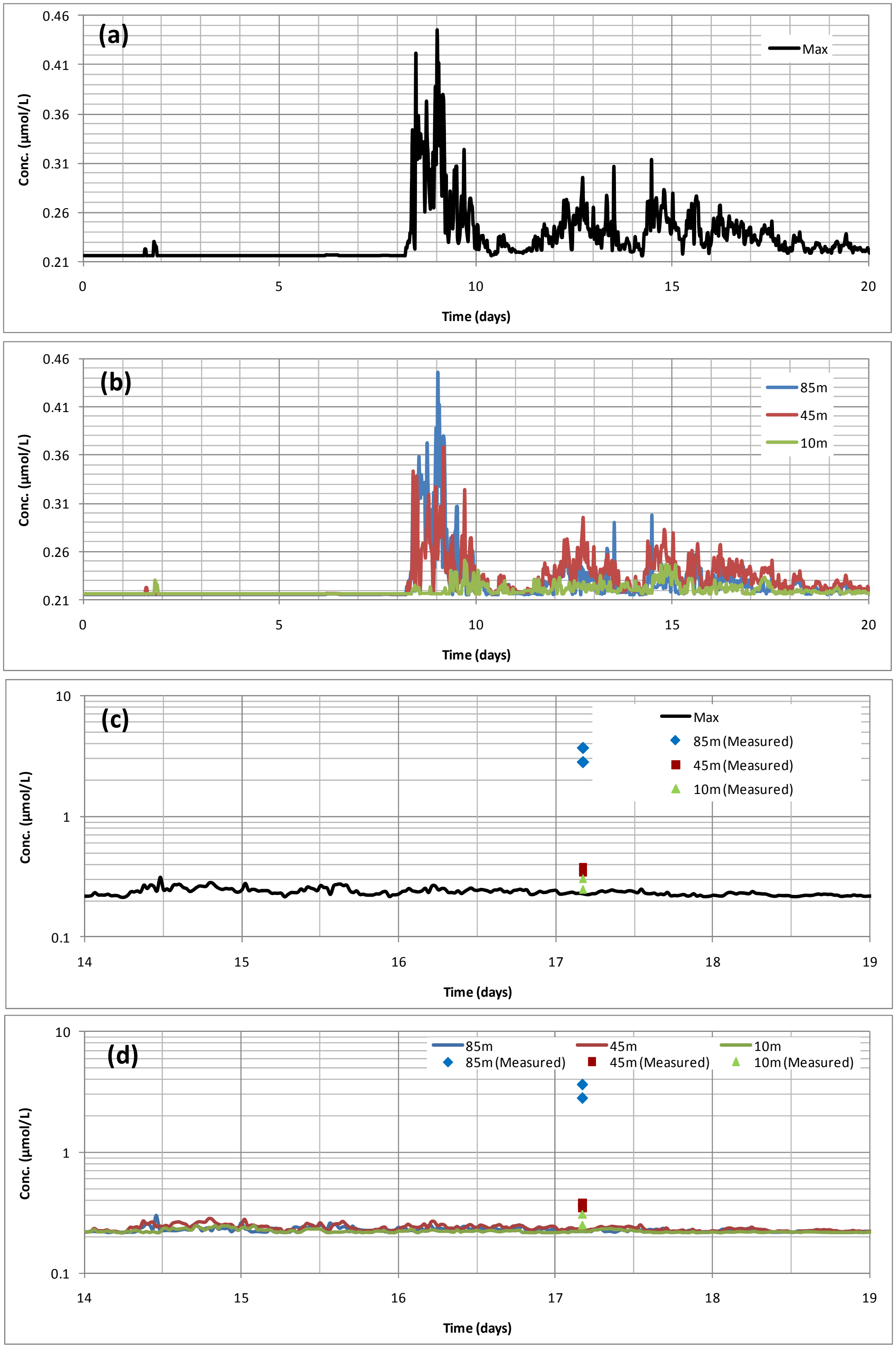

Figure 80: Concentration of Ammonia at TN5k.

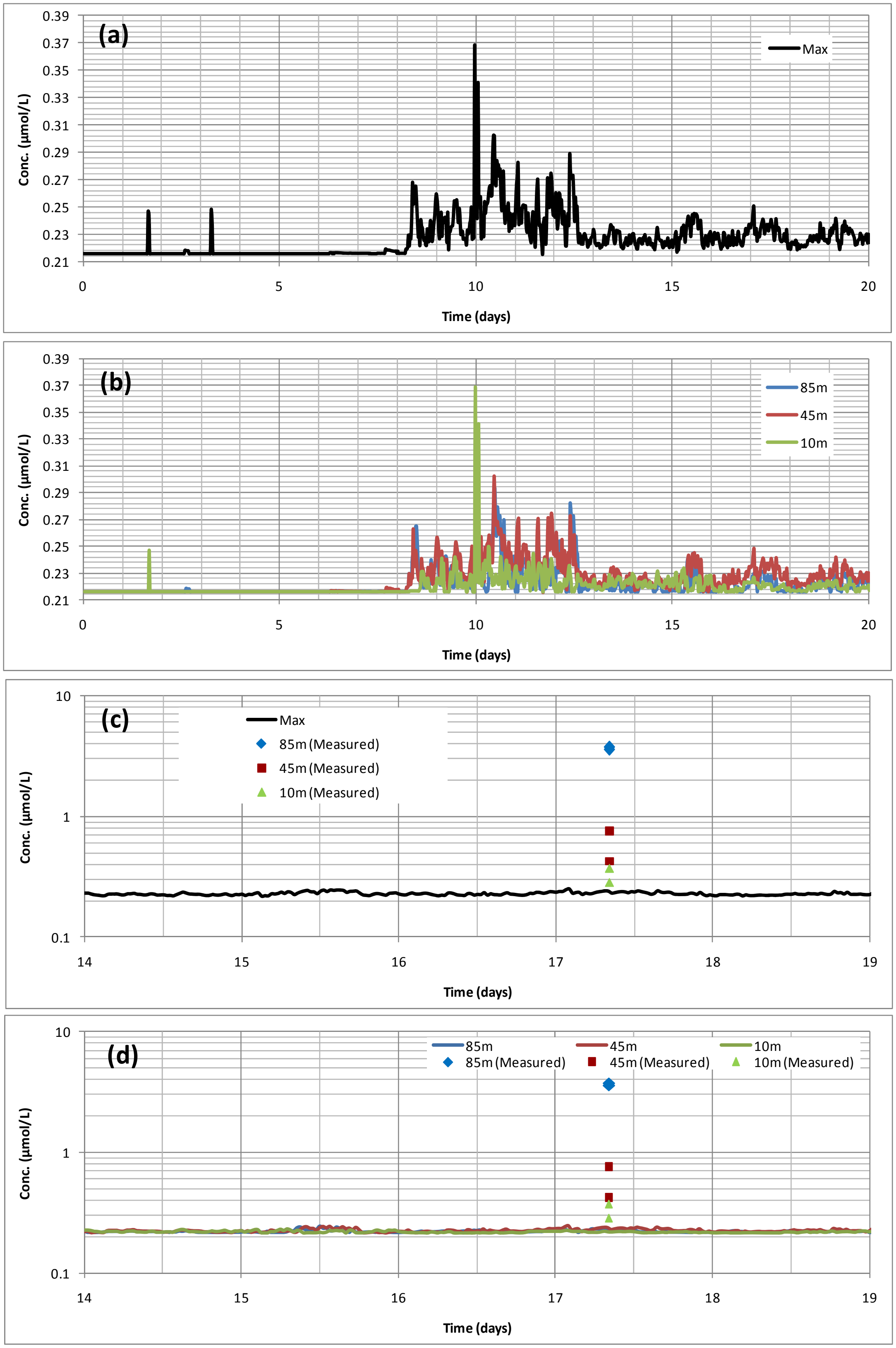

Figure 81: Concentration of Ammonia at TNW5k.

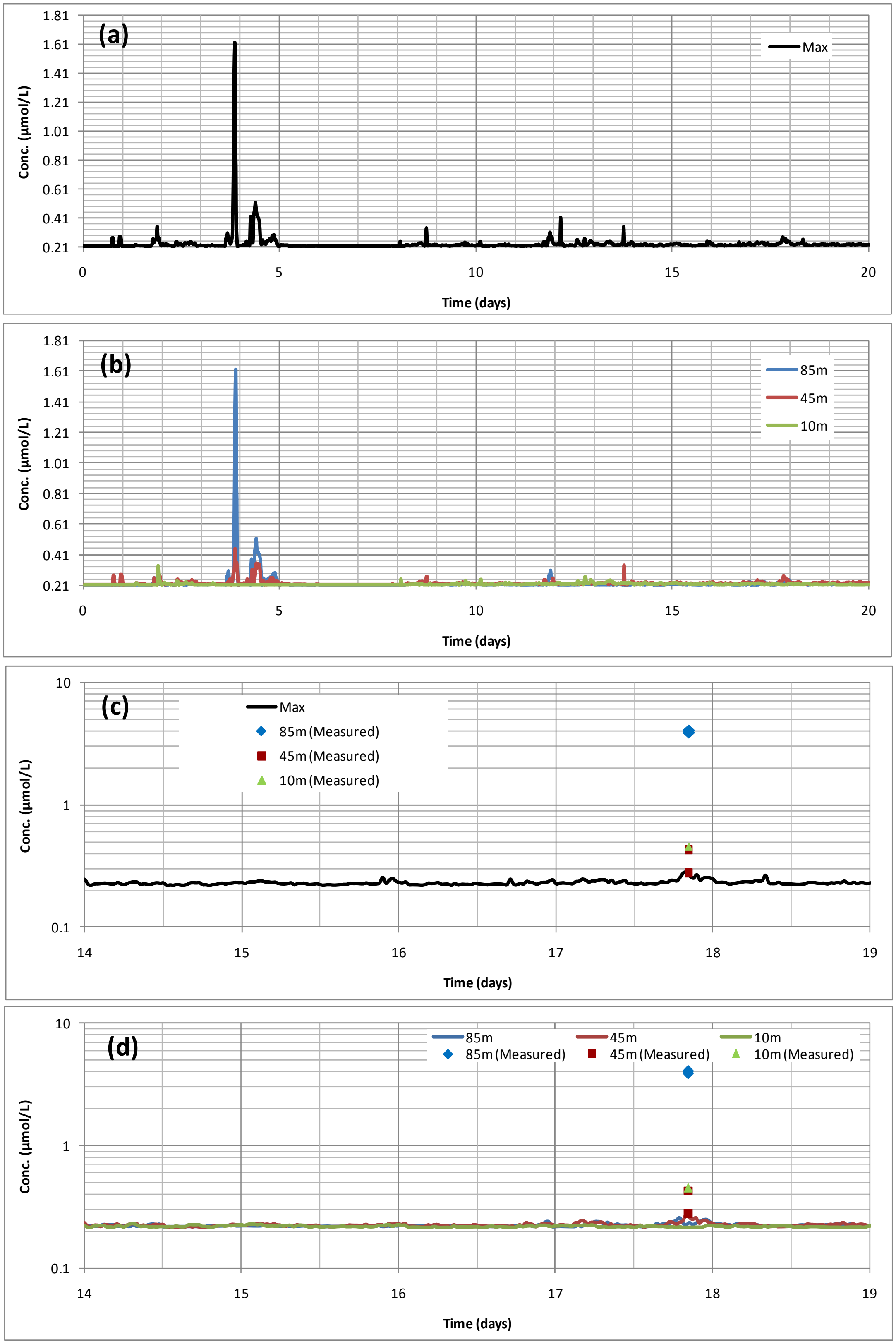

Figure 82: Concentration of Ammonia at TE3k.

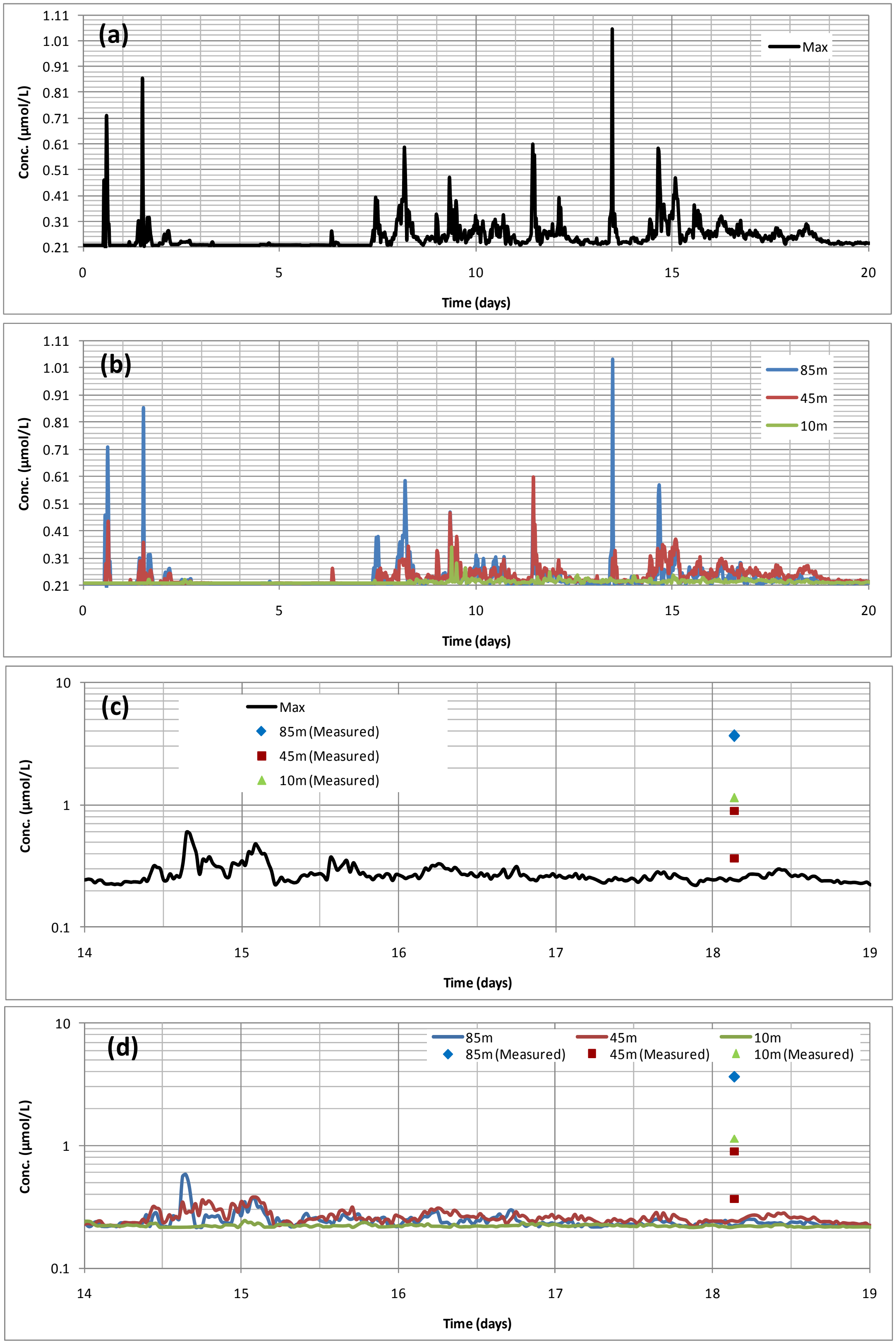

Figure 83: Concentration of Ammonia at TNW2k.

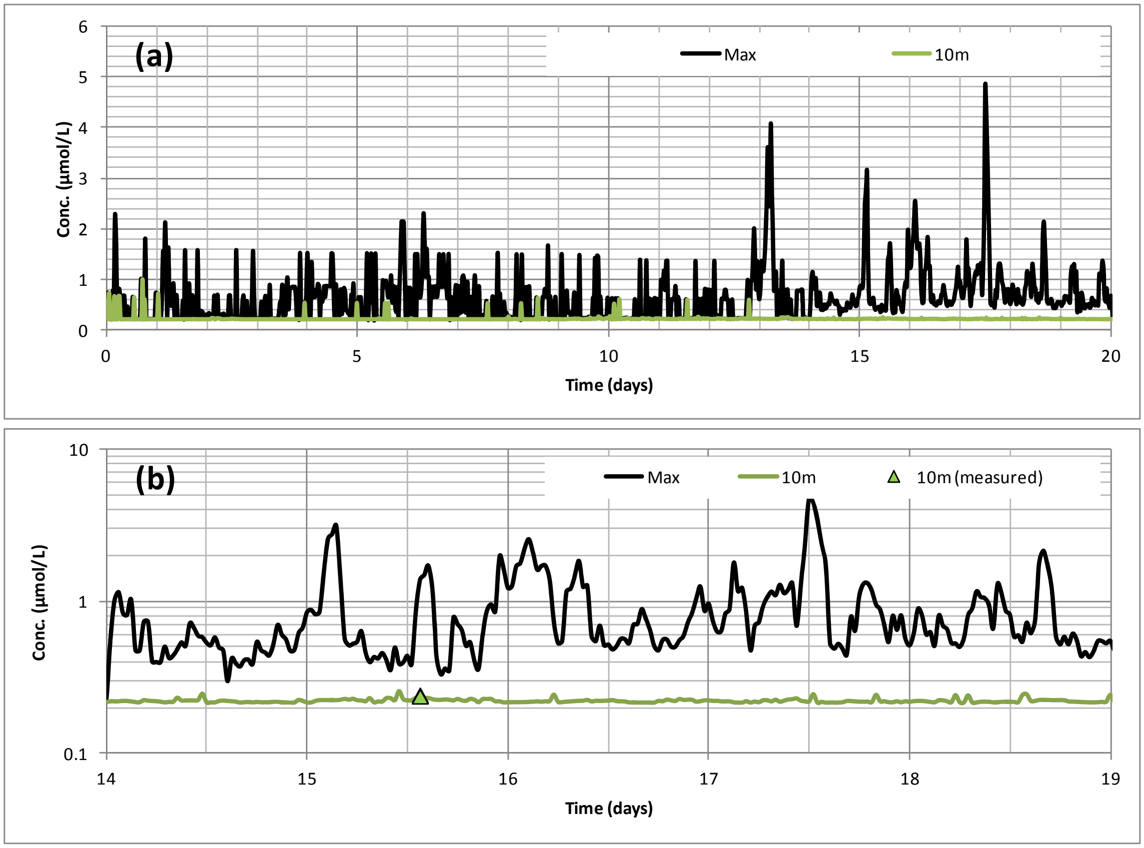

Figure 84: Concentration of Ammonia at TSW0 (FRC).

The predictions versus measurements at stations within 500 m to the FPSO are shown in Figure 84 to Figure 89. For the TSW0 station, the prediction at 10 m agrees with the measurement very well (Figure 84). The predicted maximum concentration change at this station is 4.59 µmol/L which is much greater than both the measurement uncertainty at this station (0.005 µmol/L) and the average measurement uncertainty for all stations (0.38 µmol/L). Therefore this predicted smaller increase at 10 m which agrees with measurement proves the good performance of the model at this station.

For TSW50, while one measurement agrees with the prediction very well, the other measurement is about 1.4 times the first measurement and therefore there is a small difference between measurement and prediction. The predicted maximum concentration lies between the two measurements and shows good agreements.

For TSW500, both measurements are slightly higher than predicted at 10 m. The prediction is about 0.70 – 0.75 times the measurement. However, both measurements agree with the predicted maximum concentration well (P/M=0.93 and 1.00). Given that the measurements have great uncertainties, the agreement is considered reasonably well.

The TN0 is more similar to TSW500 where the measurement is slightly higher than prediction at 10 m but both agree with the predicted maximum concentration well (there is a small time lag for this case).

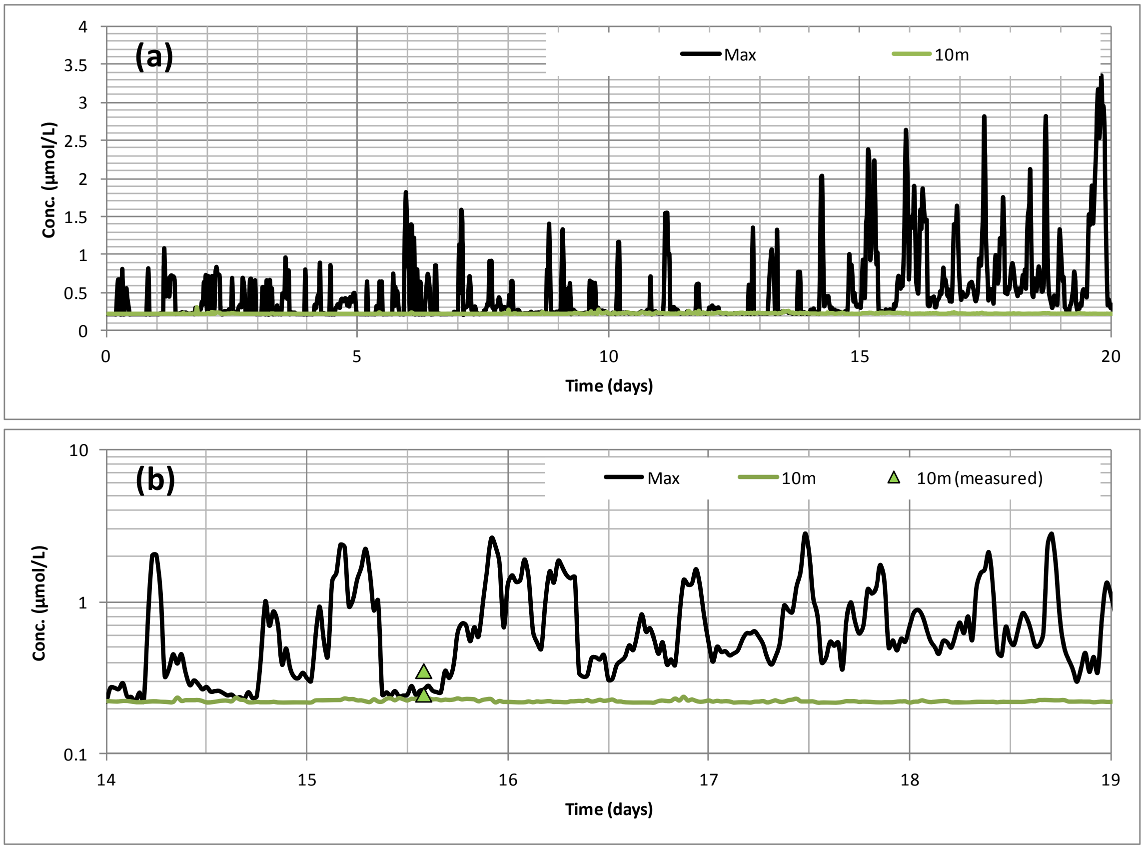

Figure 85: Concentration of Ammonia at TSW50 (FRC).

Similar to TSW500 and TN0, the predicted concentration at 10 m for TN50 is also slightly lower than measured. However, the predicted maximum concentration does not agree with the measurement as good as it is for TSW500 and TN0. The predicted maximum concentration is higher than measurements in this station.

The TN500 is again similar to TSW500 and TN0 where the measurement is slightly higher than prediction at 10 m but both agree with the predicted maximum concentration well.

The predicted maximum concentration changes for all stations are plotted in Figure 90 together with the measurement uncertainty levels. It can be seen that the maximum changes at stations within 500 m are about 10 times the average uncertainty and therefore is significant enough for comparison. For this reason, the further comparison below using data of Fe will only focus on stations within 500 m.

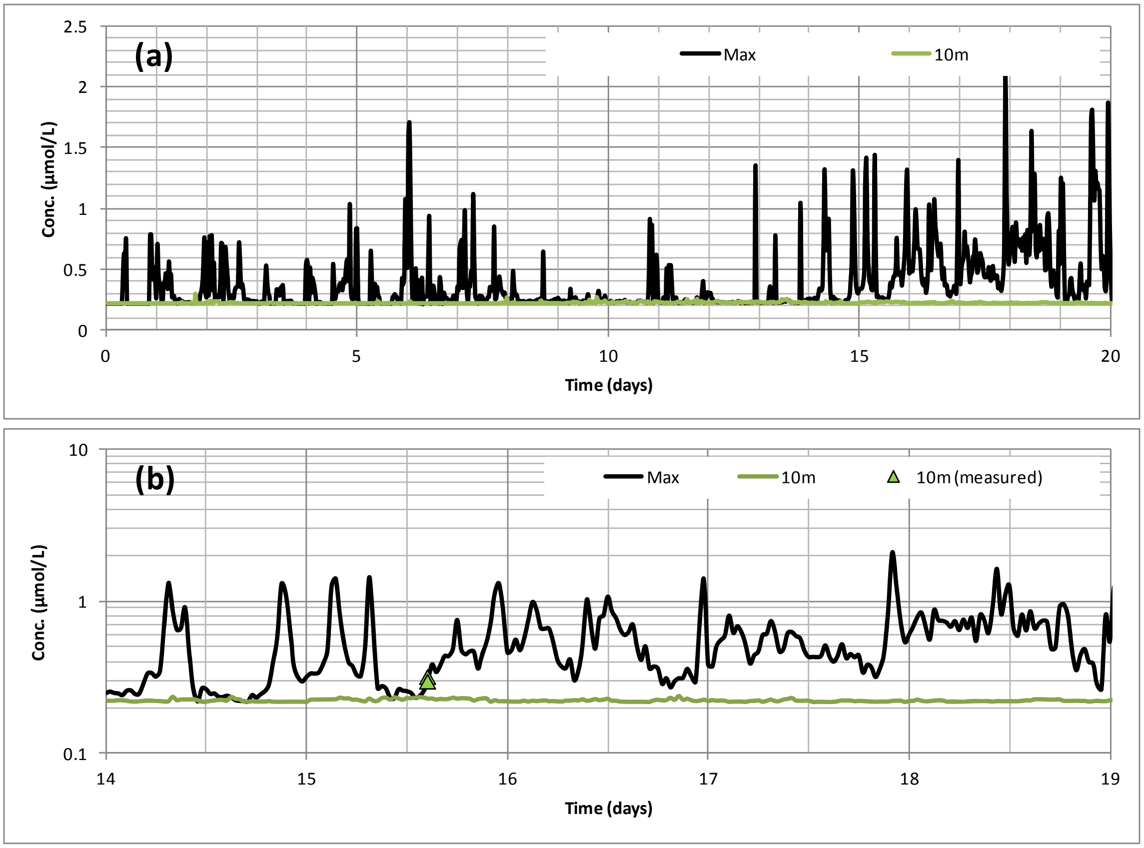

Figure 86: Concentration of Ammonia at TSW500 (FRC).

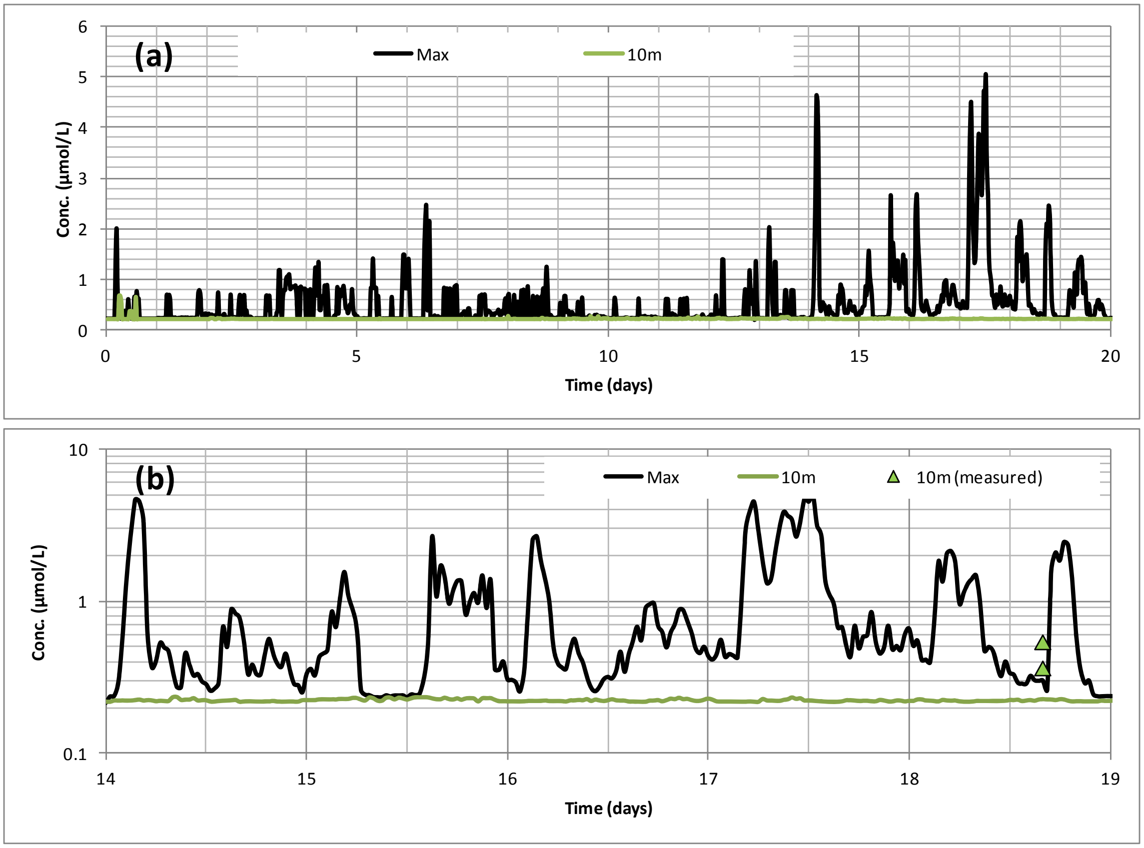

Figure 87: Concentration of Ammonia at TN0 (FRC).

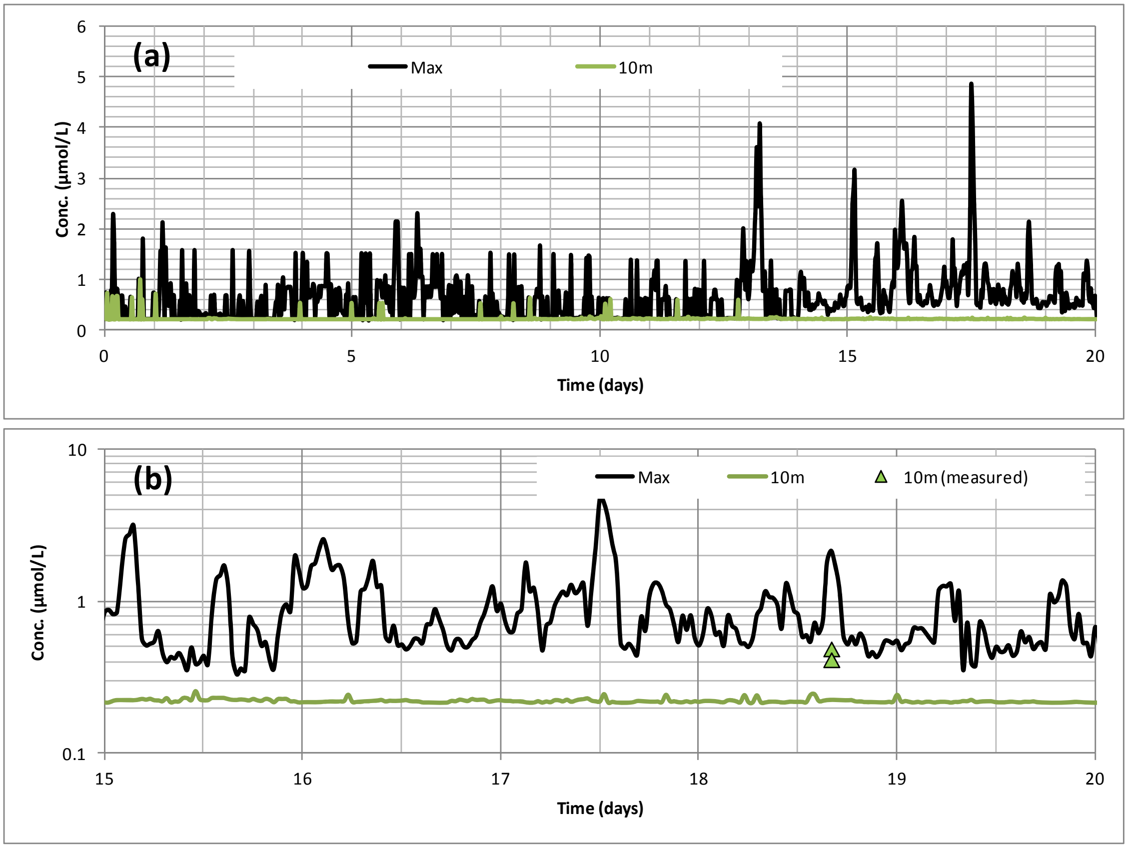

Figure 88: Concentration of Ammonia at TN50 (FRC).

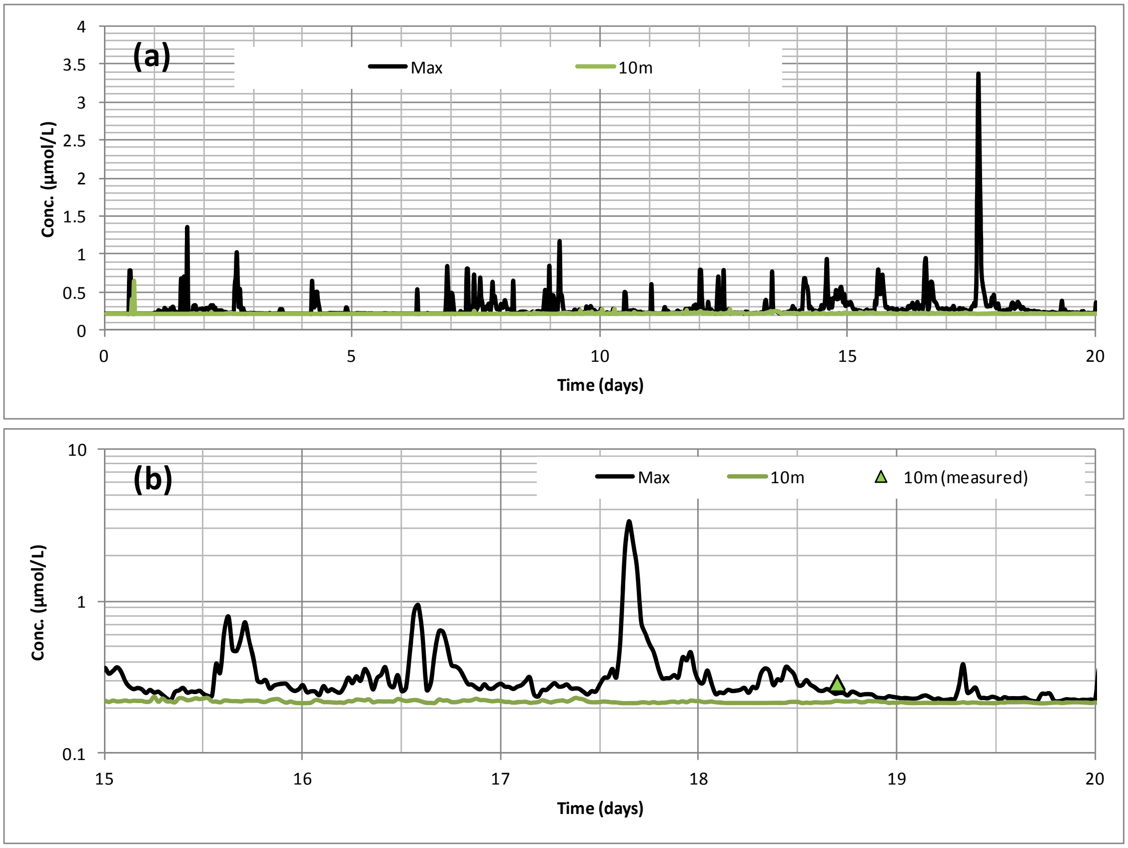

Figure 89: Concentration of Ammonia at TN500 (FRC).

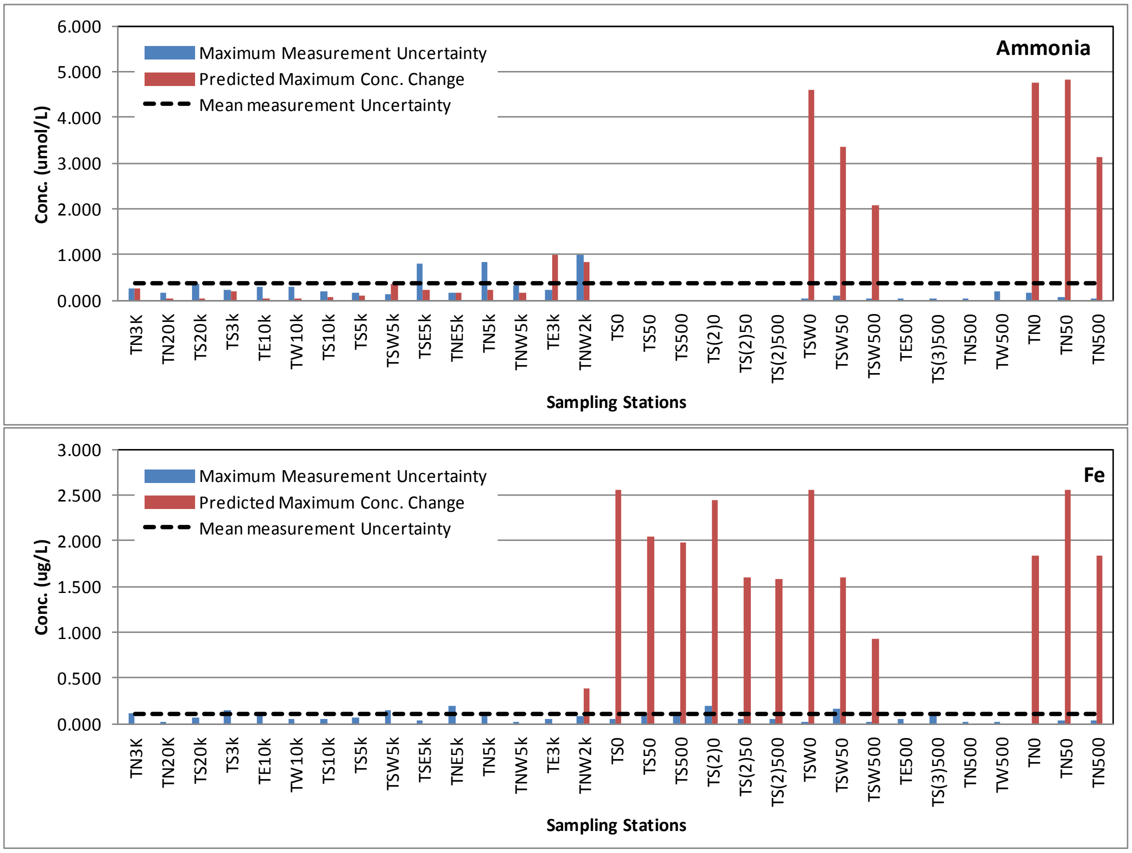

Figure 90: Maximum predicted concentration change compared with uncertainty levels of measurement.

The predicted concentrations of Fe compared with measurements are plotted in Figure 91 to Figure 102. For TSW0 (Figure 91), it can be seen that the prediction at 10 m is also slightly lower than the measurements, but the predicted maximum concentration agrees with the measurements well. This trend is similar to that of ammonia.

At TSW50, both prediction at 10 m and the predicted maximum concentration are lower than the measurements. The measurements are 3 to 5 times higher than the prediction. At TSW500, the trend is similar to that of TSW0 where the prediction at 10 m is also slightly lower than measurements, but the predicted maximum concentration agree with the measurements well. This trend is similar to that of ammonia. At TN0, TN50, and TN500, the trend for Fe is similar to that of ammonia where the prediction at 10 m is also slightly lower than the measurements, but the predicted maximum concentration agrees with the measurements well.

While good agreement is found at TS0 and TS50, the TS500 is more similar to TSW50 where both the prediction at 10 m and the predicted maximum concentration are lower than the measurements.

The TS(2)0 is similar to TS500 and TSW50 but the difference is even higher. Unlike the ammonia case, these high levels are only detected in this station and one other station

(TE10k). It is likely to be a sign of produced water presence which the model fails to produce, or a possible contamination of the sample. Unfortunately, there is no other data available to cross-check and no conclusion can be drawn for this station.

The TS(2)50 and TS(2)500 are similar to most of the stations in that the prediction at 10 m is also slightly lower than the measurements, but the predicted maximum concentration agrees with the measurements well.

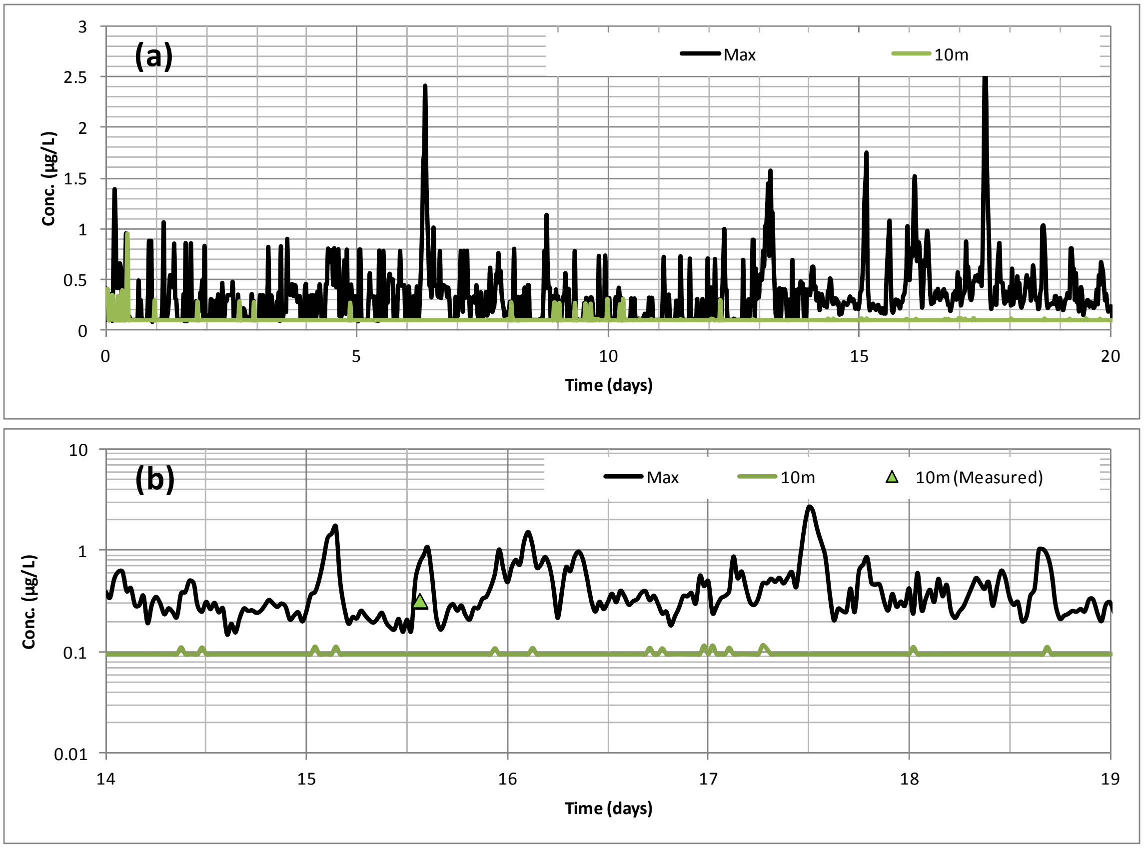

Figure 91: Concentration of Fe at TSW0 (FRC).

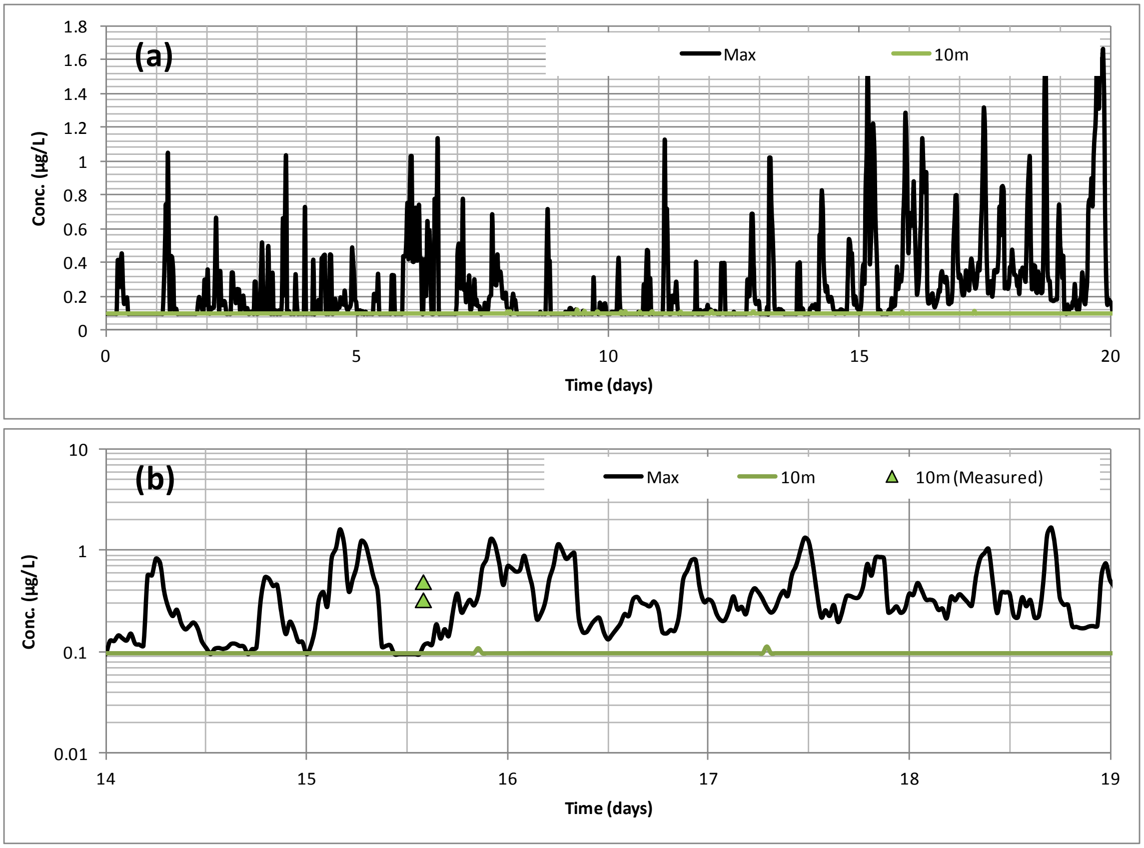

Figure 92: Concentration of Fe at TSW50 (FRC).

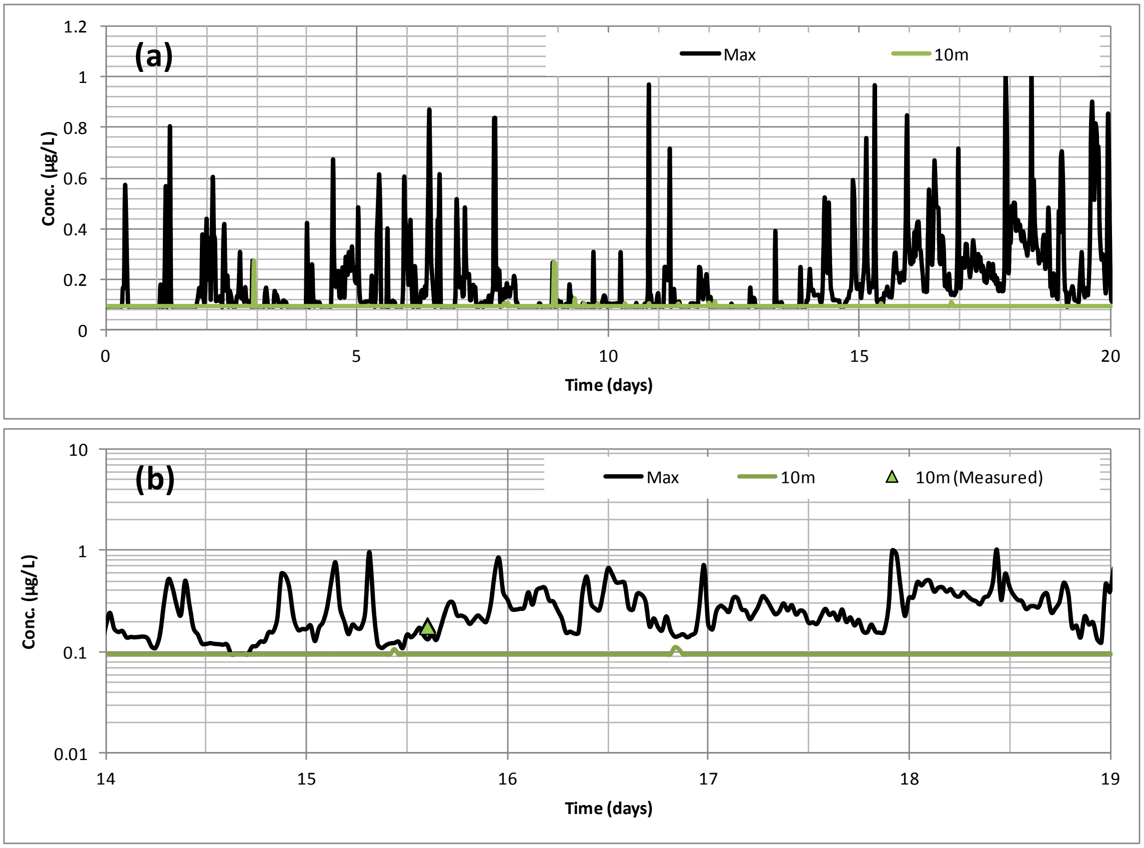

Figure 93: Concentration of Fe at TSW500 (FRC).

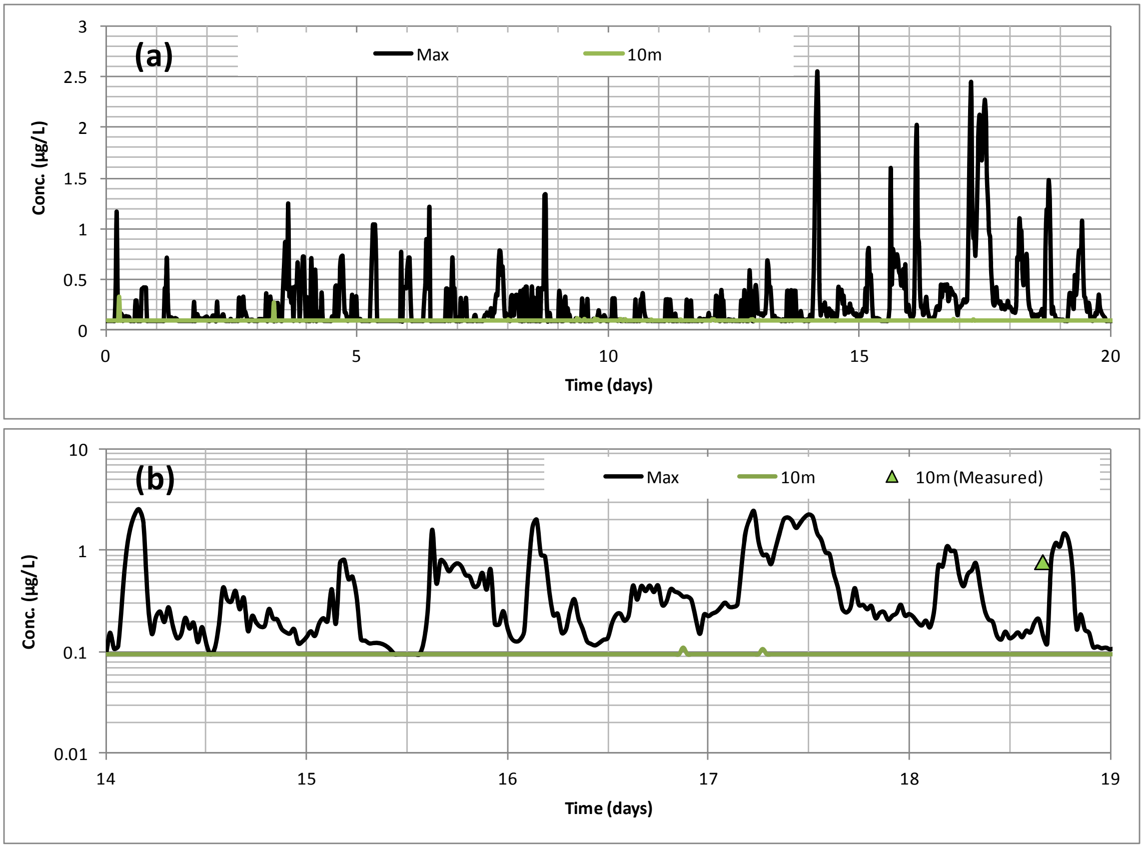

Figure 94: Concentration of Fe at TN0 (FRC).

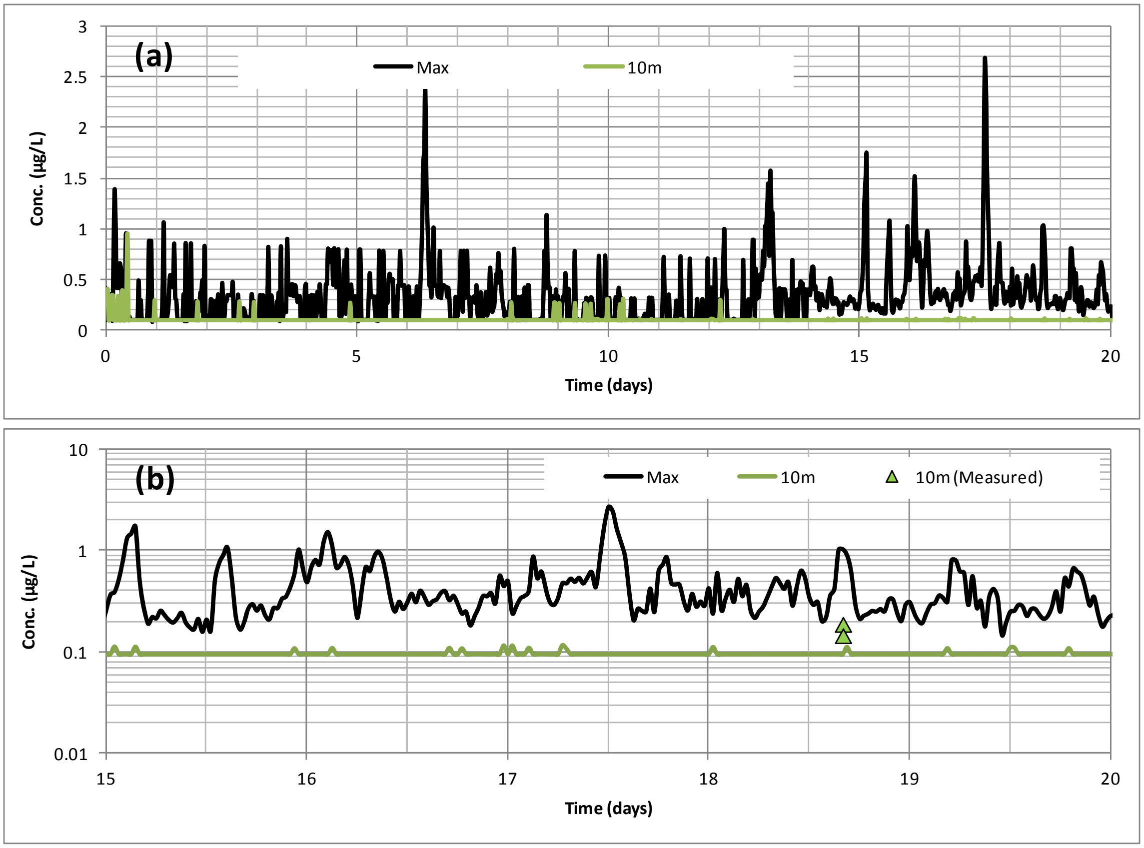

Figure 95: Concentration of Fe at TN50 (FRC).

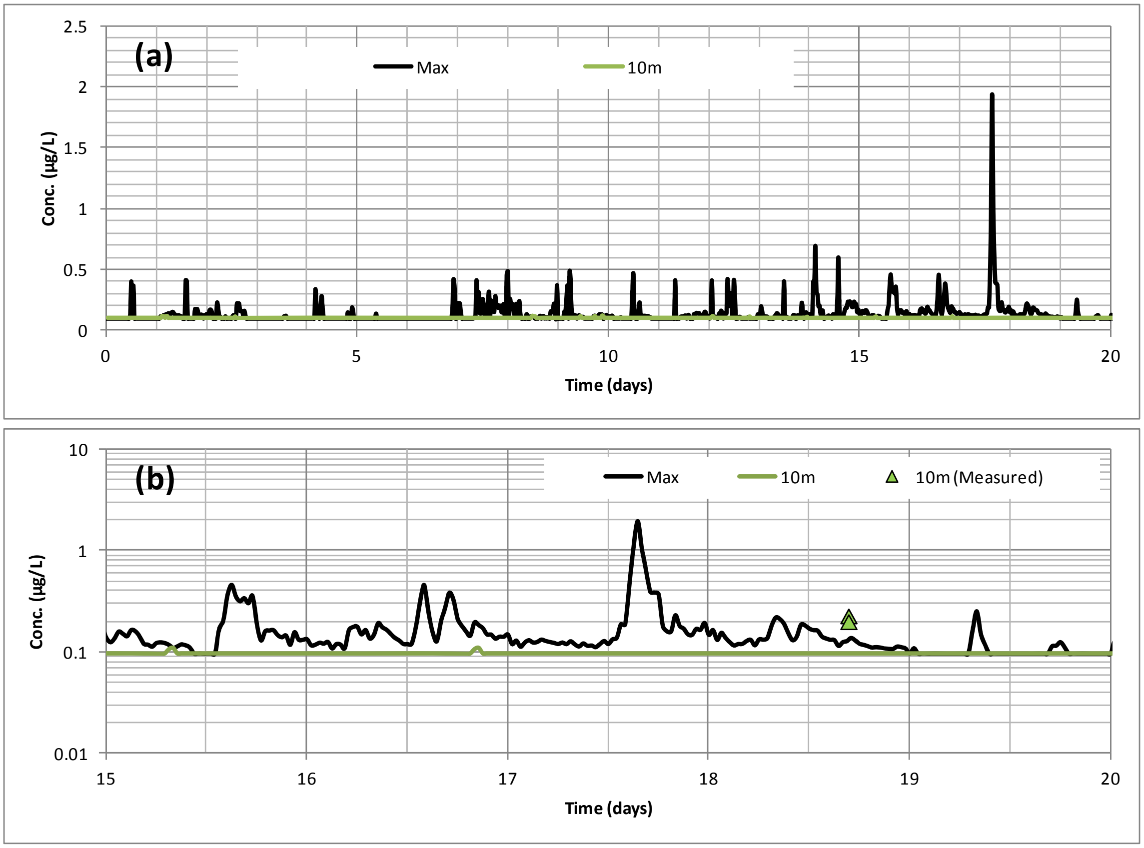

Figure 96: Concentration of Fe at TN500 (FRC).

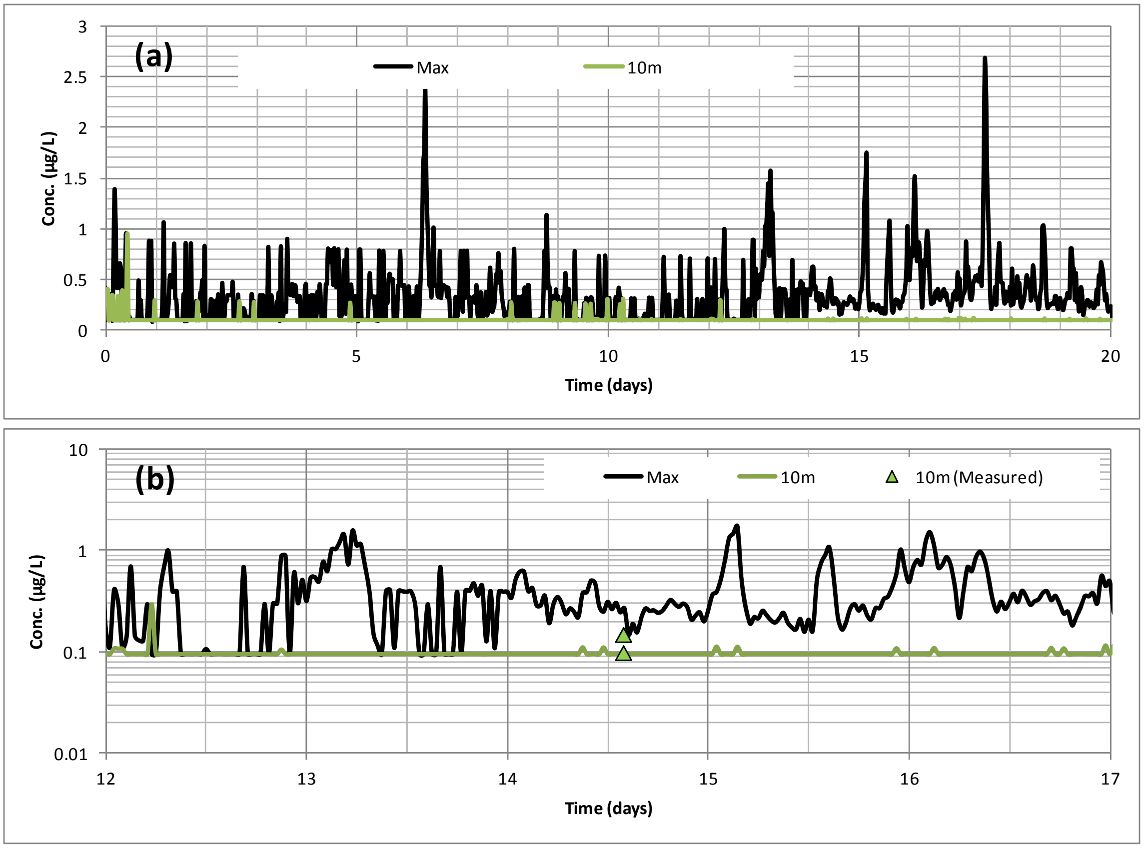

Figure 97: Concentration of Fe at TS0 (FRC).

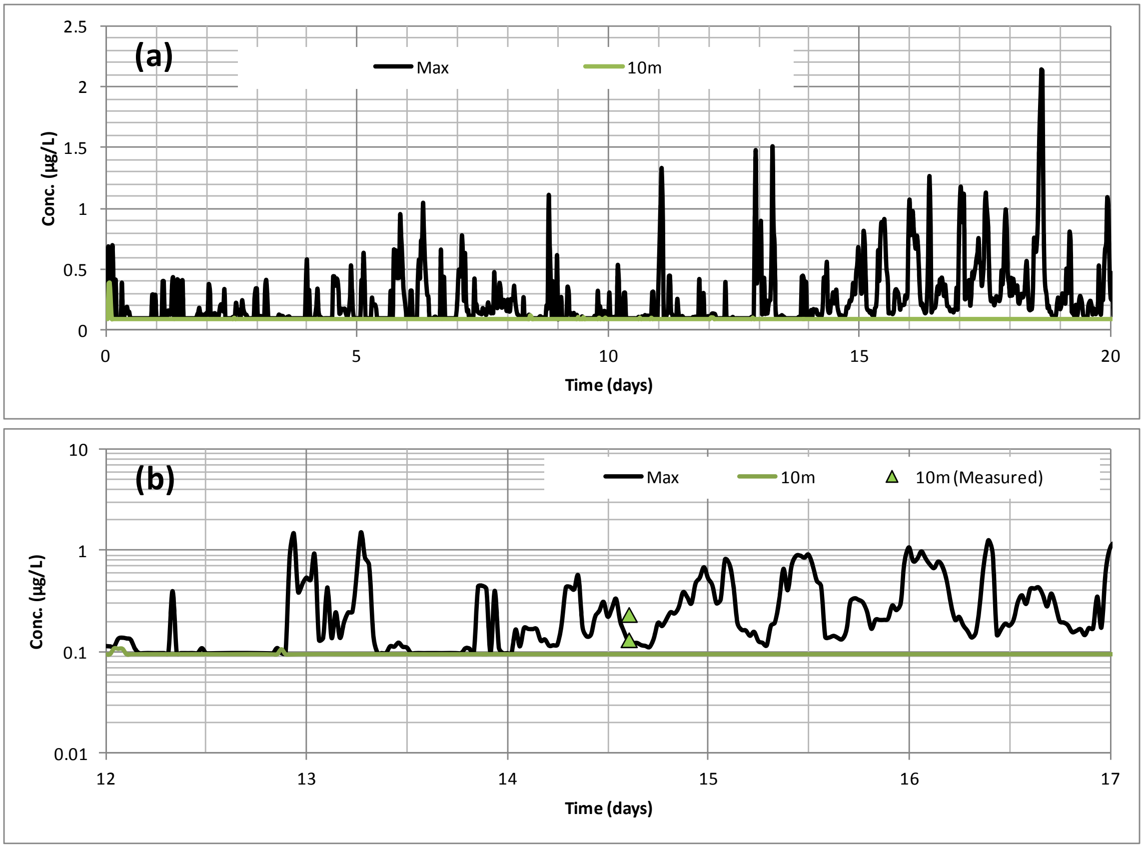

Figure 98: Concentration of Fe at TS50 (FRC).

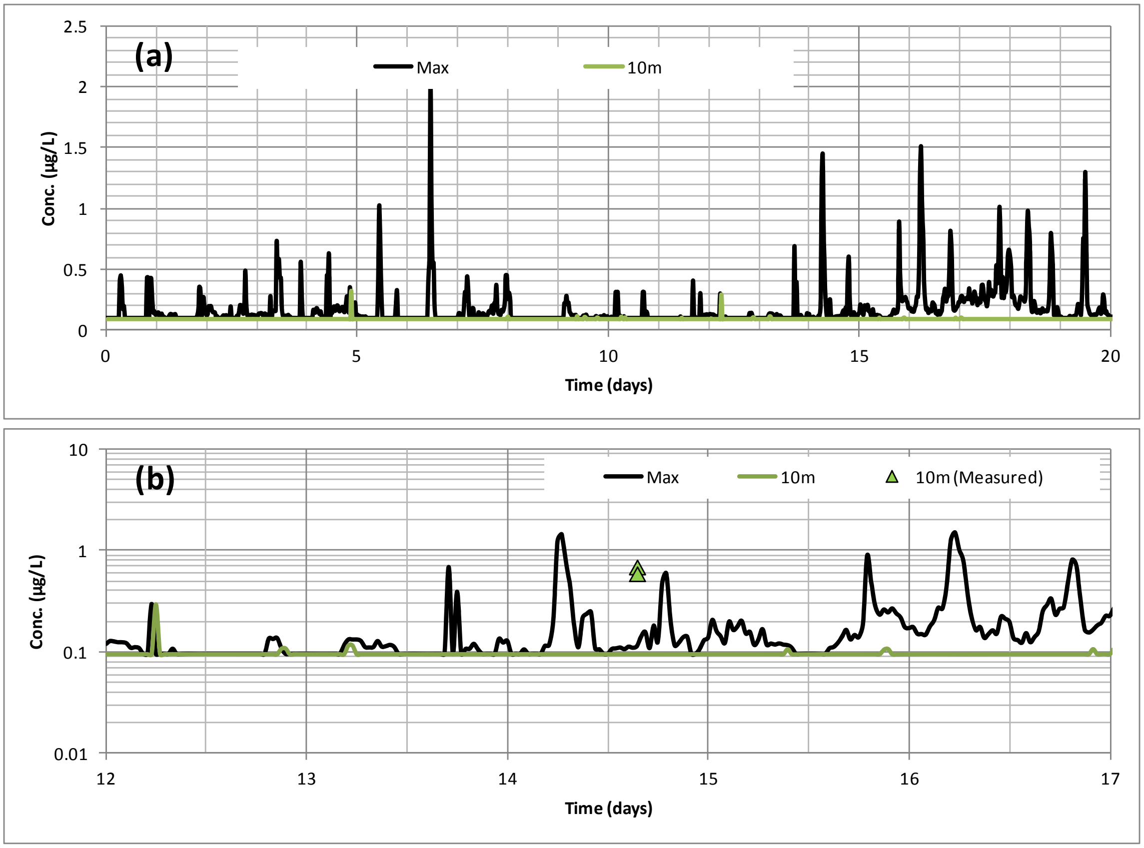

Figure 99: Concentration of Fe at TS500 (FRC).

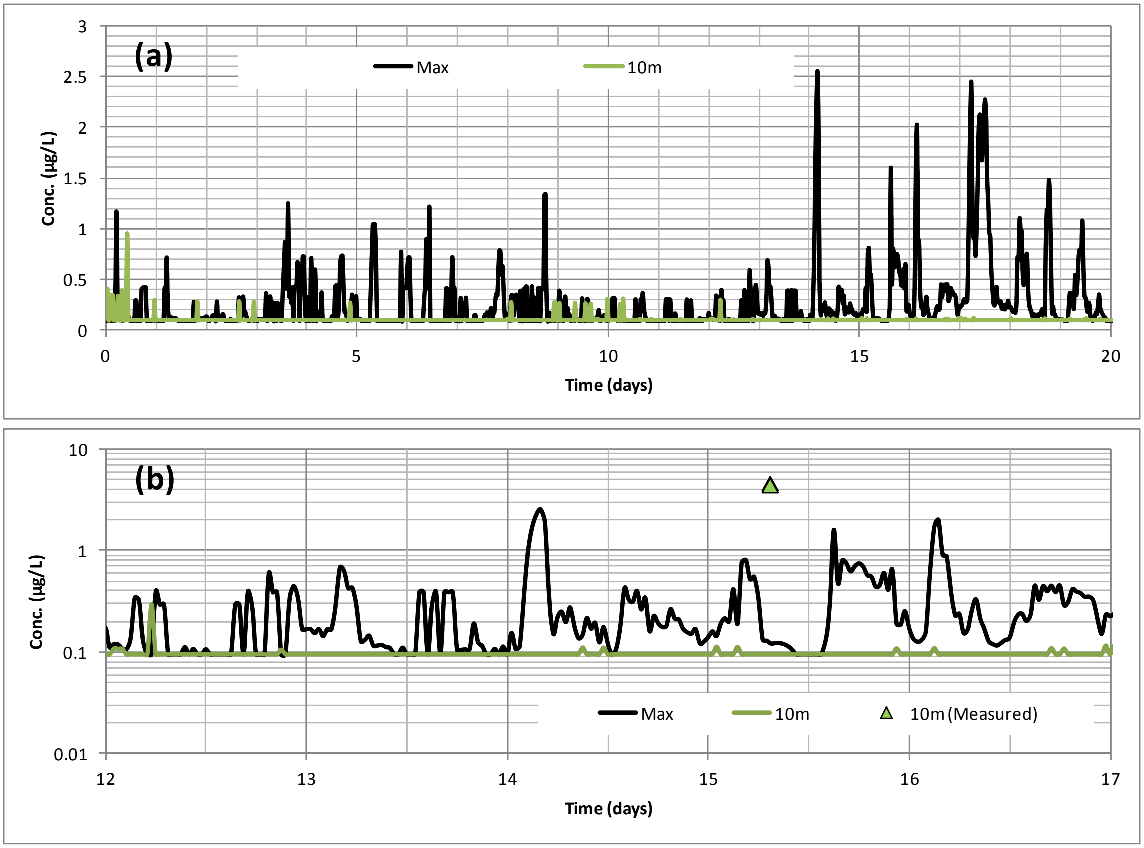

Figure 100: Concentration of Fe at TS(2)0 (FRC).

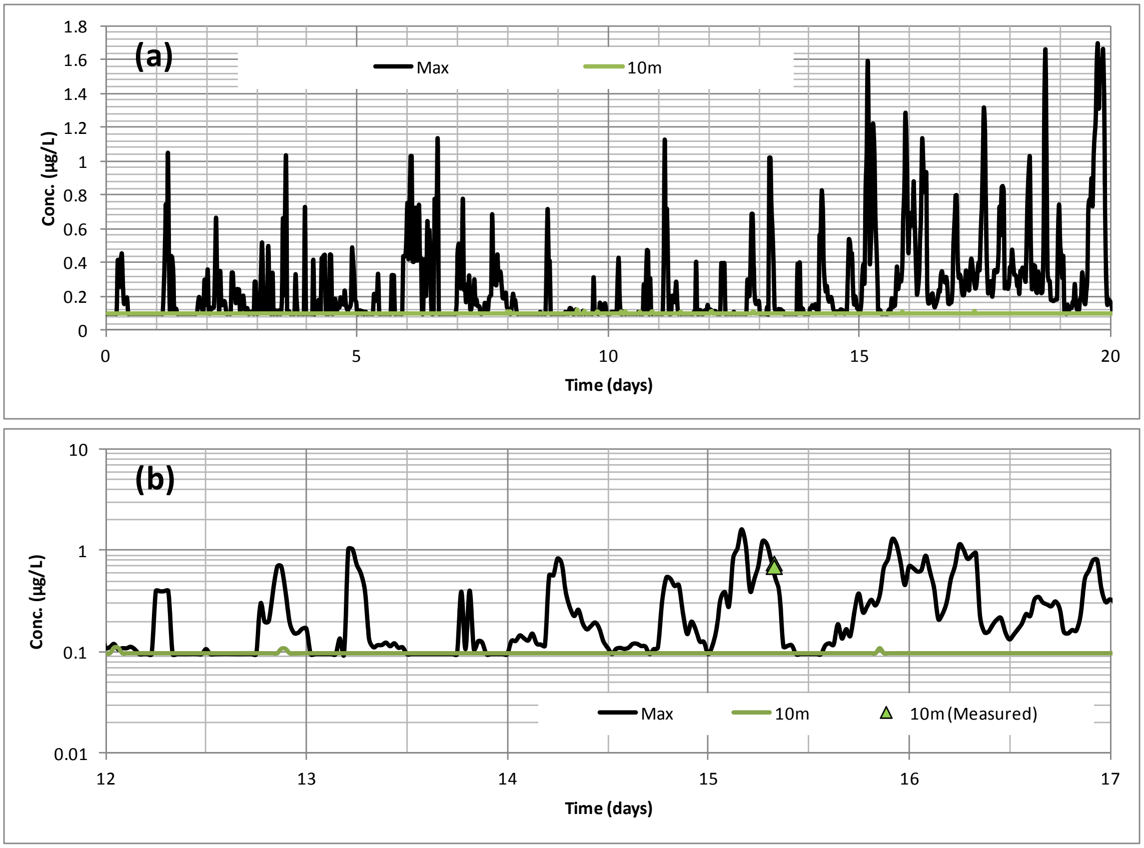

Figure 101: Concentration of Fe at TS(2)50 (FRC).

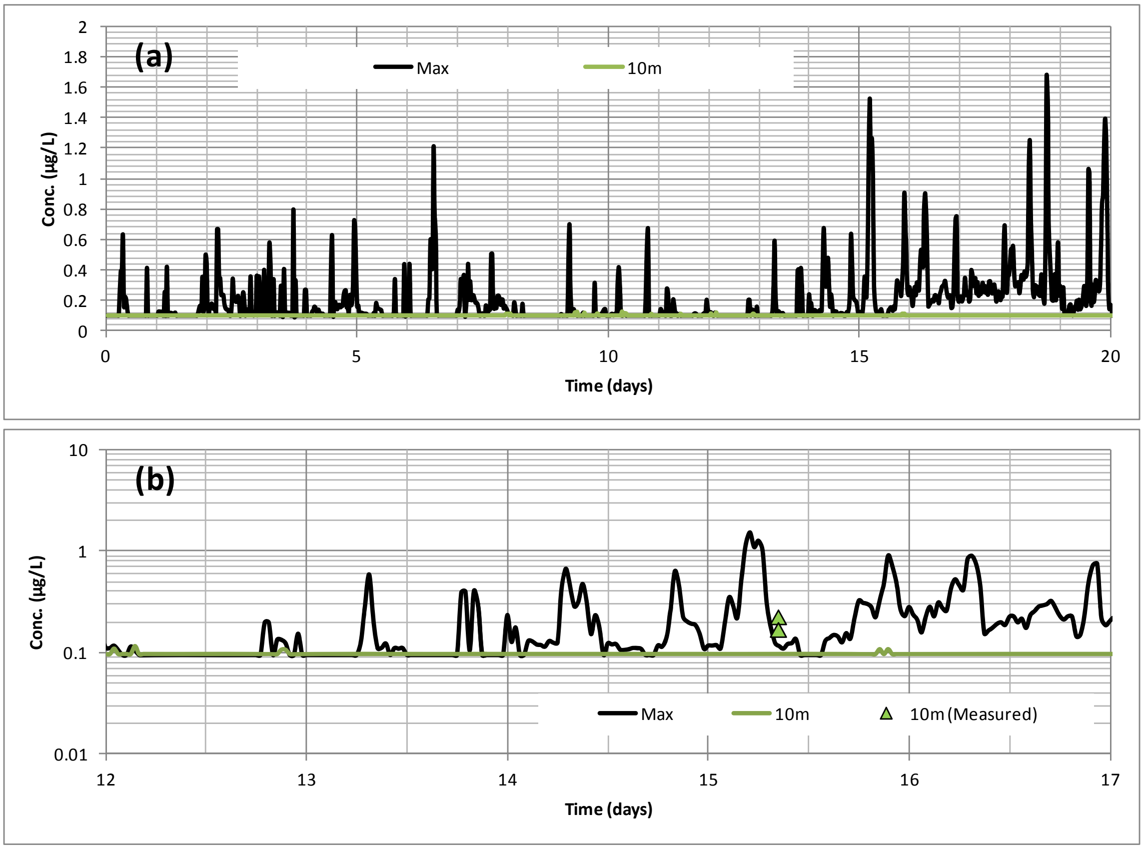

Figure 102: Concentration of Fe at TS(2)500 (FRC).

4.7 Summary of Model Validation

The time series concentrations at 27 stations (four stations were excluded due to missing GPS data) around Terra Nova were compared with measurements. From the direct visual comparison described in the previous section and Figure 103 to Figure 105, it can be concluded that:

- Both model and measurements show higher concentrations at deep layers than at the surface layer (10 m).
- While the prediction at 10 m for most stations agrees with measurements reasonably well, the prediction is slightly lower than measurements. Besides the possible reason of model imperfection, the great degree of background uncertainty also contributes to the difference.
- Figure 103 shows that most of the pairs are close to the dashed line (measurement=predicted) with few exceptions that measurements are much higher than predictions.
- Figure 104 shows that the ratio of prediction (10 m) to measurement for ammonia ranging from 0.41 to 0.97 and the average ratio is 0.71. The ratio of prediction (max) to measurement for ammonia ranging from 0.55 to 4.32 and the average ratio is 1.49. For Fe, the ratio (10 m) ranging from 0.19 to 0.96 with an average

ratio of 0.37. The ratio (max) ranging from 0.03 to 6.88 with an average ratio of 1.33. This again indicates that the prediction is generally lower than the measurement at 10 m. The contribution could either be caused by the model itself or due to uncertainty in background concentration.

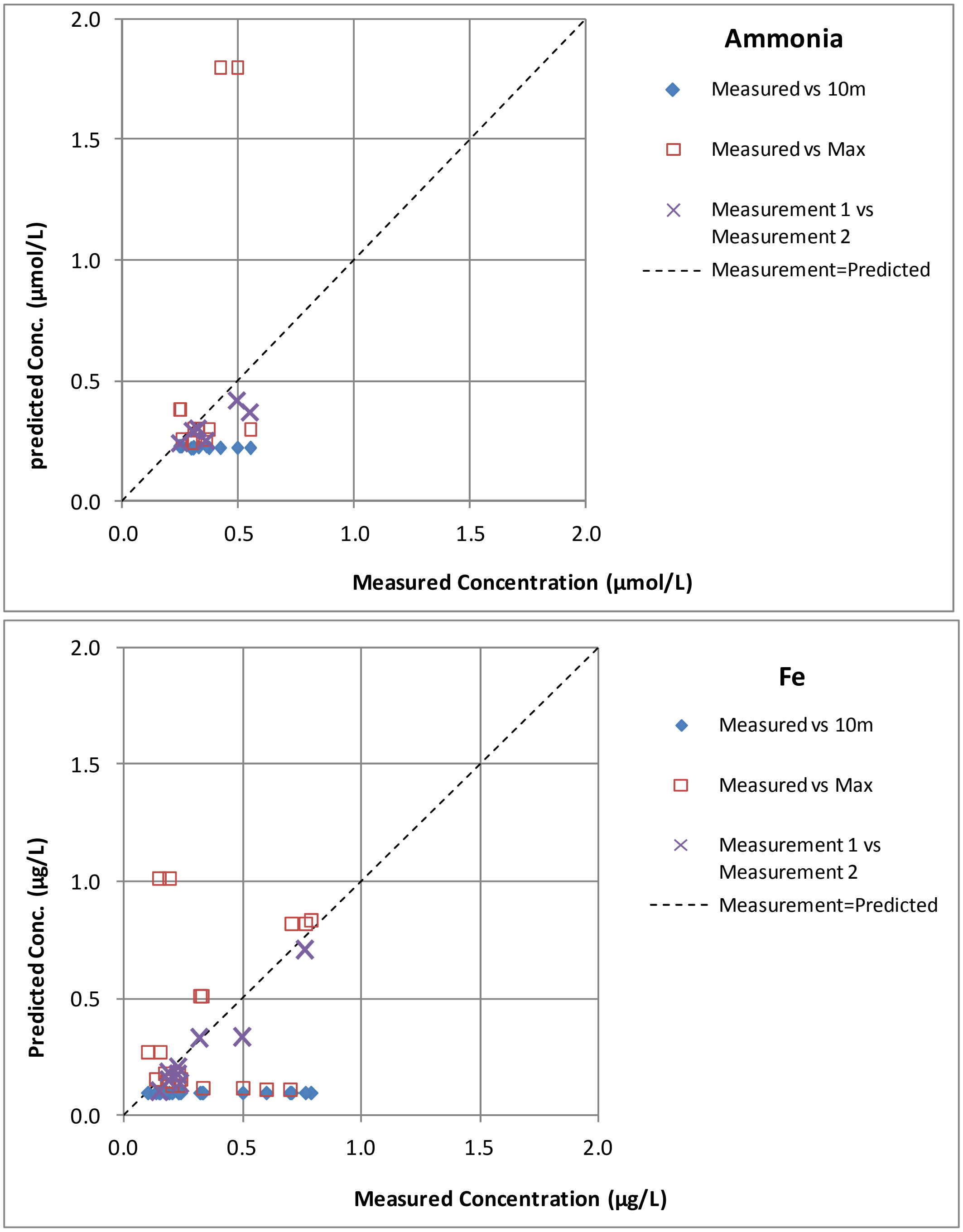

Figure 103: Goodness of Prediction: Prediction versus Measurement.

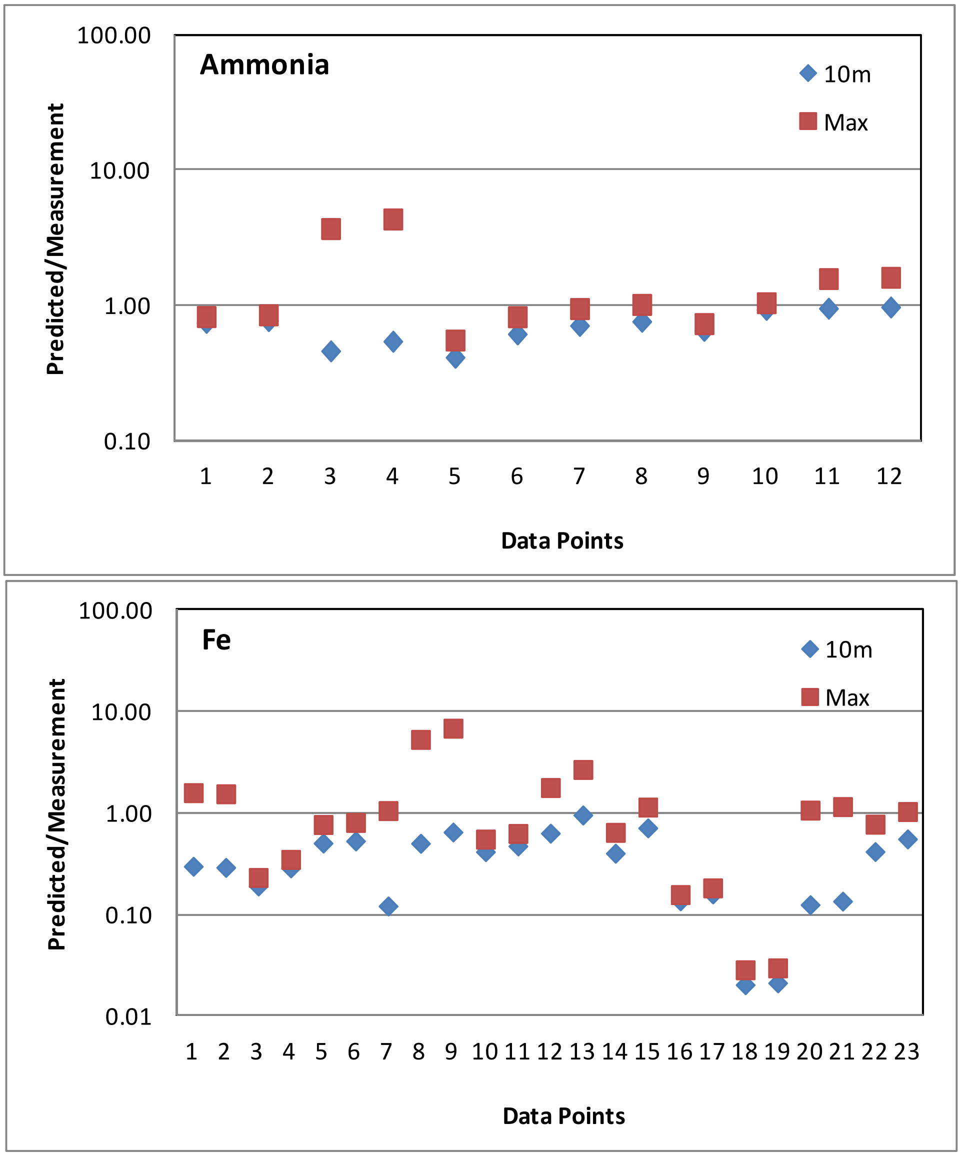

Figure 104: Goodness of Prediction: Ratio of Prediction to Measurement.

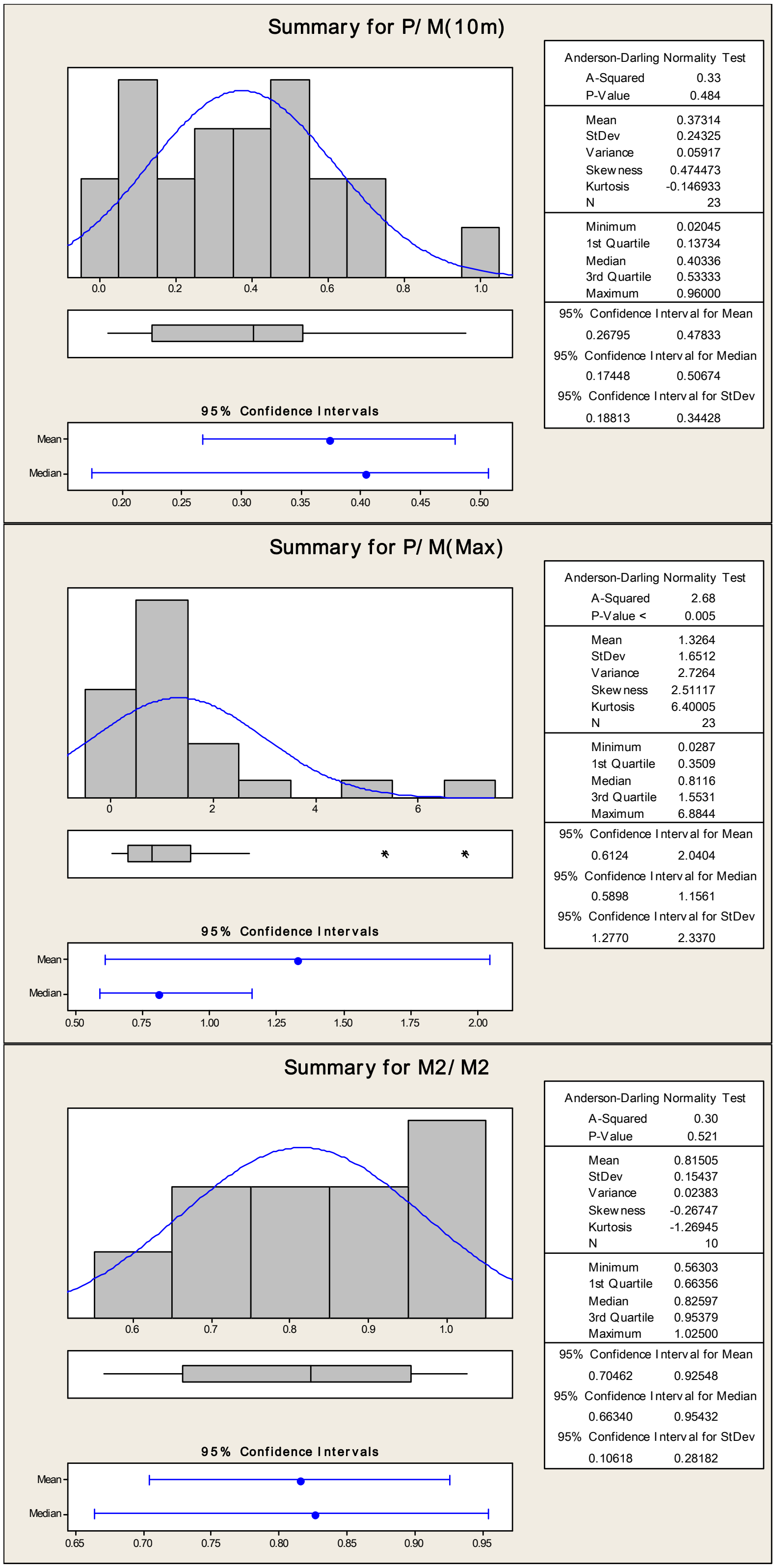

Figure 105: Summary statistics of prediction to measurement ratio.

4.8 Remarks

Considering the great level of uncertainty in the sampling, analysis, and modeling, an overall 30% to 40% difference between prediction and measurement is considered small and the model is considered to perform well for this site. However, the model does have some limitations that affect its performance; the following recommendations for model improvement are suggested:

- Provide the capability of using profile rather than single value for background chemicals;
- Provide the capability of using time dependent salinity/temperature profile for cases with long simulation periods.

5. Regional Produced Water Toxicity Data

The risk caused by any chemical in the mixture is related to the PEC/PNEC ratio, where PEC, as described before, is the Predicted Environmental Concentration, and PNEC is the Predicted No Effect Concentration. To assess the risk on specific species that is important for the Atlantic region, toxicity tests were conducted by researchers at the St. Andrews Biological Station, NB, with funding support from ESRF.

To date, toxicity tests have been conducted with produced water from Hibernia, Terra Nova, Thebaud and Venture. The test with produced water from the Sea Rose platform is ongoing.

The results have found that none of the products is particularly toxic. It takes percentages of the produced water to have significant effects on cod. It seems that the produced water for the two gas platforms (Thebaud and Venture) are more toxic than those from the two oil platforms (Hibernia and Terra Nova).

The following toxicity data have been added to the DREAM database:

Terra Nova:
Fertilization of cod eggs is not affected by the PW water. The maximum exposure concentration was 12% of the exposure medium.
Hatching success of fertilized eggs is not different from controls at all concentrations tested (maximum = 12% PW).
Lethality (24-h LC50) of Terra Nova PW to larval cod is ~42%, i.e. the exposure solution must contain at least 42% PW to kill 50% of the exposed larvae.

Hibernia:
Fertilization of cod eggs is not affected by the PW water. The maximum exposure concentration was 12% of the exposure medium.
Hatching success of fertilized eggs is not different from controls at all concentrations tested (maximum = 12% PW).
There is no calculable 24-h LC50 for Hibernia PW to larval cod. Less than 50% of the larvae died when exposed to 100% PW

Thebaud:
Fertilization of cod eggs is affected by Thebaud PW water at concentrations equal to or greater than 3.6 % of the exposure medium.
Hatching success of fertilized eggs was affected by exposure to PW when the exposure concentration was greater than 12%.
The 24-h LC50 for Thebaud PW to larval cod is 1.25%.

Venture:

Fertilization of cod eggs is affected by Venture PW water at concentrations equal to or greater than 12 % of the exposure medium.
Hatching success of fertilized eggs was affected by exposure to PW when the exposure concentration was greater than 3.6 %.
The 24-h LC50 for Venture PW to larval cod is 0.88%.

Juvenile cod growth:

Individually tagged cod were exposed to PW from either Hibernia or Venture for a number of weeks. Samples were collected periodically for biochemical analyses and to determine growth.
Hibernia PW (45 day continuous exposure) had no effect on cod growth compared to controls.
Venture PW (pulsed exposure 3 times per week for 14 weeks) affected growth of juvenile cod when the concentration of PW was 200 ppm.

An example application of the regional toxicity data is shown in Figure 106. The results show that the risks based on regional toxicity data are smaller than those based on PNEC values for the Venture scenario.

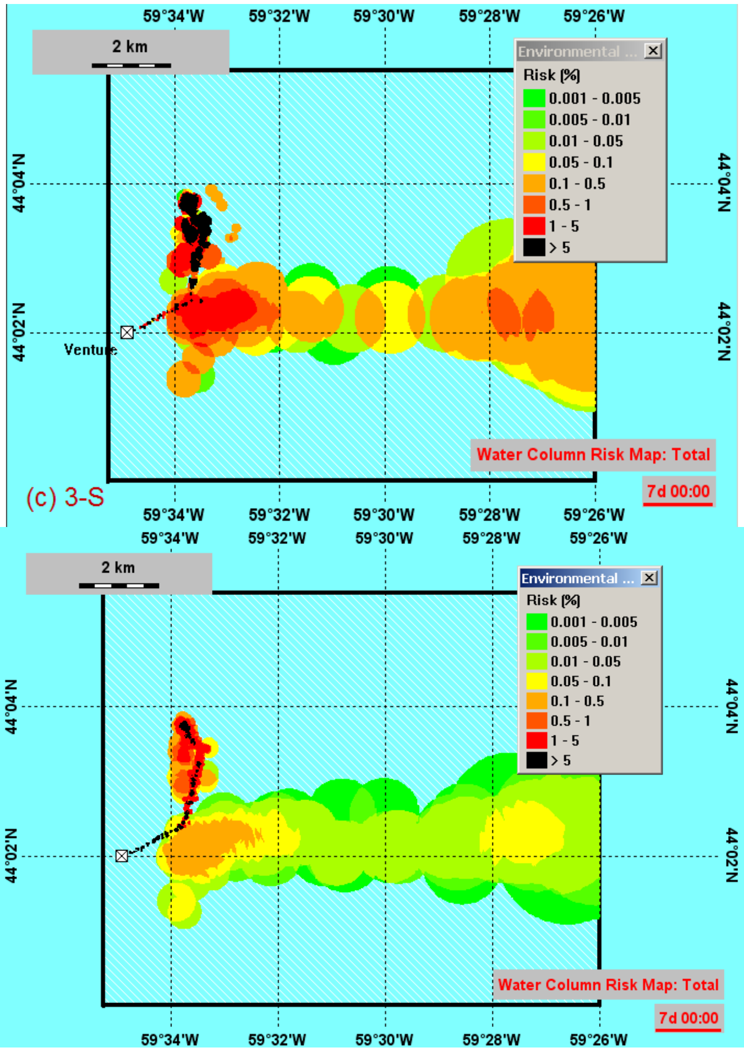

Figure 106: Total environmental risks for the near field: Risks were computed based on PNECs of individual chemical components (top), and based on toxicity tests on whole produced water (bottom).

6. Drilling Mud Cross-Validation Study

In addition to the discharge of produced water, the exploration and extraction of offshore oil and gas also generates drilling muds that are often discharged from the platform at sea. These discharges may pose both toxic and non-toxic impacts to marine organisms, such as growth inhibition, mortality and smothering. The DREAM model can be used to predict the environmental concentrations and understand the risks of discharged drilling muds. Since comparisons of DREAM with different drilling mud transport models are scarce in literature, we have expanded our study scope to include a case study of drilling waste transport, and compare it with the benthic boundary layer transport (bblt) model (Drozdowski et al, 2004).

6.1 Model Description

6.1.1 DREAM (ParTrack)

ParTrack (a module of DREAM) is a software tool developed by SINTEF Marine Environmental Technology, Norway, for modeling the transport of drilling wastes (both cuttings and muds). It is now integrated and operated within the Marine Environmental Modeling Workbench (MEMW). ParTrack simulates the release and spreading of drilling wastes as two sequential steps: a near-field descent or ascent process using the newly implemented Plume3D model, and the far-field advection and diffusion using a particle tracking approach. The latest version of ParTrack included a re-suspension process.

The formulation of ParTrack has evolved over the past few years. The earlier version of ParTrack used a near-field model similar to what is used in the Offshore Operators Committee (OOC) model (Brandsma and Sauer, 1983; Rye et al., 1998) and the latest version adopted a newly developed Plume3D model (Johansen and Durgut, 2006). Plume3D is a Lagrangian based model which represents the plume by a series of non-interfacing elements. Each element, which can be treated as a cylinder or section of a bent cone, is characterized by its mass, location, width (radius), length (thickness), average velocity, pollutant concentration, temperature and salinity. The mineral particles contained inside the elements are defined in terms of particle size classes and density categories and their position x, y, z at a given time t is determined by time interpolation of the element coordinate X, Y, Z. As the densities of the mineral particles are generally different from that of the plume element, they will separate from the plume as they move along the trajectory. The separation rate of a particle can be derived from its concentration, separation velocity, and the projected area of the plume element (Johansen and Durgut, 2006). Once separated from the plume element, the motion of a particle depends on ambient current advection/diffusion.

For the re-distribution of settled particles, ParTrack initiates the re-suspension if the non-dimensional stress parameter, θ, is greater than a critical shield parameter, θ_c. The pick up rate for each fraction in the sediment is determined by the mass fraction of the grain size class, its settling velocity and the volumetric seabed concentration.

6.1.2 bblt

The bblt model was developed at the Bedford Institute of Oceanography to predict the transport and dispersion of suspended particulate drilling wastes in the benthic boundary layer. The model assumes that all of the discharged material enters the benthic boundary layer and thus the model neglects the mechanism of plume surfacing. The primary mechanisms modeled by bblt are the horizontal dispersion and drift due to the interaction of vertical mixing and vertical shear, mud flocculation and break-up. The latest version, bblt v7.0, also integrates a biological impact module (Drozdowski et al., 2004).

The bblt is a particle-based model which treats the drilling waste load mass M as N pseudo-particle packets with mass $m=M/N$ and settling velocity w. The basic output of the bblt is the time series packet positions, $X_n(t)$, $Y_n(t)$, $Z_n(t)$. The movement of the packets has two parts, horizontal dispersion and vertical distribution. The horizontal dispersion is statistically defined by the horizontal variance of the packets distribution σ^2 (m^2). The effective diffusivity, K (m^2/s), is defined by Csanady (1973) as

$$K = \frac{1}{2}\frac{\partial \overline{\sigma^2}}{\partial t}, \tag{23}$$

where the overbar denotes a time averaging. In two dimensions, the variances, $\sigma^2_{\max}$ and $\sigma^2_{\min}$, along the major and minor axes of the horizontal projection of the distribution are calculated. The effective diffusivity for this case is defined as

$$D = \sqrt{K_{\max} K_{\min}}, \tag{24}$$

where $K_{\max}$ and $K_{\min}$ are the effective horizontal diffusivities along the major and minor axes, respectively. The $K_{\max}$ and $K_{\min}$ are defined by equation (24).

The vertical distribution of the packets is parameterized by a sediment concentration Rouse profile $c(z)$ as

$$c(z) = \begin{cases} c_a (a/z)^{p_1} & z \le \delta \\ c_\delta (\delta / z)^{p_2} & z > \delta \end{cases}, \tag{25}$$

where z is the vertical coordinates, a is the sediment reference height below which the particle motion is negligible, c_a is the reference concentration $c(a)$ at height a, δ is the height of the current-wave boundary layer, c_δ is the reference concentration $c(\delta)$ at height δ, p_1 and p_2 are the Rouse numbers defined as

$$p = \frac{w}{\kappa u_*} \tag{26}$$

where the κ is the von Karman constant ($\kappa = 0.4$), w is the settling velocity, $u_* = \sqrt{\tau_b / \rho}$ is the friction velocity, τ_b is the magnitude of bottom stress, and ρ is the density of sea water.

6.2 Methods

To compare the ParTrack and bblt models, a hypothetical study was conducted. Although ParTrack has the capability to simulate coarse drill-cutting particles and fine drilling mud particles, bblt can only be used for fine drilling mud particles. Therefore, only drilling mud was simulated in this study. It is assumed that there was a batch discharge of 10,000 tons of drilling muds into the ocean at the release site with coordinates (0, 0).

While the two models are formulated quite differently, it is expected that the way that the models introduce barite will impact the results. As mentioned earlier, bblt assumes that all of the discharged material enters the benthic boundary layer and it does not have a near-field plume module. On the contrary, ParTrack can model the plume dynamics using a near-field Plume3D model. To make the results more comparable, a near-bottom batch scenario was used in ParTrack and the near field Plume3D model was switched off in the simulation. Even without the modeling of near field plume dynamics, ParTrack still requires the user to specify a discharge depth. This is because the discharge depth affects the duration of particles in the water column before they encounter the seabed, and therefore affects the sediment concentration. To study the effects of discharge depth, two sets of simulations were conducted by specifying discharge depths at 1 m and 5 m above the seabed.

A square study area of about 20 km × 20 km around the release site (0, 0) was selected. This area was divided into grid cells of 250 m × 250 m. The water depth was assumed to be 70 m. A spatially constant rotary current with a constant speed of 0.5 m/s was used in the simulation. The current direction changed at a constant rate of about 29 degrees per hour. The time series u- and v-components of this rotary current are plotted in Figure 107. For a bblt simulation, a near bottom current profile (log-layer file) needs to be specified so that the model can calculate the current velocity below the bottom current meter. As shown in Figure 108, the linear log-layer with a height *hL* describes the currents below the bottom current meter. As the bblt may be sensitive to the user specified log-layer file, two scenarios with 0.1 m and 0.5 m linear bottom currents were conducted to study the effects of log-layer height on model prediction.

The material simulated was fine barite particles with a density of 4,200 kg/m^3. The particle size distribution and settling velocity for the barite are shown in Table 10. The ParTrack model can simulate the transport of particles of multiple sizes by automatically calculating their settling velocity based on the input of particle size distribution. ParTrack requires only one simulation to model the transport of particles of various sizes. However, bblt can only simulate the transport of single-sized particles by specifying its corresponding settling velocity. To obtain results as close as possible, the same settling velocity for particles of the same size class must be used by both models. As there are eight size classes specified in ParTrack, eight simulations using bblt were conducted. The settling velocity in each of the eight bblt simulations was calculated based on the mean diameter of the eight size classes specified in ParTrack (Table 10). For each bblt simulation, the mass of barite introduced is the product of the total mass (10 ton) and the weight percentage of the corresponding size class. The eight predicted concentrations for each of the grid cells are then summed to give the total concentration for that cell.

Table 10: Particle size distribution and settling velocity

Model	Simulation No.	Particle Size Distribution		Settling Velocity (m/s)
		Diameter (μm)	Weight (%)	
ParTrack	1	1< >2	30	model calculation
		2< >4	10	
		4< >7	10	
		7< >12	10	
		12< >16	10	
		16< >23	10	
		23< >30	10	
		30< >50	10	
bblt	1	1.5	30	2.04E-06
	2	3	10	8.17E-06
	3	5.5	10	2.75E-05
	4	9.5	10	8.22E-05
	5	14	10	1.79E-04
	6	19.5	10	3.47E-04
	7	26.5	10	6.41E-04
	8	40	10	1.46E-03

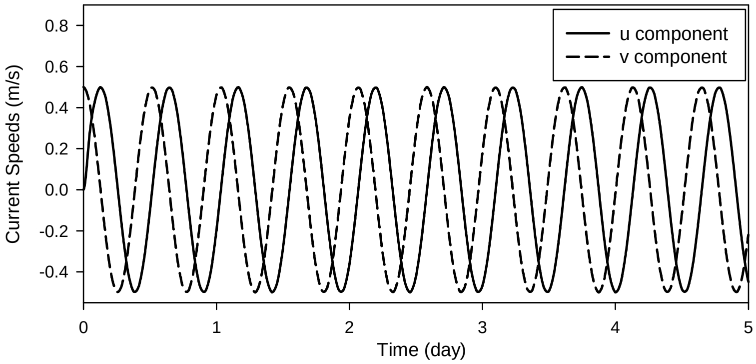

Figure 107: Time series of the rotary currents.

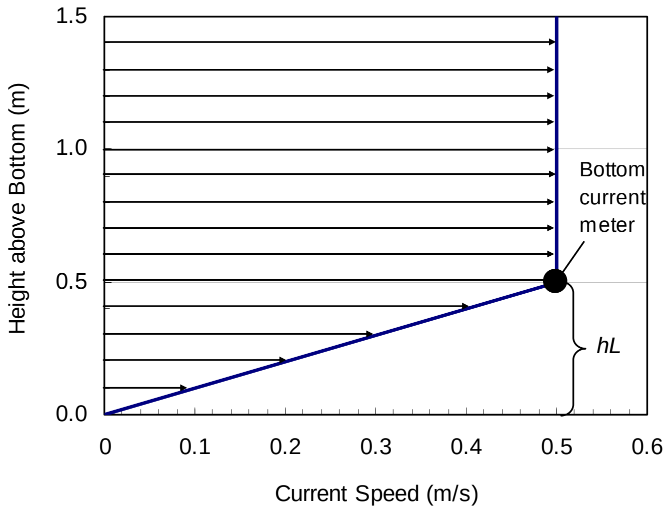

Figure 108: Near bottom current profile in bblt simulation.

6.3 Results

The predicted sediment concentrations by ParTrack and bblt at the end of the 4 day simulation are shown in Figure 109. The overall trend is that the sediment concentrations predicted by ParTrack are higher than those predicted by bblt. It can also be seen that there are noticeable differences in the location of concentration peaks. For example, the location of the peak predicted by ParTrack is about 2,000 m east of discharge while the location predicted by bblt is about 6,000 m east.

Although the contour plots give a whole picture of the concentration fields, the differences between the two models cannot be clearly determined. To compare the predictions more quantitatively, concentrations from four cross-sections (Figure 110) at times 1, 2, 3, and 4 days after discharge were compared. The sediment concentrations at the four cross-sections are shown in Figure 111 to Figure 114. It can be seen from Figure 111 that the concentration from ParTrack is indeed higher than that of the bblt. These differences are mainly seen at locations close to the center of mass (or concentration peaks). For locations far from the center, for example at 3,000 to 4,000 m away from the discharge point, both models give predictions within similar orders of magnitude. Also, the difference between the locations of two concentration peaks becomes more significant as time progresses. The locations of the two peaks are about the same at day 1. At 4 days after discharge, the bblt peak is at about 4,000 m east, while the ParTrack peak remains at about 1,000 m east. The figure also shows that the discharge depth did affect the concentrations predicted by ParTrack. This effect seems only important at locations close to the discharge point. The sensitivity of bblt to the log-layer file is depicted in Figure 111 by a comparison of the bblt-0.1m and bblt-0.5m curve. The concentration increased up to 5-fold with a small change of log-layer height.

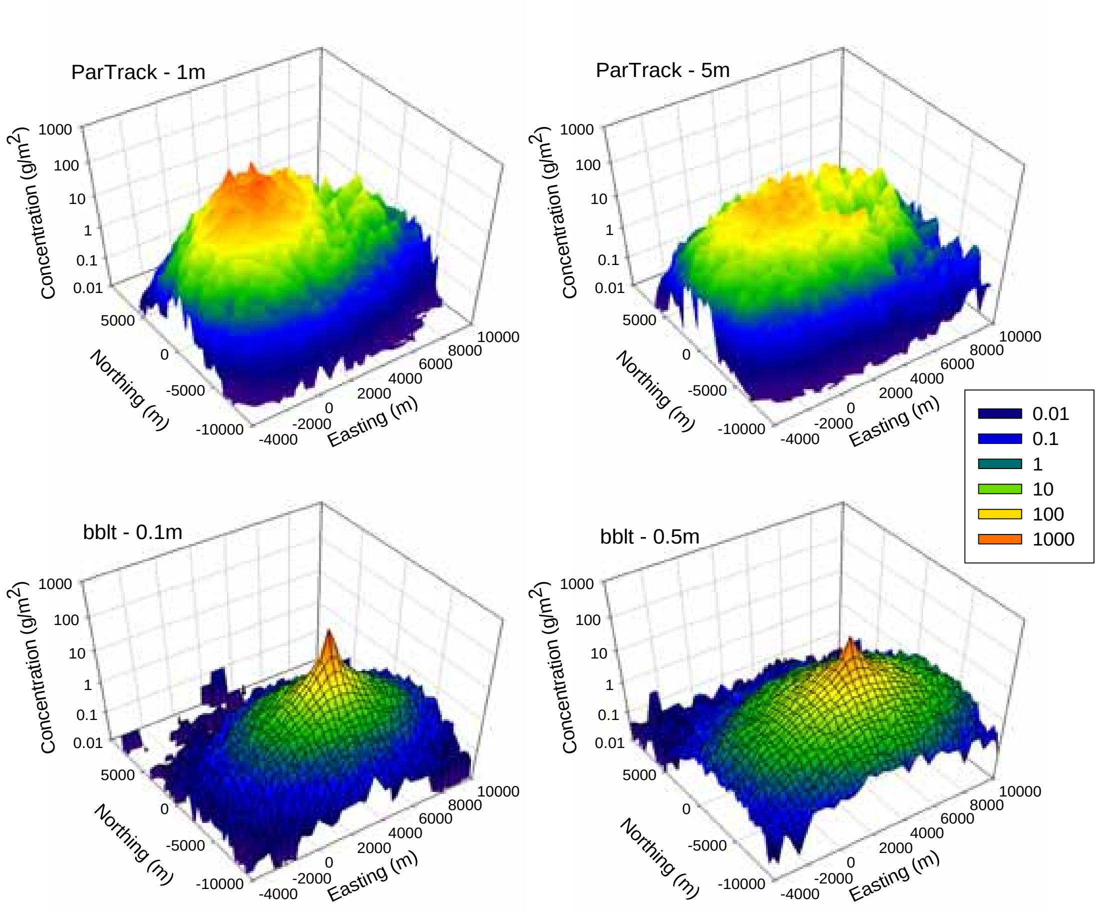

Figure 109: Contour plot of sediment concentration predicted by ParTrack and bblt.

The trend in Figure 112 is slightly different from Figure 111. While the bblt predicted lower concentration than ParTrack at both sides of the peak at cross-section I, it predicted higher concentration at the left side and lower concentration at the right side of the peak than ParTrack at cross-section II. This indicates that the locations of the two concentration peaks are divergent. It can be seen that the bblt peak is located to the south of the ParTrack peak. The trend for cross-section III is similar to cross-section I, except that there is no noticeable difference in peak locations for the two ParTrack cases at cross-section I, but the shift can be observed at cross-section III. The peak of the ParTrack-1m case is located about 500 m southwest of the ParTrack-5m case. The cross-section IV is also similar to cross-section II but with a noticeable difference of peak locations for the two ParTrack cases. The peak of the ParTrack-1m case is located about 500 m northwest of the ParTrack-5m case.

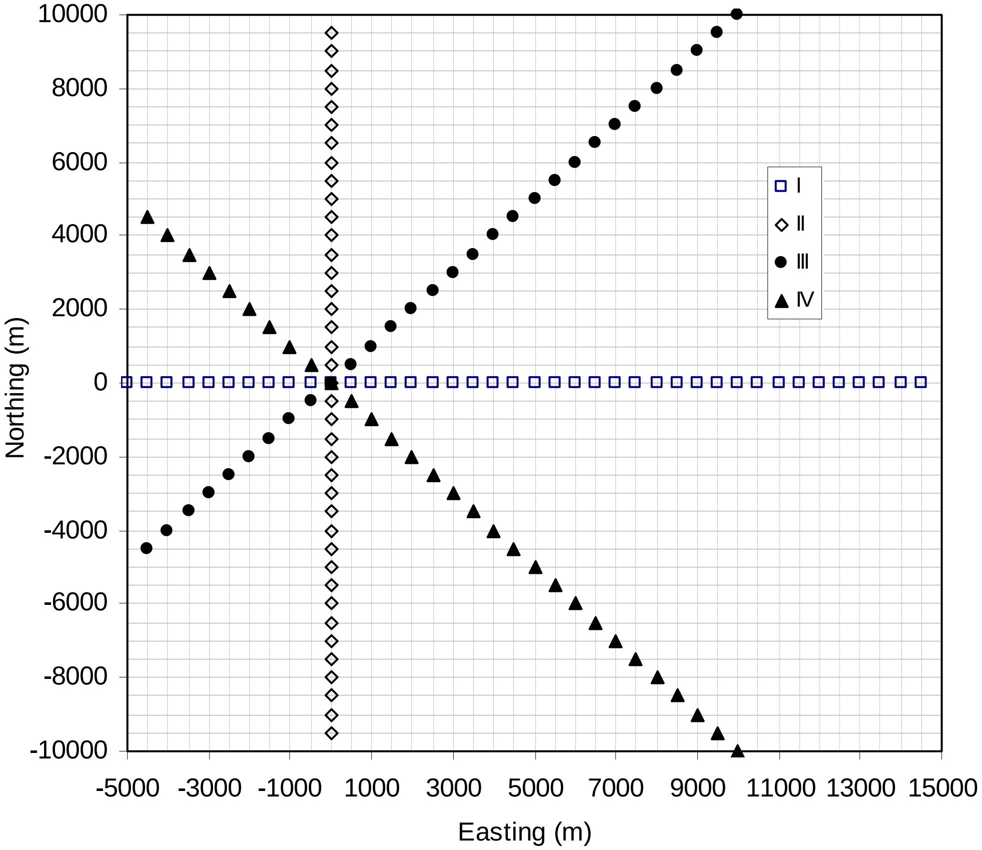

Figure 110: Locations of the four cross-sections for concentration comparison.

To find out the spatial extent of the spreading and how the concentration changes relative to the peak, the concentrations at cross-section I and II were adjusted by offsetting the bblt peak to the location of the ParTrack peak (Figure 115 and Figure 116). For cross-section I, the ranges impacted by the sediment are about the same (Figure 115). The concentration predicted by the two models shows similar trends and are about the same order of magnitude. This is especially true for locations at about 3,000 m away from the point of discharge. At locations closer than 3,000 m, the ParTrack concentration is up to 5 times that of the bblt. The trend for cross-section II is similar to that of cross-section I. However, the concentration difference for this cross-section is much smaller. The differences are only shown on days 3 and 4 at locations close to the peak. The two models agree well on days 1 and 2. In summary, the following results can be observed from the four simulations:

- Both ParTrack and bblt model are sensitive to some modeling parameters. For ParTrack, a slight change of discharge depth affected the predicted concentration, but this is only important for locations close to the concentration peak. The locations of concentration peak are also affected by changes in discharge depth. For the bblt model, the change of log-layer height has significant effects on the concentration throughout the simulation area. The concentrations increased up to 5-fold by changing the log-layer height from 0.1 to 0.5m.

- Although the model setup of bblt-0.1m is similar to ParTrack-1m, the two cases do not agree well. On the contrary, better agreement can be found between the bblt-0.5m and ParTrack-5m cases.
- The differences between the bblt and the ParTrack predictions are mainly the concentration near the peak, and the locations of the peak.

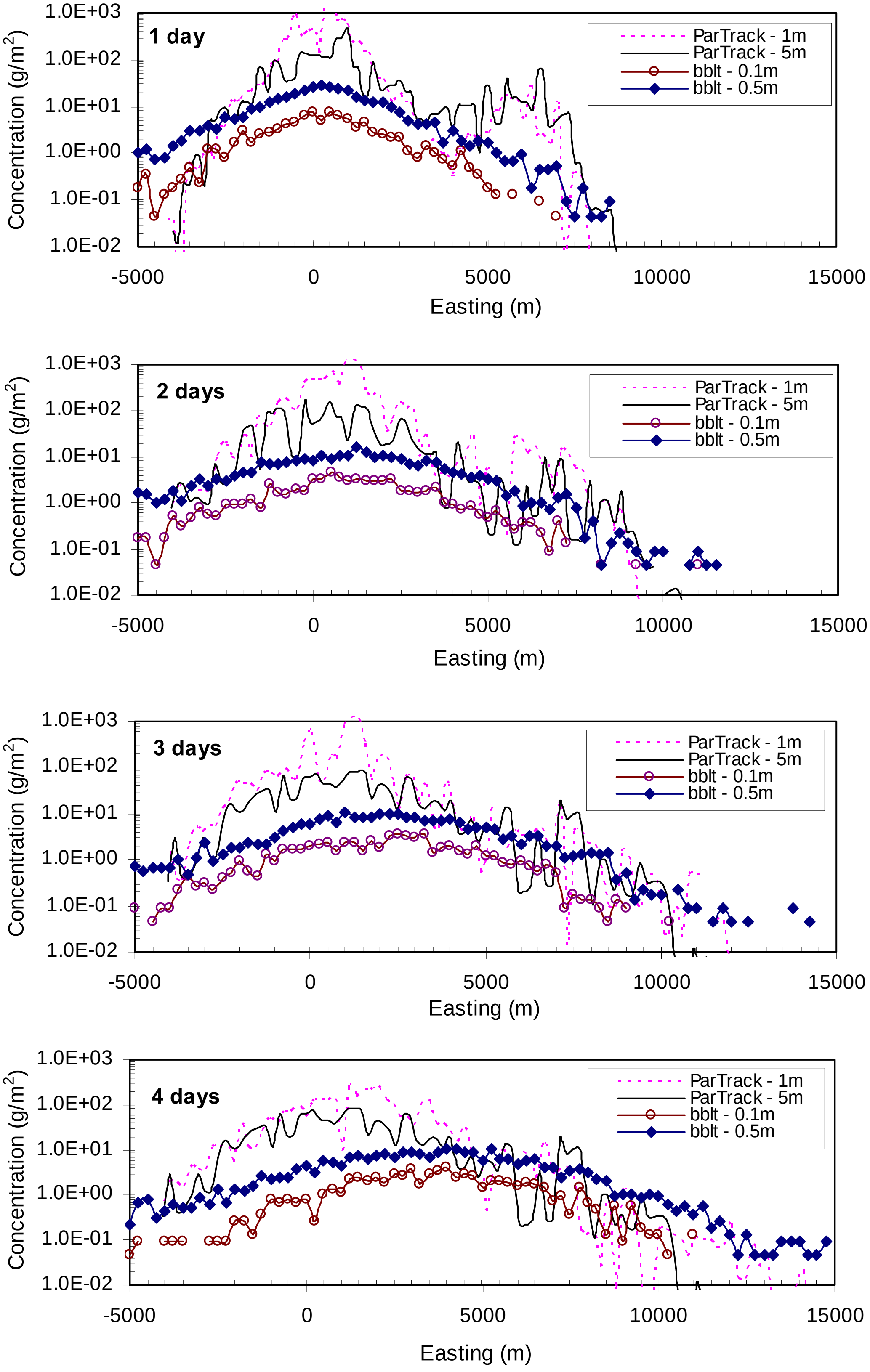

Figure 111: Predicted concentration for cross-section I.

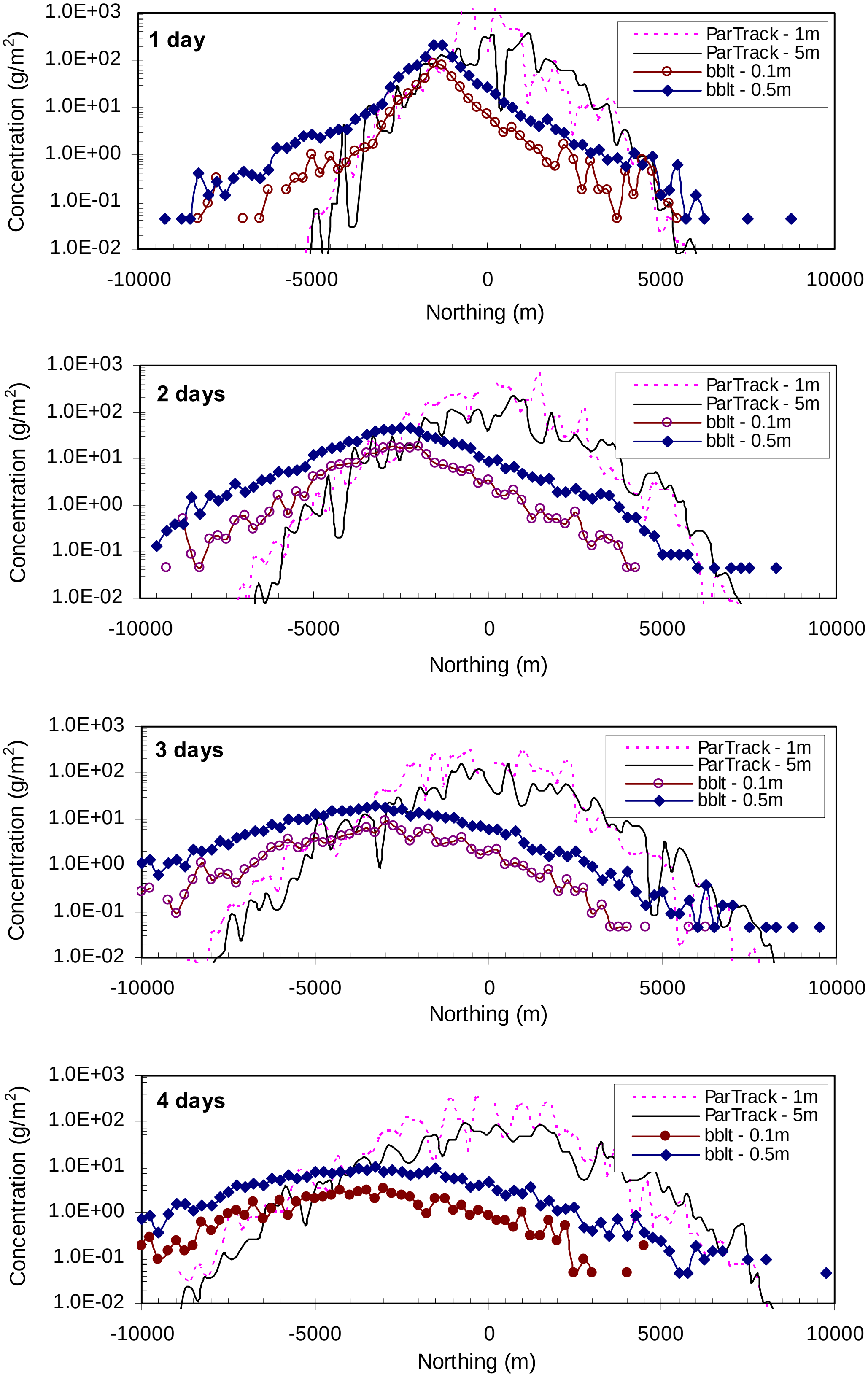

Figure 112: Predicted concentration for cross-section II.

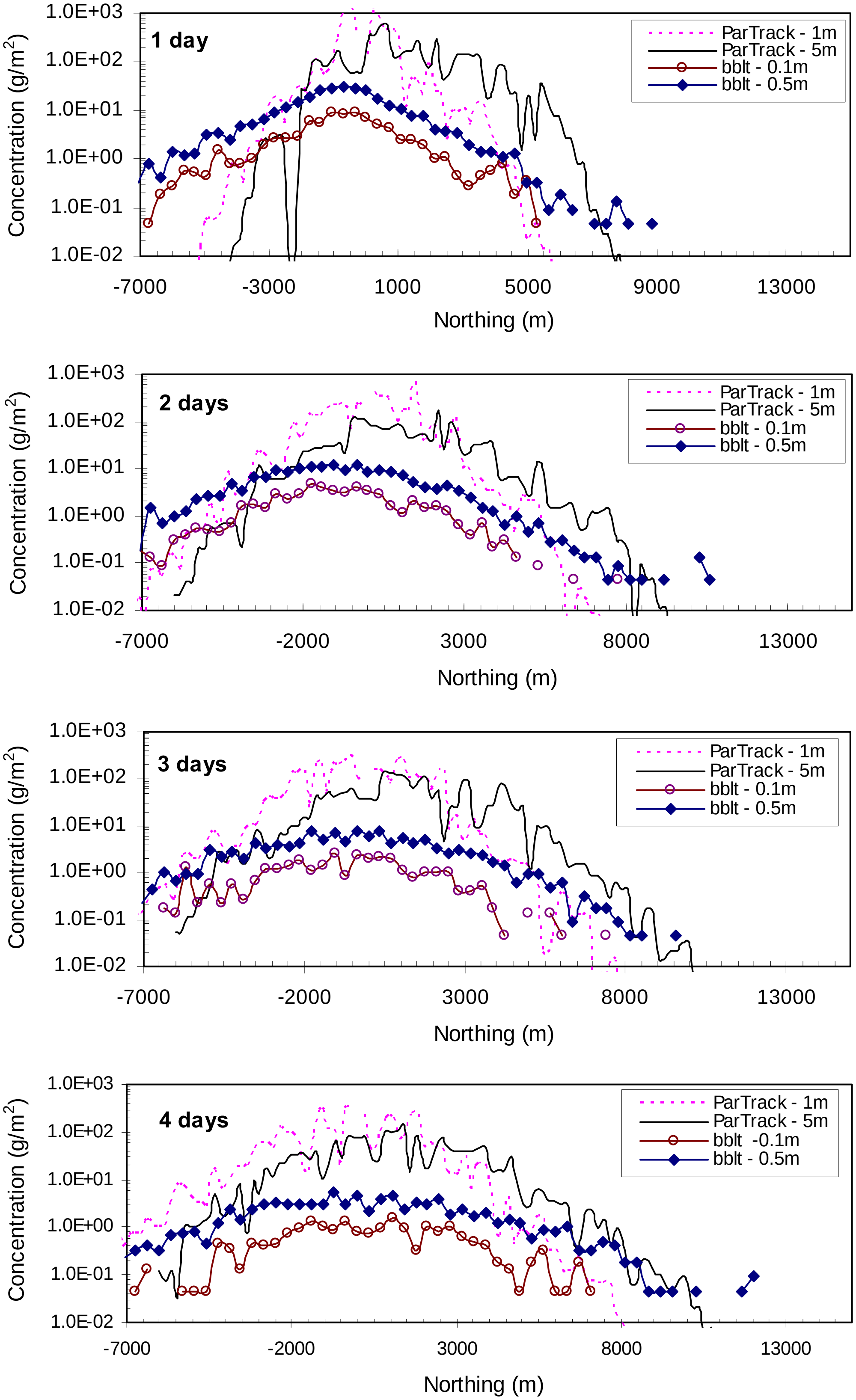

Figure 113: Predicted concentration for cross-section III.

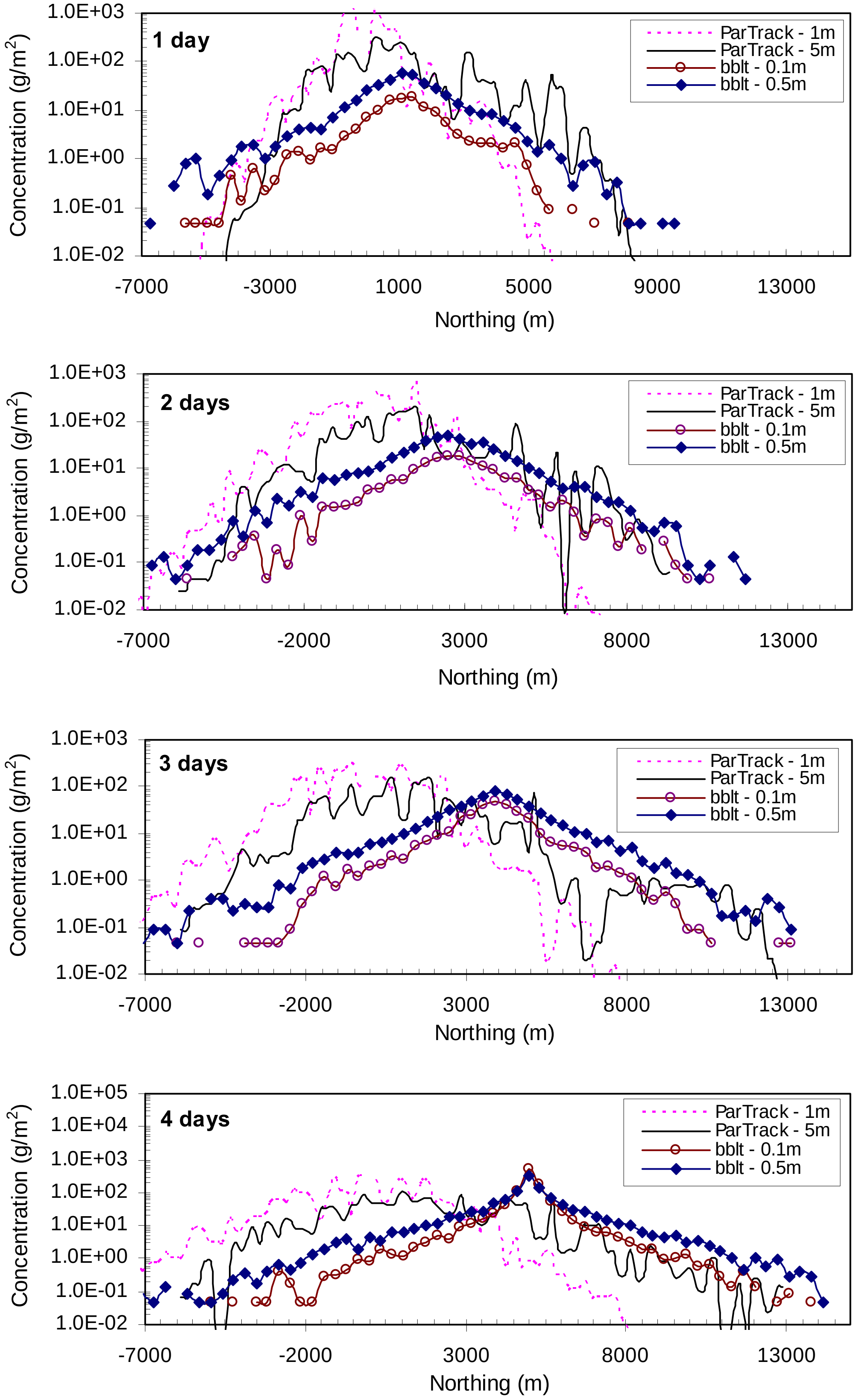

Figure 114: Predicted concentration for cross-section IV.

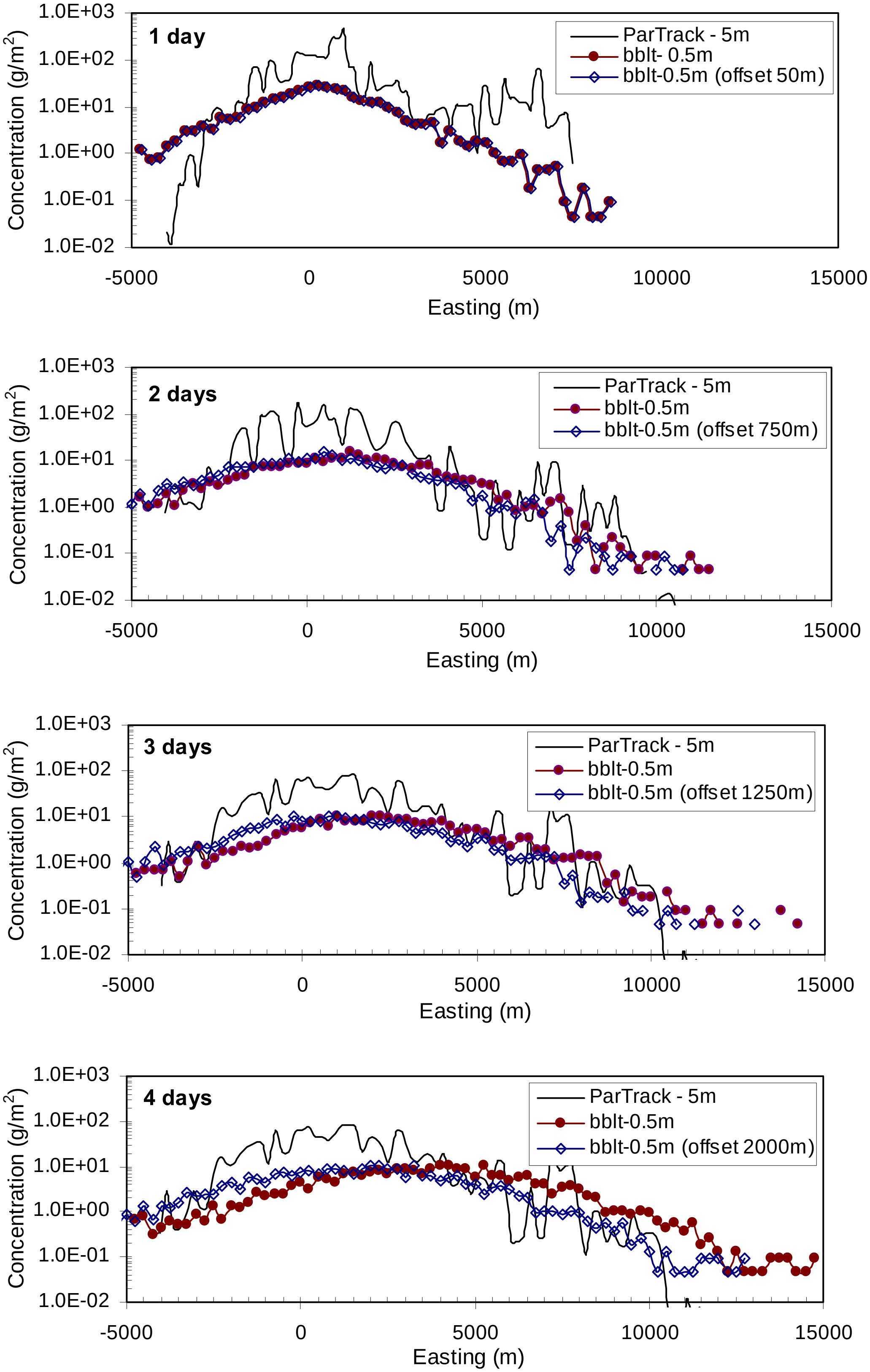

Figure 115: Concentration for cross-section I after offset.

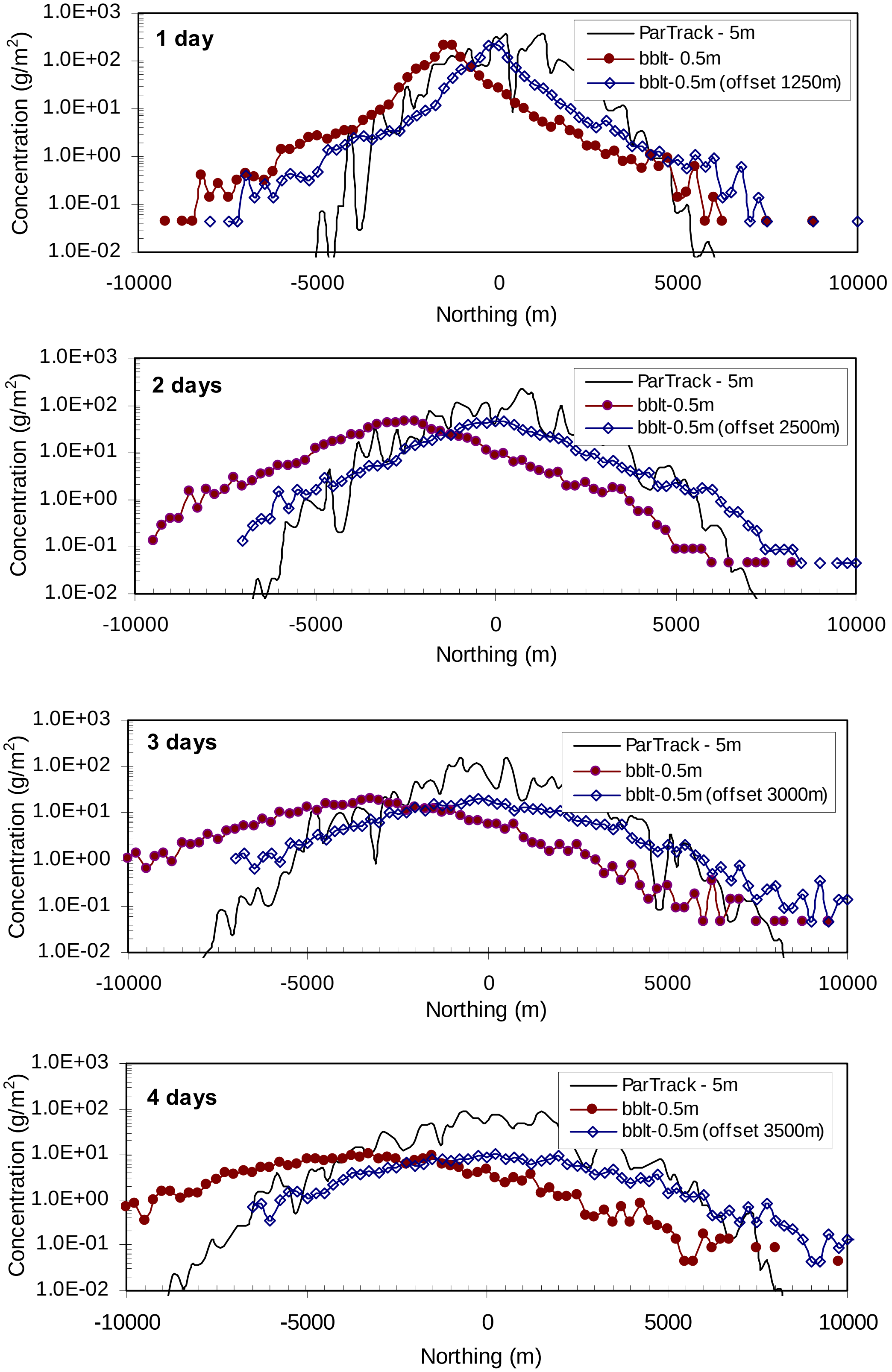

Figure 116: Concentration for cross-section II after offset.

6.4 Discussion

There are many factors that may contribute to the differences in the model predictions. First, the bblt underestimates the horizontal (lateral) diffusion. The horizontal dispersion in bblt is achieved by vertical shuffling of particles while they are advected by a non-uniform vertical current (Figure 117). For example, for an initial line of particles in a tidal period, the particles are tilted back and forth but there is no net dispersion in the absence of vertical mixing. On the other hand, horizontal dispersion can be achieved at the same time they are shuffled vertically in the presence of vertical mixing. It can be seen that this horizontal dispersion is only longitudinal at the direction of current and there is no lateral dispersion at directions perpendicular to the currents. In a special case of steady current with constant direction, one can imagine that the width of a plume predicted by bblt will be constant, while it is expected to expand laterally as well. While a higher concentration is expected with an underestimate of lateral dispersion, the concentrations predicted by bblt are generally lower than those of the ParTrack in this scenario. This implies that the underestimation of lateral dispersion is not a dominant factor here.

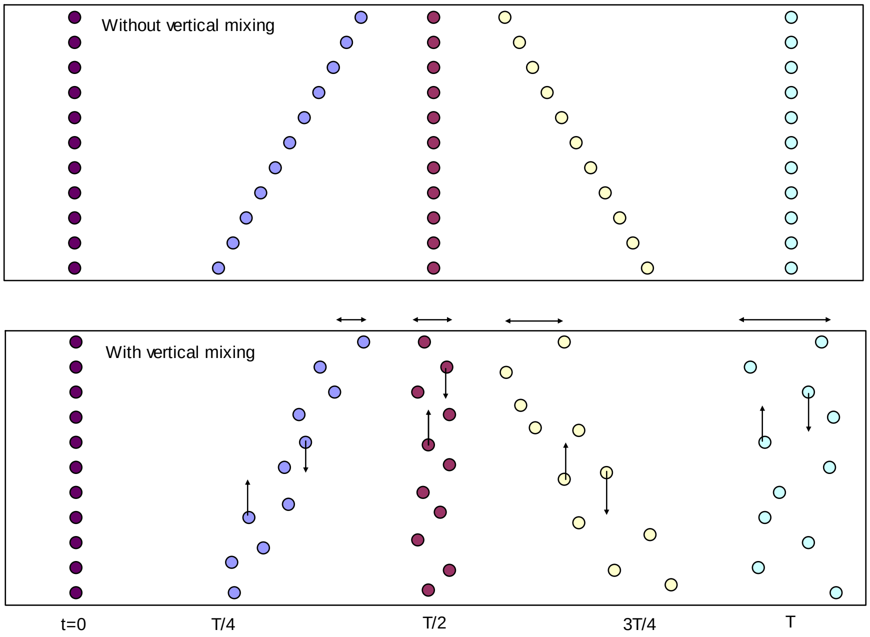

Figure 117: Schematic of shear dispersion mechanism in bblt model.

The second factor that affects the results is the log-layer height (Figure 111 to Figure 114). The current profile for bblt-0.1m was more similar to the ParTrack case. The two models had the same current profile for the upper 69.9 m and the only difference was within the bottom 0.1 m. However, the result of bblt-0.1m did not agree well with ParTrack. The reason is probably that the log-layer height was set too small and did not produce enough shear. Consider the case shown in Figure 118. If the log-layer is too small (*hL* = 0), the horizontal spreading will be very small (none for *hL* = 0). The only process that occurs is advection by currents. The increasing of the log-layer height increases the horizontal diffusion, but this will affect the advection because a smaller current within the log-layer will be used for advection. For this reason, the bblt-0.5m case gave more reasonable results and was in better agreement with ParTrack.

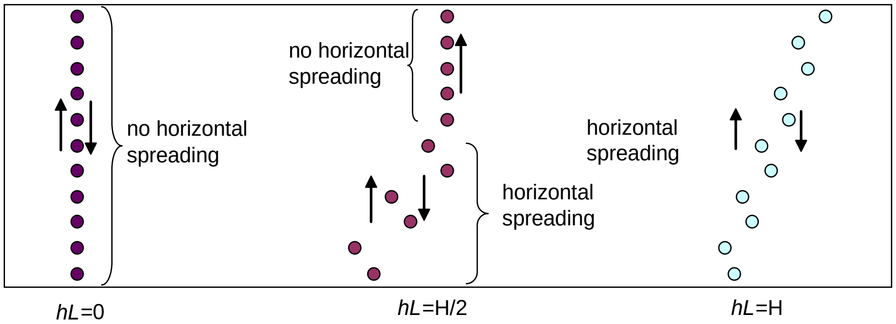

Figure 118: Effects of log-layer height on horizontal spreading.

Unlike the log-layer height for bblt, which is a more subjective parameter depending on the modeler, the 1 m and 5 m release depths for ParTrack were used for the purpose of setting up a near-bottom discharge case similar to bblt. The ParTrack-1m predicted higher peak concentration than ParTrack-5m. This was because the longer distance to the bottom gave ParTrack-5m more time to advect the particles in the water column. As a result, the ParTrack-5m case had less barite accumulation near the discharge point.

To further investigate the difference in prediction, it is worth studying the trajectory of the particles. Figure 119 shows the trajectories of particles predicted by the two models after one rotary cycle. The predicted trajectories are very similar and agree well. The trajectory circle predicted by the ParTrack model is slightly larger than that of the bblt. This is probably due to a stronger bottom current used in the ParTrack model. Although the trajectories are similar, the contour plots show differences in sediment concentration (Figure 120). The trajectory circle can be identified in the ParTrack contour but it is not observed in the bblt contour. The results imply that ParTrack predicted deposition of barite particles on the seabed while they were advected and diffused. However, the dominant mechanisms in the bblt simulation were advection and diffusion, while deposition was insignificant. The deposition shown in Figure 120 along the ParTrack trajectory also explains the double concentration peak in Figure 111 and Figure 115 that occurred at day 1 after discharge. As time progressed, the deposited material was re-suspended and redistributed. The double peak pattern started to diminish during this process and cannot be seen in the plots at later time steps. The deposition of barite at locations close to the discharge point by ParTrack also explains why ParTrack predicted higher concentrations than bblt near the concentration peak.

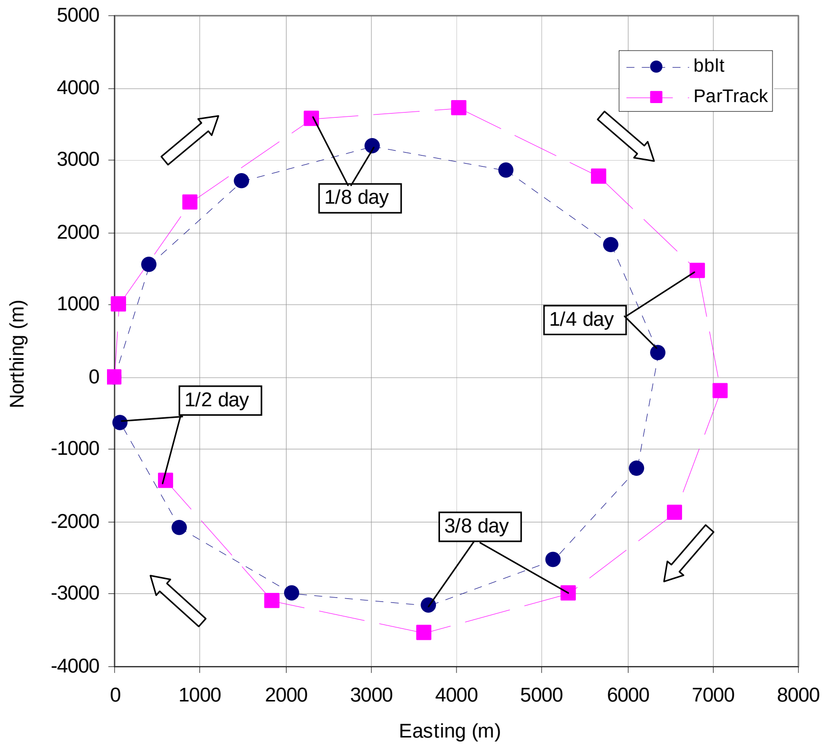

Figure 119: Trajectory of suspended particles as predicted by bblt and ParTrack.

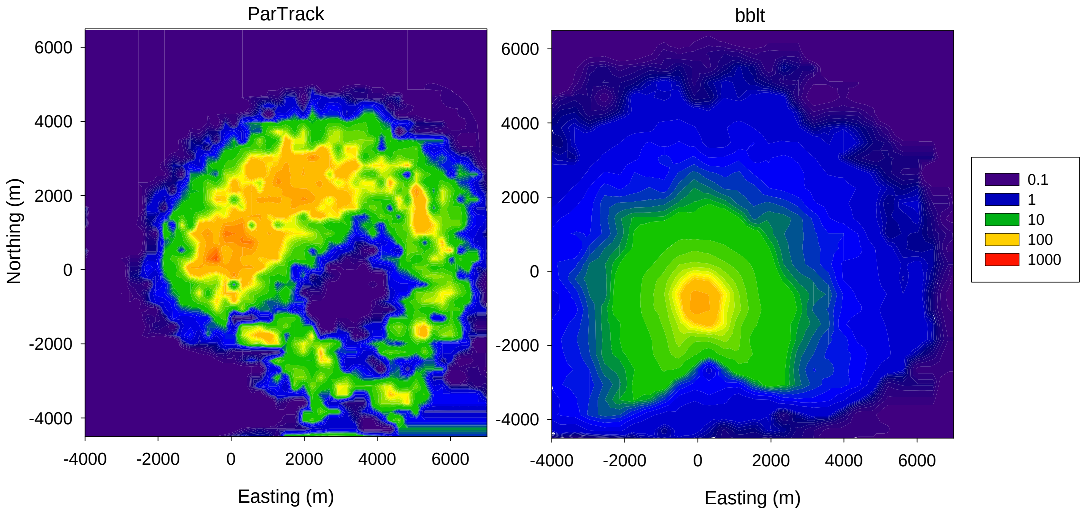

Figure 120: Contour plot of sediment concentration (g/m^2) at 0.5 day after discharge.

6.5 Conclusions

To cross-validate the ParTrack and bblt model, a case study was conducted to simulate a near bottom discharge of barite under a rotary current of 0.5 m/s. Two bblt scenarios with different log-layer heights, and two ParTrack scenarios with different discharge depths were the focus of the study.

The results showed that while the discharge depth affects the sediment concentration in the ParTrack simulation, the bblt model seems to be more highly affected by the log-layer height. Although ParTrack and bblt are formulated quite differently, the case study shows that the bblt-0.5m case is comparable to that of ParTrack, especially for locations in the far field. At locations close to the discharge point, ParTrack predicted higher concentration due to the deposition of particles. On the contrary, bblt did not predict significant deposition and the dominant transport mechanisms were advection and diffusion. The two models also predicted a similar extent of spreading. The major difference between the two models was the location of the center of mass or the peak of concentration. Although the possible factors that may contribute to the differences in model predictions have been identified, the environmental significance of these factors has not been evaluated.

Discharge depth is an important parameter that may affect results; therefore, the application of bblt must be limited to near-bottom discharge as the effect of release depth is not modeled in the current version of the model. The case studied in this work was under a spatially constant current due to the limitation of present version of bblt. A 3D version of bblt is being developed and a similar comparison study using the 3D version under a spatially changing current is needed for further cross-validation of the two models.

7. Summary and Recommendations

The DREAM model was cross-validated with CORMIX (for produced water) and bblt (for drilling muds). Although agreements have been found in general for cases with small densimetric Froude numbers (*Fr*) and small velocity ratios (*K*), significant differences were found under other conditions. This prompted further validation of DREAM with measured data or other models.

The validation of DREAM with field data from Venture was performed and good agreements were found. The limitation is of the comparison is that the amount of data available for validation is limited for the Venture case.

The further comparison with Terra Nova data shows reasonably good agreements but there is a consistent trend of slight underestimation of environmental concentration at 10 m. Due to the model's limitation on single value background data input, the model fails to explain the observed consistent high concentration near bottom (80 m).

Toxicity tests using produced water collected from Atlantic Canada have been conducted and the results were incorporated into the model, allowing a more reliable estimation of potential environmental impacts.

The comparison of DREAM with bblt indicated that although DREAM and bblt are formulated quite differently, the case study shows that the bblt-0.5m case is comparable to that of ParTrack, especially for locations in the far field. Both the densimetric Froude number and the velocity ratio can affect the dilution ratio for a given discharge rate, therefore it is recommended to conduct a series of simulations with different Froude numbers in the design of produced water outfall by varying port diameter (*D*) and discharge velocity (U_j) to maximize the dilution and minimize environmental impacts.

Acknowledgement

Financial support from the Environmental Studies Research Funds (ESRF), Panel of Energy Research and Development (PERD), and ExxonMobil Canada are greatly appreciated. SINTEF Marine Environmental Research is thanked for providing the Marine Environmental Modeling Workbench (MEMW) software. We gratefully acknowledge Peter Thamer for his technical assistance in the field and laboratory; Jennifer Mason and Thomas King for organic chemistry analysis; Byron Amirault for metal analysis; Xiaowei Ma for microbiological analysis; Carol Anstey for nutrient analysis; Rod Doane and Gary Wohlgeschaffen for logistical coordination and editorial assistance.

References

Bowden, K.F. 1983. *Physical Oceanography of Coastal Waters*. Ellis Hardwood Ltd UK. 312 p.

Brandsma, M. G., Saucer, R. C., 1983. The OOC model: Prediction of short term fate of drilling fluids in the ocean. Proceedings of Mineral Management Service Workshop on Discharged Modeling, Santa Barbara, CA, U.S., February 7-10, 1983.

Clark, C.E., and Veil, J.A. 2009. Produced Water Volumes and Management Practices in the United States. Report prepared by Environmental Science Division, Argonne National Laboratory for U.S. Department of Energy, Office of Fossil Energy, National Energy Technology Laboratory. Available from http://www.ead.anl.gov/pub/doc/ANL_EVS__R09_produced_water_volume_report_2437.pdf

Csanady, G. T., 1973. Turbulent Diffusion in the Environment. D. Reidel Publishing Company.

Doneker, R.L., and G.H. Jirka, 1990. *Expert System for Hydrodynamic Mixing Zone Analysis of Conventional And Toxic Submerged Single Port Discharges (CORMIX1)*, U.S. Environmental Protection Agency, EPA/600/3-90/012, February 1990.

Doneker, R.L. and G.H. Jirka, 2007. CORMIX User Manual: A Hydrodynamic Mixing Zone Model and Decision Support System for Pollutant Discharges into Surface Waters. US EPA Report EPA-823-K-07-001.

Drozdowski, A., Hannah, C., Tedford, T., 2004. bblt Version 7 user's manual. Canadian Technical Report of Hydrography and Ocean Science, 69 pp.

Ichiye, T. 1967. Upper Ocean Boundary Layer Flow Determined by Dye Diffusion, *Physics of Fluids Supplement*, *10*, pp. 270-277.

Jirka, G. H., 2004. Integral Model for Turbulent Buoyant Jets in Unbounded Stratified Flows, Part I: Single Round Jet, *Environmental Fluid Mechanics,* 4(1): 1-56.

Johansen, Ø., Durgut, I., 2006. Implementation of the near-field module in the ERMS model. ERMS Report No. 23, SINTEF Marine Environmental Technology, Norway. Available from http://www.sintef.com/project/ERMS/Reports/ERMS report no 23_ Near-field module.pdf

Jones, J. M., Jirka, G. H., and Caughey, D. A. 1983. *Numerical Techniques for Steady Two-Dimensional Transcritical Stratified Flow Problems, with an Application to the Intermediate Field Dynamics of Ocean Thermal Energy Conservation Plants*, Technical Report, School of Civil and Environmental Engineering, Cornell University, Ithaca, New York, U.S.

Lee, J. H. W., and Chu, V. H., 2003. *Turbulent Jets and Plumes: A Lagrangian Approach*, Kluwer Academic Publishers.

Lee, K., and Neff, J. 2011. *Produced Water: Environmental Risks and Advances in Mitigation Technologies*. Springer.

Nedwed, T.J., Smith, J.P., and Brandsma, M.G., (2004). Verification of the OOC Mud and Produced Water Discharge Model using Lab-scale Plume Behaviour Experiments. *Environmental Modelling & Software*, 19:655-670.

Reed, M., and B. Hetland, 2002. DREAM: a Dose-related Exposure Assessment Model Technical Description of Physical-Chemical Fates Components", In *Proceedings of the SPE International Conference on Health, Safety and Environment in Oil and Gas Exploration and Production*, Kuala Lumpur, Malaysia, 23 pages.

Rye, H., Reed, M., Frost, T. K., Utvik, T. I. R., 1998. Comparison of the ParTrack mud/cuttings release model with field data based on use of synthetic-based drilling fluids. *Environmental Modelling & Software*, 21, 190-203.

Smit, M.G., Frost, T.K., and Johnsen, S., 2011. Achievements of risk-based produced water management on the Norwegian continental shelf (2002-2008). Integrated *Environmental Assessment and Management*, 7(4): 668-677.

Sundt, R.C., Ruus, A., Jonsson, H., Skarphéðinsdóttir, H., Meier, S., Grung, M., Beyer, J., Pampanin, D.M. 2012. Biomarker responses in Atlantic cod (Gadus morhua) exposed to produced water from a North Sea oil field: laboratory and field assessments. *Marine Pollution Bulletin*, 64(1):144-152.